Revealing the conversion mechanisms in metal-sulfur batteries

via computational methodology and in-situ spectroscopy

Huan Li

A thesis submitted for the degree of Doctor of Philosophy

School of Chemical Engineering and Advanced Materials

The University of Adelaide

October 2022

Table of Contents

Abstracts

Rechargeable metal-sulfur batteries are composed of a metal anode and a sulfur cathode. They present the merits of high energy and low cost, however, the practical applications are still impeded by low specific capacity, a large dosage of electrolyte, and unsatisfactory cycling stability. This is possibly due to the unclear mechanistic insights into the conversion reactions in metal-sulfur batteries. The instability of both polysulfides intermediates and metallic anode under atmosphere restricts comprehensive characterizations and deep understandings. This leads to the lack of targeted designs for metal anode and sulfur cathode, for example, the host materials for metal anode and catalysts for sulfur cathode. This thesis developed a series of in-situ spectroscopic techniques and computational methodologies to explore the conversion mechanisms in metal-sulfur batteries, which provides fundamental knowledge and practical inspirations for battery applications.

First, we innovatively employed the in-situ synchrotron X-ray diffraction, in-situ Raman spectroscopy, in-situ electrochemical impedance spectra and theoretical computations to obtain better understanding of the Li nucleation/deposition processes. A design principle was suggested for Li host to overcome the electrolyte loss, that is, uneven growth of Li structure and the crack of SEI layer must be simultaneously controlled. Benefitting from the 3D low-surface-area defective graphene host, Li metal anode achieves stable cycles (e.g., 1.0 mAh cm^{-2}) with a low electrolyte loading (10 μL).

Second, we demonstrate, for the first time, the reversible sulfur oxidation process in $AlCl_3$/carbamide ionic liquid, where sulfur is electrochemically oxidized by $AlCl_4^-$ to form $AlSCl_7$. The reaction pathways, $AlSCl_7$ oxidized products, and SCl_3^+ intermediates are well

confirmed by means of in-situ synchrotron-based analysis, high-resolution microscopic images, spectroscopic analysis, and theoretical computations. The sulfur oxidation is: 1) highly reversible with an efficiency of ~94%; and 2) workable within a wide range of high potentials. As a result, the Al−S battery based on sulfur oxidation can be cycled steadily around ~1.8 V, which is the highest operation voltage in Al−S batteries.

Third, we formulate for the first time, design principles to boost electrocatalytic sulfur reduction reaction (SRR) activity by controlling the Gibbs free energy of polysulfide species in a group of 3d unary and binary transition-metal clusters. SRR reactivity trend is established through a quantitative correlation of 3d-orbital charges with Gibbs free energy and catalytic activity. The design principles and reactivity trend are 1) readily applied to boost SRR activity through adjustment of natural material property, and 2) appear universal for rational design of more-efficient catalysts.

Fourth, we have proposed a general rule to boost lean-electrolyte sulfur reduction by controlling the catalyst-solvent interactions. As evidenced by synchrotron-based analysis, in-situ spectroscopy and theoretical computations, the catalyst-solvent binding strength plays a crucial role in lean-electrolyte performance. Benefitting from the strong interaction between solvent molecules and cobalt catalyst, the lithium−sulfur battery achieves stable cycling with only 0.22% capacity decay per cycle under lean-electrolyte conditions. Compared to the battery with flooded electrolyte, the lean-electrolyte battery with an electrolyte/sulfur mass ratio of 4.2 maintains 79% capacity, which is the highest capacity retention among systems with lowest electrolyte dosages reported so far.

Last, we demonstrate the SRR catalyst failure caused by electrophilic substitution

between polysulfides and catalyst. This leads to the surface vulcanization of catalyst and more severely, the concomitant catalyst dissolution into electrolyte. Unlike other conventional electrocatalytic reactions, the failure of SRR catalyst does not depend on applied overpotentials. It is confirmed via a series of operando techniques including in-situ synchrotron X-ray diffraction, Infrared and ultraviolet–visible spectra together with theoretical computations. The proposed catalyst failure mechanism is universally extended to 3d, 4d and 5d (e.g. Co, Rh and Pt) metal catalysts.

Declaration

I certify that this work contains no material which has been accepted for the award of any other degree or diploma in my name, in any university or other tertiary institution and, to the best of my knowledge and belief, contains no material previously published or written by another person, except where due reference has been made in the text. In addition, I certify that no part of this work will, in the future, be used in a submission in my name, for any other degree or diploma in any university or other tertiary institution without the prior approval of the University of Adelaide and where applicable, any partner institution responsible for the joint award of this degree.

The author acknowledges that copyright of published works contained within the thesis resides with the copyright holder(s) of those works.

I give permission for the digital version of my thesis to be made available on the web, via the University's digital research repository, the Library Search and also through web search engines, unless permission has been granted by the University to restrict access for a period of time.

I acknowledge the support I have received for my research through the provision of an Australian Government Research Training Program Scholarship.

Name of Candidate: Huan Li

Signature:

Date: 20/June/2022

Acknowledgments

This thesis would not be accomplished without the support and help from my supervisors, friends, and families. Here, I would like to express my gratitude to them all.

First and foremost, I would like to thank my principal supervisor, Professor Shi-Zhang Qiao, for his inspiring guidance, supportive encouragement, and professional supervision throughout my PhD candidature. He also gives me the room to take challenge and adventure when conducting research in some emerging fields, which I appreciate the most during my study. I could not get any achievements without his guidance and support in my PhD study. And I will benefit from his training as a researcher in my future career. I sincerely appreciate my co-supervisor Dr. Jingrun Ran, for her insightful suggestions and continuous encouragement.

I am also grateful to all the members in Qiao's group who give me many supports and suggestions during my PhD study. Many thanks go to Dr. Yan Jiao, Dr. Xing Zhi and Dr. Xin Liu for their great help in theoretical computations; many thanks to Prof. Dongliang Chao for his guidance and discussion; many thanks to Dr. Chao Ye's helpful discussion on metal-sulfur batteries; many thanks to Dr. Jieqiong Shan, Mrs Xin Xu for encourage and daily help; many thanks to Dr. Junnan Hao and Dr. Fangxi Xie for the synchrotron analysis. I would like to thank all the battery group members Jiahao Liu, Chun-Chuan Kao, Shao-Jian Zhang and Han Wu for their help. Also, I would like to thank all the group members from "electrocatalysis or photocatalysis group" that allows draw their experiences and inspirations into metal-sulfur batteries. For example, Dr. Yao Zheng, Dr. Huanyu Jin, Dr. Cheng Tang, Dr. Pengtang Wang, Mr. Xianlong Zhou, Dr. Laiquan Li, Mr. Dazhi Yao, Mr. Yanzhao Zhang,

Chapter 1: Introduction

1.1 Significance of this project

Rechargeable metal-sulfur batteries present high energy density and low cost, which hold great promise for next-generation battery application beyond lithium-ion batteries.[1-5] However, the practical uses are still impeded by low specific capacity, a large dosage of electrolyte, and unsatisfactory cycling stability.[6-8] This is possibly due to the unclear mechanistic insights into the conversion reactions in metal-sulfur batteries.[9-11] This thesis developed a series of in-situ spectroscopic techniques and computational methodologies to explore the conversion mechanisms in metal-sulfur batteries, which provides fundamental knowledge and practical inspirations for battery applications.[12, 13]

This thesis will contribute to:

➢ *An innovative guidance* to design stable lithium metal anode under lean-electrolyte conditions, which will help to improve the energy density of Li-S batteries.

➢ *A better understanding* of novel sulfur chemistry in Al-S batteries, improving the operation voltage of Al-S batteries.

➢ *A deep mechanistic insight* into the sulfur reduction electrocatalysis in Li-S batteries, which clarifies the activity origin and catalyst design principles.

➢ *A clear demonstration* for the interaction between metal catalysts and electrolyte solvent in sulfur reduction electrocatalysis, which will contribute to the design of lean-electrolyte Li-S batteries.

➢ *A comprehensive operando investigation* on the catalyst failure for sulfur reduction electrocatalysis, guiding the future design of more durable electrocatalyst in Li-S batteries.

1.2 Research objectives

The main goal of this thesis is to reveal the conversion mechanisms in metal-sulfur batteries by developing a series of in-situ spectroscopy and computational methodology. In particular, the objectives of this thesis are:

✧ To investigate the Li plating/stripping process under lean-electrolyte conditions and to suggest a design principle for Li host design to overcome the electrolyte loss.

✧ To explore the sulfur oxidation chemistry and improve operation voltage of Al-S batteries.

✧ To clarify the activity origin of catalysts in sulfur reduction electrocatalysis and to suggest a catalyst design principle for further design of catalysts.

✧ To reveal the interactions between SRR catalysts and electrolyte solvent and improve the Li-S battery performances under lean electrolyte conditions.

✧ To unravel catalyst failure in sulfur reduction electrocatalysis and explore the design of more durable catalysts for long-life Li-S batteries.

1.3 Thesis outline

This thesis is presented in the form of journal publications. It contains research results on battery tests, in-situ spectra, density functional theory (DFT) computations and synchrotron analysis in metal-sulfur batteries. Recent progress and challenges were reviewed, followed by discussions and prospective of further develop of metal-sulfur batteries. Specifically, the chapters in the Thesis are presented in the following sequence:

■ *Chapter 1* introduces the significance of this project, research objectives and key contributions to the understanding of reaction mechanisms in metal-sulfur batteries.

■ *Chapter 2* reviews the recent progresses and challenges of conversion mechanisms in metal-sulfur batteries, especially using in-situ spectroscopy and theoretical computations.

■ *Chapter 3* presents a principle for design lean-electrolyte lithium metal anode via in-situ spectroscopy.

■ *Chapter 4* demonstrates the reversible sulfur electrochemical oxidation in ionic liquid for high-voltage Al-S batteries.

■ *Chapter 5* clarifies the activity origin and proposes catalyst design principle for sulfur reduction electrocatalysis.

■ *Chapter 6* reveals a mechanistic insight into the catalyst-solvent interactions for design of lean-electrolyte sulfur reduction electrocatalysts.

■ *Chapter 7* unravels the mechanism of catalyst failure in sulfur reduction electrocatalysis.

■ *Chapter 8* presents the conclusion and perspectives for further work on revealing the conversion mechanism in metal-sulfur batteries.

1.4 References

1. Chung, S.-H.; Manthiram, A., Current Status and Future Prospects of Metal-Sulfur Batteries. *Advanced Materials* **2019,** *31* (27), 1901125.

2. Salama, M.; Rosy; Attias, R.; Yemini, R.; Gofer, Y.; Aurbach, D.; Noked, M., Metal-Sulfur Batteries: Overview and Research Methods. *ACS Energy Letters* **2019,** *4* (2), 436-446.

3. Yu, X.; Manthiram, A., A Progress Report on Metal-Sulfur Batteries. *Advanced Functional Materials* **2020,** *30* (39), 2004084.

4. Hong, X.; Mei, J.; Wen, L.; Tong, Y.; Vasileff, A. J.; Wang, L.; Liang, J.; Sun, Z.; Dou, S. X., Nonlithium Metal-Sulfur Batteries: Steps Toward a Leap. *Advanced Materials* **2019,** *31* (5), 1802822.

5. Yu, X.; Manthiram, A., Ambient-Temperature Energy Storage with Polyvalent Metal-Sulfur Chemistry. *Small Methods* **2017,** *1* (11), 1700217.

6. Zhao, M.; Li, B. Q.; Peng, H. J.; Yuan, H.; Wei, J. Y.; Huang, J. Q., Lithium-Sulfur Batteries under Lean Electrolyte Conditions: Challenges and Opportunities. *Angewandte Chemie International Edition* **2020,** *59* (31), 12636-12652.

7. Zhao, C.; Xu, G.-L.; Yu, Z.; Zhang, L.; Hwang, I.; Mo, Y.-X.; Ren, Y.; Cheng, L.; Sun, C.-J.; Ren, Y.; Zuo, X.; Li, J.-T.; Sun, S.-G.; Amine, K.; Zhao, T., A High-energy and Long-cycling Lithium–sulfur Pouch Cell via a Macroporous Catalytic Cathode with Double-end Binding Sites. *Nature Nanotechnology* **2020,** *16*, 166-173.

8. Ye, C.; Jin, H.; Shan, J.; Jiao, Y.; Li, H.; Gu, Q.; Davey, K.; Wang, H.; Qiao, S.-Z., A Mo_5N_6 Electrocatalyst for Efficient Na_2S Electrodeposition in Room-Temperature Sodium-Sulfur Batteries. *Nature Communications* **2021,** *12* (1), 7195.

9. Peng, L.; Wei, Z.; Wan, C.; Li, J.; Chen, Z.; Zhu, D.; Baumann, D.; Liu, H.; Allen, C. S.; Xu, X.; Kirkland, A. I.; Shakir, I.; Almutairi, Z.; Tolbert, S.; Dunn, B.; Huang, Y.; Sautet, P.; Duan, X., A Fundamental Look at Electrocatalytic Sulfur Reduction Reaction. *Nature Catalysis* **2020,** *3* (9), 762-770.

10. Chen, H.; Wu, Z.; Zheng, M.; Liu, T.; Yan, C.; Lu, J.; Zhang, S., Catalytic Materials for Lithium-sulfur Batteries: Mechanisms, Design strategies and Future perspective. *Materials Today* **2022,** *52*, 364-388.

11. Zhang, L.; Qian, T.; Zhu, X.; Hu, Z.; Wang, M.; Zhang, L.; Jiang, T.; Tian, J. H.; Yan, C., In situ Optical Spectroscopy Characterization for Optimal Design of Lithium-sulfur Batteries. *Chem Soc Rev* **2019,** *48* (22), 5432-5453.

12. Li, H.; Chao, D.; Chen, B.; Chen, X.; Chuah, C.; Tang, Y.; Jiao, Y.; Jaroniec, M.; Qiao, S.-Z., Revealing Principles for Design of Lean-Electrolyte Lithium Metal Anode via In situ Spectroscopy. *Journal of the American Chemical Society* **2020,** *142* (4), 2012-2022.

13. Li, H.; Meng, R.; Guo, Y.; Chen, B.; Jiao, Y.; Ye, C.; Long, Y.; Tadich, A.; Yang, Q.-H.; Jaroniec, M.; Qiao, S.-Z., Reversible Electrochemical Oxidation of Sulfur in Ionic Liquid for High-voltage Al−S Batteries. *Nature Communications* **2021,** *12* (1), 5714.

Chapter 2: Literature Review

2.1 Introduction of metal-sulfur batteries

Sulfur is often an industrial waste with megaton stockpiles accumulating on earth.[1-5] It is a widely available but underused material.[6-9] It is critical to convert it into renewable energy and useful chemicals.[10-14] This would benefit environmental sustainability, waste valorisation and energy-related applications. Sulfur is quite stable and an insulator under atmosphere. Therefore, it is essential to design targeted catalysts for diverse sulfur reactions. Electrocatalytic sulfur conversion is an emerging new electrochemical process, where catalyst promotes sulfur conversions driven by electric fields (**Figure 1a**).[2] This process produces electrical energy or value-added chemicals. For example, electrocatalytic sulfur conversions have been widely used in metal-sulfur batteries, flow cells and synthesis of useful chemicals or polymers (**Figure 1b**).[10-21]

For the electronic structure of sulfur, each atom has six valence electrons that distributed in its outermost $3s$ and $3p$ shell (**Figure 1c**). Four electrons occupy the $3p$ orbital, and two of them are unpaired. These unpaired valence electrons tend to hybridize with electron donors, such as metals. In the molecular structure, eight sulfur atoms form cyclic octatomic molecules with a chemical formula S_8 (**Figure 1d**). Each sulfur atom bonds with adjacent two sulfur atoms with sp^3 hybridization, therefore eight sulfur atoms hold together to form S_8 molecule via sigma bonds. In the crystal structure of sulfur, the periodically aggregated S_8 molecules form several crystal structures. The best-known allotrope is orthorhombic sulfur (α-sulfur) because it is the most stable crystal structure
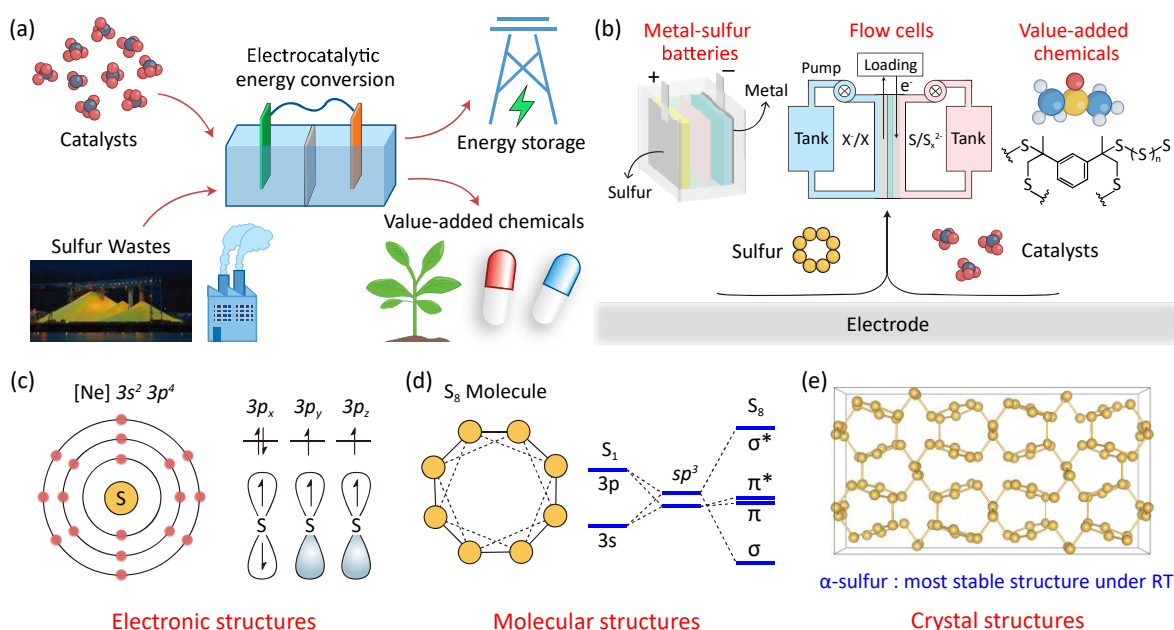
Figure 1 Sulfur chemistry for electrocatalytic energy conversions. (a) Sulfur can be used to energy storage or to produce value-added chemicals with electrocatalysis; (b) The applications of sulfur in metal-sulfur batteries, flow cells and producing useful chemicals; (c) Electronic structure of single sulfur atom, (d) molecule structure of S_8 molecule and (e) crystal structure of α-sulfur.

under atmosphere. The monoclinic β- and densest-packed γ-sulfurs only exist under elevated temperatures (**Figure 1e**).

In metal-sulfur batteries, sulfur cathode based on S/S^{2-} redox shows a very high theoretical capacity of 1675 mAh g^{-1}.[15-19] Therefore, sulfur is a promising choice for low-cost and high-energy battery material. While coupling elemental sulfur with metal anodes, the afforded metal-sulfur batteries are attractive for future energy storage because these batteries compensate the low energy density of currently commercial lithium-ion batteries.[22-24] In metal-sulfur batteries, the energy is stored and released through the reversible redox reactions between metal anode and sulfur cathode. The configurations of these batteries depend on the use of different metal anodes. Li-S battery was mostly investigated due to its high energy density.[25-32] However, the major shortcoming is the low

Table 1 Theoretical parameters and material costs of different configurations in metal-sulfur batteries.

Battery	Reactions	[a]Energy change / kJ mol	Voltage / V	Theoretical capacity / mAh g^{-1}	Energy density / Wh kg^{-1}	[b]Price of metal / AUD\$ kg^{-1}	Price of sulfur / AUD\$ kg^{-1}
Li-S	$2Li+1/8S_8 \rightarrow Li_2S$	-441.4, ΔH_f^0	2.29	1165	2668	3070	
Na-S	$2Na+1/8S_8 \rightarrow Na_2S$	-349.8, ΔG_f^0	1.81	687	1243	286	
K-S	$2K+1/8S_8 \rightarrow K_2S$	-364.0, ΔG_f^0	1.89	487	921	4200	
Mg-S	$Mg+1/8S_8 \rightarrow MgS$	-341.8, ΔG_f^0	1.77	952	1685	319	63
Al-S	$2Al+3/8S_8 \rightarrow Al_2S_3$	-724.0, ΔH_f^0	1.25	1072	1340	466	
Ca-S	$Ca+1/8S_8 \rightarrow CaS$	-468.1, ΔG_f^0	2.43	744	1809	826	
Fe-S	$Fe+1/8S_8 \rightarrow FeS$	-100.4, ΔG_f^0	0.52	609	317	55	
Cu-S	$Cu+1/8S_8 \rightarrow CuS$	-53.6, ΔG_f^0	0.28	561	157	131	
Zn-S	$Zn+1/8S_8 \rightarrow ZnS$	-206.0, ΔG_f^0 sphalerite	1.07	550	589	109	

[a]The energy values are extracted from the handbook of chemistry and physics; [b]The prices are obtained from the Sigma-Aldrich websites.

sulfur utilization, poor rate performance, severe electrolyte loss and unsatisfactory cycling stability. Additionally, Li-S batteries also suffer from safety concern and high cost due to the use of Li metal anode. Therefore, other non-lithium metal-sulfur batteries such as Na-S, Al-S batteries have been proposed as potential alternative to Li-S batteries.[15] The significant advantage of these batteries is their low cost. These metal anodes are much richer in the earth's crust and often found in the ocean and salt lakes around the world, making them accessible to most countries and inexpensive to exploit. However, non-lithium metal-sulfur batteries suffer from low operation voltage, low specific capacity and low energy density. **Table 1** summarizes the theoretical parameters of different configurations in metal-sulfur batteries. Taking Li-S and Al-S batteries as typical comparative examples, Li-S batteries show a much higher operation voltage and energy density.[22-24] Al-S batteries exhibit a low cost merit but with lower energy density.[34-43] Therefore, these metal-sulfur batteries should be mutually complementary to each other under different practical conditions, e.g. portable, automotive, and stationary energy storage.[44-56]

Highly reversible and efficient interfacial reactions on sulfur cathodes-electrolyte and electrolyte-metal anodes interfaces are crucial for metal-sulfur batteries.[32, 58] For the sulfur cathode, sulfur undergoes consecutive reduction from elemental sulfur to soluble polysulfides, and from polysulfides to metal sulfide.[59-63] At the metal anode part, metal plating/stripping repeats during the charge-discharge process.[64-70] The reversibility and efficiency of these complex heterogeneous reactions significantly affects the performance of metal-sulfur batteries. Recent advances have resulted in an improved understanding of the electrochemistry of the interfacial reactions at the atomic/molecular level based on a judicious combination of experimental nanotechnology and computational quantum chemistry.[71] For example, varies of in-situ spectroscopic techniques with high time resolution have been developed for metal-sulfur batteries, such as in-situ Raman spectra, in-situ X-ray diffraction (XRD) patterns, in-situ infrared spectra (IR), and in-situ ultraviolet–visible spectra (UV-vis), etc.[72-77] These in-situ techniques have allowed identification of specific sulfur intermediates and the tracking of dynamic conversion processes, as well as the quantification of polysulfide intermediates.[78-80] With theoretical investigations, researchers are capable now of obtaining growing fundamental insight into the adsorption and reaction origin on cathode or anode interfaces between sulfur species or solvation Li^+ and the electrode material. For example, it is practically possible to obtain a series of adsorption energies and decomposition energies of sulfur intermediates for a particular stage, based on thermo chemical models and transition-states theory via theoretical computations.

2.2 Theoretical Computations

Theoretical computations can be used to develop insight into the relationship between

electrochemical behavior of sulfur redox and metal stripping-plating.[71] Due to the remarkable developments in the density functional theory (DFT) and the availability of powerful computing, nowadays the researchers are capable of investigating catalysts at the atomic level.[81-83] Consequently, many topics in this area have been extensively studied, including the nature of active centers present on the surface of catalysts, the evaluation of the catalytic activity at the atomic level, and ultimately the design of better catalysts toward specific electrochemical processes. The apparent activity of catalyst in both sulfur cathode and metal anode is widely described by experimental parameters including, exchange current density and overpotential.[84-88] However, the intrinsic electronic structures that are related to catalytic activity have been overlooked. Rational design and any optimization of catalysts therefore require an increased understanding of relation between apparent activity and intrinsic electronic structure of catalysts. DFT theoretical computations are widely used to investigate adsorption energetics, reaction thermodynamics and electronic structures.[89-93] By correlating these parameters with experimentally measured catalytic activities, the reactivity trend can give insight into activity origin of a group of catalysts, and importantly, a quantitative relation to optimize catalytic activity via adjustment of natural properties of the catalyst. The reactivity trend has been established for other electrocatalytic reactions, such as oxygen reduction. However because the sulfur conversion and metal deposition have not received significant research attention, there is a present, limited understanding of catalysis mechanisms that restricts rational design of more-efficient catalysts.
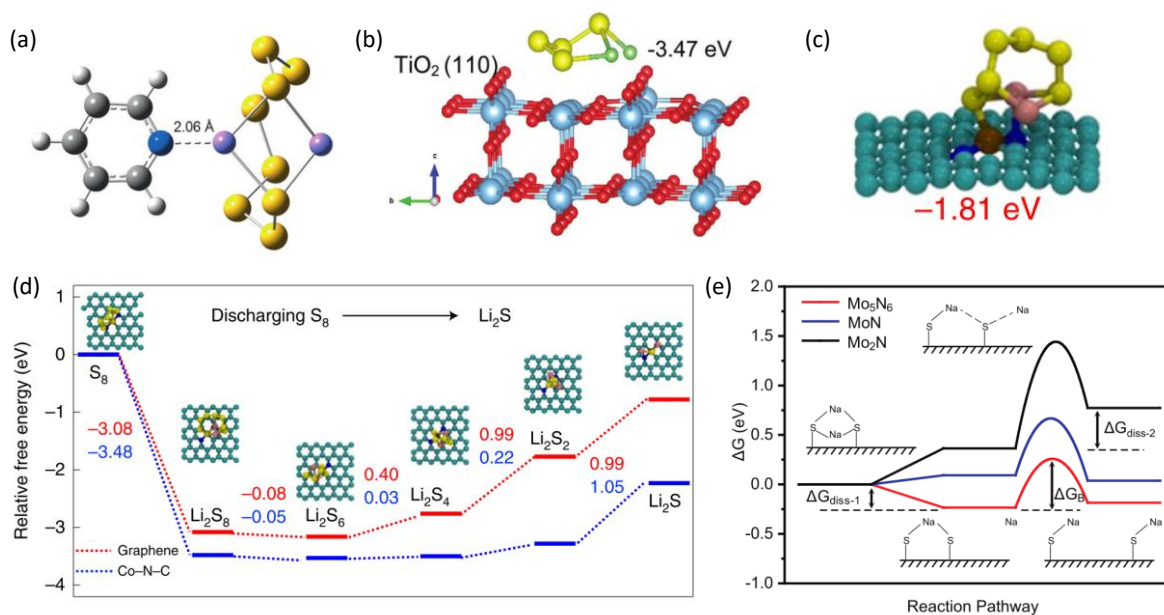
Figure 2 DFT computations for sulfur cathodes. The optimized structures of (a) Li_2S_8-adsorbed pyridine via N-Li binding; (b) Li_2S_4 on TiO_2 via Ti-S binding; (c) Li_2S_6 on Co-N-C via double-end binding, Co-S bond and N-Li bond; (d) Reaction pathways of sulfur reduction with pristine graphene and Co-N-C catalysts; (e) Gibbs free energy diagram of Na_2S decomposition on the surfaces of different metal nitrides.

At the cathode part, sulfur hosts have been widely introduced to promote the sulfur conversion kinetics and restrain the shuttle effect.[59, 60] Theoretical computations can be used to model the binding energy, reaction pathways, decomposition energy, etc.[32, 71] Considering the metal polysulfide molecule includes both metal and sulfur atoms, the designed host catalyst can bind polysulfide via host-lithium, host-sulfur or double-ending interactions. **Figure 2a-2c** present the modeling structures of polysulfides binding with pyridine, TiO_2 and single Co atom embedded in N-doped carbon matrix (Co-N-C).[52, 62, 94] These structures present different bond types adsorbed with polysulfides. For example, pyridine binds with lithium polysulfides via N-Li bond, and TiO_2 binds it with Ti-S bonds. The adsorption of polysulfides on Co-N-C forms both Co-S and N-Li bonds. These various bond types exhibit different binding energies, depending on the electronic structures of these catalysts. Except

for the binding energy, DFT computations can be also used to determine the reaction pathway of sulfur reduction and decomposition of metal sulfur. These two processes correspond to the discharge and charge steps for metal-sulfur batteries. **Figure 2d** compares the sulfur reduction pathways on pristine graphene and Co-N-C catalysts.[62] The discharging process is more thermodynamically favorable on the Co-N-C surface compared to graphene. Specifically, the reaction energy from solid S_8 to liquid Li_2S_8 on the Co-N-C surface is more exothermic than that on the graphene surface. For the rating-determining step (from Li_2S_2 to Li_2S), energy barrier of the endothermic precipitation process is effectively lowered with Co-N-C catalyst (1.27 eV). These results confirm the usefulness of DFT computations to describe the sulfur reduction process. The decomposition pathway of metal sulfide (Na_2S) is presented in **Figure 2e**.[53] When the kinetics of NaS* formation step is considered, the Mo_5N_6 surface exhibits a substantially lower energy barrier of 0.48 eV than on MoN of 0.58 eV and Mo_2N of 1.06 eV. Therefore, from a kinetic viewpoint, Mo_5N_6 demonstrates the most favorable electrodeposition efficiency amongst the three molybdenum nitride structures. Therefore, DFT computation is also an effective protocol to simulate the decomposition process of metal sulfides.

At the anode part, DFT computation was widely used to investigate the dendrite growth and metal plating kinetics. **Figure 3a** and **3b** depict the simulated models of Li growth on pristine carbon and –NH treated carbon surfaces.[95] Li tends to nucleate and grow into 2D Li clusters around the –NH sites on the carbon surface due to the more favorable energy, which navigates the Li deposition along the surface of the carbon fibres. In contrast, on the untreated carbon surface, Li favours the vertical direction of growth, which leads to
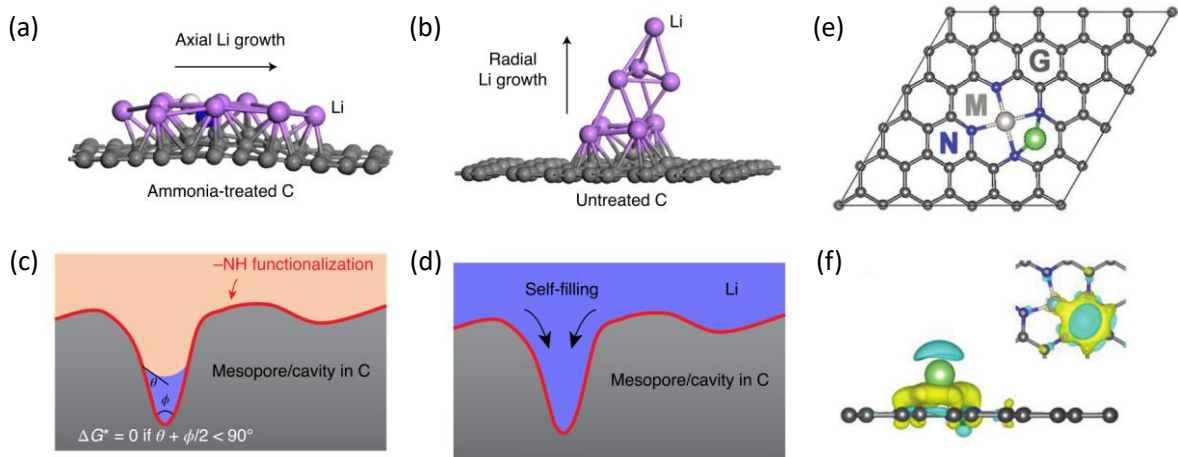
Figure 3 DFT computations for metal anodes. DFT calculation of Li growth on –NH treated (a) and untreated (b) carbon surfaces; Schematics of (c) Li nucleation and (d) Li deposition on –NH treated carbon surface; (e) Li adsorption on Ni-N$_4$-C single atom catalyst, and (f) the corresponding charge-transfer figure.

the formation of the commonly observed Li dendrites on flat Li metal or the heterogeneous growth of large Li particles aggregated on untreated carbon. The computational results coincide with the experimental observations (**Figure 3c** and **3d**). Except for the dendrite growth, the metal plating kinetic can be also described by DFT computations. **Figure 3e** shows the Li adsorption on a Ni-N-C single atom catalyst.[96] There is obviously charge transfer between surface Li atom and catalyst (**Figure 3f**), resulting in an accelerated Li plating kinetics. The DFT result agrees with the experimentally observed lower Li nucleation/deposition overpotential.

2.3 In-situ spectroscopy

In-situ spectroscopy is an analytical methodology wherein the spectroscopic characterization of materials undergoing reaction is coupled simultaneously with measurement of catalytic activity and selectivity.[78, 79] In metal-sulfur batteries, in-situ spectroscopy was widely used to track the polysulfide intermediates and identify the metal plating/stripping. In the sulfur cathode, questions have been proposed in this research field

with regard to structural evolution of the electrodes, the loss of active materials, phase transformation, and the kinetics and thermodynamics of polysulfide migration. Advanced characterization techniques are of great importance to assist in understanding the limiting mechanisms in battery systems. Among them, various in-situ characterization techniques have been intensively utilized. It is important to recognize the limitations and complexity of in situ characterization techniques, as it may be necessary to couple a range of techniques in acquiring a detailed understanding of the physicochemistry of metal-sulfur batteries. The spectroscopic techniques should be combined to obtain a better understanding on the conversion mechanisms. For example, in-situ Raman spectroscopy was often used to track the evolution of polysulfide intermediates because the polysulfide molecules present obvious vibration signal while subjected to Raman laser.[75] To identify the bond types such as S-S bond or metal-S bond, in-situ IR spectroscopy is a good protocol to detect the binding environment.[74] Different from Raman and IR spectroscopy, UV-vis spectroscopy is a type of absorption method across a wide range of absorption bands. It can be used to detect the polysulfide in the UV-vis region, and more importantly, to quantify the polysulfide evolutions.[73] Besides, considering that sulfur and metal sulfides are crystals, in-situ XRD is effective to track the dissolution and evolution of sulfur and metal sulfides. Especially, synchrotron light source would be more sensitive to detect the phase transformation.[53-55]

Figure 4a presents typical in-situ synchrotron-based XRD stacked plots of sulfur cathode in Na-S battery with a 2D MOF catalyst.[54] Main intermediates can be identified from the diffraction peaks, where peaks at 11.6º, 12.1º and 10.6º correspond to
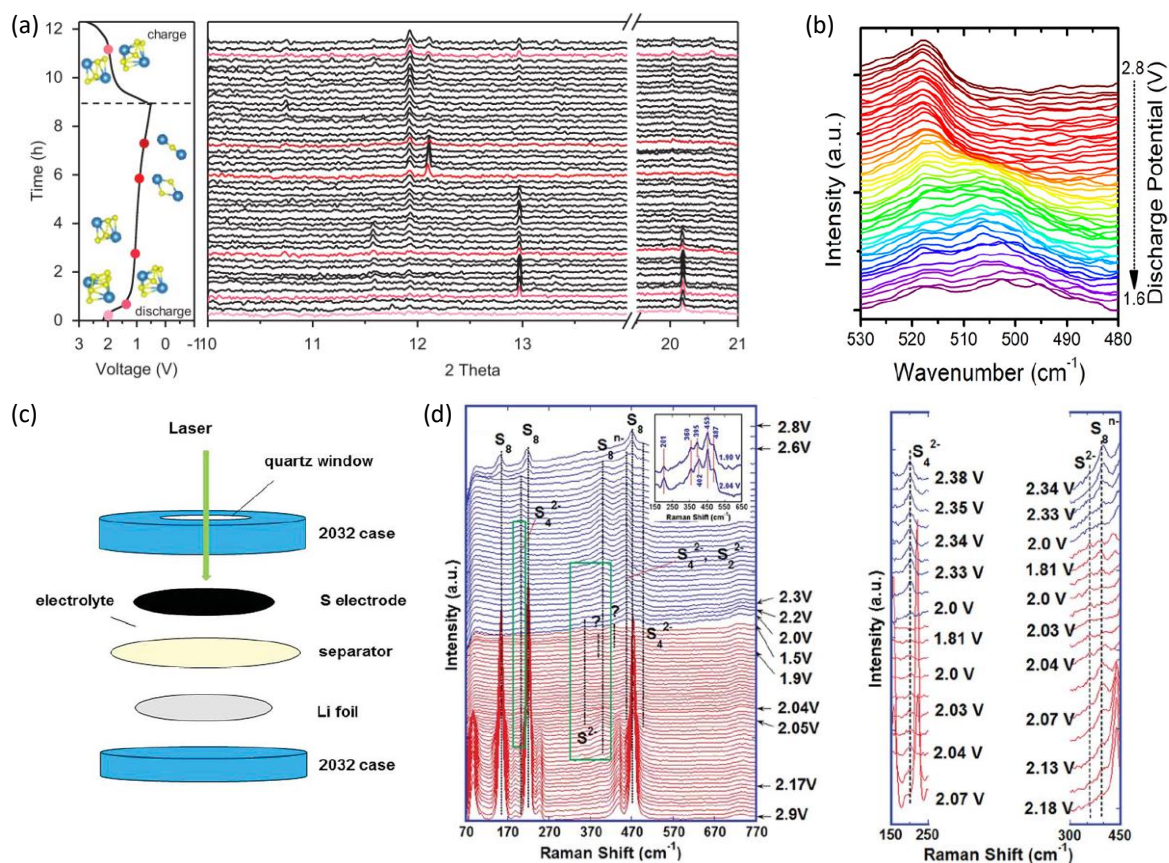
Figure 4 In-situ spectra to track the polysulfide intermediates in sulfur cathode. (a) In-situ synchrotron XRD stacked plots of MOF-catalyzed sulfur cathode in a Na-S battery; (b) In-situ IR stacked plots of sulfur cathode during the discharge process in a Li-S battery; (c) Schematic of cell case for in-situ Raman test; (d) The in-situ Raman plots of sulfur cathode at different voltages in a Li-S battery.

the Na_2S_4, Na_2S_2 and Na_2S, respectively. The evolution and dissolution of these intermediates can be used to deduce the catalytic activity of a catalyst. **Figure 4b** shows the in-situ IR spectra of sulfur cathode with carbon host in Li-S batteries.[97] During the discharge process from 2.8 V to 1.6 V, obvious S-S bond derived from polysulfides was identified. The in-situ IR technique is useful to judge the catalyst-polysulfide interactions. For example, the S-S peak position would shift to a higher wave number with a metal catalyst. **Figure 4c** and **4d** show the in-situ Raman cell and corresponding stacked Raman spectra of sulfur cathode in Li-S battery.[76] S_8^{n-} was detected as the dominant species at the
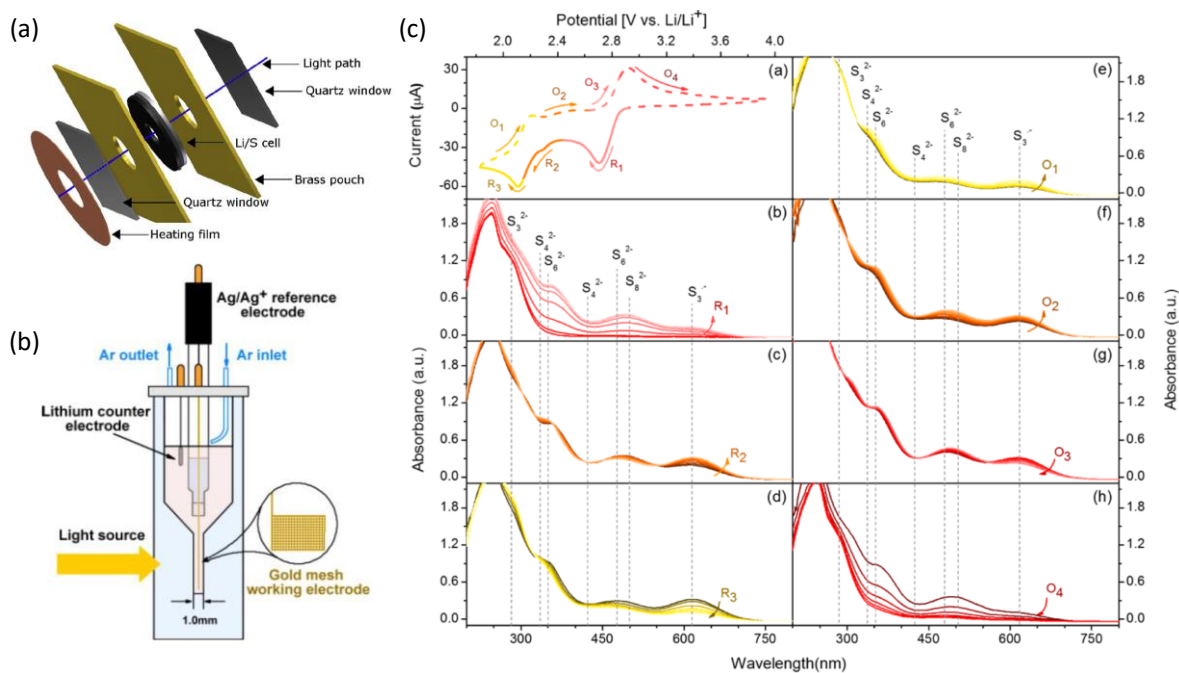
Figure 5 In-situ UV-vis spectra to detect the polysulfide evolution. (a) The coin-cell case for in-situ UV-vis test; (b) A three-electrode cell case for in-situ UV-vis test; (c) CV of 2.0 mM S_8-1.0 M lithium salt solute in DMSO, and the in-situ UV-vis spectra of each reaction step. Color from dark to light with the arrow in each panel represents the changes over time.

high discharge voltage plateau together with S_8, S_4^{2-}, S_2^{2-} were detected soon when the potential reaches the low-voltage plateau. The in-situ Raman spectra is powerful to detect the polysulfide orders at different operation voltages.

Despite the useful functions of in-situ XRD, IR and Raman spectroscopy, these techniques fail to quantify the polysulfide intermediates. In this regard, in-situ UV-vis spectroscopy was developed to detect polysulfides, while concomitantly provide quantitative information of these polysulfide intermediates. **Figure 5a** and **5b** show typical cell cases for in-situ UV-vis test. It can be carried out in a two-electrode coin cell or a three-electrode system by setting up an organic reference electrode.[98, 99] **Figure 5c** shows the CV curves of 2.0 mM S_8 in electrolyte and in situ UV-vis spectra of each reaction step.[99] The color change from dark to light with the arrow in each panel represents the changes over time. Except for

the detected S_8^{2-}, S_6^{2-} and S_4^{2-} intermediates, the absorbance can be used to quantify their concentration because the UV-vis absorbance is positively correlated to the polysulfide contents.

At the anode part, the above in-situ spectroscopy can be used to characterize the metal plating/stripping and change of solid electrolyte interphase (SEI) layer. Taking Li metal anode as a typical example, in-situ XRD, Raman and IR spectra were also widely used to characterize Li/electrolyte interfaces. For example, Goodenough et al. verified the stability of the graphite fluoride and LiF modified Li electrode (GF-LiF-Li) in air and the electrolyte by in situ XRD based on X-ray scattering.[100] As displayed in **Figure 6a**, the first cycle of bare Li results in the decomposition of the electrolyte due to the formation of the SEI and dendritic Li. On the contrary, there is no obvious diffraction peak change in the GF-LiF-Li electrode, which indicates that the artificial SEI is stable. Besides, in-situ Raman and IR spectra were often used to characterize the composition of SEI formation. **Figure 6b** shows the charge-discharge curve of Li metal anode and stacked spectra at different voltages.[101] In-situ Raman has an advantage over XRD in that it can be used to analyze amorphous or poorly crystallized compounds. It is figured out that a trace amount of the O_2 additive will react with Li rapidly to form an SEI rich in Li_2O, Li_2O_2 and LiOH, thus protecting the Li metal from further side reactions with solvents and salts. **Figure 6c** shows the in-situ IR spectra of Li metal anode during Li plating/stripping.[102] All the peaks correspond to the TFSI⁻ and DFOB⁻ anions, forming an SEI layer on the surface of deposited lithium. Peak intensities significantly change, indicating the unstable SEI layer on the anode surface. Considering the plating/stripping process of metal anode, in-situ microscopic imaging
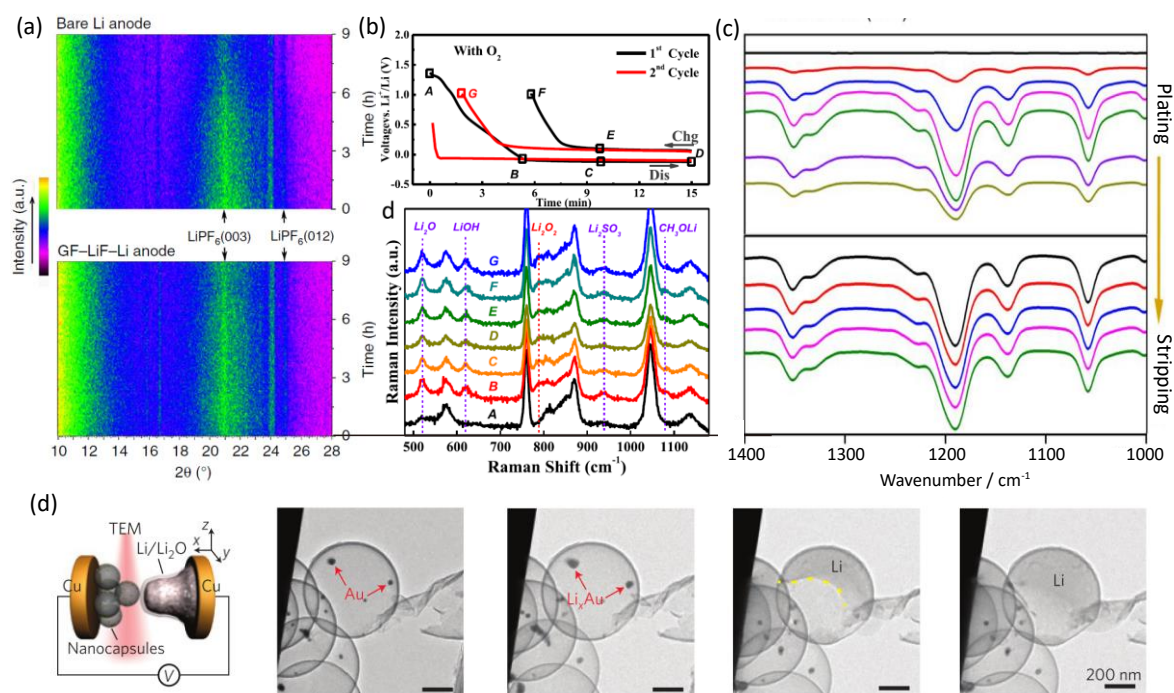
Figure 6 In-situ spectra to detect the Li plating/stripping and SEI layer. (a) In-situ XRD contour patterns of bare Li anode (up) and GF-LiF-Li anode (down); (b) Charge-discharge curves of Li metal anode and the corresponding in-situ Raman stacked plots; (c) In-situ IR spectra of Li plating on Cu substrate; (d) In-situ TEM images showing the selective deposition of metallic Li on Au nanoparticles.

techniques have been extensively applied to visualize metal deposition, such as the in-situ optical microscopic, in-situ scanning electron microscopy (SEM), in-situ transmission electron microscopy (TEM), etc.[80] **Figure 6d** shows an in-situ TEM observation of Li deposition on Au nanoparticles inside a carbon sphere.[103] These pictures clearly present the selective deposition of Li on Au, rather than Li deposition on the surface of carbon spheres. Therefore, the above in-situ spectroscopic techniques are powerful tool to provide precise information for both metal anode and sulfur cathode in metal-sulfur batteries.

2.4 References

1. Worthington, M. J. H.; Kucera, R. L.; Chalker, J. M., Green chemistry and polymers made from sulfur. *Green Chemistry* **2017,** *19* (12), 2748-2761.

2. Huang, X.; Luo, B.; Chen, P.; Searles, D. J.; Wang, D.; Wang, L., Sulfur-based redox

chemistry for electrochemical energy storage. *Coordination Chemistry Reviews* **2020,** *422*, 213445.

3. Mutlu, H.; Ceper, E. B.; Li, X.; Yang, J.; Dong, W.; Ozmen, M. M.; Theato, P., Sulfur Chemistry in Polymer and Materials Science. *Macromolecular Rapid Communications* **2019,** *40* (1), 1800650.

4. Zhang, L.; Qiu, Y. Y.; Zhou, Y.; Chen, G. H.; van Loosdrecht, M. C. M.; Jiang, F., Elemental sulfur as electron donor and/or acceptor: Mechanisms, applications and perspectives for biological water and wastewater treatment. *Water Research* **2021,** *202*, 117373.

5. Teng, Y.; Zhou, Q.; Gao, P., Applications and challenges of elemental sulfur, nanosulfur, polymeric sulfur, sulfur composites, and plasmonic nanostructures. *Critical Reviews in Environmental Science and Technology* **2019,** *49* (24), 2314-2358.

6. Salman, M. K.; Karabay, B.; Karabay, L. C.; Cihaner, A., Elemental sulfur-based polymeric materials: Synthesis and characterization. *Journal of Applied Polymer Science* **2016,** *133* (28), 43655-43664.

7. Huang, H.; Deng, G.-J.; Liu, S., Recent Advances in Sulfur-Containing Heterocycle Formation via Direct C–H Sulfuration with Elemental Sulfur. *Synlett* **2020,** *32* (02), 142-158.

8. Lim, J.; Pyun, J.; Char, K., Recent approaches for the direct use of elemental sulfur in the synthesis and processing of advanced materials. *Angewandte Chemie International Edition* **2015,** *54* (11), 3249-3258.

9. Lee, T.; Dirlam, P. T.; Njardarson, J. T.; Glass, R. S.; Pyun, J., Polymerizations with Elemental Sulfur: From Petroleum Refining to Polymeric Materials. *Journal of the American Chemical Society* **2022,** *144* (1), 5-22.

10. Cai, J.; Zheng, P.; Qaisar, M.; Zhang, J., Elemental sulfur recovery of biological sulfide removal process from wastewater: A review. *Critical Reviews in Environmental Science and Technology* **2017,** *47* (21), 2079-2099.

11. Nguyen, T. B., Recent Advances in the Synthesis of Heterocycles via Reactions Involving Elemental Sulfur. *Advanced Synthesis & Catalysis* **2020,** *362* (17), 3448-3484.

12. Nguyen, T. B., Recent Advances in Organic Reactions Involving Elemental Sulfur. *Advanced Synthesis & Catalysis* **2017,** *359* (7), 1066-1130.

13. Griebel, J. J.; Glass, R. S.; Char, K.; Pyun, J., Polymerizations with elemental sulfur: A novel route to high sulfur content polymers for sustainability, energy and defense. *Progress in Polymer Science* **2016,** *58*, 90-125.

14. Young, C. G., Facets of early transition metal-sulfur chemistry: metal-sulfur ligand redox, induced internal electron transfer, and the reactions of metal-sulfur complexes with alkynes. *Journal of Inorganic Biochemistry* **2007,** *101* (11-12), 1562-85.

15. Hong, X.; Mei, J.; Wen, L.; Tong, Y.; Vasileff, A. J.; Wang, L.; Liang, J.; Sun, Z.; Dou, S. X., Nonlithium Metal-Sulfur Batteries: Steps Toward a Leap. *Advanced Materials* **2019,** *31* (5), 1802822.

16. Yu, X.; Manthiram, A., A Progress Report on Metal-Sulfur Batteries. *Advanced Functional Materials* **2020,** *30* (39), 2004084.

17. Chung, S.-H.; Manthiram, A., Current Status and Future Prospects of Metal-Sulfur Batteries. *Advanced Materials* **2019,** *31* (27), 1901125.

18. Salama, M.; Rosy; Attias, R.; Yemini, R.; Gofer, Y.; Aurbach, D.; Noked, M., Metal-Sulfur Batteries: Overview and Research Methods. *ACS Energy Letters* **2019,** *4* (2), 436-446.

19. Yu, X.; Manthiram, A., Ambient-Temperature Energy Storage with Polyvalent Metal-Sulfur Chemistry. *Small Methods* **2017,** *1* (11), 1700217.

20. Zhang, H.; Lu, W.; Li, X., Progress and Perspectives of Flow Battery Technologies. *Electrochemical Energy Reviews* **2019,** *2* (3), 492-506.

21. Li, Z.; Lu, Y.-C., Polysulfide-based redox flow batteries with long life and low levelized cost enabled by charge-reinforced ion-selective membranes. *Nature Energy* **2021,** *6* (5), 517-528.

22. Bruce, P. G.; Freunberger, S. A.; Hardwick, L. J.; Tarascon, J. M., Li-O$_2$ and Li-S batteries with high energy storage. *Nature Materials* **2012,** *11* (1), 19-29.

23. Li, G.; Chen, Z.; Lu, J., Lithium-Sulfur Batteries for Commercial Applications. *Chem* **2018,** *4* (1), 3-7.

24. Li, M.; Lu, J.; Chen, Z.; Amine, K., 30 Years of Lithium-Ion Batteries. *Advanced Materials* **2018**, *30* (33), 1800561.

25. Peng, H.-J.; Huang, J.-Q.; Cheng, X.-B.; Zhang, Q., Review on High-Loading and High-Energy Lithium-Sulfur Batteries. *Advanced Energy Materials* **2017,** *7* (24), 1700260.

26. Li, G.; Lei, W.; Luo, D.; Deng, Y.; Deng, Z.; Wang, D.; Yu, A.; Chen, Z., Stringed "tube on cube" nanohybrids as compact cathode matrix for high-loading and lean-electrolyte lithium–sulfur batteries. *Energy & Environmental Science* **2018,** *11* (9), 2372-2381.

27. Qie, L.; Zu, C.; Manthiram, A., A High Energy Lithium-Sulfur Battery with Ultrahigh-Loading Lithium Polysulfide Cathode and its Failure Mechanism. *Advanced Energy Materials* **2016,** *6* (7), 1502459.

28. Cheng, X.-B.; Yan, C.; Huang, J.-Q.; Li, P.; Zhu, L.; Zhao, L.; Zhang, Y.; Zhu, W.; Yang, S.-T.; Zhang, Q., The gap between long lifespan Li-S coin and pouch cells: The importance of lithium metal anode protection. *Energy Storage Materials* **2017,** *6*, 18-25.

29. Manthiram, A.; Fu, Y.; Chung, S. H.; Zu, C.; Su, Y. S., Rechargeable lithium-sulfur batteries. *Chemical Reviews* **2014,** *114* (23), 11751-87.

30. Fang, R.; Zhao, S.; Sun, Z.; Wang, D. W.; Cheng, H. M.; Li, F., More Reliable Lithium-Sulfur Batteries: Status, Solutions and Prospects. *Advanced Materials* **2017,** *29* (48), 1606823.

31. Yang, X.; Luo, J.; Sun, X., Towards high-performance solid-state Li-S batteries: from fundamental understanding to engineering design. *Chemical Society Reviews* **2020,** *49* (7), 2140-2195.

32. Pang, Q.; Liang, X.; Kwok, C. Y.; Nazar, L. F., Advances in lithium-sulfur batteries based on multifunctional cathodes and electrolytes. *Nature Energy* **2016,** *1*, 16132.

33. Hosein, I. D., The Promise of Calcium Batteries: Open Perspectives and Fair Comparisons. *ACS Energy Letters* **2021,** *6* (4), 1560-1565.

34. Chu, W.; Zhang, X.; Wang, J.; Zhao, S.; Liu, S.; Yu, H., A low-cost deep eutectic solvent electrolyte for rechargeable aluminum-sulfur battery. *Energy Storage Materials* **2019,** *22*, 418-423.

35. Hu, Z.; Guo, Y.; Jin, H.; Ji, H.; Wan, L.-J., A rechargeable aqueous aluminum-sulfur battery through acid activation in water-in-salt electrolyte. *Chemical Communications* **2020,** *56* (13), 2023-2026.

36. Zheng, X.; Tang, R.; Zhang, Y.; Ma, L.; Wang, X.; Dong, Y.; Kong, G.; Wei, L., Design of a composite cathode and a graphene coated separator for a stable room-temperature aluminum-sulfur battery. *Sustainable Energy & Fuels* **2020,** *4* (4), 1630-1641.

37. Zhang, Y.; Ma, L.; Tang, R.; Zheng, X.; Wang, X.; Dong, Y.; Kong, G.; Zhao, F.; Wei, L., The host hollow carbon nanospheres as cathode material for nonaqueous room-temperature Al-S batteries. *International Journal of Hydrogen Energy* **2021,** *46* (7), 4936-4946.

38. Lampkin, J.; Li, H.; Furness, L.; Raccichini, R.; Garcia-Araez, N., A Critical Evaluation of the Effect of Electrode Thickness and Side Reactions on Electrolytes for Aluminum-Sulfur Batteries. *ChemSusChem* **2020,** *13* (13), 3514-3523.

39. Guo, Y.; Hu, Z.; Wang, J.; Peng, Z.; Zhu, J.; Ji, H.; Wan, L.-J., Rechargeable Aluminium-Sulfur Battery with Improved Electrochemical Performance by Cobalt-Containing Electrocatalyst. *Angewandte Chemie International Edition* **2020,** *59* (51), 22963-22967.

40. Bian, Y.; Li, Y.; Yu, Z.; Chen, H.; Du, K.; Qiu, C.; Zhang, G.; Lv, Z.; Lin, M.-C., Using an $AlCl_3$/Urea Ionic Liquid Analog Electrolyte for Improving the Lifetime of Aluminum-Sulfur Batteries. *ChemElectroChem* **2018,** *5* (23), 3607-3611.

41. Yu, X.; Boyer, M. J.; Hwang, G. S.; Manthiram, A., Room-Temperature Aluminum-Sulfur Batteries with a Lithium-Ion-Mediated Ionic Liquid Electrolyte. *Chem* **2018,** *4* (3), 586-598.

42. Gao, T.; Li, X.; Wang, X.; Hu, J.; Han, F.; Fan, X.; Suo, L.; Pearse, A. J.; Lee, S. B.; Rubloff, G. W.; Gaskell, K. J.; Noked, M.; Wang, C., A Rechargeable Al/S Battery with an Ionic-Liquid Electrolyte. *Angewandte Chemie International Edition* **2016,** *55* (34), 9898-9901.

43. Cohn, G.; Ma, L.; Archer, L. A., A novel non-aqueous aluminum sulfur battery. *Journal of Power Sources* **2015,** *283*, 416-422.

44. Li, Z.; Vinayan, B. P.; Diemant, T.; Behm, R. J.; Fichtner, M.; Zhao-Karger, Z., Rechargeable Calcium-Sulfur Batteries Enabled by an Efficient Borate-Based Electrolyte. *Small* **2020,** *16* (39), 2001806.

45. Wu, X.; Markir, A.; Xu, Y.; Zhang, C.; Leonard, D. P.; Shin, W.; Ji, X., A Rechargeable Battery with an Iron Metal Anode. *Advanced Functional Materials* **2019,** *29* (20), 1900911.

46. Wu, X.; Markir, A.; Xu, Y.; Hu, E. C.; Dai, K. T.; Zhang, C.; Shin, W.; Leonard, D. P.; Kim, K. i.; Ji, X., Rechargeable Iron–Sulfur Battery without Polysulfide Shuttling. *Advanced Energy Materials* **2019**, *9* (40), 1902422.

47. Liu, D.; He, B.; Zhong, Y.; Chen, J.; Yuan, L.; Li, Z.; Huang, Y., A durable ZnS cathode

for aqueous Zn-S batteries. *Nano Energy* **2022**, DOI: 10.1016/j.nanoen.2022.107474.

48. Zhou, T.; Wan, H.; Liu, M.; Wu, Q.; Fan, Z.; Zhu, Y., Regulating uniform nucleation of ZnS enables low-polarized and high stable aqueous Zn–S batteries. *Materials Today Energy* **2022,** *27*, 101025.

49. Li, W.; Wang, K.; Jiang, K., A Low Cost Aqueous Zn-S Battery Realizing Ultrahigh Energy Density. *Advanced Science* **2020,** *7* (23), 2000761.

50. Zhang, H.; Shang, Z. T.; Luo, G.; Jiao, S. H.; Cao, R. G.; Chen, Q. W.; Lu, K., Redox Catalysis Promoted Activation of Sulfur Redox Chemistry for Energy-Dense Flexible Solid-State Zn-S Battery. *ACS Nano* 2022, 16 (5), 7344-7351.

51. Zhao, Y.; Wang, D.; Li, X.; Yang, Q.; Guo, Y.; Mo, F.; Li, Q.; Peng, C.; Li, H.; Zhi, C., Initiating a Reversible Aqueous Zn/Sulfur Battery through a "Liquid Film". *Advanced Materials* **2020,** *32* (32), 2003070.

52. Zhou, T.; Lv, W.; Li, J.; Zhou, G.; Zhao, Y.; Fan, S.; Liu, B.; Li, B.; Kang, F.; Yang, Q.-H., Twinborn TiO_2–TiN heterostructures enabling smooth trapping–diffusion–conversion of polysulfides towards ultralong life lithium–sulfur batteries. *Energy & Environmental Science* **2017,** *10* (7), 1694-1703.

53. Ye, C.; Jin, H.; Shan, J.; Jiao, Y.; Li, H.; Gu, Q.; Davey, K.; Wang, H.; Qiao, S.-Z., A Mo5N6 electrocatalyst for efficient Na_2S electrodeposition in room-temperature sodium-sulfur batteries. *Nature Communications* **2021,** *12* (1), 7195.

54. Ye, C.; Jiao, Y.; Chao, D.; Ling, T.; Shan, J.; Zhang, B.; Gu, Q.; Davey, K.; Wang, H.; Qiao, S. Z., Electron-State Confinement of Polysulfides for Highly Stable Sodium-Sulfur Batteries. *Advanced Materials* **2020**, 32 (12), 1907557.

55. Ye, C.; Jiao, Y.; Jin, H. Y.; Slattery, A. D.; Davey, K.; Wang, H. H.; Qiao, S. Z., 2D MoN-VN Heterostructure To Regulate Polysulfides for Highly Efficient Lithium-Sulfur Batteries. *Angewandte Chemie International Edition* **2018,** *57* (51), 16703-16707.

56. Ye, C.; Shan, J.; Chao, D.; Liang, P.; Jiao, Y.; Hao, J.; Gu, Q.; Davey, K.; Wang, H.; Qiao, S. Z., Catalytic Oxidation of K_2S via Atomic Co and Pyridinic N Synergy in Potassium-Sulfur Batteries. *Journal of the American Chemical Society* **2021,** *143* (41), 16902-16907.

57. Wei, S.; Xu, S.; Agrawral, A.; Choudhury, S.; Lu, Y.; Tu, Z.; Ma, L.; Archer, L. A., A stable room-temperature sodium-sulfur battery. *Nature Communications* **2016,** *7*, 11722.

58. Tikekar, M. D.; Choudhury, S.; Tu, Z. Y.; Archer, L. A., Design principles for electrolytes and interfaces for stable lithium-metal batteries. *Nature Energy* **2016,** *1* (9), 16114-16120.

59. Chen, H.; Wu, Z.; Zheng, M.; Liu, T.; Yan, C.; Lu, J.; Zhang, S., Catalytic materials for lithium-sulfur batteries: mechanisms, design strategies and future perspective. *Materials Today* **2022,** *52*, 364-388.

60. Liu, D. H.; Zhang, C.; Zhou, G. M.; Lv, W.; Ling, G. W.; Zhi, L. J.; Yang, Q. H., Catalytic Effects in Lithium-Sulfur Batteries: Promoted Sulfur Transformation and Reduced Shuttle Effect. *Advanced Science* **2018,** *5* (1), 1700270.

61. Peng, L.; Wei, Z.; Wan, C.; Li, J.; Chen, Z.; Zhu, D.; Baumann, D.; Liu, H.; Allen, C. S.; Xu, X.; Kirkland, A. I.; Shakir, I.; Almutairi, Z.; Tolbert, S.; Dunn, B.; Huang, Y.; Sautet, P.; Duan, X., A fundamental look at electrocatalytic sulfur reduction reaction. *Nature Catalysis* **2020,** *3* (9), 762-770.

62. Zhao, C.; Xu, G.-L.; Yu, Z.; Zhang, L.; Hwang, I.; Mo, Y.-X.; Ren, Y.; Cheng, L.; Sun, C.-J.; Ren, Y.; Zuo, X.; Li, J.-T.; Sun, S.-G.; Amine, K.; Zhao, T., A high-energy and long-cycling lithium–sulfur pouch cell via a macroporous catalytic cathode with double-end binding sites. *Nature Nanotechnology* **2020,** *16*, 166-173.

63. Bhargav, A.; He, J.; Gupta, A.; Manthiram, A., Lithium-Sulfur Batteries: Attaining the Critical Metrics. *Joule* **2020,** *4* (2), 285-291.

64. Cheng, X. B.; Zhang, R.; Zhao, C. Z.; Zhang, Q., Toward Safe Lithium Metal Anode in Rechargeable Batteries: A Review. *Chemical Reviews* **2017,** *117* (15), 10403-10473.

65. Manthiram, A.; Yu, X. W.; Wang, S. F., Lithium battery chemistries enabled by solid-state electrolytes. *Nature Reviews Materials* **2017,** *2* (4), 16103.

66. Li, S.; Jiang, M. W.; Xie, Y.; Xu, H.; Jia, J. Y.; Li, J., Developing High-Performance Lithium Metal Anode in Liquid Electrolytes: Challenges and Progress. *Advanced Materials* **2018,** *30* (17), 1706375.

67. Lin, D.; Liu, Y.; Cui, Y., Reviving the lithium metal anode for high-energy batteries. *Nature Nanotechnology* **2017,** *12* (3), 194-206.

68. Liu, J.; Bao, Z.; Cui, Y.; Dufek, E. J.; Goodenough, J. B.; Khalifah, P.; Li, Q.; Liaw, B. Y.; Liu, P.; Manthiram, A.; Meng, Y. S.; Subramanian, V. R.; Toney, M. F.; Viswanathan, V. V.; Whittingham, M. S.; Xiao, J.; Xu, W.; Yang, J.; Yang, X.-Q.; Zhang, J.-G., Pathways for

practical high-energy long-cycling lithium metal batteries. *Nature Energy* **2019,** *4* (3), 180-186.

69. Duan, H.; Zhang, J.; Chen, X.; Zhang, X. D.; Li, J. Y.; Huang, L. B.; Zhang, X.; Shi, J. L.; Yin, Y. X.; Zhang, Q.; Guo, Y. G.; Jiang, L.; Wan, L. J., Uniform Nucleation of Lithium in 3D Current Collectors via Bromide Intermediates for Stable Cycling Lithium Metal Batteries. *Journal of the American Chemical Society* **2018,** *140* (51), 18051-18057.

70. Zhang, X. Q.; Chen, X.; Cheng, X. B.; Li, B. Q.; Shen, X.; Yan, C.; Huang, J. Q.; Zhang, Q., Highly Stable Lithium Metal Batteries Enabled by Regulating the Solvation of Lithium Ions in Nonaqueous Electrolytes. *Angewandte Chemie International Edition* **2018,** *57* (19), 5301-5305.

71. Ye, C.; Chao, D.; Shan, J.; Li, H.; Davey, K.; Qiao, S.-Z., Unveiling the Advances of 2D Materials for Li/Na-S Batteries Experimentally and Theoretically. *Matter* **2020,** *2* (2), 323-344.

72. Hongyou, K.; Hattori, T.; Nagai, Y.; Tanaka, T.; Nii, H.; Shoda, K., Dynamic in situ fourier transform infrared measurements of chemical bonds of electrolyte solvents during the initial charging process in a Li ion battery. *Journal of Power Sources* **2013,** *243*, 72-77.

73. Patel, M. U.; Dominko, R., Application of in operando UV/Vis spectroscopy in lithium-sulfur batteries. *ChemSusChem* **2014,** *7* (8), 2167-2175.

74. Cheng, H.; Zhu, C. B.; Lu, M.; Yang, Y., In situ micro-FTIR study of the solid–solid interface between lithium electrode and polymer electrolytes. *Journal of Power Sources* **2007,** *174* (2), 1027-1031.

75. Hagen, M.; Schiffels, P.; Hammer, M.; Dörfler, S.; Tübke, J.; Hoffmann, M. J.; Althues, H.; Kaskel, S., In-Situ Raman Investigation of Polysulfide Formation in Li-S Cells. *Journal of the Electrochemical Society* **2013,** *160* (8), A1205-A1214.

76. Zhu, W.; Paolella, A.; Kim, C. S.; Liu, D.; Feng, Z.; Gagnon, C.; Trottier, J.; Vijh, A.; Guerfi, A.; Mauger, A.; Julien, C. M.; Armand, M.; Zaghib, K., Investigation of the reaction mechanism of lithium sulfur batteries in different electrolyte systems by in situ Raman spectroscopy and in situ X-ray diffraction. *Sustainable Energy & Fuels* **2017,** *1* (4), 737-747.

77. Barchasz, C.; Molton, F.; Duboc, C.; Lepretre, J. C.; Patoux, S.; Alloin, F., Lithium/sulfur cell discharge mechanism: an original approach for intermediate species identification.

Analytical Chemistry **2012,** *84* (9), 3973-3980.

78. Li, M.; Amirzadeh, Z.; De Marco, R.; Tan, X. F.; Whittaker, A.; Huang, X.; Wepf, R.; Knibbe, R., In Situ Techniques for Developing Robust Li-S Batteries. *Small Methods* **2018,** *2* (11), 1800133.

79. Zhang, L.; Qian, T.; Zhu, X.; Hu, Z.; Wang, M.; Zhang, L.; Jiang, T.; Tian, J. H.; Yan, C., In situ optical spectroscopy characterization for optimal design of lithium-sulfur batteries. *Chemical Society Reviews* **2019,** *48* (22), 5432-5453.

80. Pu, J.; Zhong, C.; Liu, J.; Wang, Z.; Chao, D., Advanced in situ technology for Li/Na metal anodes: an in-depth mechanistic understanding. *Energy & Environmental Science* **2021,** *14* (7), 3872-3911.

81. Grajciar, L.; Heard, C. J.; Bondarenko, A. A.; Polynski, M. V.; Meeprasert, J.; Pidko, E. A.; Nachtigall, P., Towards operando computational modeling in heterogeneous catalysis. *Chem Soc Rev* **2018,** *47* (22), 8307-8348.

82. Jiao, Y.; Zheng, Y.; Jaroniec, M.; Qiao, S. Z., Design of electrocatalysts for oxygen- and hydrogen-involving energy conversion reactions. *Chemical Society Reviews* **2015,** *44* (8), 2060-2086.

83. Jiao, Y.; Zheng, Y.; Davey, K.; Qiao, S.-Z., Activity origin and catalyst design principles for electrocatalytic hydrogen evolution on heteroatom-doped graphene. *Nature Energy* **2016,** *1* (10), 16130.

84. Hua, W.; Li, H.; Pei, C.; Xia, J.; Sun, Y.; Zhang, C.; Lv, W.; Tao, Y.; Jiao, Y.; Zhang, B.; Qiao, S. Z.; Wan, Y.; Yang, Q. H., Selective Catalysis Remedies Polysulfide Shuttling in Lithium-Sulfur Batteries. *Advanced Materials* **2021**, *33* (38) 2101006.

85. Zhong, Y. R.; Yin, L. C.; He, P.; Liu, W.; Wu, Z. S.; Wang, H. L., Surface Chemistry in Cobalt Phosphide-Stabilized Lithium-Sulfur Batteries. *Journal of the American Chemical Society* **2018,** *140* (4), 1455-1459.

86. Xue, W.; Shi, Z.; Suo, L.; Wang, C.; Wang, Z.; Wang, H.; So, K. P.; Maurano, A.; Yu, D.; Chen, Y.; Qie, L.; Zhu, Z.; Xu, G.; Kong, J.; Li, J., Intercalation-conversion hybrid cathodes enabling Li–S full-cell architectures with jointly superior gravimetric and volumetric energy densities. *Nature Energy* **2019,** *4*, 374-382.

87. Du, Z.; Chen, X.; Hu, W.; Chuang, C.; Xie, S.; Hu, A.; Yan, W.; Kong, X.; Wu, X.; Ji,

H.; Wan, L. J., Cobalt in Nitrogen-Doped Graphene as Single-Atom Catalyst for High-Sulfur Content Lithium-Sulfur Batteries. *Journal of the American Chemical Society* **2019,** *141* (9), 3977-3985.

88. Zhou, G.; Tian, H.; Jin, Y.; Tao, X.; Liu, B.; Zhang, R.; Seh, Z. W.; Zhuo, D.; Liu, Y.; Sun, J.; Zhao, J.; Zu, C.; Wu, D. S.; Zhang, Q.; Cui, Y., Catalytic oxidation of Li_2S on the surface of metal sulfides for Li-S batteries. *Proceedings of the National Academy of Sciences of the United States of America* **2017,** *114* (5), 840-845.

89. Seh, Z. W.; Kibsgaard, J.; Dickens, C. F.; Chorkendorff, I. B.; Norskov, J. K.; Jaramillo, T. F., Combining theory and experiment in electrocatalysis: Insights into materials design. *Science* **2017,** *355* (6321), eaad4998.

90. Ross, M. B.; De Luna, P.; Li, Y.; Dinh, C.-T.; Kim, D.; Yang, P.; Sargent, E. H., Designing materials for electrochemical carbon dioxide recycling. *Nature Catalysis* **2019,** *2* (8), 648-658.

91. Seo, D. H.; Lee, J.; Urban, A.; Malik, R.; Kang, S.; Ceder, G., The structural and chemical origin of the oxygen redox activity in layered and cation-disordered Li-excess cathode materials. *Nature Chemistry* **2016,** *8* (7), 692-697.

92. Hwang, J.; Rao, R. R.; Giordano, L.; Katayama, Y.; Yu, Y.; Shao-Horn, Y., Perovskites in catalysis and electrocatalysis. *Science* **2017,** *358* (6364), 751-756.

93. Tian, X.; Zhao, X.; Su, Y.-Q.; Wang, L.; Wang, H.; Dang, D.; Chi, B.; Liu, H.; Hensen, E. J. M.; Lou, X. W.; Xia, B. Y., Engineering bunched Pt-Ni alloy nanocages for efficient oxygen reduction in practical fuel cells. *Science* **2019,** *366* (6467), 850-856.

94. Hou, T. Z.; Xu, W. T.; Chen, X.; Peng, H. J.; Huang, J. Q.; Zhang, Q., Lithium Bond Chemistry in Lithium-Sulfur Batteries. *Angewandte Chemie International Edition* **2017,** *56* (28), 8178-8182.

95. Niu, C.; Pan, H.; Xu, W.; Xiao, J.; Zhang, J. G.; Luo, L.; Wang, C.; Mei, D.; Meng, J.; Wang, X.; Liu, Z.; Mai, L.; Liu, J., Self-smoothing anode for achieving high-energy lithium metal batteries under realistic conditions. *Nature Nanotechnology* **2019,** *14* (6), 594.

96. Zhai, P.; Wang, T.; Yang, W.; Cui, S.; Zhang, P.; Nie, A.; Zhang, Q.; Gong, Y., Uniform Lithium Deposition Assisted by Single-Atom Doping toward High-Performance Lithium Metal Anodes. *Advanced Energy Materials* **2019,** *9* (18), 1804019.

97. Dillard, C.; Singh, A.; Kalra, V., Polysulfide Speciation and Electrolyte Interactions in Lithium–Sulfur Batteries with in Situ Infrared Spectroelectrochemistry. *The Journal of Physical Chemistry C* **2018,** *122* (32), 18195-18203.

98. Marceau, H.; Kim, C.-S.; Paolella, A.; Ladouceur, S.; Lagacé, M.; Chaker, M.; Vijh, A.; Guerfi, A.; Julien, C. M.; Mauger, A.; Armand, M.; Hovington, P.; Zaghib, K., In operando scanning electron microscopy and ultraviolet–visible spectroscopy studies of lithium/sulfur cells using all solid-state polymer electrolyte. *Journal of Power Sources* **2016,** *319*, 247-254.

99. Zou, Q.; Lu, Y. C., Solvent-Dictated Lithium Sulfur Redox Reactions: An Operando UV-vis Spectroscopic Study. *The Journal of Physical Chemistry Letters* **2016,** *7* (8), 1518-1525.

100. Shen, X.; Li, Y.; Qian, T.; Liu, J.; Zhou, J.; Yan, C.; Goodenough, J. B., Lithium anode stable in air for low-cost fabrication of a dendrite-free lithium battery. *Nature Communications* **2019,** *10* (1), 900.

101. Qiu, F.; Zhang, X.; Qiao, Y.; Zhang, X.; Deng, H.; Shi, T.; He, P.; Zhou, H., An ultra-stable and enhanced reversibility lithium metal anode with a sufficient O_2 design for $Li\text{-}O_2$ battery. *Energy Storage Materials* **2018,** *12*, 176-182.

102. Hu, Z.; Xian, F.; Guo, Z.; Lu, C.; Du, X.; Cheng, X.; Zhang, S.; Dong, S.; Cui, G.; Chen, L., Nonflammable Nitrile Deep Eutectic Electrolyte Enables High-Voltage Lithium Metal Batteries. *Chemistry of Materials* **2020,** *32* (8), 3405-3413.

103. Yan, K.; Lu, Z. D.; Lee, H. W.; Xiong, F.; Hsu, P. C.; Li, Y. Z.; Zhao, J.; Chu, S.; Cui, Y., Selective deposition and stable encapsulation of lithium through heterogeneous seeded growth. *Nature Energy* **2016,** *1* (3), 16010-16017.

Chapter 3: Revealing principles for design of lean-electrolyte lithium metal anode via in-situ spectroscopy

3.1 Introduction and significance

Lean electrolyte conditions are highly pursued for the practical lithium (Li) metal batteries. The previous studies on the Li metal anodes, in general, exhibited good stability with a large excess of electrolyte. However, the targeted design of Li hosts under relatively low electrolyte conditions has been rarely studied so far. Herein, we have shown that the electrolyte consumption severely affects the cycling stability of Li metal anode. Considering carbon hosts as typical examples, we innovatively employed the in-situ synchrotron X-ray diffraction, in-situ Raman spectroscopy and theoretical computations to obtain better understanding of the Li nucleation/deposition processes. Besides, we showed the usefulness of in-situ electrochemical impedance spectra to analyze interfacial fluctuation at the Li/electrolyte interface, and together with the nuclear magnetic resonance data to quantify electrolyte consumption. We have found that uneven Li nucleation/deposition and the crack of surface-area-derived solid-electrolyte-interface (SEI) layer both leads to a great consumption of electrolyte. Then, we suggested a design principle for Li host to overcome the electrolyte loss, that is, uneven growth of Li structure and the crack of SEI layer must be simultaneously controlled. As a proof of concept, we demonstrated the usefulness of a 3D low-surface-area defective graphene host (L-DG) to control Li nucleation/deposition and stabilize SEI layer, contributing to a highly reversible Li plating/stripping. As a result, such a Li host can achieve stable cycles (e.g., 1.0 mAh cm-2) with a low electrolyte loading (10 μL). This work demonstrates the necessity to design Li metal anodes under lean electrolyte

conditions and brings the Li metal batteries a step closer to their practical applications. The highlights of this work include:

➢ **Design principle for Li hosts under lean electrolyte conditions** – Uneven Li nucleation/deposition and the crack-reformation of high-surface-area derived SEI layer must be simultaneously controlled to restrain the electrolyte loss. We demonstrate the usefulness of a 3D low-surface-area defective graphene host to control Li nucleation and deposition. Such a host can achieve stable cycles under lean electrolyte conditions.

➢ **Advanced *in-situ* techniques reveal the Li plating behavior and the properties of the Li/electrolyte interface** – The *in-situ* synchrotron X-ray diffraction and *in-situ* Raman spectroscopy are used to provide a deep insight into the Li nucleation/deposition behavior. Then, we demonstrate the usefulness of an *in-situ* electrochemical impedance spectroscopy to analyze the interfacial fluctuation of Li anode.

➢ **DFT calculations** –We employed the DFT calculations to clarify the interaction between Li* and the substrate at the atomic level, which give more details on the Li affinity to different substrates. This will guide the experimental design for Li host materials.

3.2 Revealing principles for design of lean-electrolyte lithium metal anode via in-situ spectroscopy

This Chapter is included as it appears as a journal paper published by **Huan Li**, Dongliang Chao, Biao Chen, Xiao Chen, Clarence Chuan, Youhong Tang, Yan Jiao, Mietek Jaroniec and Shi-Zhang Qiao*. Revealing principles for design of lean-electrolyte lithium metal anode via in-situ spectroscopy. ***Journal of The American Chemical Society***, 2020, 142, 2012-2022.

Statement of Authorship

Title of Paper	Revealing Principles for Design of Lean-Electrolyte Lithium Metal Anode via In Situ Spectroscopy
Publication Status	☑ Published ☐ Accepted for Publication ☐ Submitted for Publication ☐ Unpublished and Unsubmitted work written in manuscript style
Publication Details	Huan Li, Dongliang Chao, Biao Chen, Xiao Chen, Clarence Chuah, Youhong Tang, Yan Jiao, Mietek Jaroniec, and Shi-Zhang Qiao*, Journal of the American Chemical Society, 2020, 142, 4, 2012-2022.

Principal Author

Name of Principal Author (Candidate)	Huan Li		
Contribution to the Paper	Conducted material synthesis, carried out electrochemical tests and wrote the paper		
Overall percentage (%)	70		
Certification:	This paper reports on original research I conducted during the period of my Higher Degree by Research candidature and is not subject to any obligations or contractual agreements with a third party that would constrain its inclusion in this thesis. I am the primary author of this paper.		
Signature		Date	14 June 2022

Co-Author Contributions

By signing the Statement of Authorship, each author certifies that:

i. the candidate's stated contribution to the publication is accurate (as detailed above);

ii. permission is granted for the candidate in include the publication in the thesis; and

iii. the sum of all co-author contributions is equal to 100% less the candidate's stated contribution.

Name of Co-Author	Dongliang Chao		
Contribution to the Paper	Guided experimental design		
Signature		Date	14 June 2022

Name of Co-Author	Biao Chen		
Contribution to the Paper	Assisted with material characterizations		
Signature		Date	14 June 2022

Name of Co-Author	Xiao Chen		
Contribution to the Paper	Captured the microscopic images		
Signature		Date	14 June 2022

Name of Co-Author	Clarence Chuah		
Contribution to the Paper	Helped with nuclear magnetic resonance tests		
Signature		Date	14 June 2022

Name of Co-Author	Youhong Tang		
Contribution to the Paper	Helped with nuclear magnetic resonance tests		
Signature		Date	14 June 2022

Name of Co-Author	Yan Jiao		
Contribution to the Paper	Helped with theoretical computations		
Signature		Date	14 June 2022

Name of Co-Author	Mietek Jaroniec		
Contribution to the Paper	Revised the manuscript		
Signature		Date	14 June 2022

Name of Co-Author	Shi-Zhang Qiao		
Contribution to the Paper	Supervised the research project		
Signature		Date	14 June 2022

Please cut and paste additional co-author panels here as required.

Article

Revealing Principles for Design of Lean-Electrolyte Lithium Metal Anode via In Situ Spectroscopy

Huan Li, Dongliang Chao, Biao Chen, Xiao Chen, Clarence Chuah, Youhong Tang, Yan Jiao, Mietek Jaroniec, and Shi-Zhang Qiao*

Read Online

ACCESS | Metrics & More | Article Recommendations | Supporting Information

ABSTRACT: Lean-electrolyte conditions are highly pursued for practical lithium (Li) metal batteries. The previous studies on the Li metal anodes, in general, exhibited good stability with a large excess of electrolyte. However, the targeted design of Li hosts under relatively low electrolyte conditions has been rarely studied so far. Herein, we have shown that electrolyte consumption severely affects the cycling stability of Li metal anode. Considering carbon hosts as typical examples, we innovatively employed in situ synchrotron X-ray diffraction, in situ Raman spectroscopy, and theoretical computations to obtain a better understanding of the Li nucleation/deposition processes. We also showed the usefulness of in situ electrochemical impedance spectra to analyze interfacial fluctuation at the Li/electrolyte interface, together with nuclear magnetic resonance data to quantify electrolyte consumption. We have found that uneven Li nucleation/deposition and the crack of surface-area-derived solid-electrolyte interface (SEI) layer both lead to a great consumption of electrolyte. Then, we suggested a design principle for Li host to overcome the electrolyte loss, that is, uneven growth of the Li structure and the crack of the SEI layer must be simultaneously controlled. As a proof of concept, we demonstrated the usefulness of a 3D low-surface-area defective graphene host (L-DG) to control Li nucleation/deposition and stabilize the SEI layer, contributing to a highly reversible Li plating/stripping. As a result, such a Li host can achieve stable cycles (e.g., 1.0 mAh cm^{-2}) with a low electrolyte loading (10 μL). This work demonstrates the necessity to design Li metal anodes under lean-electrolyte conditions and brings Li metal batteries a step closer to their practical applications.
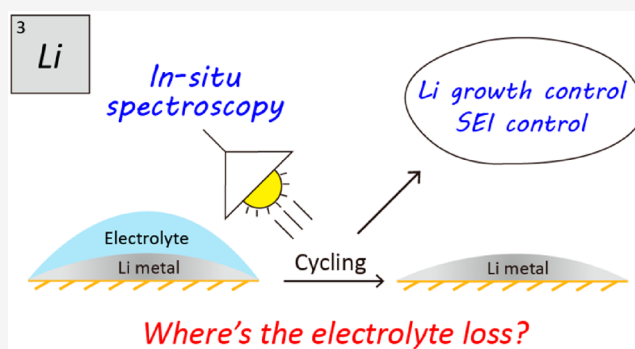
INTRODUCTION

Metallic lithium (Li) has been considered as one of the most promising anodes because of its high specific capacity (3860 mAh g^{-1}) and low electrochemical potential (-3.04 V vs standard hydrogen electrode).[1] Previous studies in this field were mainly focused on the growth of dendritic structures,[2−4] but the cyclic stability with limited electrolyte amount has not received much attention. Up to now, the growth of dendrites has been well-controlled by designing a proper host to promote an even Li deposition.[5−13] Hence, the current Li anodes can achieve excellent cyclic stability by using different protection schemes, such as electrolyte engineering, 3D Li metal host, artificial SEI layer, etc.[14−21] Unfortunately, most of these undertakings ensure cycling stability when a large excess of electrolyte is used (the electrolyte-to-capacity ratio is normally >40 μL mAh^{-1}), which sacrifices the energy density of batteries.[22−24] For example, if a Li−S battery is loaded with 40 μL mAh^{-1} electrolyte (electrolyte/sulfur mass ratio E/S $\approx$ 24), its energy density is dramatically lowered to ~150 Wh kg^{-1}, making it not competitive even with commercial lithium-ion batteries.[25−27] In contrast, a Li−S battery with ~6 μL

mAh^{-1} electrolyte (E/S $\approx$ 4) is expected to deliver a much higher energy density of >300 Wh kg^{-1}.[28] Therefore, the electrolyte usage affects both the energy density and the cyclic stability, which must be optimized to transfer the high-energy benefits of Li anode to a real Li metal battery.[22−24,29] In this regard, the mass and volume of electrolyte should be carefully controlled, for example, below 10 μL mAh^{-1}. However, the inferior cyclic stability caused by electrolyte consumption is supposed to be more serious under lean-electrolyte conditions.[30−32] The targeted design of Li hosts for overcoming electrolyte loss remains a great challenge.

Electrolyte consumption is tightly related to many factors.[29−34] The dendrite growth and sequential formation of "dead" Li lead to continuous electrolyte loss.[35] Thus, it is important to guide Li nucleation on the host materials to

38

control the growth of Li structures and achieve a uniform Li deposition.[19,36,37] More importantly, the fragile SEI layer on the Li anode is mechanically unstable under fluctuating interfacial changes and large volume expansion. This electrolyte-derived layer tends to crack and reform during the repeated cycling of a Li anode, leading to a great consumption of electrolyte and rapid battery failure.[31,38,39] To construct a stable Li anode, porous carbons were widely used as host materials because of their chemical stability, tailored pore structure, and high electrical conductivity.[40,41] Their 3D structures possess large pore volume to accommodate the volume expansion, and their interconnected networks help to decrease the local current density, suppressing dendrite growth. However, they normally have a high specific surface area, which contributes to a large-area SEI layer prone to a higher possibility of cracking. Consequently, efficient operation of Li anodes under lean-electrolyte conditions is more challenging because a comprehensive host design, considering Li nucleation/deposition, volume changes, and crack reformation of the SEI layer, is needed.

In this work, we first demonstrate that the electrolyte consumption severely affects the cycling stability of Li metal anodes. Then, we suggest a design principle for Li host under lean-electrolyte conditions based on the studies of Li nucleation and deposition via in situ synchrotron X-ray diffraction and Raman and electrochemical impendence spectroscopies. Taking carbon hosts as typical examples, we found that both uneven Li nucleation/deposition and crack reformation of surface-area-derived SEI layer consume the electrolyte during cycling. To overcome the electrolyte loss, these two factors must be simultaneously controlled. As a proof of concept, we demonstrate the use of a 3D low-surface-area defective graphene host (L-DG) to control Li nucleation/deposition and stabilize the SEI layer, contributing to a highly reversible Li plating/stripping. The 3D structure of L-DG helps to accommodate volume changes, and the abundant carbon defects guide Li nucleation and growth of the Li structure. More importantly, the low specific surface area contributes to a more homogeneous Li/electrolyte interface, which decreases the exposed area of the SEI layer in the electrolyte, restraining the crack reformation of this layer during cycling. As a result, such a Li host can achieve stable cycles (e.g., 1.0 mAh cm^{-2}) under lean-electrolyte conditions (10 μL). After coupling the Li anode with the sulfur (S) cathode, the assembled Li−S battery can achieve stable cycles with a desirable electrolyte loading (E/S $\approx$ 8.3).

EXPERIMENTAL SECTION

Material Synthesis. Graphite oxide (GO) was synthesized by the modified Hummers' method.[42] A graphene monolith was prepared by using a previously reported recipe.[43] Typically, 20 mg of GO was ultrasonicated in 20 mL of deionized water for 2 h (1 mg mL^{-1}). Forty mg of L-ascorbic acid sodium salt was added into the GO suspension under continuous stirring. Then, the mixed suspension was heated at 70 °C for 10 h to obtain a graphene hydrogel, which was continuously washed using deionized water to remove the sodium salt. Then, the graphene hydrogel was freeze-dried for ~12 h to obtain a graphene monolith followed by heat treatment at 800 °C (5 °C min^{-1}) for 1 h in Ar gas. The heat treatment can tune the pore structure of the graphene monolith and help to remove the oxygen-containing groups. This process resulted in a 3D high-surface-area defective graphene (H-DG). Similarly, heat treatments of such graphene monolith at 1500 °C (10 °C min^{-1}) and 2800 °C (20 °C

min^{-1}) under Ar atmosphere afforded low-surface-area defective graphene (L-DG) and low-surface-area graphene (L-G), respectively.

Characterization Techniques. The morphology and structure of the samples were characterized by scanning electron microscopy (SEM, Hitachi S4800, Japan) and transmission electron microscopy (TEM, JEOL, Japan). X-ray diffraction (XRD) data were collected on a Rigaku Mini Flex 600 X-ray Diffractometer. X-ray photoelectron spectra (XPS) analysis was conducted with a Physical Electronics PHI5802 instrument using a magnesium anode (monochromatic Kα X-rays at 1253.6 eV) as the source. The synchrotron-based near-edged X-ray absorption fine structure (NEXAFS) was performed on the soft X-ray spectroscopy beamline in the Australian Synchrotron Radiation Facility, Melbourne. N$_2$ adsorption−desorption isotherms (77 K) were measured by using a Belsorp-Mini instrument (BEL, Inc., Japan).

In Situ Synchrotron X-ray Diffraction. In situ synchrotron XRD data were collected on the powder diffraction beamline at the Australian Synchrotron with a wavelength of 0.6868 Å. Data were collected continuously in 30 s acquisitions. The coin cells were used here for the data collection and were discharged at a current density of 1 mA cm^{-2} with an areal capacity of 0.67 mAh cm^{-2}. The cell cases on both the negative and positive sides together with the Li foil anode were punched with d = 0.5 mm holes, and polyimide films were used to seal the holes but allowed the X-ray transmission.

In Situ Raman Spectroscopy. Raman spectra were collected with Labram HR Evolution (Horiba Scientific). The stainless-steel cell with a quartz window on the negative shell was used for in situ Raman spectroscopy. A hole with a diameter of 0.4 mm was punched both on lithium foil and the glass fiber separator to allow the laser shed on the carbon host. The cells were discharged−charged at a current density of 1 mA cm^{-2} with an areal capacity of 0.5 mAh cm^{-2}. A low magnitude 50× objective was used, and Raman signals were recorded simultaneously by a 532 nm laser during Li plating/stripping.

In Situ Electrochemical Impedance Spectrum. The electrochemical impedance spectrum (EIS) plots were obtained from a CHI660D electrochemical workstation. The frequency was set from 10^5 to 0.1 Hz with a voltage amplitude of 5 mV. The Li plating/stripping test was carried out as stated in the previous section. At the beginning of each cycle, an EIS plot was recorded prior to the Li plating/stripping.

Nuclear Magnetic Resonance Analysis. The electrolyte component used in this work is 1 M bis(trifluoromethane)sulfonimide lithium salt (LiTfSi) in 1,3-dioxolane (DOL)/1,2-dimethoxyethane (DME) (1:1 volume ratio) with 0.4 M LiNO$_3$. For the ^{19}F nuclear magnetic resonance (NMR) analysis, the electrolyte from the cycled cells was extracted with 0.3 mL of DOL. The solution was then mixed with 0.2 mL of a deuterated dimethyl sulfoxide (D-DMSO) solution of fluorobenzene (0.1 M) in an NMR tube. The electrolyte amount, corresponding to the peak area of TfSi$^-$ anions, was normalized to 100% by comparing it with 0.1 M fluorobenzene. Owing to the known content of the internal reference, the peak area of TfSi$^-$ anions can be used to quantify the electrolyte retention.

Electrochemical Test. For the Li plating/stripping tests, the L-DG/H-DG/L-G raw material was mixed with 10% LA-133 binder to prepare the electrode. Then, the coin cell (CR2032) was assembled in an Ar-filled glovebox with a Li foil anode, a polypropylene (PP) separator, and the discussed electrolyte. The battery was cycled from 1 to 0.01 V at 0.2 mA cm^{-2} with excess electrolyte to stabilize the SEI layer. Then, the batteries were disassembled, and the cathode was washed with fresh DOL solvent. Afterward, the cathode was reassembled with a Li anode and a certain amount of electrolyte (e.g., 10 μL). The battery was discharged at a given current density and areal capacity, followed by charging to 0.5 V to allow for Li stripping (Figure S1). For the Li−S battery test, the sulfur cathode was prepared by mixing 80 wt % S with 20 wt % mesoporous carbon (CMK3) under 155 °C for 12 h. Then, the CMK3/S mixture was ball-milled with Super P and LA133 binder with a mass ratio of 80:10:10. The total sulfur content in the cathode was 64 wt %. For the preparation of the Li anode, the L-DG/H-DG electrode was
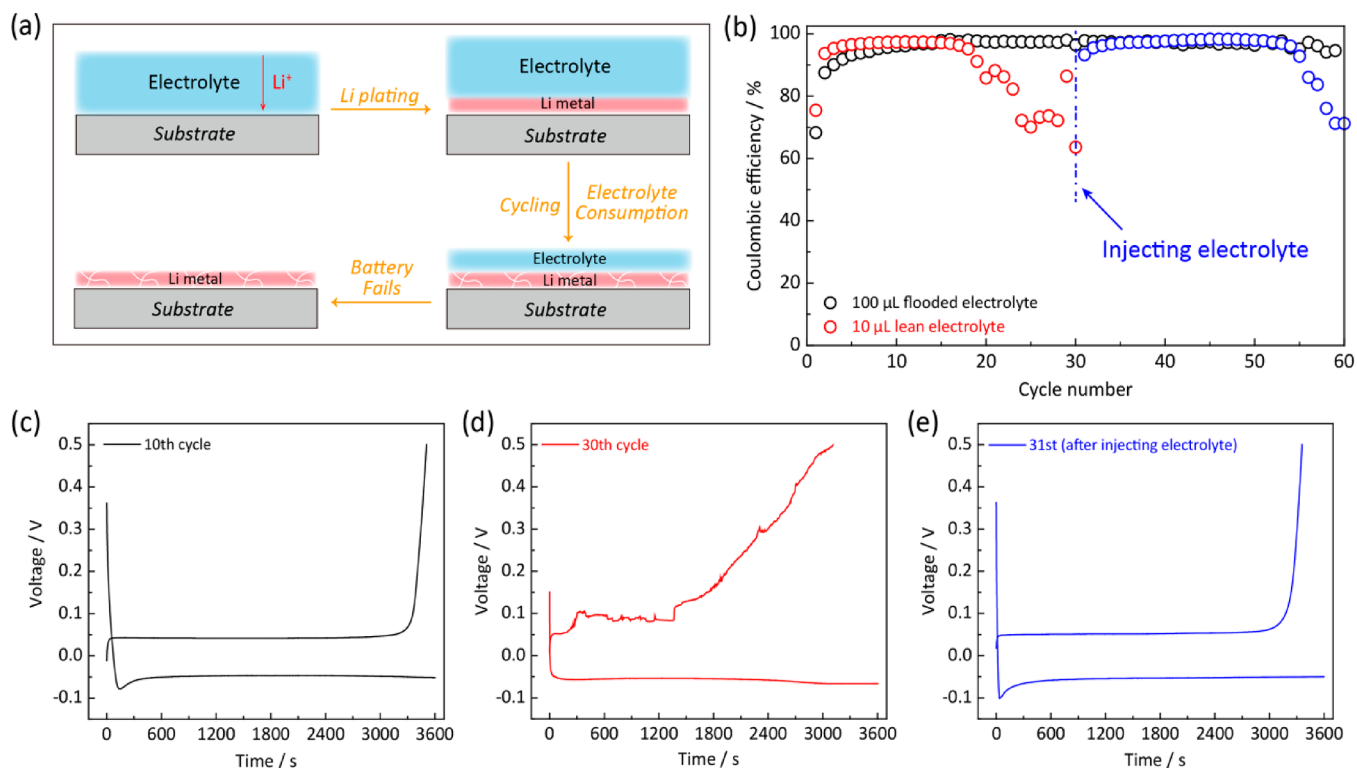
Figure 1. Li metal anode under lean-electrolyte conditions. (a) Scheme for electrolyte consumption during Li cycling. (b) Cycling performance with 100 μL of flooded electrolyte and 10 μL of lean electrolyte. (c−e) Charge−discharge curves for Li plating/stripping with 10 μL of electrolyte: (c) the 10th cycle, (d) the 30th cycle before injecting electrolyte, and (e) the 31st cycle after injecting electrolyte.

discharged at 0.2 mA cm^{-2} for Li plating. The S mass loading on the cathode was set as 1.2 mg cm^{-2}, and the plated Li capacity was controlled at ∼6.03 mAh. The anode/cathode capacity ratio was kept at ∼3 to ensure a good cycling performance. On the sulfur cathode part, a low but adequate E/S ratio of ∼8.3 (10 μL electrolyte) was used to optimize sulfur utilization. The assembled Li−S battery was discharged−charged from 1.7 to 2.8 V at different rates (1 C = 1675 mAh g^{-1}) by using a LAND or a Neware battery tester.

Theoretical Calculation. All calculations in this work were carried out using density functional theory (DFT) method as implemented in the VASP code.[44] The electronic exchange-correlation energy was modeled using the Perdew−Burke−Ernzerhof (PBE) functional within the generalized gradient approximation (GGA). The projector augmented wave (PAW) method was used to describe the ionic cores. For the plane-wave expansion, a 450 eV kinetic energy cutoff was used after testing a series of different cutoff energies. A Monkhorst−Pack 3 × 3 × 1 k-point grid was used to sample the Brillouin zone. The convergence criterion for the electronic structure iteration was set to be 10^{-4} eV, and that for geometry optimizations was set to be 0.01 eV/Å on the force. Gaussian smearing of 0.1 eV was applied during the geometry optimization and for the total energy computations. The constructed supercell was built with a 20 Å slam layer in the z-direction. Denser k-points (5 × 5 × 1) were used to improve the quality of the density of states (DOS) computations.

■ RESULTS AND DISCUSSION

Battery Failure Caused by Electrolyte Consumption. Figure 1a schematically shows the electrolyte consumption during the Li plating/stripping process. Under an electric field, the Li-ion flux in the bulk electrolyte moves toward the substrate to plate metallic Li. In this process, dendrite growth and SEI crack may occur on the surface of the Li metal. There is continuous electrolyte loss due to the formation of dendrites or dead Li as well as the crack reformation of the SEI layer

during cycling. This will lead to battery failure once the electrolyte is depleted. To confirm this idea, we conducted the Li plating/stripping tests on a 3D high-surface-area defective graphene (H-DG) host (Figure S2) and investigated the effect of electrolyte loadings on the cyclic stability. The H-DG host was cycled at 1 mA cm^{-2} with an areal capacity of 1 mAh cm^{-2}. As shown in Figure 1b, the Coulombic efficiency (CE%) is stable at the initial cycles but shows a dramatic decrease after tens of cycles with limited electrolyte amounts (10 μL as shown by the red scatters). For example, it shows a good Li plating/stripping behavior at the 10th cycle but degrades down at the 30th cycle (Figure 1c and d). After injecting an extra 10 μL of electrolyte, the normal Li plating/stripping recovers and CE% returns to ∼93% (blue scatters in Figure 1b and curve in Figure 1e). In contrast, such an H-DG host can achieve stable cycling with flooded electrolyte over 60 cycles (100 μL, black curve of Figures 1b and S3). These results reveal the significance of electrolyte loading on cycling stability, which confirms that electrolyte consumption is one of the main reasons for the failure of Li anode.

To overcome the electrolyte consumption, it is pivotal to modify the discussed carbon host to inhibit the dendrite growth and construct a homogeneously stable SEI layer. Heat treatment is a facile yet effective way to engineer the carbon nanostructures.[45,46] Note that the carbon defects disappeared under ultrahigh temperature (e.g., 2800 °C), which is unfavorable for Li nucleation/deposition (Figure S4).[47] Meanwhile, annealing at a relatively low temperature (e.g., 800 °C) preserves a high specific surface area, increasing the cracking possibility of the SEI layer. Therefore, a well-balanced temperature should be established to obtain a low specific surface area while preserving the amounts of carbon defects. In
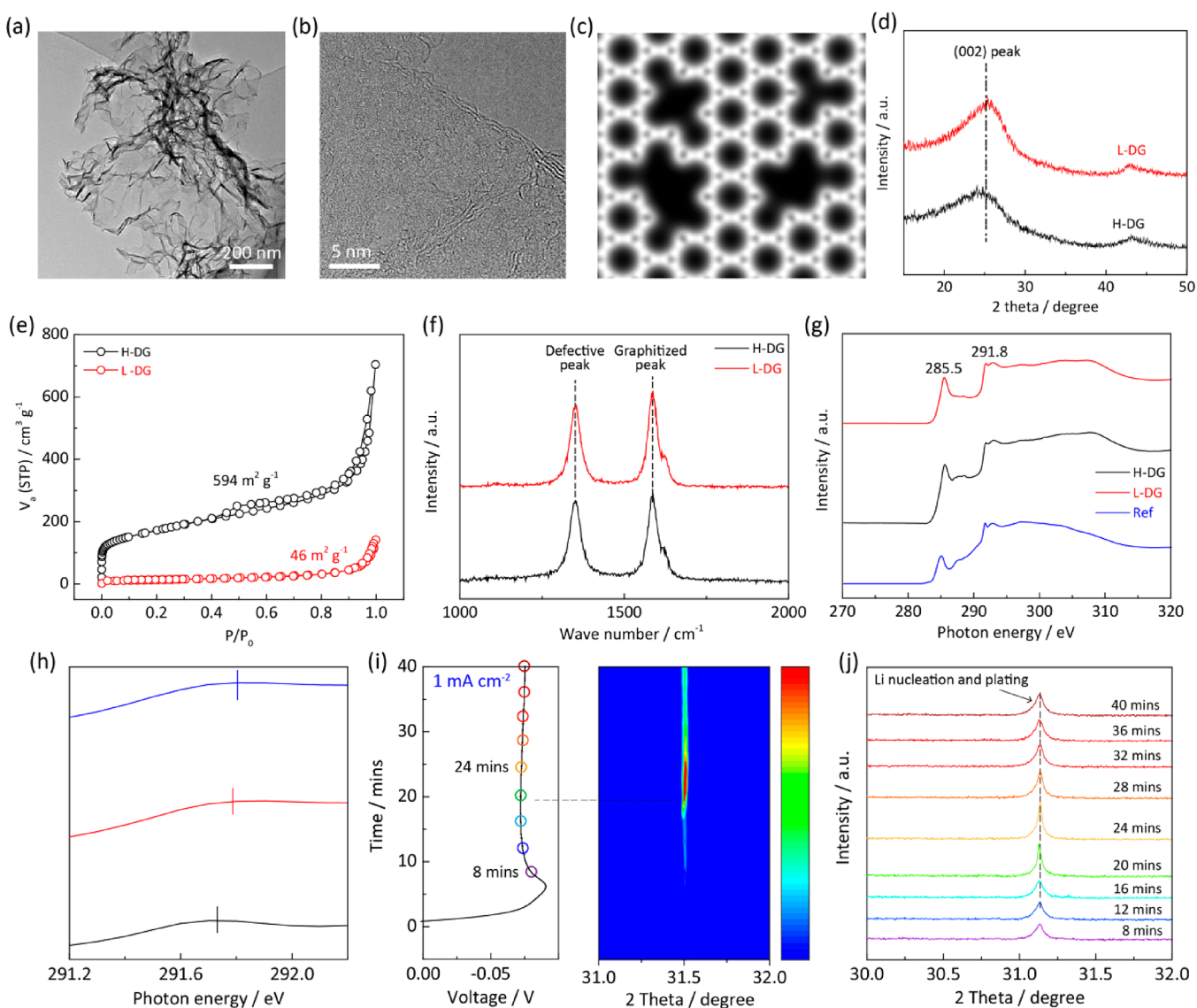
Figure 2. Structure and defect chemistry of 3D low-surface-area defective graphene (L-DG). (a, b) TEM images of L-DG. (c) Simulated image of C1, C2, C3, and C4 vacancies. (d) XRD patterns of L-DG and H-DG. (e) N_2 adsorption−desorption isotherms (77 K) measured for L-DG and H-DG. (f) Raman spectra of L-DG, H-DG, and L-G. (g, h) NEXAFS spectra of L-DG and H-DG. (i) In situ synchrotron XRD contour map during Li nucleation/deposition. (j) Selected XRD patterns with a time interval of 4 min starting from 8 min.

this regard, the H-DG material was heat-treated at 1500 °C in an argon atmosphere to obtain L-DG. After the heat treatment, L-DG inherits the 3D structure and retains carbon defects, which can be identified on the TEM images in Figure 2a and b. Figure 2c simulates the C1−C4 (CX indicates the number X of removal carbon atoms from the pristine graphene unit) defects on the graphene unit, and they are expected to guide the Li nucleation/deposition, which will be discussed later. Notably, X-ray diffraction (XRD) patterns (Figure 2d) show a broad (002) peak around 26°, indicating that L-DG keeps the graphene characteristics after the heat treatment rather than changes to a layer-stacked graphite structure. N_2 adsorption−desorption isotherms (77 K) were further used to reveal the pore evolution (Figure 2e). The H-DG host shows a 3D interconnected structure with large amounts of micropores (~1.4 nm) and mesopores (~3−7 nm) (Figure S5). These pores contribute to a high specific surface area of 594 m² g⁻¹. After heat treatment at 1500 °C, L-DG shows a sharp decrease in the volume of micropores and mesopores, resulting in a low

specific surface area of 46 m² g⁻¹. This is mainly due to the rearrangement of the graphene units. However, L-DG inherits the 3D interconnected structure of the graphene monolith with an abundant amount of micron-size large pores. These pores are mainly responsible for the Li plating and help to accommodate the accompanying volume changes. More importantly, a low specific surface area is favorable for achieving a more stable Li/electrolyte interface by decreasing the cracking possibility of the SEI layer. Raman spectra were further used to demonstrate the carbon defects in L-DG. Peaks located at ~1350 and ~1580 cm⁻¹ correspond to the defective peak and graphitized peak for sp^2 carbons. The ratio of D peak and G peak (I_D/I_G) is an important parameter to reflect the carbon defects, and a high ratio indicates a more defective nature. As shown in Figure 2f, after 1500 °C heat treatment, the I_D/I_G changes slightly from 0.95 to 0.86, indicating that the amounts of carbon defects have been well-retained. In contrast, heat treatment at 2800 °C (L-G) results in a low specific surface area, but it will simultaneously eliminate the carbon

2041
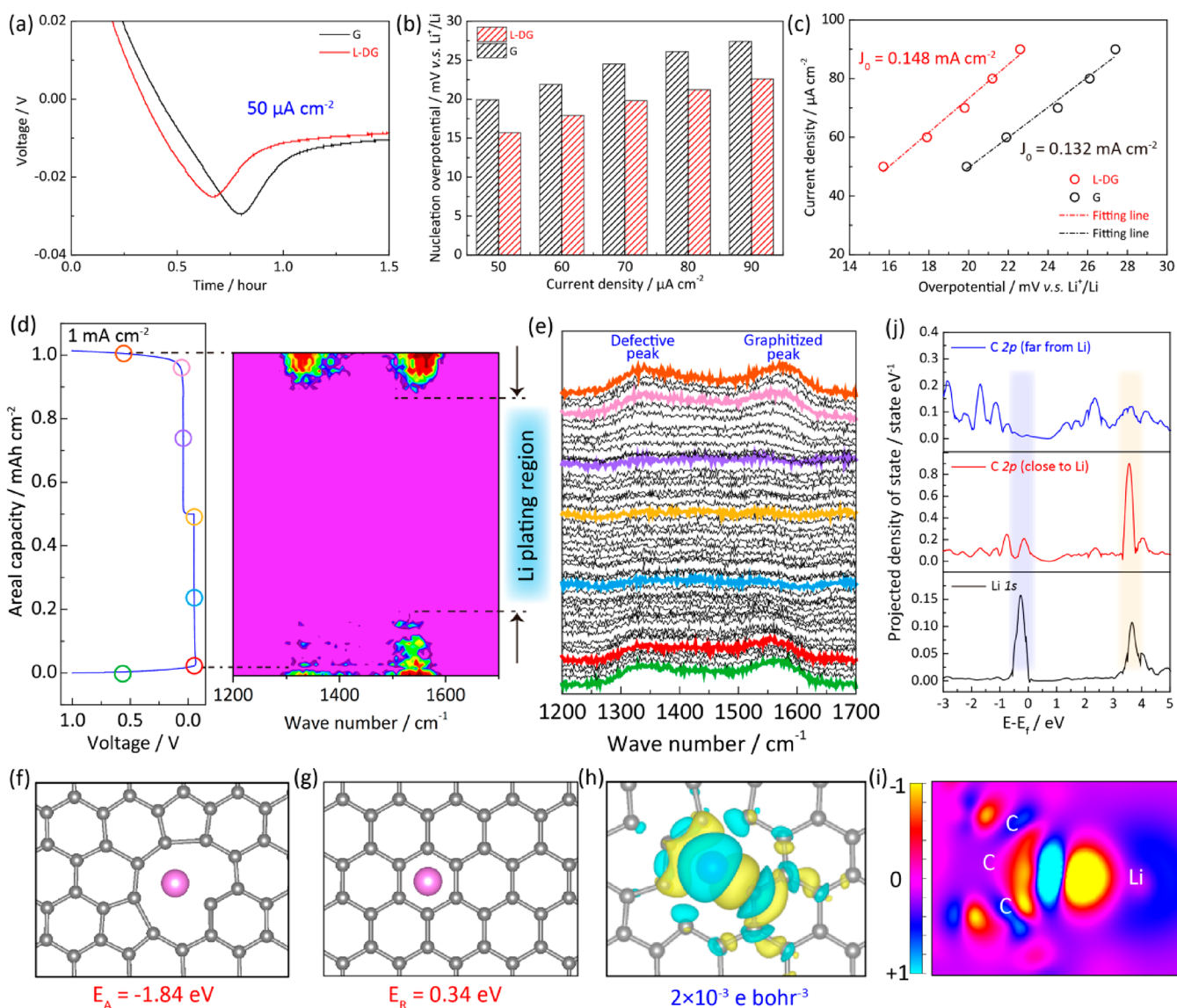
Figure 3. Uniform nucleation guided by carbon defects. (a, b) Discharge curves of L-DG and L-G under 50 $\mu A \ cm^{-2}$. (b) Li plating overpotential of L-DG and L-G. (c) Exchange current densities of L-DG and L-G. (d) Li plating/stripping curve obtained for L-DG and its real-time Raman contour map. The current density was set as 1 $mA \ cm^{-2}$ with an areal capacity of 0.5 $mAh \ cm^{-2}$. (e) Stacked Raman spectra for Li nucleation and deposition process. The colored lines correspond to the dots in the charge−discharge curve (left). (f, g) Binding energy and repulsive energy of L-DG and L-G. (h, i) 3D and 2D charge difference between C3 defective substrate and surface Li. (j) Projected DOS of Li, C (close to Li and far from Li).

defects in the graphene units ($I_D/I_G = 0.06$, Figure S6), which is unfavorable for the Li nucleation and deposition.

To reveal more information about the carbon speciation associated with the D-band feature, near-edged X-ray absorption fine structure (NEXAFS) spectroscopy was used to further investigate the defective nature (Figure 2g). In C K-edge NEXAFS, two main peaks at 285.5 and 291.9 eV are assigned to 1s → π^* and 1s → σ^* transitions in the hexagonal graphite layers. The σ^* state at 291.9 eV is sensitive to distortions and strain of the carbon bonds in hexagonal graphite. The peaks for both H-DG and L-DG shift to higher energy compared to those observed for the HOPG (highly oriented pyrolytic graphite) reference, suggesting the preservation of carbon defects in L-DG after heat treatment (Figure 2h). To get a better understanding of how the metallic lithium nucleates and deposits on the carbon host, we employed in situ synchrotron XRD on the L-DG host with real-time electro-

chemical Li plating. As shown in Figure 2i, the contour map reveals that the metallic Li starts to be nucleated onto the L-DG host after overcoming a Li plating overpotential (the tip in the discharge curve). Then, the Li signal becomes more protruded upon prolonging the Li plating time. This is more obvious by analyzing the stacked XRD curves, which are selected with a time interval of 4 min starting from 8 min (Figure 2j). Accordingly, the peak intensity corresponding to the Li (220) peak becomes much higher during Li deposition, confirming the Li nucleation and deposition stages on the L-DG host. The synchrotron XRD is effective here to detect the facile Li nucleation and deposition on various host materials. Both Li nucleation and deposition occur during the Li cycling process. Thus, it is important to regulate the beginning of Li nucleation and then control the sequential Li deposition process.

Uniform Li Nucleation/Deposition Guided by Carbon Defects. Li nucleation is an important electrochemical process because it not only guides the beginning of Li nucleation but also determines the sequential growth of Li structure.[31,32] To further evaluate Li nucleation guided by carbon defects, we compared the discharge curves of L-DG (with defects) and L-G (without defects) at 50 μA cm^{-2} (Figure 3a). The Li plating overpotential is defined as the voltage difference between the sharp tip voltage and the later stable mass-transfer-controlled voltage plateau, and these values are 15.7 and 19.9 mV for L-DG and L-G, respectively. Hence, the L-DG host exhibits a lower resistance for metallic Li to be plated on its surface. Then, we prepared the graphene hosts with different degrees of defects, which was achieved by altering the heating temperatures. As expected, the L-DG host with more defective sites shows a lower Li nucleation potential (see detailed discussion in Figure S7). Figure 3b summarizes the nucleation overpotentials for L-DG and L-G at different current densities ranging from 50 to 90 μA cm^{-2} (Figure S8). As expected, the overpotentials of L-DG are much lower than those of L-G under varying current densities. The amounts of carbon defects present on the L-DG surface are favorable for the Li nucleation, which is proved by a lower overpotential that allows the metallic Li to be nucleated. These results reveal that the carbon defects can guide the Li nucleation onto the L-DG surface. Moreover, the exchange current density (J_0) was then calculated to demonstrate the Li nucleation kinetics. At low overpotentials, the Butler−Volmer equation can be approximated to a linear relationship between the overpotential (η) and the current densities (j); hence, J_0 can be extracted from the slope of η−j lines (Figure 3c).[21,48] The L-G material shows a lower exchange current density of 0.132 mA cm^{-2}. With the help of abundant carbon defects, the L-DG host exhibits a much higher J_0 of 0.148 mA cm^{-2}, indicating enhanced Li nucleation kinetics guided by carbon defects. Notably, the exchange current density in the Tafel region (η − log j) is much higher than that in the above linear region (see detailed discussion in Figure S8). This is because the Tafel region includes both the Li nucleation and the Li deposition process. More metallic Li is involved in this region, and hence, a higher exchange current density is observed. Here, we want to show that Li prefers to nucleate on the defective sites, and therefore, the exchange current densities obtained at lower nucleation overpotentials in the linear region are more convincing and reasonable.

To further demonstrate the effect of carbon defects on the Li nucleation, we recorded the in situ Raman spectra as shown in Figure 3d and e. Note that Raman spectroscopy is a spatially local technique. Hence, a lower objective magnitude should be selected to reveal the overall electrode information; for example, a 50× objective was selected in this work. Raman spectroscopy is an effective technique to detect the vibration frequency for molecular structures; however, it cannot detect the metallic signals, such as Li. Hence, one can compare the Raman signals before and after Li plating, where the vanished peaks should be attributed to the Li plating sites. More importantly, the nucleation sites with higher Li affinity can be deduced by the sequential orders of the Raman peaks that disappeared. Taking the L-DG host as an example, at the initial stage, there are obvious peaks related to defective and graphitized domains located at ~1350 and ~1580 cm^{-1} for a fresh host. In Figure 3d, Li plating begins at the red dot and Li stripping starts at the yellow dot. During the Li plating

(discharging) process, the defect-related peaks gradually disappear due to the deposited surface Li inside the carbon defects (no Raman peaks for metallic Li). In the following Li plating process, the peak related to graphitic domains starts to vanish owing to the Li coating. These results confirm that the metallic Li tends to be nucleated inside the carbon defects in the beginning stage and then expands over the host surface. While charging the Li anode, the deposited Li strips gradually disappear from the host surface into the bulk electrolyte in the form of Li ions. Hence, the peaks related to defect and graphitic domains gradually recover, illustrating a reversible Li plating/stripping process on an L-DG host. In situ Raman spectroscopy offers a powerful way to reveal the Li nucleation and deposition behavior on the host materials.

To clarify the Li nucleation at the atomic level, DFT computational results were used to model the interaction between surface Li and the graphene substrate. A negative energy value indicates the binding interaction, whereas a positive one means the repulsion. As expected, all the C2, C3, and C4 defects present a binding interaction with the surface Li atom (Figure S9). Taking the C3 defect as an example (Figure 3f), there exists binding energy of −1.84 eV between the surface Li and the carbon substrate. However, for a pristine graphene unit without carbon defects, repulsive energy of 0.34 eV was obtained (Figure 3g). Such a comparison confirms a stronger binding interaction between the surface Li and the carbon defects. Moreover, we constructed the charge-difference maps to illustrate the charge transfer between Li and carbon defects (Figure 3h and i). The observed negative charges accumulated at the Li/C interface, suggesting an effective electron transfer from defective carbons to the surface Li. In other words, as the Li ion or Li* intermediate moves toward the carbon substrate, the surrounding defective carbons are more likely to supply electrons for the metallic Li to be nucleated inside the carbon defects. This can also be confirmed by the partial density of the state (PDOS) of the surface Li 1s, C 2p far from Li, and C 2p close to Li (Figure 3j). At the relative energies (E−E_{Fermi}) of −0.5−0 eV and 3−4 eV, there is obvious 1s−2p orbital overlapping between the surface Li and the nearby C. In contrast, the overlapped peak intensity between Li and the distant C atom is weak, and the nucleated Li prefers to form bonds with the defective carbons. In this section, we have presented (1) in situ Raman spectra, (2) nucleation overpotentials, (3) exchange current densities, and (4) DFT calculations to prove that Li prefers to nucleate on the defect sites. These uniform Li seeds on the defective sites are the key to the formation of smooth Li deposits (Figure S10).

Limited Electrolyte Consumption Enabled by Low-Surface-Area Derived SEI Layer. As discussed earlier, the carbon defects can guide the uniform Li nucleation, which is a good precondition for the Li cycling process. The next step is to demonstrate the advantages of low specific surface area on the stability of the SEI layer. The SEI layer consists of insoluble and partially soluble reduction products of electrolyte components, such as LiF, LiCO$_3$, polymeric species, etc.[33] This layer is formed on the exposed surface area by electrolyte decomposition at low operation potentials, and hence, its stability should be highly dependent on the specific surface area. The amounts of micropores and mesopores contribute to a high specific surface area, generating a large percentage of SEI layer. Unfortunately, they have limited ability to accommodate metallic Li because of their small pore volumes.
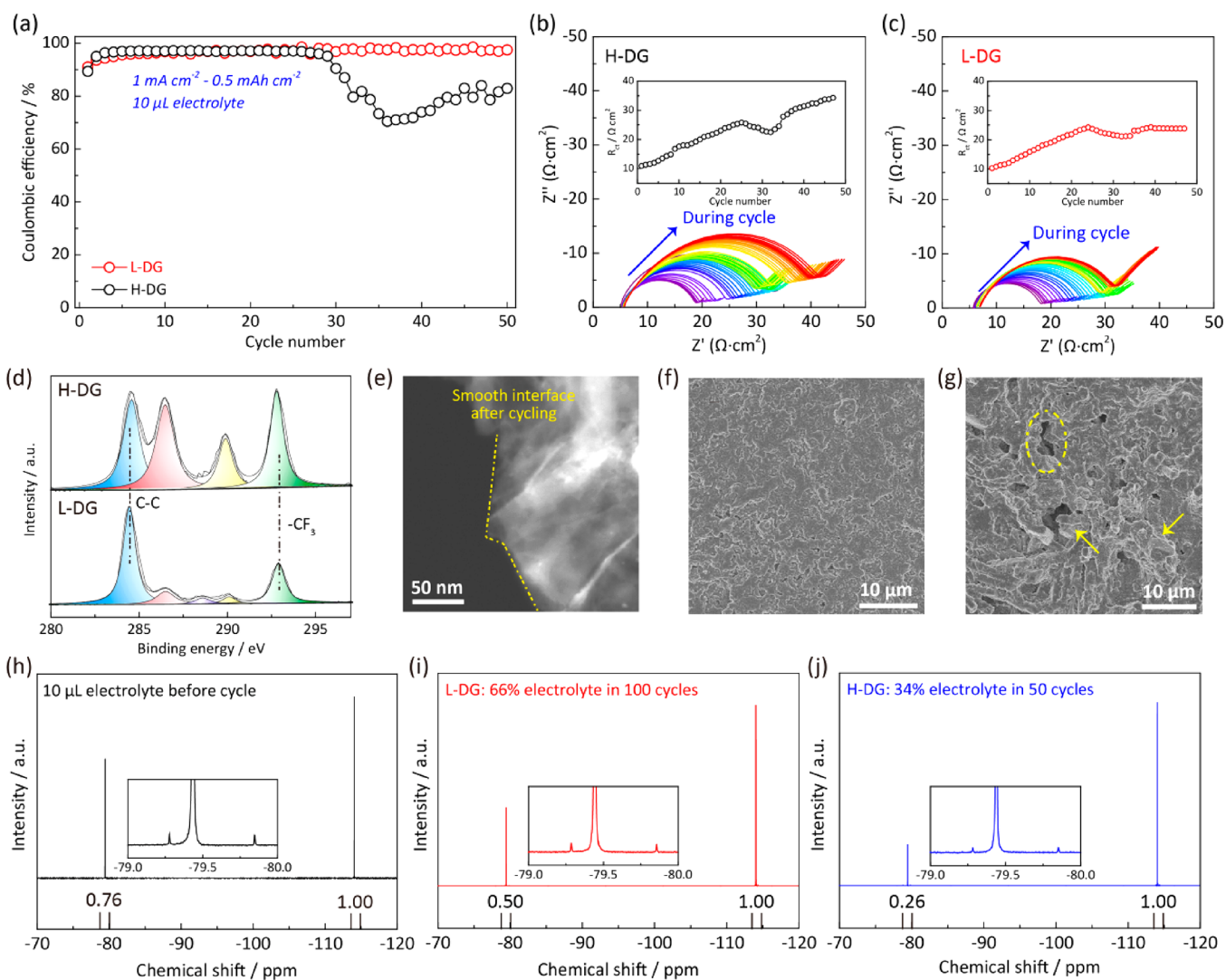
Figure 4. Changes at the Li/electrolyte interface for L-DG and H-DG. (a) Coulombic efficiency of H-DG and L-DG with an areal capacity of 0.5 mAh cm^{-2} at 1 mA cm^{-2}. In situ EIS plots of (b) H-DG and (c) L-DG during cycling. (d) XPS spectra of L-DG and H-DG. (e) TEM image and (f) SEM image of L-DG after cycling. (g) SEM image of H-DG after cycling. NMR spectra of (h) fresh cell, (i) L-DG after 100 cycles, and (j) H-DG after 50 cycles. The inset figures show the detailed F coupling of LiTfSi salt in the electrolyte.

More seriously, they aggravate the SEI crack reformation during cycling, leading to continuous electrolyte consumption. To reveal the effect of surface area on the cyclic stability, we compared the CE% of L-DG and H-DG by repeated charging–discharging at 1 mA cm^{-2} with an areal capacity of 0.5 mAh cm^{-2} with lean electrolyte (10 μL) (Figures 4a and S11). Both the L-DG and H-DG remain stable at the beginning cycles due to sufficient electrolytes. However, at around the 30th cycle, CE% of H-DG shows a dramatic decrease because of the continuous electrolyte loss. The fluctuation of CE% can be ascribed to the uneven Li nucleation/deposition, cracking of the SEI layer, and soft shorts caused by the highly irregular Li deposits. These unwanted issues will actually lead to electrolyte loss. As a result, the battery shows a rapid failure after running out of the electrolyte. In contrast, L-DG keeps a stable CE% of ~98.5%, contributing a more stable Li/electrolyte interface and lower electrolyte consumption. Analysis of the Li/electrolyte interface at different cycles provides additional insight into the role played by L-DG. As a frequency-domain technique, the electrochemical impedance spectroscopy (EIS) is well-suited to characterize the Li/electrolyte interfacial

resistance, which is related to the width of the curves (e.g., Figure 4b and c).[49,50] The in situ EIS plots for different cycles can reveal the interfacial changes after Li plating/stripping in real time. Parts b and c of Figure 4 show the EIS plots for H-DG and L-DG, respectively, from the first to the 50th cycle. The ohmic resistance (R_{Ω}), which correlates to the intercept on the x-axis near the high-frequency region, shows a slight increase for both H-DG and L-DG hosts. This suggests that R_{Ω} is not a dominating factor that affects the cyclic stability. More obviously, the Li/electrolyte interfacial impedance (R_{ct}) increases from 10 to ~35 Ω cm^2 for the H-DG host (Figure S12). This is mainly due to the unstable Li/electrolyte interface, involving the crack reformation of the SEI layer and the consumption of electrolyte. In contrast, the R_{ct} values for L-DG increase at the beginning cycles and then remain stable, indicating a much more stable SEI layer and electrolyte conditions.

The surface chemistries of the SEI layers formed on both H-DG and L-DG were further investigated by XPS (Figure 4d), which contains the carbon–oxygen, carboxyl, and carbon–fluorine species, corresponding to the peaks located at 286.5,

44
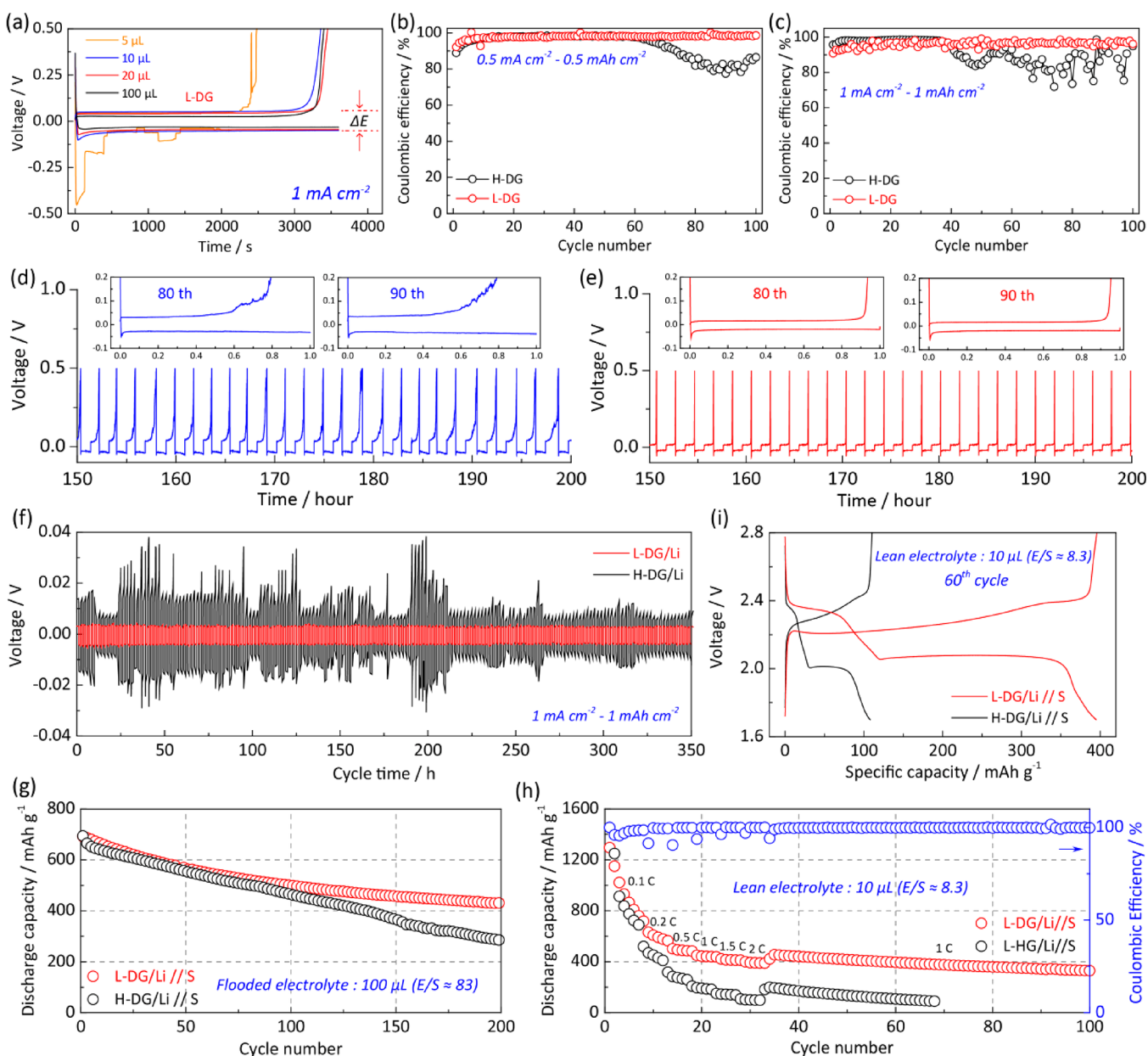
Figure 5. Li−S batteries working under lean-electrolyte conditions. (a) Charge−discharge curves of L-DG at 1 mA cm^{-2} with an areal capacity of 1 mAh cm^{-2} and different electrolyte amounts ranging from 5 to 100 μL. (b, c) Coulombic efficiency of H-DG and L-DG with different current densities and areal capacities. Typical charge−discharge curves of (d) H-DG and (e) L-DG at the 80th and 90th cycles. The current density is 1 mA cm^{-2} with an areal capacity of 1 mAh cm^{-2}. (f) Long-time galvanostatic cycling for L-DG/Li and H-DG/Li symmetric cells. (g) Cyclic stability of L-DG/Li//S and H-DG/Li//S full cells with excess electrolyte (100 μL). (h) Rate capacity from 0.1 to 2 C and cycling performance of L-DG/Li//S and H-DG/Li//S full cells with lean electrolyte (10 μL). (i) Typical charge−discharge curves of L-DG/Li//S and H-DG/Li//S full cells at the 60th cycle.

290.1, and 292.9 eV, respectively. The peak intensities of H-DG are much higher than those of L-DG, confirming the larger percentage of SEI layer on the H-DG host. This leads to a higher possibility of the SEI cracking during cycles and, hence, higher consumption of the electrolyte. To quantitatively compare the SEI contributions among host materials, we present the percentages of carbon−fluorine bonds in L-DG and H-DG by normalizing the carbon−fluorine peaks using carbon−carbon peaks (284.5 eV). As a result, the $-CF_3$ percentage in H-DG is ∼46.6%, which is ∼1.6 times higher than that of L-DG (∼29.5%) (green area in Figure 4d). After cycling, the surface morphologies of H-DG and L-DG were compared with SEM and TEM images. L-DG keeps a smooth

interface without cracking, as shown in Figure 4e and f. However, H-DG shows a more protruded surface caused by the uneven deposition of metallic Li (Figure 4g). To compare the electrolyte retention between L-DG and H-DG, the changes of electrolyte amounts after cycling were monitored by tracking the quantity of TfSi$^-$ anions in the cell using ^{19}F NMR, because F signals come exclusively from the LiTfSi salt in the electrolyte. The TfSi$^-$ anions in the fresh electrolyte show three F coupling peaks located at −79.3, −79.4, and −79.8 ppm. Because of the known amount of an internal reference (fluorobenzene, −114 ppm), the integrated area of these peaks can be used to quantify the electrolyte retention. The amounts of electrolyte before cycling were normalized to

100% (Figure 4h). As a result, the L-DG host can retain 66% electrolyte after 100 cycles at 1 mA cm^{-2} and 1 mAh cm^{-2} (Figure 4i). In contrast, the H-DG host only maintains 34% electrolyte after 50 cycles (Figure 4j), and the cell cannot operate (Figure S13). These results quantitatively confirm the electrolyte consumption caused by the large-surface-area induced SEI layer. Therefore, owing to its low surface area, L-DG contributes to a smoother surface with a stable SEI layer during the Li plating/stripping process, which can limit the electrolyte consumption under lean-electrolyte conditions.

Li−S Batteries under Lean-Electrolyte Conditions. To explore the specified electrolyte conditions, we loaded different amounts of electrolyte ranging from 5 to 100 μL, and the batteries were discharged−charged at 1 mA cm^{-2} with an areal capacity of 1 mAh cm^{-2} (Figure 5a). The Li plating/stripping behavior is stable at the electrolyte loadings of 10, 20, and 100 μL. However, the electrolyte amount affects both the Li nucleation and Li plating process. While decreasing the electrolyte loading from 100 to 20 to 10 μL, the Li nucleation overpotential increases from 11.1 to 26.5 to 48.0 mV, respectively. Moreover, the polarization voltage plateau (ΔE), which is defined as the voltage difference in the plateau region, also shows an obvious increase from 56.7 to 87.8 to 105.1 mV, respectively. These results suggest a more sluggish Li nucleation and plating process under lean-electrolyte conditions, which is mainly due to the poor wettability of the electrode/electrolyte interface. Meanwhile, the cell cannot operate with 5 μL of electrolyte. Hence, 10 μL was chosen as the lower limit of the electrolyte loading. Then, we cycled the H-DG and L-DG host at different current densities and areal capacities with 10 μL of electrolyte (Figure 5b and c). As expected, the CE% of the L-DG host remains stable during cycling, but the H-DG degrades after tens of cycles. Figure S14 compares the beginning charge−discharge curves recorded for L-DG and H-DG, and they both keep stable cycles owing to the sufficient electrolyte loading. During cycling, the discharging and charging plateaus of H-DG become fluctuant and the CE% dramatically decreases (Figure 5d). In contrast, L-DG remains stable over a wide range of cycles due to the uniform Li deposition and homogeneous SEI layer (Figure 5e). We then assembled the symmetric cells and conducted the long-time galvanostatic cycling, which was stable with smooth voltage output and presents rare changes during cycling (Figure 5e). Voltage hysteresis is defined as the sum of overpotential for Li plating and stripping, which is plotted from the 30th to 50th cycles in Figure S15.[51] H-DG/Li presents a larger voltage hysteresis of ~40 mV compared to ~9 mV for L-DG, which is possibly due to the polarization caused by dendrite formation and cracking of the SEI layer. To demonstrate the practical use of the L-DG host, the Li−S batteries were assembled using an L-DG/Li anode coupled with an S cathode with different electrolyte loadings. The Li anode capacity was kept at ~3-fold excess to ensure a stable cycling performance (see details in the Experimental Section). With excess electrolyte (Figure 5g, 100 μL, E/S ≈ 83), the battery capacity remained stable at the initial cycles while using either an L-DG/Li or H-DG/Li anode. However, the dendrite formation and cracking of the SEI layer certainly affected the battery stability after ~100 cycles (Figure S16). In contrast, battery failure will be more serious under lean-electrolyte conditions. It should be noted that a low electrolyte amount not only affects the stability of Li anode but also restricts the dissolution of lithium polysulfides on the cathode part.

Therefore, we employed a low but adequate E/S ratio of ~8.3 to ensure optimal sulfur utilization. Figure 5h compares both the rate capacity and the cyclic stability of H-DG/Li and L-DG/Li anodes for Li−S batteries under lean-electrolyte conditions (10 μL, E/S ≈ 8.3). The Li−S battery with an H-DG/Li anode shows a more degraded capacity during cycling, and the charge−discharge curve presents a large voltage polarization (Figure 5i). By comparison, L-DG/Li exhibits good stability even at different current densities (from 0.1 to 2 C) due to its effective suppression of electrolyte decomposition (Figure S17). These results verify that the stable interface and restrained electrolyte loss decisively determine the cycling stability of Li metal batteries.

■ CONCLUSIONS

We have shown a design principle of Li host for lean-electrolyte Li metal anode. To restrain the electrolyte loss, the uneven Li nucleation/deposition and the crack reformation of the high-surface-area derived SEI layer need to be simultaneously controlled. Such a design principle is concluded by studying the Li nucleation and deposition behavior by in situ spectroscopy, including in situ synchrotron XRD, in situ Raman spectra, and in situ EIS spectra. Then, we employed the DFT calculations to clarify the interaction between Li* and the substrate at an atomic level, which gives more details on the Li affinity to different substrates. As a proof of concept, we demonstrated a low-surface-area but defective 3D graphene for use as a Li anode host, which was prepared by a controlled ultrahigh-temperature treatment on a graphene monolith. It was found that abundant carbon defects can guide Li nucleation and control the sequential Li growth structure. The low specific surface area contributes to a more homogeneous Li/electrolyte interface, which decreases the exposed area of the SEI layer into the electrolyte, restraining the crack reformation of the SEI layer and electrolyte consumption. As a result, such a Li host can achieve stable cycles with desirable areal capacities under lean-electrolyte conditions. This work shows how to overcome electrolyte consumption during cycling. We hope it can provide valuable inspiration for the design of lean-electrolyte lithium metal batteries.

■ ASSOCIATED CONTENT

ⓈI Supporting Information

The Supporting Information is available free of charge at https://pubs.acs.org/doi/10.1021/jacs.9b11774.

> Material characterization, computational models, and electrochemical performance (PDF)

■ AUTHOR INFORMATION

Corresponding Author

  Shi-Zhang Qiao − *The University of Adelaide, Adelaide, Australia;* ⓞ orcid.org/0000-0002-4568-8422; Email: s.qiao@adelaide.edu.au

Other Authors

  Huan Li − *The University of Adelaide, Adelaide, Australia;* ⓞ orcid.org/0000-0003-0662-6939
  Dongliang Chao − *The University of Adelaide, Adelaide, Australia;* ⓞ orcid.org/0000-0001-7793-0044

Biao Chen − *The University of Adelaide, Adelaide, Australia, and Tianjin University, Tianjin, P. R. China;* orcid.org/0000-0002-6181-2155

Xiao Chen − *Tsinghua University, Beijing, P. R. China*

Clarence Chuah − *Flinders University, Adelaide, Australia*

Youhong Tang − *Flinders University, Adelaide, Australia*

Yan Jiao − *The University of Adelaide, Adelaide, Australia;* orcid.org/0000-0003-1329-4290

Mietek Jaroniec − *Kent State University, Kent, Ohio;* orcid.org/0000-0002-1178-5611

Complete contact information is available at:
https://pubs.acs.org/10.1021/jacs.9b11774

Notes
The authors declare no competing financial interest.

◼ REFERENCES

(1) Cheng, X. B.; Zhang, R.; Zhao, C. Z.; Zhang, Q. Toward Safe Lithium Metal Anode in Rechargeable Batteries: A Review. *Chem. Rev.* **2017**, *117* (15), 10403−10473.

(2) Lin, D.; Liu, Y.; Cui, Y. Reviving the lithium metal anode for high-energy batteries. *Nat. Nanotechnol.* **2017**, *12* (3), 194−206.

(3) Xu, W.; Wang, J.; Ding, F.; Chen, X.; Nasybulin, E.; Zhang, Y.; Zhang, J.-G. Lithium metal anodes for rechargeable batteries. *Energy Environ. Sci.* **2014**, *7* (2), 513−537.

(4) Tikekar, M. D.; Choudhury, S.; Tu, Z. Y.; Archer, L. A. Design principles for electrolytes and interfaces for stable lithium-metal batteries. *Nat. Energy* **2016**, *1* (9), 16114.

(5) Gao, Y.; Zhao, Y. M.; Li, Y. G. C.; Huang, Q. Q.; Mallouk, T. E.; Wang, D. H. Interfacial Chemistry Regulation via a Skin-Grafting Strategy Enables High-Performance Lithium-Metal Batteries. *J. Am. Chem. Soc.* **2017**, *139* (43), 15288−15291.

(6) Ye, H.; Xin, S.; Yin, Y. X.; Li, J. Y.; Guo, Y. G.; Wan, L. J. Stable Li Plating/Stripping Electrochemistry Realized by a Hybrid Li Reservoir in Spherical Carbon Granules with 3D Conducting Skeletons. *J. Am. Chem. Soc.* **2017**, *139* (16), 5916−5922.

(7) Liu, K.; Pei, A.; Lee, H. R.; Kong, B.; Liu, N.; Lin, D. C.; Liu, Y. Y.; Liu, C.; Hsu, P. C.; Bao, Z. A.; Cui, Y. Lithium Metal Anodes with an Adaptive "Solid-Liquid" Interfacial Protective Layer. *J. Am. Chem. Soc.* **2017**, *139* (13), 4815−4820.

(8) Duan, H.; Zhang, J.; Chen, X.; Zhang, X. D.; Li, J. Y.; Huang, L. B.; Zhang, X.; Shi, J. L.; Yin, Y. X.; Zhang, Q.; Guo, Y. G.; Jiang, L.; Wan, L. J. Uniform Nucleation of Lithium in 3D Current Collectors via Bromide Intermediates for Stable Cycling Lithium Metal Batteries. *J. Am. Chem. Soc.* **2018**, *140* (51), 18051−18057.

(9) Liang, X.; Pang, Q.; Kochetkov, I. R.; Sempere, M. S.; Huang, H.; Sun, X.; Nazar, L. F. A facile surface chemistry route to a stabilized lithium metal anode. *Nat. Energy* **2017**, *2* (9), 17119.

(10) Yun, Q. B.; He, Y. B.; Lv, W.; Zhao, Y.; Li, B. H.; Kang, F. Y.; Yang, Q. H. Chemical Dealloying Derived 3D Porous Current Collector for Li Metal Anodes. *Adv. Mater.* **2016**, *28* (32), 6932−6939.

(11) Yan, K.; Lu, Z.; Lee, H.-W.; Xiong, F.; Hsu, P.-C.; Li, Y.; Zhao, J.; Chu, S.; Cui, Y. Selective deposition and stable encapsulation of lithium through heterogeneous seeded growth. *Nat. Energy* **2016**, *1* (3), 16010.

(12) Li, G.; Liu, Z.; Huang, Q.; Gao, Y.; Regula, M.; Wang, D.; Chen, L.-Q.; Wang, D. Stable metal battery anodes enabled by polyethylenimine sponge hosts by way of electrokinetic effects. *Nat. Energy* **2018**, *3* (12), 1076−1083.

(13) Zhang, Y.; Luo, W.; Wang, C. W.; Li, Y. J.; Chen, C. J.; Song, J. W.; Dai, J. Q.; Hitz, E. M.; Xu, S. M.; Yang, C. P.; Wang, Y. B.; Hu, L. B. High-capacity, low-tortuosity, and channel-guided lithium metal anode. *Proc. Natl. Acad. Sci. U. S. A.* **2017**, *114* (14), 3584−3589.

(14) Li, N. W.; Yin, Y. X.; Yang, C. P.; Guo, Y. G. An Artificial Solid Electrolyte Interphase Layer for Stable Lithium Metal Anodes. *Adv. Mater.* **2016**, *28* (9), 1853−1858.

(15) Manthiram, A.; Yu, X. W.; Wang, S. F. Lithium battery chemistries enabled by solid-state electrolytes. *Nat. Rev. Mater.* **2017**, *2* (4), 16103.

(16) Basile, A.; Bhatt, A. I.; O'Mullane, A. P. Stabilizing lithium metal using ionic liquids for long-lived batteries. *Nat. Commun.* **2016**, *7*, 11794.

(17) Zheng, J. M.; Engelhard, M. H.; Mei, D. H.; Jiao, S. H.; Polzin, B. J.; Zhang, J. G.; Xu, W. Electrolyte additive enabled fast charging and stable cycling lithium metal batteries. *Nat. Energy* **2017**, *2* (3), 17012.

(18) Ding, F.; Xu, W.; Graff, G. L.; Zhang, J.; Sushko, M. L.; Chen, X.; Shao, Y.; Engelhard, M. H.; Nie, Z.; Xiao, J.; Liu, X.; Sushko, P. V.; Liu, J.; Zhang, J. G. Dendrite-free lithium deposition via self-healing electrostatic shield mechanism. *J. Am. Chem. Soc.* **2013**, *135* (11), 4450−4456.

(19) Zhai, P.; Wang, T.; Yang, W.; Cui, S.; Zhang, P.; Nie, A.; Zhang, Q.; Gong, Y. Uniform Lithium Deposition Assisted by Single-Atom Doping toward High-Performance Lithium Metal Anodes. *Adv. Energy Mater.* **2019**, *9* (18), 1804019−1804026.

(20) Jin, S.; Sun, Z.; Guo, Y.; Qi, Z.; Guo, C.; Kong, X.; Zhu, Y.; Ji, H. High Areal Capacity and Lithium Utilization in Anodes Made of Covalently Connected Graphite Microtubes. *Adv. Mater.* **2017**, *29* (38), 1700783−1700789.

(21) Guo, Y.; Niu, P.; Liu, Y.; Ouyang, Y.; Li, D.; Zhai, T.; Li, H.; Cui, Y. An Autotransferable g-C$_3$N$_4$ Li$^+$-Modulating Layer toward Stable Lithium Anodes. *Adv. Mater.* **2019**, *31* (27), 1900342−1900351.

(22) Niu, C.; Pan, H.; Xu, W.; Xiao, J.; Zhang, J. G.; Luo, L.; Wang, C.; Mei, D.; Meng, J.; Wang, X.; Liu, Z.; Mai, L.; Liu, J. Self-smoothing anode for achieving high-energy lithium metal batteries under realistic conditions. *Nat. Nanotechnol.* **2019**, *14* (6), 594−602.

(23) Gao, Y.; Yan, Z.; Gray, J. L.; He, X.; Wang, D.; Chen, T.; Huang, Q.; Li, Y. C.; Wang, H.; Kim, S. H.; Mallouk, T. E.; Wang, D. Polymer-inorganic solid-electrolyte interphase for stable lithium metal batteries under lean electrolyte conditions. *Nat. Mater.* **2019**, *18* (4), 384−389.

(24) Fang, R.; Zhao, S.; Sun, Z.; Wang, D. W.; Cheng, H. M.; Li, F. More Reliable Lithium-Sulfur Batteries: Status, Solutions and Prospects. *Adv. Mater.* **2017**, *29* (48), 1606823−1606849.

(25) Eroglu, D.; Zavadil, K. R.; Gallagher, K. G. Critical Link between Materials Chemistry and Cell-Level Design for High Energy Density and Low Cost Lithium-Sulfur Transportation Battery. *J. Electrochem. Soc.* **2015**, *162* (6), A982−A990.

(26) Emerce, N. B.; Eroglu, D. Effect of Electrolyte-to-Sulfur Ratio in the Cell on the Li-S Battery Performance. *J. Electrochem. Soc.* **2019**, *166* (8), A1490−A1500.

(27) Hagen, M.; Fanz, P.; Tubke, J. Cell energy density and electrolyte/sulfur ratio in Li-S cells. *J. Power Sources* **2014**, *264*, 30−34.

(28) Zhang, S. S. Improved Cyclability of Liquid Electrolyte Lithium/Sulfur Batteries by Optimizing Electrolyte/Sulfur Ratio. *Energies* **2012**, *5* (12), 5190−5197.

(29) Liu, J.; Bao, Z.; Cui, Y.; Dufek, E. J.; Goodenough, J. B.; Khalifah, P.; Li, Q.; Liaw, B. Y.; Liu, P.; Manthiram, A.; Meng, Y. S.; Subramanian, V. R.; Toney, M. F.; Viswanathan, V. V.; Whittingham, M. S.; Xiao, J.; Xu, W.; Yang, J.; Yang, X.-Q.; Zhang, J.-G. Pathways for practical high-energy long-cycling lithium metal batteries. *Nat. Energy* **2019**, *4* (3), 180−186.

(30) Ren, X. D.; Zou, L. F.; Cao, X.; Engelhard, M. H.; Liu, W.; Burton, S. D.; Lee, H.; Niu, C. J.; Matthews, B. E.; Zhu, Z. H.; Wang, C. M.; Arey, B. W.; Xiao, J.; Liu, J.; Zhang, J. G.; Xu, W. Enabling High-Voltage Lithium-Metal Batteries under Practical Conditions. *Joule* **2019**, *3* (7), 1662−1676.

(31) Nagpure, S. C.; Tanim, T. R.; Dufek, E. J.; Viswanathan, V. V.; Crawford, A. J.; Wood, S. M.; Xiao, J.; Dickerson, C. C.; Liaw, B. Impacts of lean electrolyte on cycle life for rechargeable Li metal batteries. *J. Power Sources* **2018**, *407*, 53−62.

(32) Jiao, S.; Zheng, J.; Li, Q.; Li, X.; Engelhard, M. H.; Cao, R.; Zhang, J.-G.; Xu, W. Behavior of Lithium Metal Anodes under Various Capacity Utilization and High Current Density in Lithium Metal Batteries. *Joule* **2018**, *2* (1), 110−124.

(33) Lu, D. P.; Shao, Y. Y.; Lozano, T.; Bennett, W. D.; Graff, G. L.; Polzin, B.; Zhang, J. G.; Engelhard, M. H.; Saenz, N. T.; Henderson, W. A.; Bhattacharya, P.; Liu, J.; Xiao, J. Failure Mechanism for Fast-Charged Lithium Metal Batteries with Liquid Electrolytes. *Adv. Energy Mater.* **2015**, *5* (3), 1400993.

(34) Li, S.; Jiang, M. W.; Xie, Y.; Xu, H.; Jia, J. Y.; Li, J. Developing High-Performance Lithium Metal Anode in Liquid Electrolytes: Challenges and Progress. *Adv. Mater.* **2018**, *30* (17), 1706375.

(35) Chen, K. H.; Wood, K. N.; Kazyak, E.; LePage, W. S.; Davis, A. L.; Sanchez, A. J.; Dasgupta, N. P. Dead lithium: mass transport effects on voltage, capacity, and failure of lithium metal anodes. *J. Mater. Chem. A* **2017**, *5* (23), 11671−11681.

(36) Liu, L.; Yin, Y. X.; Li, J. Y.; Wang, S. H.; Guo, Y. G.; Wan, L. J. Uniform Lithium Nucleation/Growth Induced by Lightweight Nitrogen-Doped Graphitic Carbon Foams for High-Performance Lithium Metal Anodes. *Adv. Mater.* **2018**, *30* (10), 1706216−1706223.

(37) Zhang, R.; Chen, X. R.; Chen, X.; Cheng, X. B.; Zhang, X. Q.; Yan, C.; Zhang, Q. Lithiophilic Sites in Doped Graphene Guide Uniform Lithium Nucleation for Dendrite-Free Lithium Metal Anodes. *Angew. Chem., Int. Ed.* **2017**, *56* (27), 7764−7768.

(38) Peled, E.; Menkin, S. Review-SEI: Past, Present and Future. *J. Electrochem. Soc.* **2017**, *164* (7), A1703−A1719.

(39) Wu, B. B.; Lochala, J.; Taverne, T.; Xiao, J. The interplay between solid electrolyte interface (SEI) and dendritic lithium growth. *Nano Energy* **2017**, *40*, 34−41.

(40) Ye, H.; Xin, S.; Yin, Y. X.; Guo, Y. G. Advanced Porous Carbon Materials for High-Efficient Lithium Metal Anodes. *Adv. Energy Mater.* **2017**, *7* (23), 1700530−1700538.

(41) Zhang, C.; Huang, Z.; Lv, W.; Yun, Q.; Kang, F.; Yang, Q.-H. Carbon enables the practical use of lithium metal in a battery. *Carbon* **2017**, *123*, 744−755.

(42) Hummers, W. S., Jr.; Offeman, R. E. Preparation of Graphitic Oxide. *J. Am. Chem. Soc.* **1958**, *80* (6), 1339.

(43) Li, P.; Li, H.; Han, D.; Shang, T.; Deng, Y.; Tao, Y.; Lv, W.; Yang, Q. H. Packing Activated Carbons into Dense Graphene Network by Capillarity for High Volumetric Performance Super-capacitors. *Adv. Sci.* **2019**, *6* (14), 1802355−1802362.

(44) (a) Kresse, G.; Hafner, J. AB-initio molecular dynamics for liquid metals. *Phys. Rev. B: Condens. Matter Mater. Phys.* **1993**, *47* (1), 558−561. (b) Kresse, G.; Joubert, D. From ultrasoft pseudopotentials to the projector augmented-wave method. *Phys. Rev. B: Condens. Matter Mater. Phys.* **1999**, *59* (3), 1758−1775. (c) Blochl, P. E. Projector augmented-wave method. *Phys. Rev. B: Condens. Matter Mater. Phys.* **1994**, *50* (24), 17953−17979. (d) Perdew, J. P.; Burke, K.; Ernzerhof, M. Generalized gradient approximation made simple. *Phys. Rev. Lett.* **1997**, *78* (7), 1396−1396. (e) Perdew, J. P.; Burke, K.; Ernzerhof, M. Generalized gradient approximation made simple. *Phys. Rev. Lett.* **1996**, *77* (18), 3865−3868. (f) Kresse, G.; Furthmuller, J. Efficient iterative schemes for ab initio total-energy calculations using a plane-wave basis set. *Phys. Rev. B: Condens. Matter Mater. Phys.* **1996**, *54* (16), 11169−11186. (g) Kresse, G.; Furthmuller, J. Efficiency of ab-initio total energy calculations for metals and semiconductors using a plane-wave basis set. *Comput. Mater. Sci.* **1996**, *6* (1), 15−50. (h) Kresse, G.; Hafner, J. AB-initio molecular dynamics simulation of the liquid metal amorphous semiconductor transition in germanium. *Phys. Rev. B: Condens. Matter Mater. Phys.* **1994**, *49* (20), 14251−14269.

(45) Li, H.; Tao, Y.; Zheng, X.; Luo, J.; Kang, F.; Cheng, H.-M.; Yang, Q.-H. Ultra-thick graphene bulk supercapacitor electrodes for compact energy storage. *Energy Environ. Sci.* **2016**, *9* (10), 3135−3142.

(46) Li, H.; Tao, Y.; Zhang, C.; Liu, D.; Luo, J.; Fan, W.; Xu, Y.; Li, Y.; You, C.; Pan, Z.-Z.; Ye, M.; Chen, Z.; Dong, Z.; Wang, D.-W.; Kang, F.; Lu, J.; Yang, Q.-H. Dense Graphene Monolith for High Volumetric Energy Density Li-S Batteries. *Adv. Energy Mater.* **2018**, *8*, 1703438−1703446.

(47) Meng, Q.; Deng, B.; Zhang, H.; Wang, B.; Zhang, W.; Wen, Y.; Ming, H.; Zhu, X.; Guan, Y.; Xiang, Y.; Li, M.; Cao, G.; Yang, Y.; Peng, H.; Zhang, H.; Huang, Y. Heterogeneous nucleation and growth of electrodeposited lithium metal on the basal plane of single-layer graphene. *Energy Storage Mater.* **2019**, *16*, 419−425.

(48) Lin, D.; Liu, Y.; Chen, W.; Zhou, G.; Liu, K.; Dunn, B.; Cui, Y. Conformal Lithium Fluoride Protection Layer on Three-Dimensional Lithium by Nonhazardous Gaseous Reagent Freon. *Nano Lett.* **2017**, *17* (6), 3731−3737.

(49) Han, X. G.; Gong, Y. H.; Fu, K.; He, X. F.; Hitz, G. T.; Dai, J. Q.; Pearse, A.; Liu, B. Y.; Wang, H.; Rubloff, G.; Mo, Y. F.; Thangadurai, V.; Wachsman, E. D.; Hu, L. B. Negating interfacial impedance in garnet-based solid-state Li metal batteries. *Nat. Mater.* **2017**, *16* (5), 572−579.

(50) Lu, Y.; Tu, Z.; Archer, L. A. Stable lithium electrodeposition in liquid and nanoporous solid electrolytes. *Nat. Mater.* **2014**, *13* (10), 961−969.

(51) Liang, Z.; Lin, D. C.; Zhao, J.; Lu, Z. D.; Liu, Y. Y.; Liu, C.; Lu, Y. Y.; Wang, H. T.; Yan, K.; Tao, X. Y.; Cui, Y. Composite lithium metal anode by melt infusion of lithium into a 3D conducting scaffold with lithiophilic coating. *Proc. Natl. Acad. Sci. U. S. A.* **2016**, *113* (11), 2862−2867.

Supporting Information for

Revealing Principles for Design of Lean-electrolyte Lithium Metal Anode via *in-situ* Spectroscopy

Huan Li,[†] Dongliang Chao,[†] Biao Chen,[†,‡] Xiao Chen,[§] Clarence Chuah,[⊥] Youhong Tang,[⊥] Yan Jiao,[†] Mietek Jaroniec,[#] and Shi-Zhang Qiao[*,†]

[†]School of Chemical Engineering and Advanced Materials, The University of Adelaide, Adelaide, SA 5005, Australia

[‡]School of Materials Science and Engineering and Tianjin Key Laboratory of Composite and Functional Materials, Tianjin University, Tianjin 300350, P. R. China

[§]Beijing Key Laboratory of Green Reaction Engineering and Technology, Department of Chemical Engineering, Tsinghua University, Beijing, China

[⊥]Center for Nanoscale Science and Technology, School of Computer Science, Engineering, and Mathematics, Flinders University, Adelaide, SA 5042, Australia

[#]Department of Chemistry and Biochemistry, Kent State University, Kent, Ohio 44242, United States

TABLE OF CONTENTS

Fig. S1 (a) Charge-discharge curves before Li plating/stripping. This pre-activation process helped to stabilize the SEI layer. The current density was set as 0.2 mA cm^{-2} from 0.01 V to 1V. **(b)** Charge-discharge curves and **(c)** cyclic stability of L-DG at the cut-off voltages of 0.5 V and 1.0 V. For the Li stripping process, data show a negligible areal capacity of 0.018 mAh cm^{-2} in the range of 0.5 V-1.0 V (blue line in Fig. S2b). The stable cycling at different cut-off voltages also confirms that a cut-off voltage of 0.5 V is suitable for the Li plating/stripping tests.
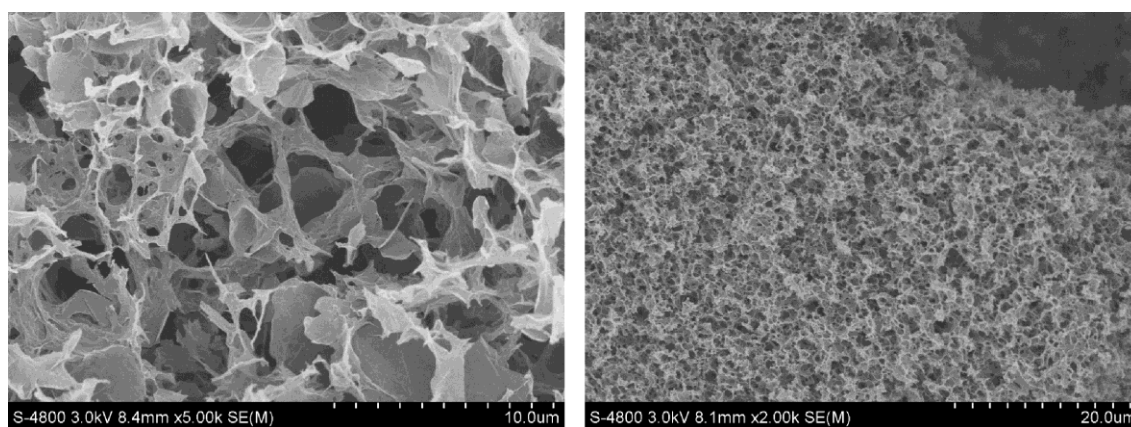
Fig. S2 SEM image of 3D high-surface-area graphene (H-DG).
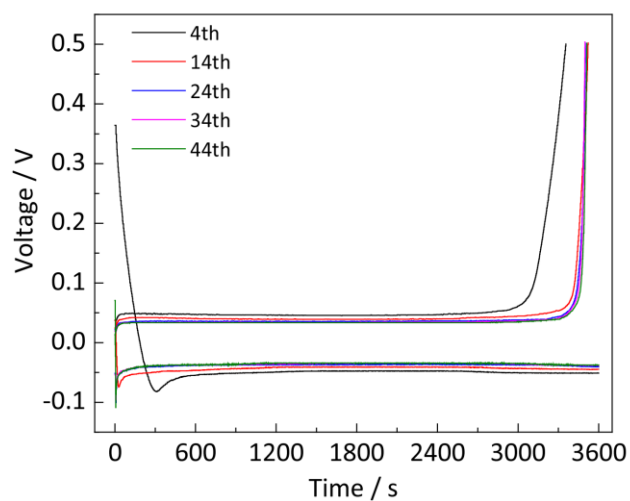
Fig. S3 Charge-discharge curves of Li plating/stripping with flooded electrolyte within a 3D graphene host. The current density is 1 mA cm^{-2} and the areal capacity is 1 mAh cm^{-2}.
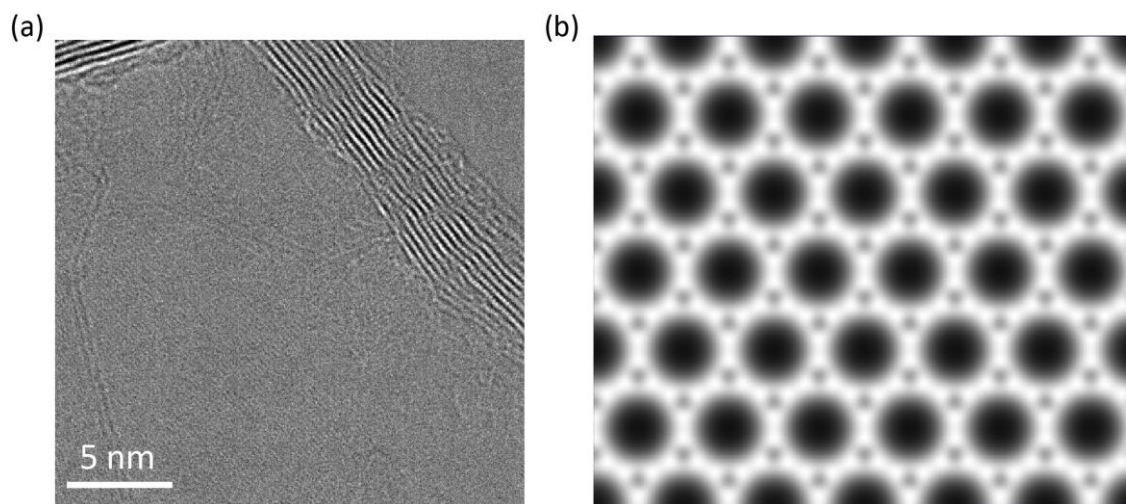
Fig. S4 (a) TEM image of 3D graphene (G) heated at 2800 ^{o}C and **(b)** its simulated ordered graphene structure. Few defects can be observed from the images.
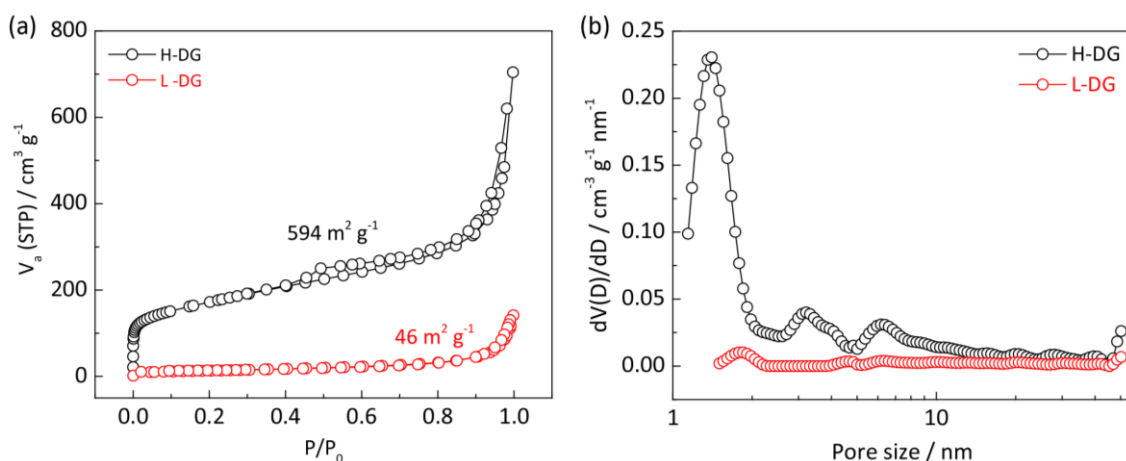
Fig. S5 (a) N_2 adsorption-desorption isotherms (77 K) measured for H-DG and L-DG; **(b)** Pore size distributions dV(D)/dD (where V is the volume of liquid adsorbate and D is the pore size) obtained for L-DG and H-DG. H-DG contains an abundant amount of micropores around ~1.4 nm and mesopores around ~3-7 nm. In contrast, these pores disappear in L-DG due to the high-temperature treatment that re-arranges the graphene units.
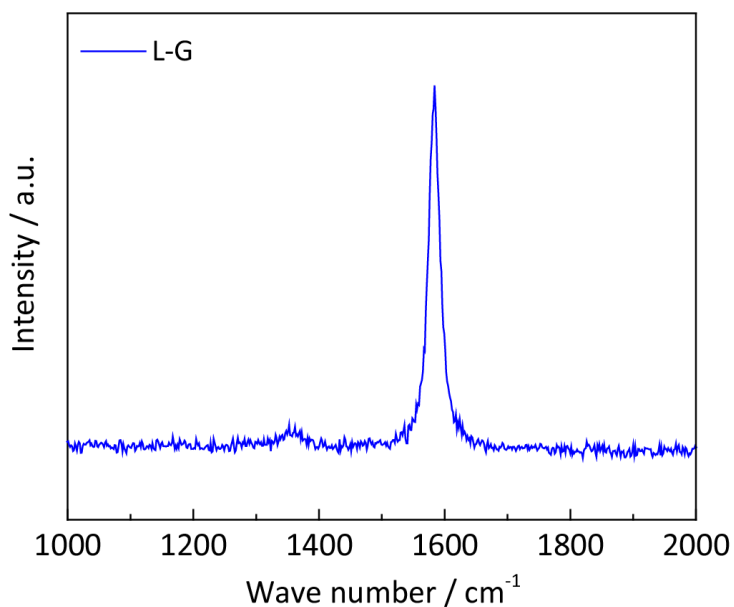
Fig. S6 Raman spectra of L-G heated at 2800 ^{o}C.
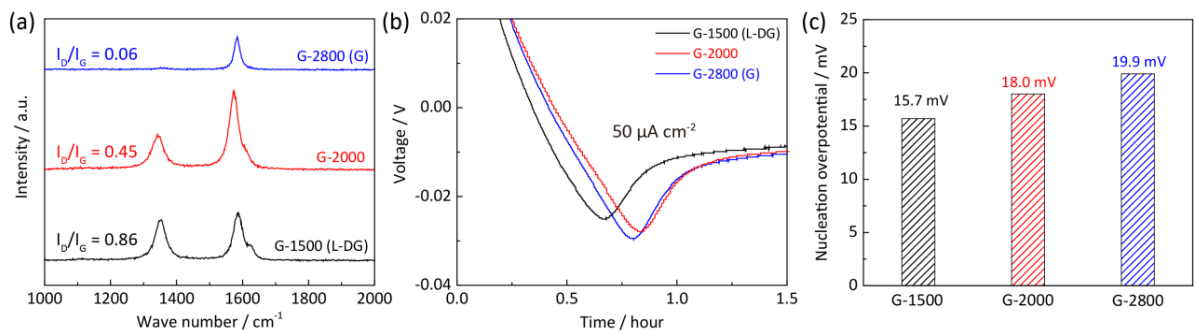
Fig. S7 Comparison of nucleation overpotentials for G-1500, G-2000 and G-2800. **(a)** Raman spectra of G-1500, G-2000 and G-2800; **(b)** Discharge curves at 50 μA cm^{-2}; **(c)** The nucleation overpotentials obtained for G-1500, G-2000 and G-2800. High-temperature treatment is an effective way to control the defect density in carbon materials. The defect density decreases with increasing heating temperature, as indentified by the I_D/I_G ratio in Fig. S7a. As expected, G-1500 shows the lowest nucleation overpotential of 15.7 mV. In contrast, G-2800 exhibits a much higher overpotential of 19.9 mV. These results confirm that Li tends to nucleate on the defective sites.
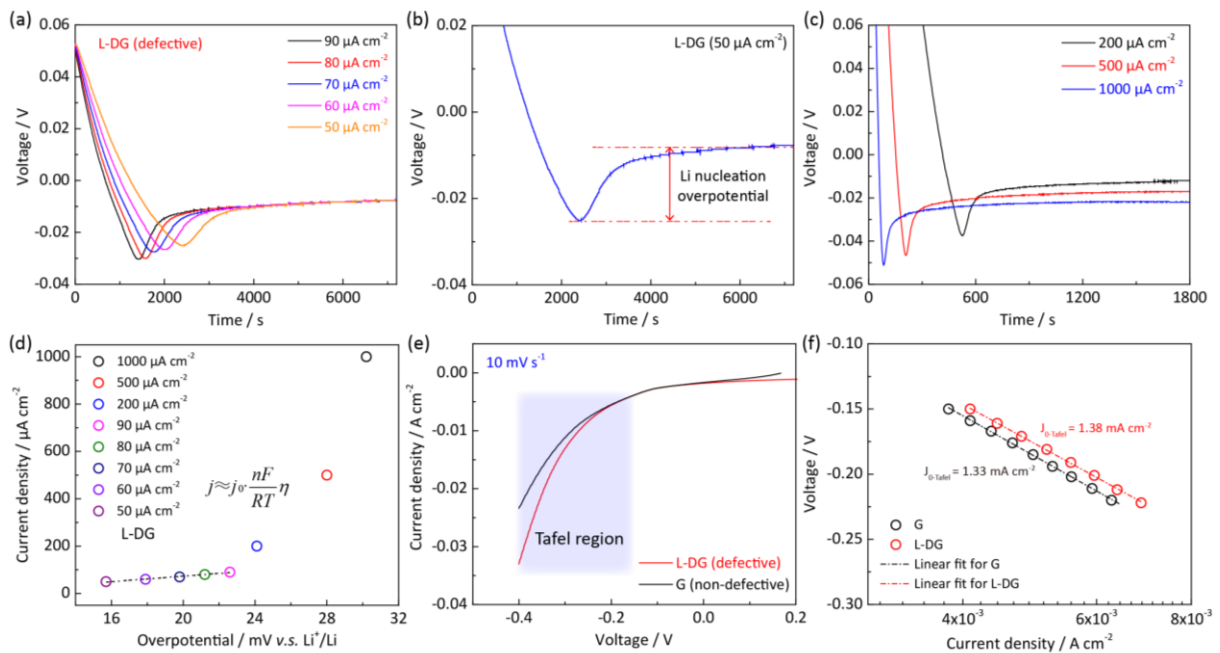
Fig. S8 Calculation of the exchange current densities in the linear region and Tafel region. **(a)** Discharge curves obtained for L-DG from 50 μA cm^{-2} to 90 μA cm^{-2}; **(b)** Calculation of the nucleation overpotential; **(c)** Discharge curves obtained for L-DG from 200 μA cm^{-2} to 1000 μA cm^{-2}; **(d)** The relationship between the current density and overpotential; A linear relationship is observed in the range from 50 μA cm^{-2} to 90 μA cm^{-2} (as shown in the inset formula); **(e)** linear scan voltammetry (LSV) plots for L-DG and G at 10 mV s^{-1}; **(f)** The Tafel plots for L-DG and G.

54
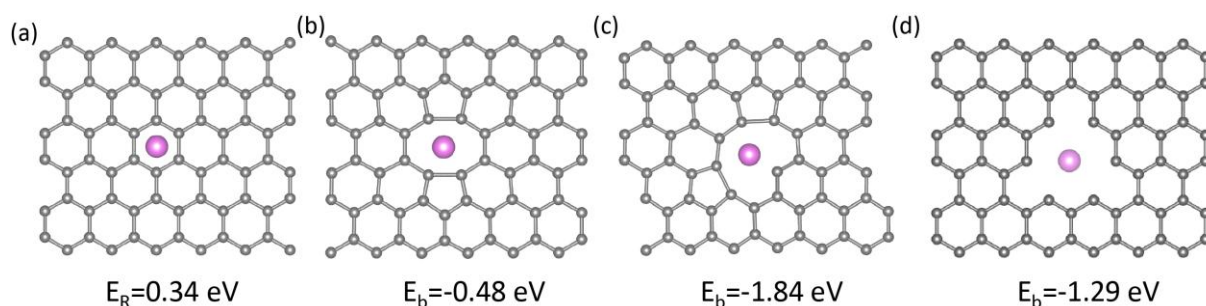
Fig. S9 The binding and repulsion energy of carbon vacancy for Li atom. (a) Li on pristine graphene, repulsion energy is 0.34 eV; **(b-d)** The binding energies of C2, C3, C4 vacancy for Li.
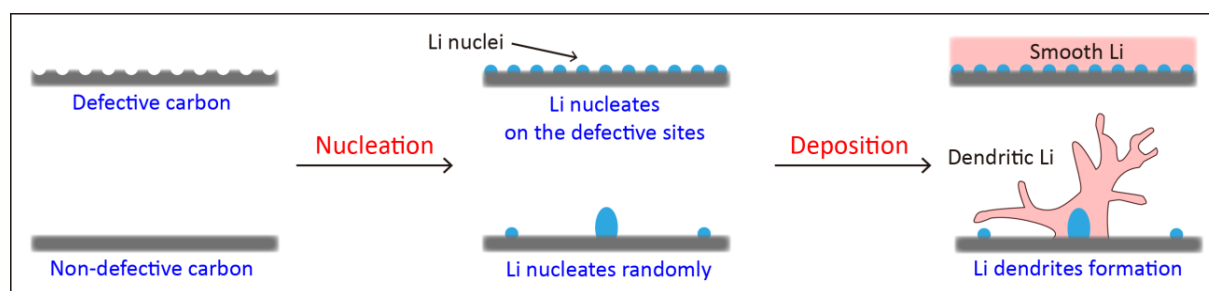
Fig. S10 Scheme illustrating Li nucleation and deposition on the defective carbon (L-DG) and non-defective carbon (L-G) hosts. Li tends to nucleate over the whole defective surface of L-DG, and the uniform Li seeds guide the formation of uniform and smooth Li deposits. In contrast, the nucleation sites for Li plating are isolated and randomly distributed on the non-defective graphene units, which leads to uneven Li deposition.
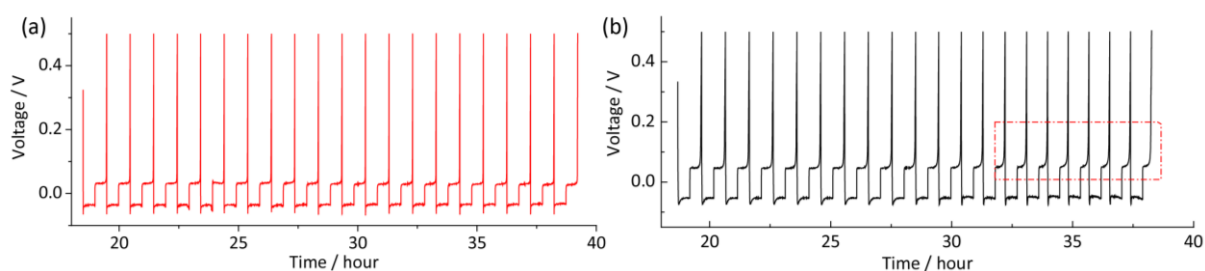
Fig. S11 Typical charge-discharge curves obtained for (a) L-DG and (b) H-DG from 20th to 40th cycles. Each charge-discharge cycle was used to calculate the coulombic efficiency (CE%) in Figure 4a.
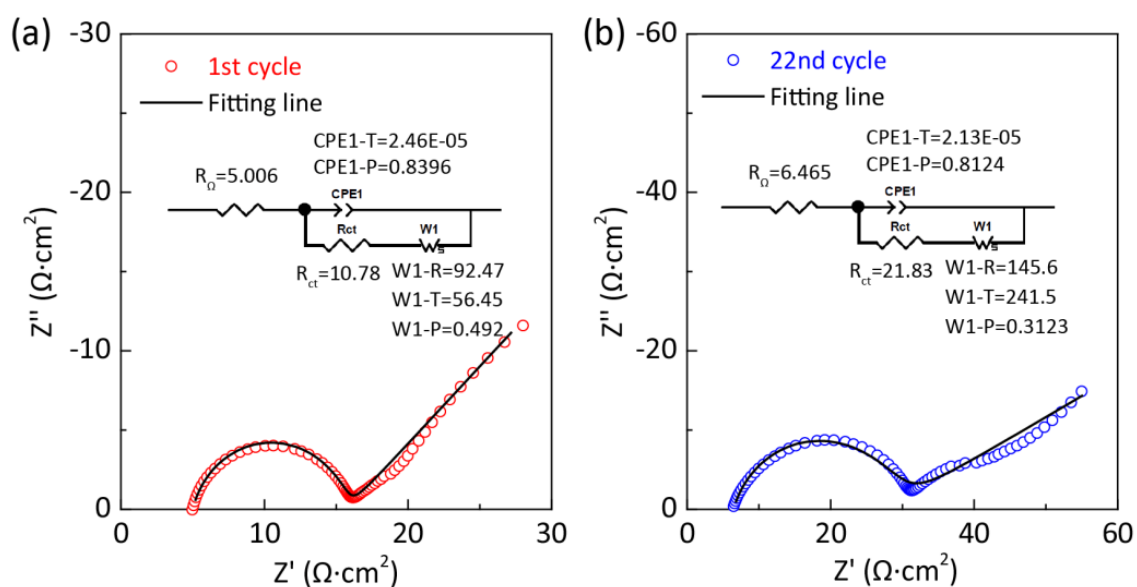
Fig. S12 Typical fitting of the EIS plots for L-DG at the (a) 1st cycle and (b) 22th cycle. R_Ω is the ohmic/internal resistance, Ω cm^2; R_{ct} is defined as the interfacial resistance, Ω cm^2; CPE is defined as a constant phase element, a parameter that describes the capacitance; W_s is the Warburg resistance, Ω cm^2 s$^{-1/2}$, which is related to the ionic diffusion.
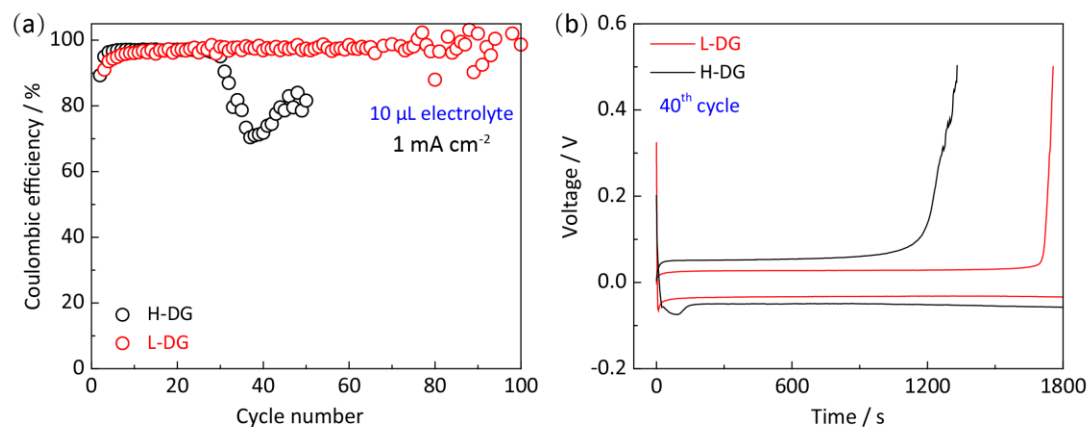
Fig. S13 The cycled cells of L-DG and H-DG for NMR test. (a) The cycling stability of Li plating/stripping on H-DG and L-DG at 1 mA cm^{-2}; (b) Charge-discharge curves of L-DG and H-DG at the 40th cycle.
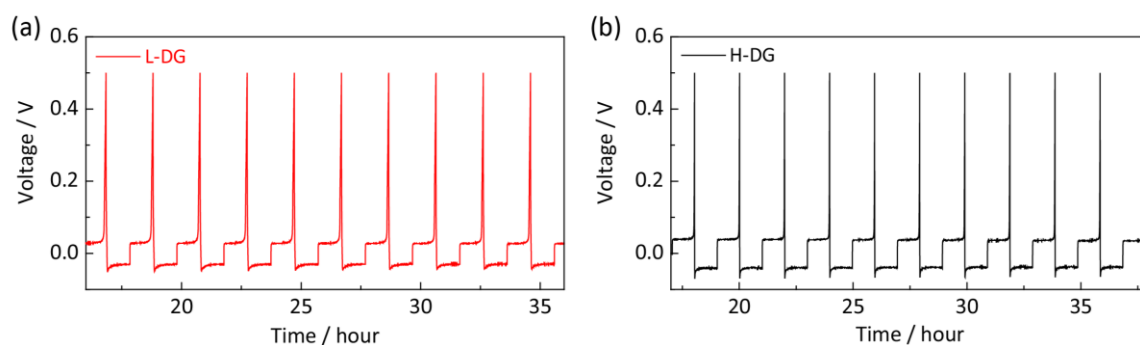
Fig. S14 Charge-discharge curves for L-DG and H-DG at the initial cycles. The current density is 1 mA cm^{-2} with an areal capacity of 1 mAh cm^{-2}.
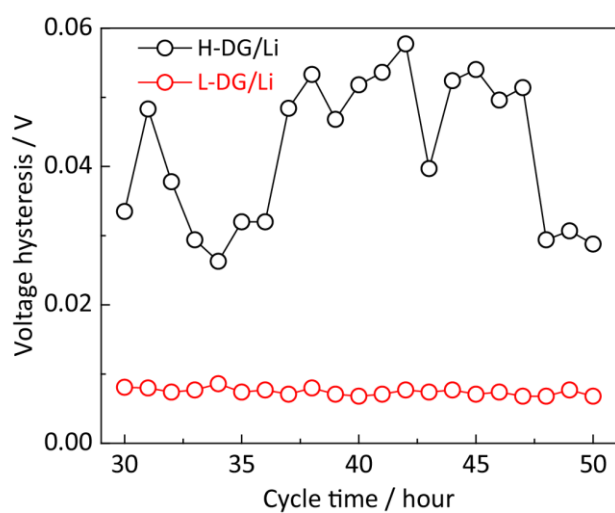
Fig. S15 Voltage hysteresis of L-DG/Li and H-DG/Li symmetric cells.
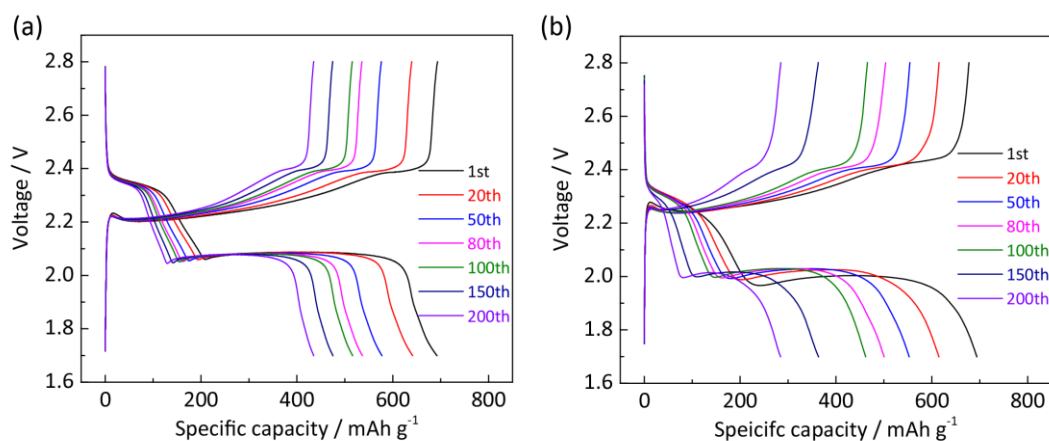
Fig. S16 Charge-discharge curves of (a) L-DG/Li//S and (b) H-DG/Li//S cells at different cycles with flooded electrolyte. The electrolyte volume is 100 μL.
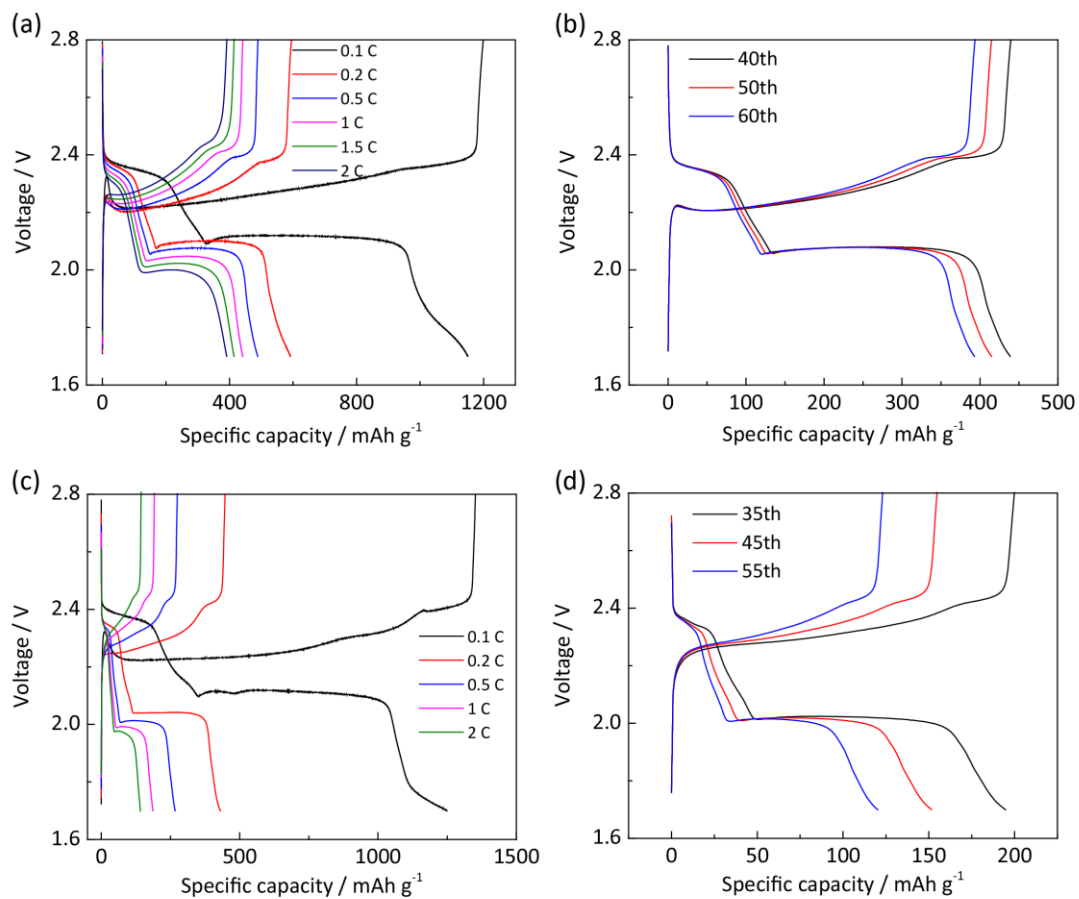
Figure S17 Charge-discharge curves of L-DG/Li//S and H-DG/Li//S cells under lean electrolyte conditions. L-DG/Li//S battery at **(a)** different rates and **(b)** different cycles; H-DG/Li//S battery at **(c)** different rates and **(d)** different cycles; The electrolyte volume is 10 μL.

Chapter 4: Reversible electrochemical oxidation of sulfur in ionic liquid for high-voltage Al−S batteries

4.1 Introduction and significance

Sulfur is an important electrode material in metal−sulfur batteries. It is usually coupled with metal anodes and undergoes electrochemical reduction to form metal sulfides. Herein, we demonstrate, for the first time, the reversible sulfur oxidation process in $AlCl_3$/carbamide ionic liquid, where sulfur is electrochemically oxidized by $AlCl_4^-$ to form $AlSCl_7$. The sulfur oxidation is: 1) highly reversible with an efficiency of ~94%; and 2) workable within a wide range of high potentials. As a result, the Al−S battery based on sulfur oxidation can be cycled steadily around ~1.8 V, which is the highest operation voltage in Al−S batteries. The study of sulfur oxidation process benefits the understanding of sulfur chemistry and provides a valuable inspiration for the design of other high-voltage metal−sulfur batteries, not limited to Al−S configurations. The highlights of this work include:

➢ **The first demonstration of reversible sufur oxidation-reduction process.** We found that sulfur can be electrochemically oxidized in $AlCl_3$/carbamide ionic liquid. The $AlCl_4^-$ anions can oxidize sulfur to form aluminum sulfide chloride ($AlSCl_7$), which can be reduced back to sulfur.

➢ **High reversibility and wide-range electrochemical potentials.** This oxidation-reduction process of sulfur is highly reversible with an efficiency of ~94%. It is workable within a wide-range of electrochemical potentials (1.0−2.4 V v.s. Al), which is much higher than that of the previously studied Al−S batteries (~0.2−1.0 V).

➢ **High-voltage and long-cycled Al−S batteries.** The Al−S battery based on sulfur oxidation can run steadily over 200 cycles around ~1.8 V, which is the highest operation voltage in Al−S batteries. By sharp contrast, the previously studied Al−S batteries exhibit much lower voltage of ~0.5 V, and its capacity dramatically declines after tens of cycles.

4.2 Reversible electrochemical oxidation of sulfur in ionic liquid for high-voltage Al−S batteries

This Chapter is included as it appears as a journal paper published by **Huan Li**, Rongwei Meng, Yong Guo, Biao Chen, Yan Jiao, Chao Ye, Yu Long, Anton Tadich, Quan-Hong Yang, Mietek Jaroniec and Shi-Zhang Qiao*, Reversible electrochemical oxidation of sulfur in ionic liquid for high-voltage Al−S batteries, *Nature Communications*, 2021, 12, 5714.

Statement of Authorship

Title of Paper	Reversible electrochemical oxidation of sulfur in ionic liquid for high-voltage Al−S batteries
Publication Status	☑ Published ☐ Accepted for Publication ☐ Submitted for Publication ☐ Unpublished and Unsubmitted work written in manuscript style
Publication Details	Huan Li, Rongwei Meng, Yong Guo, Biao Chen, Yan Jiao, Chao Ye, Yu Long, Anton Tadich, Quan-Hong Yang, Mietek Jaroniec, Shi-Zhang Qiao*, Nature Communications, 2021, 12, 5714.

Principal Author

Name of Principal Author (Candidate)	Huan Li		
Contribution to the Paper	Conducted material synthesis, carried out electrochemical tests and wrote the paper		
Overall percentage (%)	70		
Certification:	This paper reports on original research I conducted during the period of my Higher Degree by Research candidature and is not subject to any obligations or contractual agreements with a third party that would constrain its inclusion in this thesis. I am the primary author of this paper.		
Signature		Date	14 June 2022

Co-Author Contributions

By signing the Statement of Authorship, each author certifies that:

    i.   the candidate's stated contribution to the publication is accurate (as detailed above);

    ii.   permission is granted for the candidate in include the publication in the thesis; and

    iii.   the sum of all co-author contributions is equal to 100% less the candidate's stated contribution.

Name of Co-Author	Rongwei Meng		
Contribution to the Paper	Carried out electrochemical tests and in-situ Raman spectra		
Signature		Date	14 June 2022

Name of Co-Author	Yong Guo		
Contribution to the Paper	Assisted with X-ray photoelectron spectra		
Signature		Date	14 June 2022

Name of Co-Author	Biao Chen		
Contribution to the Paper	Helped with the microscopic images		
Signature		Date	14 June 2022

Name of Co-Author	Yan Jiao		
Contribution to the Paper	Helped with theoretical computations		
Signature		Date	14 June 2022

Name of Co-Author	Chao Ye		
Contribution to the Paper	Helped with design of sulfur cathode		
Signature		Date	14 June 2022

Name of Co-Author	Yu Long		
Contribution to the Paper	Helped with synthesis of ionic liquid		
Signature		Date	14 June 2022

Name of Co-Author	Anton Tadich		
Contribution to the Paper	Helped with synchrotron soft X-ray spectra		
Signature		Date	14 June 2022

Name of Co-Author	Quan-Hong Yang		
Contribution to the Paper	Provided experimental conditions for Huan Li during COVID-19 in China		
Signature		Date	14 June 2022

Name of Co-Author	Mietek Jaroniec
Contribution to the Paper	Revised the manuscript
Signature		Date	14 June 2022

Name of Co-Author	Shi-Zhang Qiao
Contribution to the Paper	Supervised the research project
Signature		Date	14 June 2022

Please cut and paste additional co-author panels here as required.

64

ARTICLE

Reversible electrochemical oxidation of sulfur in ionic liquid for high-voltage Al—S batteries

Huan Li[1,6], Rongwei Meng[2,6], Yong Guo[2], Biao Chen[3], Yan Jiao ○ [1], Chao Ye[1], Yu Long[2], Anton Tadich[4], Quan-Hong Yang[2], Mietek Jaroniec ○ [5] & Shi-Zhang Qiao ○ [1✉]

Sulfur is an important electrode material in metal—sulfur batteries. It is usually coupled with metal anodes and undergoes electrochemical reduction to form metal sulfides. Herein, we demonstrate, for the first time, the reversible sulfur oxidation process in AlCl$_3$/carbamide ionic liquid, where sulfur is electrochemically oxidized by AlCl$_4^-$ to form AlSCl$_7$. The sulfur oxidation is: 1) highly reversible with an efficiency of ~94%; and 2) workable within a wide range of high potentials. As a result, the Al—S battery based on sulfur oxidation can be cycled steadily around ~1.8 V, which is the highest operation voltage in Al—S batteries. The study of sulfur oxidation process benefits the understanding of sulfur chemistry and provides a valuable inspiration for the design of other high-voltage metal—sulfur batteries, not limited to Al—S configurations.

[1] School of Chemical Engineering and Advanced Materials, The University of Adelaide, Adelaide, SA 5005, Australia. [2] Nanoyang Group, State Key Laboratory of Chemical Engineering, School of Chemical Engineering and Technology, Tianjin University, 300072 Tianjin, China. [3] School of Materials Science and Engineering and Tianjin Key Laboratory of Composite and Functional Materials, Tianjin University, 300350 Tianjin, China. [4] Australian Synchrotron (ANSTO), 800 Blackburn Road, Clayton, VIC 3168, Australia. [5] Department of Chemistry and Biochemistry & Advanced Materials and Liquid Crystal Institute, Kent State University, Kent, OH 44242, USA. [6] These authors contributed equally: Huan Li, Rongwei Meng. ✉email: s.qiao@adelaide.edu.au

Sulfur is a promising electrode material in metal–sulfur batteries due to its earth abundance and high theoretical capacity[1–6]. Sulfur is normally coupled with metal anodes and is electrochemically reduced with metal cations to form metal sulfides[7,8]. Despite high specific capacities based on sulfur reduction, the reverse oxidation of these sulfides back to sulfur needs to overcome a high energy barrier[9,10], leading to a large overpotential and poor reversibility. Additionally, the reduction of sulfur occurs at low electrochemical potential (~ -1.0 V vs. standard hydrogen electrode, Fig. S1), and results in low operation voltage of metal–sulfur batteries[5,6]. For example, Al–S batteries based on sulfur reduction usually demonstrate ultralow cell voltage of about ~ 0.5 V[11,12]. Therefore, the limited reversibility and low electrochemical potentials are the main obstacles for the practical use of sulfur electrodes.

Many efforts have been devoted toward improving the reversibility of metal–sulfur batteries by proper designs of sulfur host and electrolyte engineering[5,6,13–15]. However, these prior attempts failed to basically address the low-voltage concerns of metal–sulfur batteries because the cell voltage is determined by the redox pathway of sulfur but these efforts did not alter the sulfur reduction path. Therefore, the batteries based on the sulfur reduction remain far from satisfactory for the high-voltage applications[5–8,16–18]. It is highly important to examine new redox pathways of sulfur to achieve viable applications of metal–sulfur batteries. In this regard, sulfur oxidation is a worthy path because it can compensate the intrinsic low-voltage shortcoming of sulfur reduction.

Considering the multivalent nature of sulfur element (-2, 0, $+2$, $+4$, $+6$), sulfur can be oxidized into high-valence sulfur compounds[19,20]. Unfortunately, the oxidation process of sulfur has been rarely studied. Due to the inert nature of sulfur, a high voltage needs to be applied to drive its electrochemical oxidation. This is normally accompanied by electrolyte decomposition, leading to a poor reversibility[21–23]. Meanwhile, the electrochemical oxidation of sulfur undergoes an electron-loss process involved with anions. The common anions in metal–sulfur batteries such as bis (trifluoromethyl) sulfonate, hexafluorophosphate are weak oxidants, which are not able to oxidize sulfur into high-valence sulfur compounds[24,25]. Therefore, anions with strong oxidizing power in an electrochemically stable electrolyte are necessary to oxidize sulfur in a highly reversible manner, but this concept has not been explored yet.

In this work, we demonstrate, for the first time, the reversible sulfur oxidation in $AlCl_3$/carbamide ionic liquid. The $AlCl_4^-$ anions can oxidize sulfur to form aluminium sulfide chloride ($AlSCl_7$), which can be reversibly reduced back to sulfur with a high efficiency of $\sim 94\%$. This oxidation–reduction process is workable within a wide range of high electrochemical potentials. Benefiting from the high reversibility and high electrochemical potential, the Al–S battery can run steadily over 200 cycles around ~ 1.8 V, which is the highest operation voltage in Al–S batteries reported so far. By sharp contrast, the previously studied Al–S battery based on sulfur reduction can only run tens of cycles with a much lower operation voltage of ~ 0.5 V. This work sheds new light on the understanding of sulfur chemistry and presents sulfur oxidation as a new pathway to achieve the high-voltage applications of metal–sulfur batteries.

Results

Evolution of $AlSCl_7$ during electrochemical sulfur oxidation.
$AlSCl_7$ is an ionic crystal with SCl_3^+ cations and $AlCl_4^-$ anions[26]. $AlCl_3$/carbamide ionic liquid contains $AlCl_4^-$, $Al_2Cl_7^-$ anions, and $[AlCl_2(\text{carbamide})_n]^+$ cations[27,28]. Al anode demonstrates high reversibility and stable electrochemical potential in $AlCl_4^-$

and $Al_2Cl_7^-$ containing electrolyte, and therefore Al anode is used as the reference electrode in this work[29–32]. Figure 1a shows the linear scanning voltammetry (LSV) curve for sulfur/carbon nanotube (S/CNT) composite cathode with 10 wt.% polyvinylidene difluoride (PVDF) binder in $AlCl_3$/carbamide electrolyte (Fig. S2). It should be noted that sulfur is not stable under high oxidation voltage in the commonly used $AlCl_3$/1-ethyl-3-methylimidazolium chloride electrolyte (Fig. S3). The sulfur content in S/CNT is 20 wt.% and the molar ratio of $AlCl_3$ to carbamide is 1.3:1 (details in the "Methods" section). The observed current densities in Fig. 1a are above ~ 2.0 V and below ~ 1.0 V, corresponding to the electrochemical oxidation and reduction of sulfur, respectively. Figure 1b summarizes the electrochemical potentials of different materials, and the potential of sulfur oxidation in this work is much higher than most of the previously reported materials (Table S1)[11,12]. Cyclic voltammetry (CV) curves are compared to demonstrate the overall process of sulfur oxidation and reduction. The electrochemical oxidation from sulfur to $AlSCl_7$ starts from ~ 2.0 V, and the reverse reduction from $AlSCl_7$ to sulfur occurs at ~ 1.8 V (Fig. 1c). For the sulfur reduction (Fig. 1d), sulfur starts to be reduced to sulfides below ~ 1.0 V. The electrochemical potential of sulfur oxidation is much higher than that of reduction. The potential difference is clearly seen in the galvanostatic charge–discharge curves. The sulfur oxidation presents obviously high discharge voltage plateau of ~ 1.8 V (Fig. 1e). However, the reduction of sulfur only shows a much lower operation voltage of ~ 0.5 V (Fig. 1f). To detect the phase evolution during the oxidation and reduction process, we carried out the in situ synchrotron-based X-ray diffraction (XRD) upon charge and discharge (Fig. 1g, h). The elemental sulfur, Al_2S_3, and $AlSCl_7$ are orthorhombic, hexagonal, and monoclinic crystals with space groups of Fddd, $P6_1$, and Pc, respectively (Fig. S4). During sulfur oxidation process, the orthorhombic sulfur transforms to the monoclinic $AlSCl_7$, while during reduction process, sulfur is reduced to hexagonal Al_2S_3. Specifically, for sulfur oxidation process (Fig. 1g), the peaks assigned to the (102), (013), and (110) facets of $AlSCl_7$ sequentially appear when the Al–S battery is charged to 2.4 V. For the reverse process from $AlSCl_7$ to sulfur, those peaks assigned to $AlSCl_7$ gradually disappear, and only the characteristic peaks of sulfur remain. It should be noted that the diffraction peak at 10.8° is assigned to the characteristic peak of sulfur and it remains during charge–discharge due to the incomplete electrochemical oxidation of sulfur. The above evidence confirms the efficient electrochemical oxidation of sulfur to $AlSCl_7$, and the reversibility from $AlSCl_7$ back to sulfur. During sulfur reduction process (Fig. 1h), the (011) and (016) diffraction peaks of Al_2S_3 appear at 8.5° and 16.6°, respectively. For the reverse charge process, these peaks gradually disappear due to the conversion of Al_2S_3 to sulfur. However, the (100) and (016) characteristic peaks of Al_2S_3 can be also found during the charge process, which is due to the difficulty of reversible decomposition of Al_2S_3 to sulfur. Both $AlSCl_7$ and Al_2S_3 are also verified by the XRD plots at different cut-off voltages (Fig. S5). The above evidence confirms sulfur oxidation and reduction chemistry, which is based on the $AlSCl_7$ and Al_2S_3 products, respectively.

A direct view of these products is shown on the scanning transmission electron microscopic (STEM) images after charging the sulfur cathode at 2.4 V and discharging at 0.2 V. S_8 octamer is visible on the TEM image of pristine sulfur (Fig. S6). After electrochemical S reduction at 0.2 V (Fig. 2a), a crystallized structure is seen with ($\bar{1}14$), ($\bar{1}15$), and (011) planes of Al_2S_3 in the Fast Fourier Transform (FFT) patterns. The high-resolution image presents an orthogonal arrangement of atoms (Fig. 2b), corresponding to the simulated Al_2S_3 images from [010]
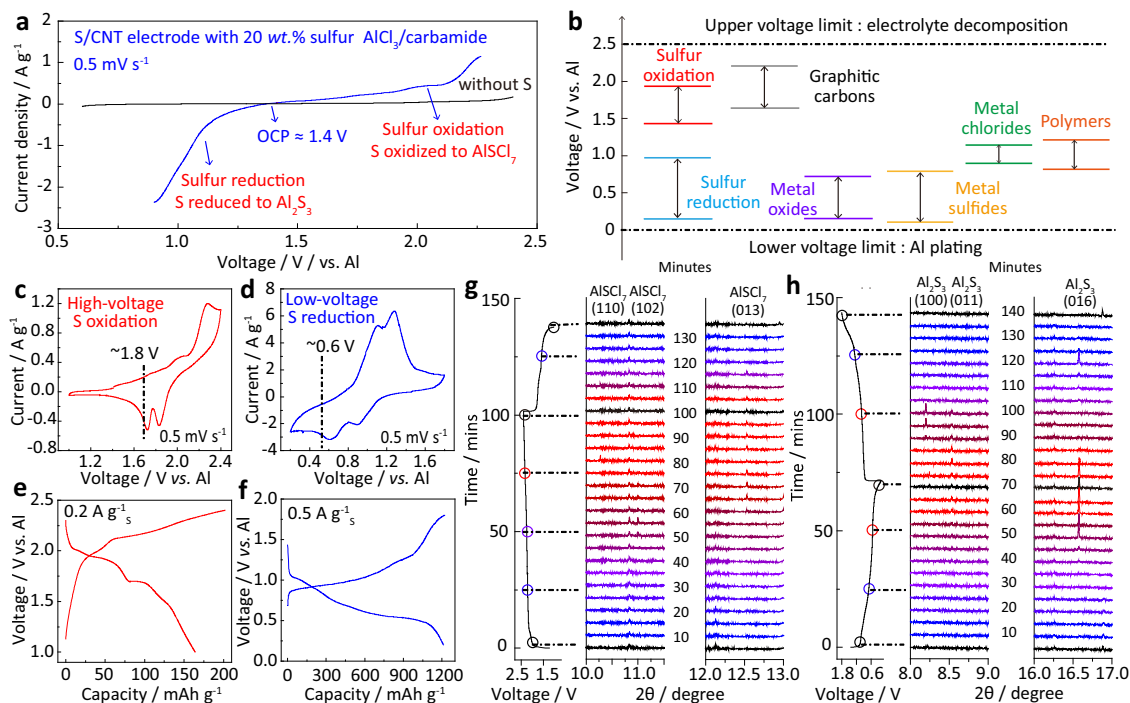
Fig. 1 The electrochemical oxidation and reduction of sulfur in ionic liquid. a LSV curves of S/CNT composite cathode in $AlCl_3$/carbamide ionic liquid at 0.5 mV s^{-1} with Al referenced electrode; the sulfur content in S/CNT is 20 wt.%; **b** the voltage comparison of sulfur oxidation and sulfur reduction with previously reported materials; CV curves of **c** sulfur oxidation and **d** sulfur reduction at 0.5 mV s^{-1}; galvanostatic charge–discharge curves of the S/CNT cathode based on **e** sulfur oxidation at 0.2 A g^{-1} and **f** sulfur reduction at 0.5 A g^{-1}; the time-dependent in situ synchrotron-based XRD patterns for **g** sulfur oxidation and **h** sulfur reduction processes and the corresponding charge–discharge curves. The current densities for sulfur oxidation and sulfur reduction are 0.2 and 0.5 A g^{-1}, respectively.
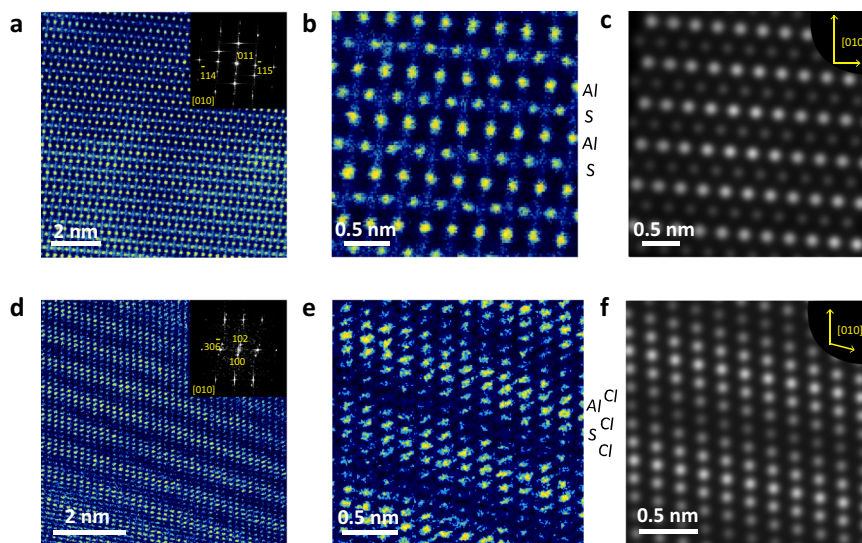
Fig. 2 Microscopic images of reduced and oxidized products of sulfur. a, **b** STEM image of Al_2S_3, and the inset in **a** shows the FFT patterns; **c** the simulated microscopic image of Al_2S_3 observed from [010] direction; **d**, **e** high-resolution TEM images of $AlSCl_7$, and the inset in **d** shows the FFT patterns; (**f**) the simulated microscopic image of $AlSCl_7$ observed from [010] direction.

observation (Figs. 2c and S4). By comparison, the oxidized product of sulfur at 2.4 V shows a periodic layered structure with (100), (102), and (30$\bar{6}$) planes in the FFT patterns. The observation of (102) plane corresponds well with the in situ XRD patterns. The ordered atom distribution can be clearly identified in Fig. 2e. Al, S, and Cl atoms are orderly arranged,

coinciding well with simulated $AlSCl_7$ images from [010] observation (Figs. 2f and S7). The Al, S, and Cl atoms can be also identified by the elemental mappings (Fig. S8). These results well characterize the phase evolution for the oxidation and reduction process of sulfur, where $AlSCl_7$ and Al_2S_3 are the main products.
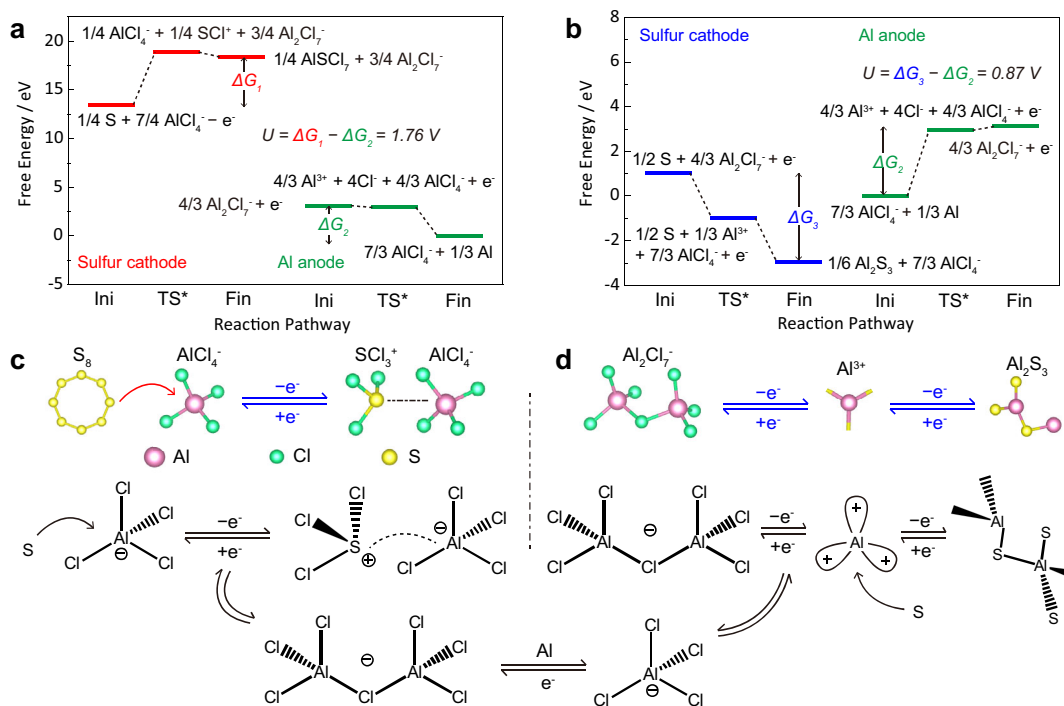
Fig. 3 Theoretical computations of reaction pathways for sulfur oxidation and sulfur reduction. The reaction pathway of sulfur cathode and Al anode for **a** sulfur oxidation and **b** sulfur reduction; schematics for **c** sulfur oxidation and **d** sulfur reduction processes with $AlCl_4^-$ and $Al_2Cl_7^-$ anions, respectively.

Theoretical computations of reaction pathways. To give an insight into the pathways of sulfur oxidation and reduction, we simulate the interactions between sulfur and $AlCl_4^-$ and $Al_2Cl_7^-$ cations based on density functional theory (DFT). The DFT-based energy, zero-point energy, entropy, and Gibbs free energy for all the intermediates are listed in Table S2, and their optimized structures are shown in Fig. S9. The details for determination of the Gibbs free energy are specified in the "Theoretical computations" part. For the sulfur oxidation process (Fig. 3a), $AlCl_4^-$ oxidizes S into $AlSCl_7$ solid accompanied by the loss of electrons (Eq. 1). Meanwhile, $Al_2Cl_7^-$ is reduced into $AlCl_4^-$ with Al plated on Al anode. The change in the Gibbs free energy (ΔG) can be calculated by using the electron-transfer numbers (n) and the difference in the electrochemical potential (ΔU). With single-electron transfer, the difference in ΔG between cathode and anode is the operation voltage[33]. As expected, the sulfur oxidation demonstrates a high voltage of ~1.76 V, which is consistent with the experimental observations of ~1.8 V (Fig. 1c). For the sulfur reduction process, sulfur is reduced by $Al_2Cl_7^-$ cations to form Al_2S_3 (Eq. 2), and meanwhile, $AlCl_4^-$ etches Al anode to form $Al_2Cl_7^-$. The voltage based on sulfur reduction is only ~0.87 V (Fig. 3b), much lower than that of sulfur oxidation. Additionally, the reverse reduction from $AlSCl_7$ to S only needs to overcome an energy barrier of 0.52 eV as calculated by the uphill of red lines in Fig. 3a. However, the energy barrier from Al_2S_3 to S is as high as 3.98 eV (blues lines in Fig. 3b). This comparison suggests the ease of reverse conversion from $AlSCl_7$ to S and therefore better reversibility of the sulfur oxidation–reduction process. Figure 3c, d schematically compares the sulfur oxidation and reduction process. The $AlCl_4^-$ and $Al_2Cl_7^-$ anions serve, respectively, as the oxidizing and reducing agents reacting with sulfur, and Al anode is used as referenced electrode to pair with these redox reactions for charge balance. We have summarized the pathways of sulfur oxidation and reduction as follows:

Sulfur oxidation:

$$\frac{1}{4}S + \frac{7}{4}AlCl_4^- - e^- \xrightarrow{\text{oxidation}} \frac{1}{4}AlSCl_7 + \frac{3}{4}Al_2Cl_7^- \quad (1)$$

Sulfur reduction:

$$\frac{1}{2}S + \frac{4}{3}Al_2Cl_7^- \xrightarrow{\text{reduction}} \frac{1}{6}Al_2S_3 + \frac{7}{3}AlCl_4^- + e^- \quad (2)$$
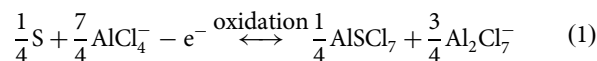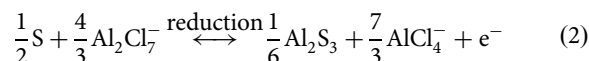
Track of reaction intermediates via spectroscopic analysis. We combined synchrotron-based near-edge X-ray absorption fine structure (NEXAFS) spectra, X-ray photoelectron spectra (XPS), and in situ Raman spectra to identify the reaction intermediates during the sulfur oxidation process. As shown in the S K-edge NEXAFS spectra (Fig. 4a), the characteristic peak of sulfur located at ~2472 eV presents an obvious positive shift with higher voltage from open circuit potential (OCP) to 2.4 V. The shifted peak position of oxidation products from 2.2 to 2.4 V is nicely located between the peaks of 0-valence and +6-valence sulfur as compared to the reference samples of elemental sulfur, $N_2S_2O_3$, and Li_2SO_4. This suggests the efficient oxidation of sulfur to higher valence at high voltages[34]. The positive shift of Cl characteristic peak is also identified from the Cl L-edge spectra at ~201.3 eV (Fig. 4b). This is attributed to the formation of S–Cl bonds in $AlSCl_7$. The electronegativity of S is stronger than Al, and therefore the photon energy of Cl atoms among Cl–S bonds is higher than those among Cl–Al bonds[35]. By contrast, there is no peak shift for Al characteristic peak because the chemical state of Al remains unchanged during the sulfur oxidation process (Fig. S10). To quantify the sulfur valence during its oxidation, we carried out the XPS measurement at different oxidation voltages (Fig. 4c). According to the S 2p XPS spectra, peaks located at ~169.4 and ~168.3 eV gradually appear between the +2 thiosulfate and +6 sulfate[36]. These doublets are assigned to the
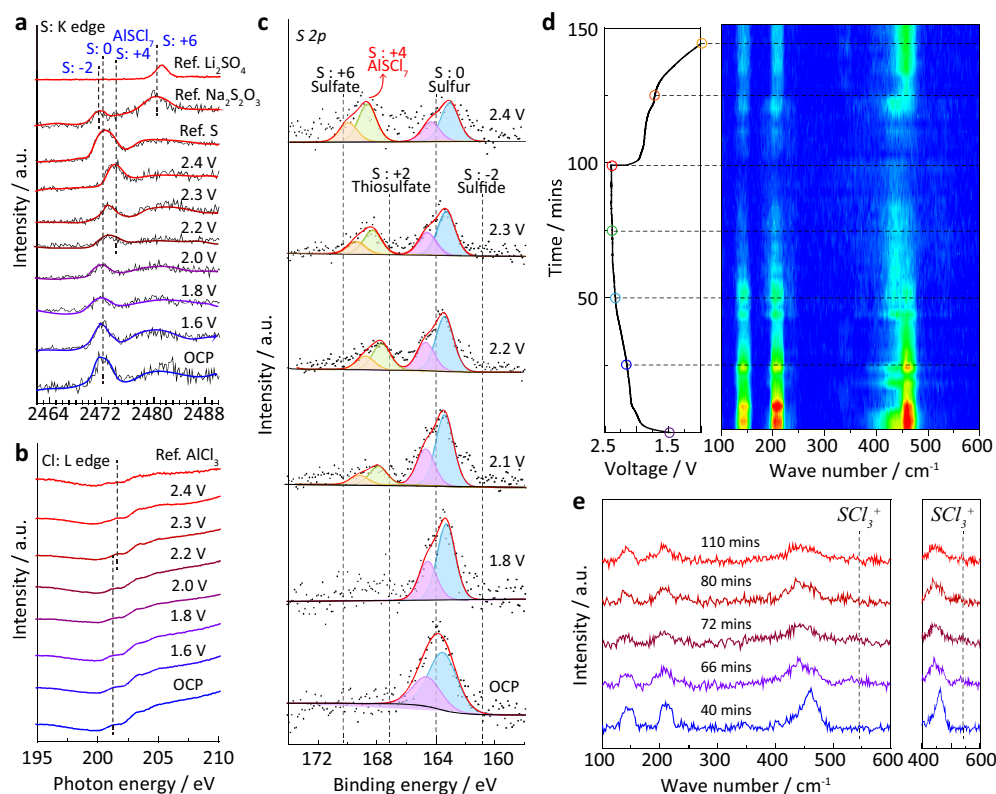
Fig. 4 Identification of oxidized intermediates of sulfur via spectroscopic analysis. NEXAFS spectra of S/CNT cathode with different voltages recorded at the **a** S K-edge and **b** Cl L-edge; **c** the S 2p XPS spectra of S/CNT cathode at different oxidation voltages; the Al–S batteries were charged from open-circuit potential (OCP) to 2.4 V at 0.2 A g^{-1}, and then the S/CNT cathodes at different cut-off voltages were extracted from the disassembled Al–S batteries for NEXAFS and XPS investigations; **d** the charge–discharge curves of Al–S batteries at 0.2 A g^{-1} and their real-time Raman contour map for S/CNT cathode; **e** Raman spectra at different times extracted from the contour pattern in **d**.

+4 sulfur, confirming the stable presence of AlSCl$_7$ oxidized products. To detect the oxidation intermediates, we further carried out in situ Raman spectra measurement (Fig. S11)[37]. As shown in Fig. 4d, Raman peaks located at ~145, ~210, and ~462 cm^{-1} are assigned to sulfur (Fig. S12)[38]. During the charging process, the intensity of these peaks gradually weakens, indicating the conversion from sulfur to AlSCl$_7$. For the reverse process, these Raman peaks of sulfur reappear, which is a strong evidence of the high reversibility of sulfur oxidation. Notably, a new peak located at 530 cm^{-1} emerges (Fig. 4e), which is attributed to the vibration of SCl$_3^+$ cations[39]. These cations are soluble in the electrolyte, which may trap into separator and shuttle to Al anode. Therefore, the sulfur valence and reversibility are well characterized by spectroscopic analysis. AlSCl$_7$ tends to decompose to AlCl$_4^-$ and SCl$_3^+$ intermediates, leading to the loss of sulfur during electrochemical cycling.

High-voltage Al–S batteries based on sulfur oxidation. To demonstrate the possible application of sulfur oxidation, we assembled Al–S batteries based on the oxidation and reduction process and compared their operation voltages and cyclic stability. Al–S batteries were assembled with S/CNT cathode, Al referenced anode, AlCl$_3$/carbamide ionic liquid, and a glass fiber separator using a 2032-coin cell type (more details in the "Electrochemical tests" section). The specific surface area of the cathode with 20 wt.% S in S/CNT composite is 154 m^2 g^{-1} (Fig. S13). As shown in Fig. 5a, Al–S batteries based on the sulfur oxidation (AlSCl$_7$ product) run steadily over 200 cycles with a highest specific capacity of 225 mAh g^{-1} (Fig. S14). Reversible redox reactions are defined as a pair of oxidation–reduction

reactions with high reversibility. Coulombic efficiency (CE%) is a good parameter to describe the reversibility of electrochemical reactions on the electrodes in batteries. In this work, CE% is defined as the percentage ratio of the specific discharge capacity to the charge capacity. For Al–S batteries based on the sulfur oxidation, the CE% stabilizes as high as ~94% upon cycling. This is ascribed to the efficient electrochemical oxidation of sulfur to AlSCl$_7$ and then highly reversible reduction from AlSCl$_7$ back to sulfur. However, it should be noted that the Al–S battery based on the sulfur oxidation also exhibits capacity decay upon long cycles. This is attributed to the gradual dissolution of SCl$_3^+$ into the electrolyte (as evidenced by the in situ Raman spectra), leading to the loss of active sulfur (Figs. S15 and S16). Future work needs to be carried out to restrain the dissolution of SCl$_3^+$ for more stable cycling performance. For the previously studied batteries based on sulfur reduction with Al$_2$S$_3$ product, the sulfur cathode showed an ultrahigh specific capacity over 1000 mAh g^{-1} at the first cycle. However, it dramatically declined after tens of cycles due to the irreversibility (Fig. 5b)[40–42]. Figure 5c, d shows a comparison of the charge–discharge curves at different cycles. The Al–S battery based on the sulfur oxidation exhibits a high voltage of ~1.8 V, and the voltage plateau remains stable during cycling. However, the Al–S batteries based on the sulfur reduction feature a much lower voltage of ~0.5 V with severe voltage decline and capacity decay. Additionally, the Al–S battery based on the sulfur oxidation demonstrates high-rate performance. The sulfur cathode still has a high specific capacity of 120 and 95 mAh g^{-1} at 0.5 and 1 A g^{-1}, respectively (Fig. S17). The Al–S battery maintains stable cycling at high current densities (Figs. S18 and S19). However, it is noteworthy that the specific capacity of sulfur
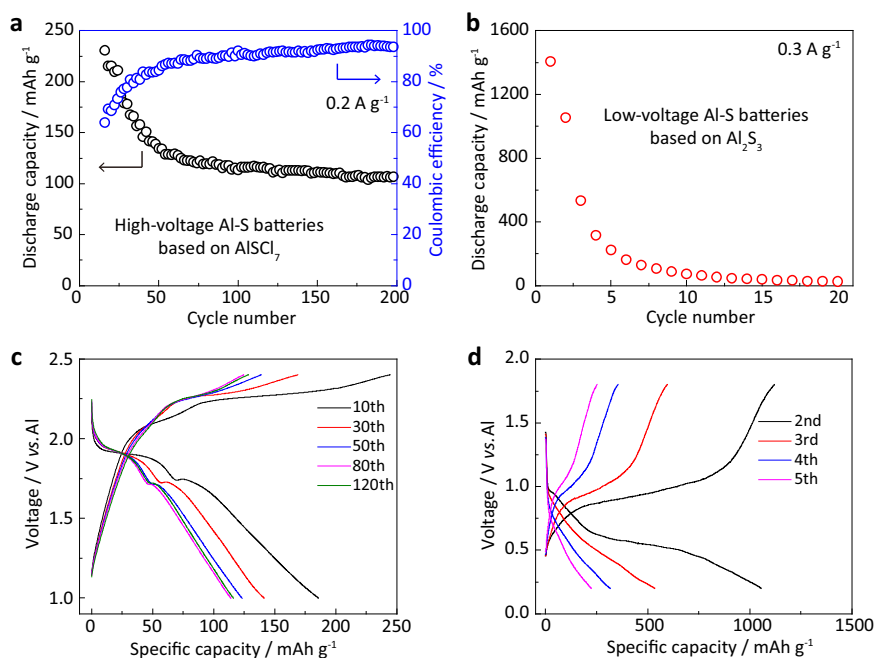
Fig. 5 Sulfur oxidation in Al–S batteries. The cycling performance of Al–S batteries based on **a** sulfur oxidation, AlSCl7 products and **b** sulfur reduction, Al2S3 products; the charge–discharge curves at different cycles of Al–S batteries based on **c** sulfur oxidation and **d** sulfur reduction.

decreases with higher sulfur contents and areal mass loadings (Figs. S20 and S21). Therefore, more attention should be paid in future on the design of sulfur host to improve the sulfur utilization with sulfur oxidation process.

Despite the above advantages of Al–S batteries, we should also evaluate their pros and cons. The maximized energy density based on the active sulfur is estimated at ~405 Wh kg^{-1} considering a specific capacity of 225 mAh g^{-1} with an average voltage plateau of ~1.8 V at the beginning cycles. However, it should be noted that this value decreases upon battery cycling, and the energy density will be also compromised while considering the practical devices, including Al anode, electrolyte, separator, cell case, etc. Further work still needs to be carried out to optimize the energy density by improving the sulfur utilization and the areal mass loading of sulfur while decreasing the dosage of non-active parts. In addition, another advantage of Al–S battery is the low cost of electrode materials such as sulfur, Al, and the AlCl3/carbamide electrolyte (Fig. S22 and Table S3). However, it should be also noted that the carbon nanotubes used in this work raise concerns about the cost-effectiveness. In the future works, it would be highly desirable to explore low-cost carbon or noncarbon hosts with lower cost and higher sulfur utilization.

Discussion

We have demonstrated that sulfur can be electrochemically oxidized in ionic liquid with high reversibility. The reaction pathways, AlSCl7 oxidized products, and SCl3$^+$ intermediates are well confirmed by means of in situ synchrotron-based analysis, high-resolution microscopic images, spectroscopic analysis, and theoretical computations. The electrochemical oxidation from sulfur to AlSCl7 is highly reversible with a stable CE% of ~94%, and the oxidation process is workable within a wide range of electrochemical potentials. As a result, the Al–S battery based on sulfur oxidation process can run steadily over 200 cycles around ~1.8 V, which is the highest operation voltage for Al–S batteries. It is expected that the sulfur oxidation process can be coupled with other metal anodes for various metal–sulfur batteries, not limited

to Al–S batteries. This work sheds new light on sulfur chemistry and shows a great advantage of the sulfur oxidation pathway for the design of viable high-voltage metal–sulfur batteries.

Methods

Preparation of S/CNT cathode and AlCl3/carbamide ionic liquid. The S/CNT material was prepared by mixing sublimed S with CNT under 155 °C for 12 h. Different sulfur contents in S/CNT can be achieved by adjusting the relative mass ratio of S and CNT. In all, 20, 40, and 80 wt.% of sulfur were used in this work. The S/CNT cathode was prepared by mixing S/CNT material with PVDF binder with a mass ratio of 90:10. The AlCl3/carbamide ionic liquid was synthesized by mixing AlCl3 and carbamide with a molar ratio of 1.3:1. Specifically, AlCl3 was gradually added into carbamide with continuous stirring in an Ar-filled glove box at the room temperature. During this process, these two solids melt with each other into liquid and finally form ionic liquid containing AlCl4$^-$, Al2Cl7$^-$, and [AlCl2(carbamide)$_n$]$^+$.

Characterization of materials. The morphology and structure of the samples were characterized by scanning electron microscopy (Hitachi S4800, Japan). High-resolution TEM and STEM images were obtained by JEM-ARM200F TEM. XPS spectra were measured with the Thermo Fisher Scientific ESCALAB Xi+, Al Kα radiation. NEXAFS of S K-edge and Cl L-edge were performed on the soft X-ray spectroscopy beamline at Australian synchrotron (Clayton) AS, part of ANSTO. In situ synchrotron XRD data were collected on the powder diffraction beamline at the Australian Synchrotron with a wavelength of 0.6868 and 0.7290 Å. Data were collected continuously in 30 s acquisitions with coin cells. For sulfur oxidation, first the cells were charged at 0.2 A g^{-1} to 2.4 V and then discharged to 1.0 V. For sulfur reduction, first the cells were discharged to 0.5 V and then charged to 1.8 V at 0.5 A g^{-1}. The cell cases on both the negative and positive sides together with the Al foil anode were punched with $d = 0.2$ cm holes, and polyimide films were used to seal the holes but allowed the X-ray transmission. In situ Raman spectra were collected with Labram HR Evolution (Horiba scientific).

Electrochemical tests. For the assembly of Al–S batteries, the as-prepared S/CNT electrodes with different sulfur contents were coupled with an Al foil reference anode (100 μm thickness). These two electrodes were sandwiched by a glass fiber separator (GF/A) with AlCl3/carbamide ionic liquid (~140 μL). These components were placed into a 2032-coin cell configuration for further electrochemical tests. The LSV curves were scanned from OCP (≈1.4 V) at 0.5 mV s^{-1}. CV was carried out from 1.0 to 2.4 V for sulfur oxidation and from 0.2 V to 1.8 V for sulfur reduction. Data of LSV and CV curves were collected on an IVIUM electrochemical workstation. Galvanostatic charge–discharge cycles were performed at different current densities using a Neware battery tester.

Theoretical computations. Computations for this work were carried out using DFT as implemented in VASP code. Electronic exchange–correlation energy was modeled using the Perdew–Burke–Ernzerhof function within a generalized gradient approximation. The projector-augmented wave method was used to describe the ionic cores. For the plane-wave expansion, a 450 eV kinetic energy cut-off was used following testing a series of different cut-off energies. Convergence criterion for the electronic structure iteration was set to 10^{-4} eV and that for geometry optimization was 0.01 eV Å^{-1} on force. A Gaussian smearing of 0.1 eV was applied during geometry optimization and for total energy computations.

The Gibbs free energy was calculated based on the DFT-based energy (E), zero-point energy (ZPE), and the entropy (TS) by using the following expression:

$$G = E + \text{ZPE} - \text{TS} \tag{3}$$

The change in the Gibbs free energy (ΔG) can be calculated by using the electron-transfer numbers (n) and the difference in the electrochemical potential (ΔU).

$$\Delta G = -n e \Delta U \tag{4}$$

The difference in ΔG between cathode and anode is the cell operation voltage with single-electron transfer ($n = 1$).

Data availability

The data that support the findings of this study are available from the corresponding author upon reasonable request.

References

1. Yang, Y., Zheng, G. Y. & Cui, Y. Nanostructured sulfur cathodes. *Chem. Soc. Rev.* **42**, 3018–3032 (2013).
2. Peng, L. et al. A fundamental look at electrocatalytic sulfur reduction reaction. *Nat. Catal.* **3**, 762–770 (2020).
3. Zhao, C. et al. A high-energy and long-cycling lithium–sulfur pouch cell via a macroporous catalytic cathode with double-end binding sites. *Nat. Nanotechnol.* **16**, 166–173 (2020).
4. Zhao, Y. et al. Initiating a reversible aqueous Zn/sulfur battery through a "liquid film". *Adv. Mater.* **32**, 2003070 (2020).
5. Hong, X. et al. Nonlithium metal-sulfur batteries: steps toward a leap. *Adv. Mater.* **31**, 1802822 (2019).
6. Yu, X. & Manthiram, A. A progress report on metal-sulfur batteries. *Adv. Funct. Mater.* **30**, 2004284 (2020).
7. Wei, S. et al. A stable room-temperature sodium-sulfur battery. *Nat. Commun.* **7**, 11722 (2016).
8. Gao, T. et al. A rechargeable Al/S battery with an ionic-liquid electrolyte. *Angew. Chem. Int. Ed.* **55**, 9898–9901 (2016).
9. Tan, G. et al. Burning lithium in CS$_2$ for high-performing compact Li$_2$S–graphene nanocapsules for Li–S batteries. *Nat. Energy* **2**, 17090 (2017).
10. Zhou, G. et al. Catalytic oxidation of Li$_2$S on the surface of metal sulfides for Li-S batteries. *Proc. Natl Acad. Sci. USA* **114**, 840–845 (2017).
11. Wu, F., Yang, H., Bai, Y. & Wu, C. Paving the path toward reliable cathode materials for aluminum-ion batteries. *Adv. Mater.* **31**, 1806510 (2019).
12. Zhang, Y., Liu, S., Ji, Y., Ma, J. & Yu, H. Emerging nonaqueous aluminum-ion batteries: challenges, status, and perspectives. *Adv. Mater.* **30**, 1706310 (2018).
13. Pang, Q., Liang, X., Kwok, C. Y. & Nazar, L. F. Advances in lithium-sulfur batteries based on multifunctional cathodes and electrolytes. *Nat. Energy* **1**, 16132 (2016).
14. Yang, H. et al. The rechargeable aluminum battery: opportunities and challenges. *Angew. Chem. Int. Ed.* **58**, 11978–11996 (2019).
15. Peng, H.-J. & Zhang, Q. Designing host materials for sulfur cathodes: from physical confinement to surface chemistry. *Angew. Chem. Int. Ed.* **54**, 11018–11020 (2015).
16. Pang, Q., Kundu, D., Cuisinier, M. & Nazar, L. F. Surface-enhanced redox chemistry of polysulphides on a metallic and polar host for lithium-sulphur batteries. *Nat. Commun.* **5**, 4759 (2014).
17. Hua, W. et al. Selective catalysis remedies polysulfide shuttling in lithium-sulfur batteries. *Adv. Mater.* **33**, 2101006 (2021).
18. Zhong, Y. R. et al. Surface chemistry in cobalt phosphide-stabilized lithium-sulfur batteries. *J. Am. Chem. Soc.* **140**, 1455–1459 (2018).
19. Worthington, M. J. H., Kucera, R. L. & Chalker, J. M. Green chemistry and polymers made from sulfur. *Green Chem.* **19**, 2748–2761 (2017).
20. Mutlu, H. et al. Sulfur chemistry in polymer and materials science. *Macromol. Rapid Commun.* **40**, 1800650 (2019).
21. Kim, H. S. et al. Structure and compatibility of a magnesium electrolyte with a sulphur cathode. *Nat. Commun.* **2**, 427 (2011).
22. Suo, L. et al. "Water-in-salt" electrolyte enables high-voltage aqueous lithium-ion chemistries. *Science* **350**, 938–943 (2015).
23. Xu, K. Nonaqueous liquid electrolytes for lithium-based rechargeable batteries. *Chem. Rev.* **104**, 4303–4417 (2004).
24. Zhang, S. S. Liquid electrolyte lithium/sulfur battery: fundamental chemistry, problems, and solutions. *J. Power Sources* **231**, 153–162 (2013).
25. Wang, M. & Tang, Y. A review on the features and progress of dual-ion batteries. *Adv. Energy Mater.* **8**, 1804766 (2018).
26. Mamantov, G. et al. SCl$_3^+$AlCl$_4^-$: improved synthesis and characterization. *J. Inorg. Nucl. Chem.* **41**, 260–261 (1979).
27. Angell, M. et al. High Coulombic efficiency aluminum-ion battery using an AlCl$_3$-urea ionic liquid analog electrolyte. *Proc. Natl Acad. Sci. USA* **114**, 834–839 (2017).
28. Bian, Y. et al. Using an AlCl$_3$/urea ionic liquid analog electrolyte for improving the lifetime of aluminum-sulfur batteries. *ChemElectroChem* **5**, 3607–3611 (2018).
29. Lin, M.-C. et al. An ultrafast rechargeable aluminium-ion battery. *Nature* **520**, 324–328 (2015).
30. Sun, H. B. et al. A new aluminium-ion battery with high voltage, high safety and low cost. *Chem. Commun.* **51**, 11892–11895 (2015).
31. Long, Y. et al. Suppressing Al dendrite growth towards a long-life Al-metal battery. *Energy Storage Mater.* **34**, 194–202 (2021).
32. Yu, X., Wang, B., Gong, D., Xu, Z. & Lu, B. Graphene nanoribbons on highly porous 3D graphene for high-capacity and ultrastable Al-ion batteries. *Adv. Mater.* **29**, 1604118 (2017).
33. Jiao, Y., Zheng, Y., Jaroniec, M. & Qiao, S. Z. Design of electrocatalysts for oxygen- and hydrogen-involving energy conversion reactions. *Chem. Soc. Rev.* **44**, 2060–2086 (2015).
34. Yagi, S. et al. Vulcanization reaction of squalene and S$_8$ powder studied by sulfur K-edge NEXAFS under liquid phase. *IOP Conf. Ser. Mater. Sci. Eng.* **76**, 012004 (2015).
35. Parent, P., Lasne, J., Marcotte, G. & Laffon, C. HCl adsorption on ice at low temperature: a combined X-ray absorption, photoemission and infrared study. *Phys. Chem. Chem. Phys.* **13**, 7142–7148 (2011).
36. Liang, X. et al. A highly efficient polysulfide mediator for lithium-sulfur batteries. *Nat. Commun.* **6**, 5682 (2015).
37. Li, H. et al. Revealing principles for design of lean-electrolyte lithium metal anode via in-situ spectroscopy. *J. Am. Chem. Soc.* **142**, 2012–2022 (2020).
38. Hagen, M. et al. In-situ Raman investigation of polysulfide formation in Li-S cells. *J. Electrochem. Soc.* **160**, A1205–A1214 (2013).
39. Doorenbos, H. E., Evans, J. C. & Kagel, R. O. Preparation, Raman and nuclear quadrupole resonance data for the complex SCl$_3^+$AlCl$_4^-$. *J. Phy. Chem.* **74**, 3385–3387 (1970).
40. Yu, X., Boyer, M. J., Hwang, G. S. & Manthiram, A. room-temperature aluminum-sulfur batteries with a lithium-ion-mediated ionic liquid electrolyte. *Chem* **4**, 586–598 (2018).
41. Cohn, G., Ma, L. & Archer, L. A. A novel non-aqueous aluminum sulfur battery. *J. Power Sources* **283**, 416–422 (2015).
42. Yang, H. et al. An aluminum-sulfur battery with a fast kinetic response. *Angew. Chem. Int. Ed.* **57**, 1898–1902 (2018).

Author contributions

S.-Z.Q. conceived and supervised this research; H.L. designed and carried out experiments and DFT computations; R.M. performed the electrochemical tests and in situ Raman spectra. Y.G. carried out the XPS spectra. B.C. assisted with the STEM images; Y.J. assisted with DFT computations; C.Y. assisted with design of sulfur cathode and the battery test; Y.L. assisted with the synthesis of AlCl$_3$/carbamide ionic liquid and battery assembly; A.T. assisted with the soft X-ray spectroscopy in Australian synchrotron; Q.-H.Y. provided experimental conditions and technical support for H.L. during COVID-19 period in China (2020–2021); S.-Z.Q. and M.J. revised the manuscript. All authors discussed results and commented on the manuscript.

Competing interests

The authors declare no competing interests.

Additional information

Supplementary information The online version contains supplementary material available at https://doi.org/10.1038/s41467-021-26056-7.

Correspondence and requests for materials should be addressed to Shi-Zhang Qiao.

Peer review information *Nature Communications* thanks Zhifeng Ding, Enyuan Hu, and the other anonymous reviewer(s) for their contribution to the peer review of this work.

Reprints and permission information is available at http://www.nature.com/reprints

Publisher's note Springer Nature remains neutral with regard to jurisdictional claims in published maps and institutional affiliations.

Supplementary Information

Reversible electrochemical oxidation of sulfur in ionic liquid for high-voltage Al−S batteries

Huan Li[1†], Rongwei Meng[2†], Yong Guo[2], Biao Chen[3], Yan Jiao[1], Chao Ye[1], Yu Long[2], Anton Tadich,[4] Quan-Hong Yang[2], Mietek Jaroniec[5] and Shi-Zhang Qiao[*1]

[1]School of Chemical Engineering and Advanced Materials, The University of Adelaide, Adelaide, SA 5005, Australia;

[2]Nanoyang Group, State Key Laboratory of Chemical Engineering, School of Chemical Engineering and Technology, Tianjin University, Tianjin 300072, China;

[3]School of Materials Science and Engineering and Tianjin Key Laboratory of Composite and Functional Materials, Tianjin University, Tianjin 300350, China.

[4]Australian Synchrotron (ANSTO), 800 Blackburn Rd, Clayton, VIC 3168, Australia

[5]Department of Chemistry and Biochemistry & Advanced Materials and Liquid Crystal Institute, Kent State University, Kent, OH 44242, USA.

[†]These authors contribute equally to this work.

* Corresponding author e-mail: s.qiao@adelaide.edu.au

Supplementary Results

$-\cdot-\cdot-\cdot-\cdot-\cdot-\cdot-$ S/AlSCl$_7$, ≈ 0.2~0.8 V, sulfur oxidation

$-\cdot-\cdot-\cdot-\cdot-\cdot-\cdot-$ H^2/H$^+$, SHE, 0 V

$-\cdot-\cdot-\cdot-\cdot-\cdot-\cdot-$ S/S^{2-}, ≈ −0.9~−0.7 V, sulfur reduction

$-\cdot-\cdot-\cdot-\cdot-\cdot-\cdot-$ Al/Al^{3+}, −1.66 V

$-\cdot-\cdot-\cdot-\cdot-\cdot-\cdot-$ Na/Na$^+$, −2.71 V

$-\cdot-\cdot-\cdot-\cdot-\cdot-\cdot-$ Li/Li$^+$, −3.04 V

Supplementary Figure S1 The estimated equilibrium electrochemical potentials of sulfur reduction and sulfur oxidation.
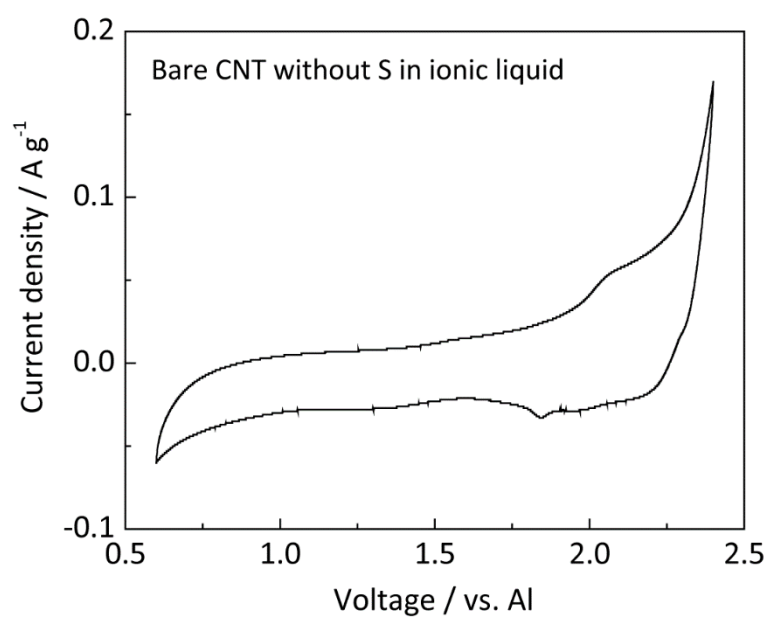
Supplementary Figure S2 CV curves of bare CNT in AlCl$_3$/urea with a scan rate of 0.5 mV s^{-1}. The CV data show much lower current density (y axis), suggesting the low electrochemical activity of CNT in ionic liquid.
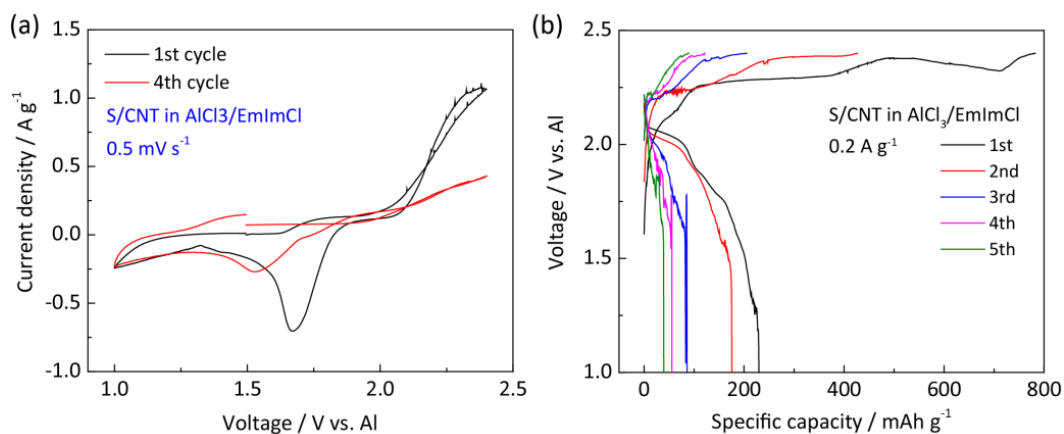
Supplementary Figure S3 The electrochemical oxidation of sulfur in AlCl$_3$/EmimCl electrolyte. The molar ratio of AlCl$_3$ to EmimCl is 1.3:1. (a) CV curves of S/CNT from 1.0 V to 2.4 V at a scan rate of 0.5 mV s^{-1}. The severely decreased peak currents can be seen from the 1st cycle and 4th cycle, indicating the poor reversibility of sulfur in this electrolyte. (b) Charge-discharge curves of S/CNT from 1.0 V to 2.4 V at 0.2 A g^{-1}. The discharge capacity dramatically decreases from 230 mAh g^{-1} to 41 mAh g^{-1} from 1st to 5th cycles, confirming the instability of sulfur in this electrolyte during electrochemical oxidation.
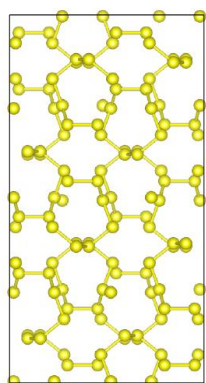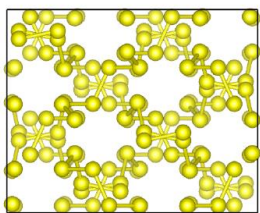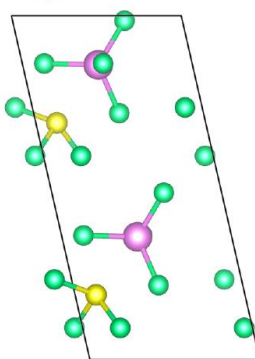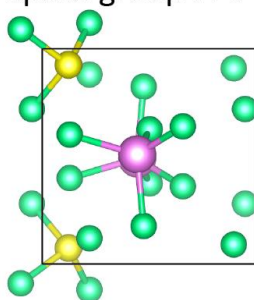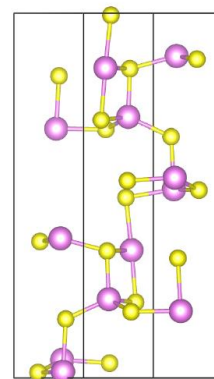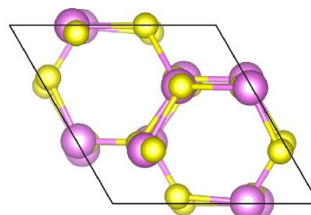
Supplementary Figure S4 The models, crystal structures and space groups of elemental sulfur, AlSCl$_7$ and Al$_2$S$_3$. The purple, yellow and green atoms denote Al, S and Cl, respectively.
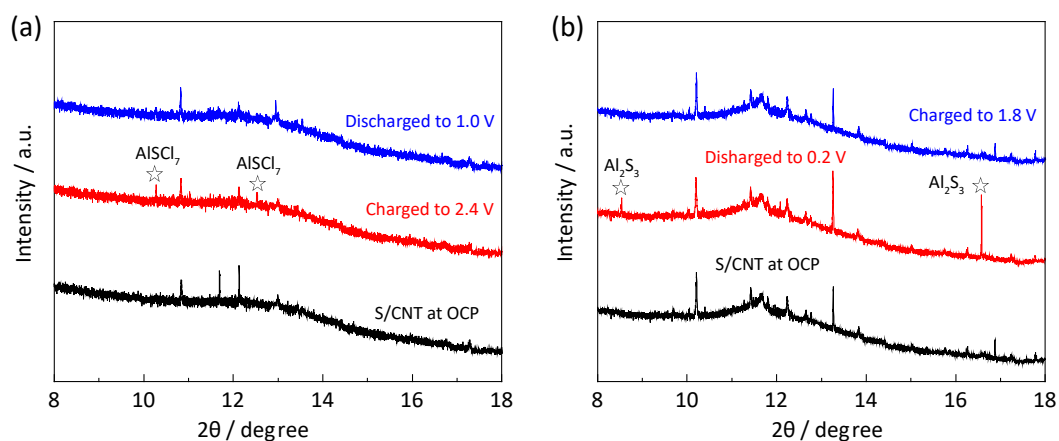
Supplementary Figure S5 The XRD patterns of S/CNT composite cathodes at different cut-off voltages based on (a) $AlSCl_7$ and (b) Al_2S_3 products. The corresponding wavelengths are 0.7290 nm and 0.6868 nm, respectively. For sulfur oxidation, the diffraction peaks of $AlSCl_7$ can be clearly observed at 2.4 V. These peaks disappear after discharging to 1.0 V due to the reversible conversion from $AlSCl_7$ to sulfur. For sulfur reduction, the peaks assigned to Al_2S_3 are seen at 0.2 V, and these peaks disappear at 1.8 V, suggesting the transformation from Al_2S_3 to sulfur during charge process.
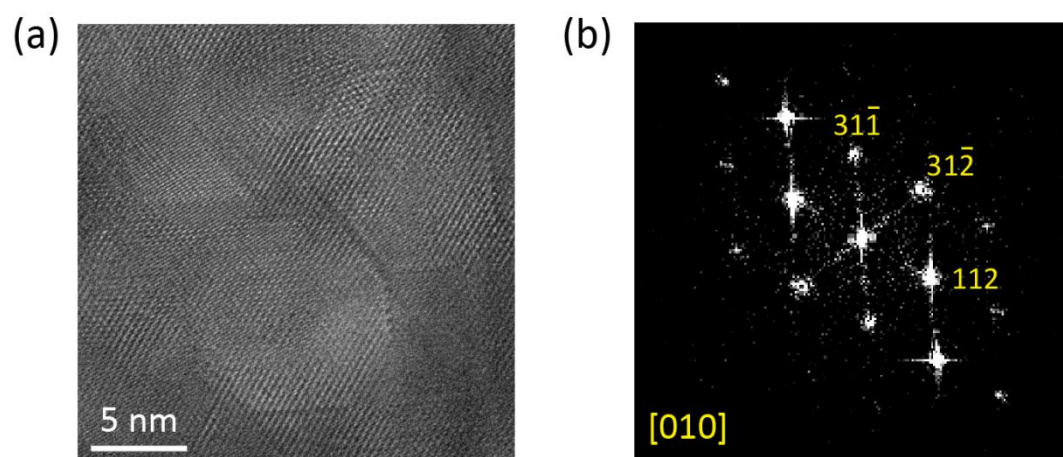
Supplementary Figure S6 (a) High-resolution TEM image of S_8; (b) The transformed FFT patterns.
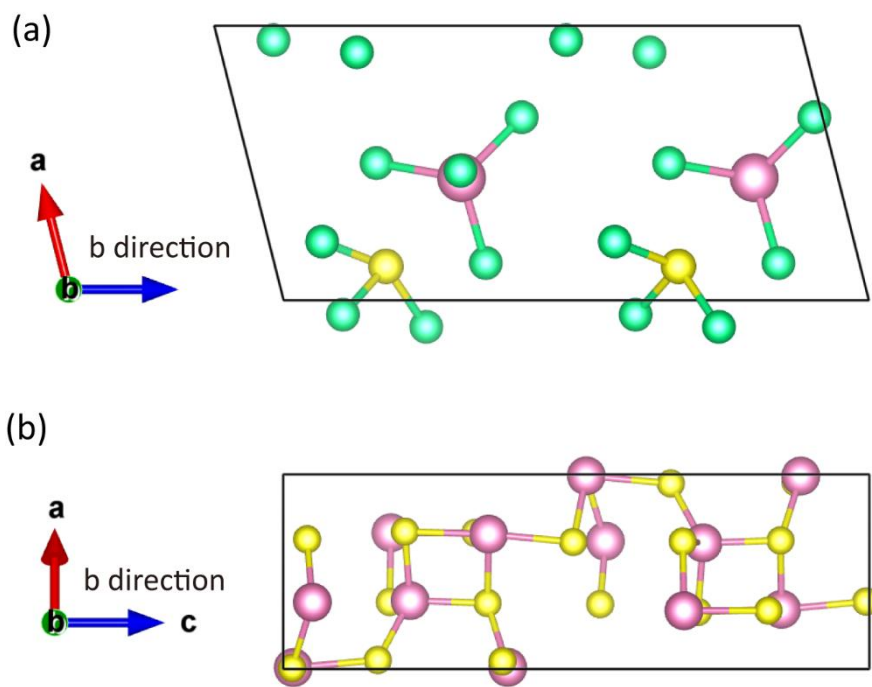
Supplementary Figure S7 The optimized models of AlSCl$_7$ and Al$_2$S$_3$. The angles between a-axis and c-axis correspond well with the STEM observation as shown in Figure 2b and 2d.
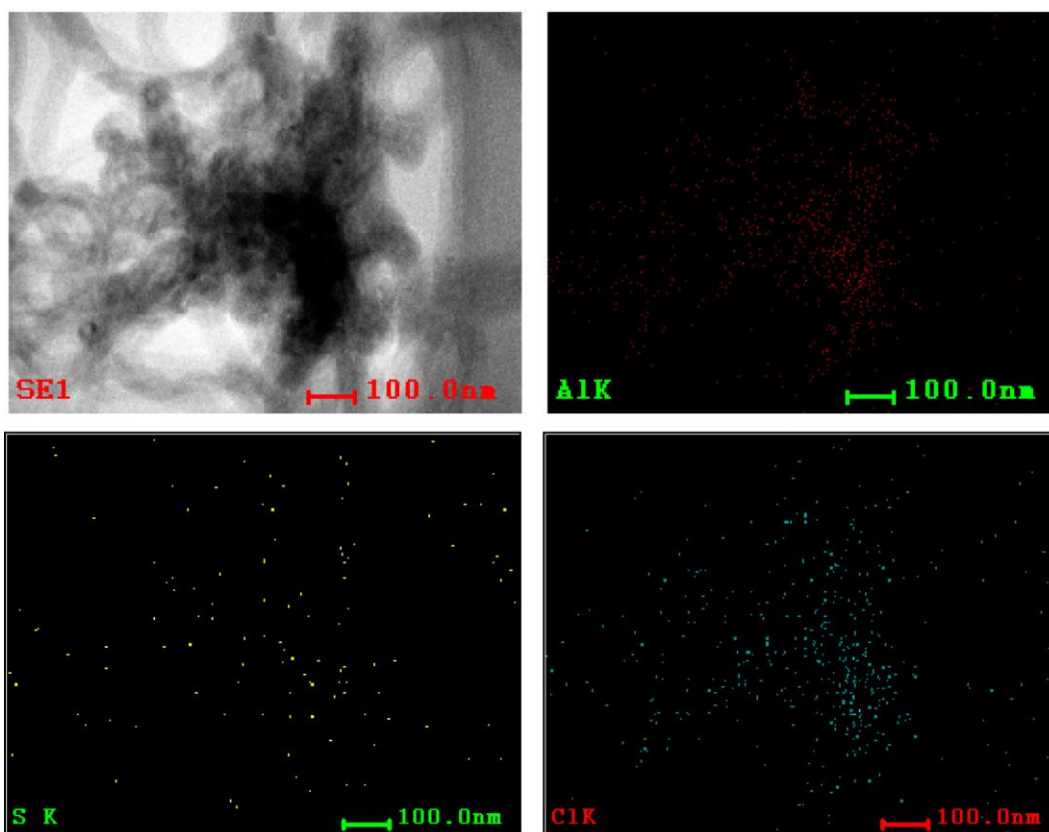
Supplementary Figure S8 TEM image of $AlSCl_7$ and its elemental mapping of Al, S, Cl. $AlSCl_7$ was obtained by disassembly of the Al−S battery after charging to 2.4 V. Obvious Al and Cl are observed on these images, suggesting the formation of $AlSCl_7$ during charging process.
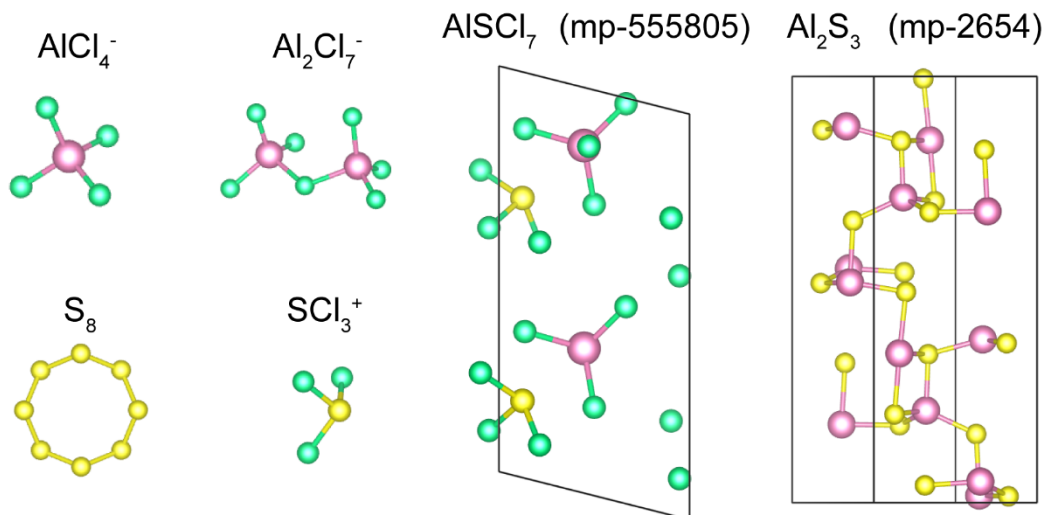
Supplementary Figure S9 The optimized theoretical structures of $AlCl_4^-$, $Al_2Cl_7^-$, S_8, SCl_3^+, $AlSCl_7$ and Al_2S_3.
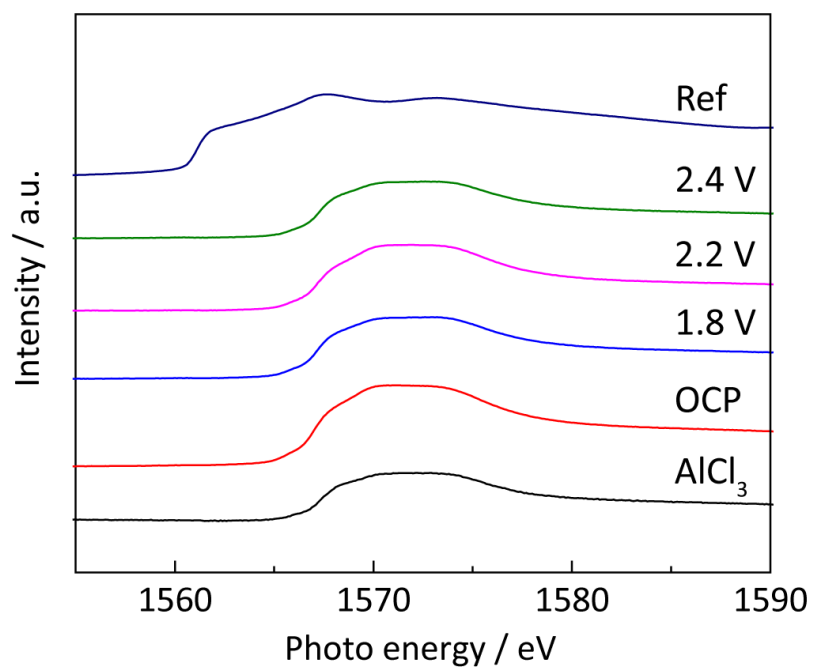
Supplementary Figure S10 The Al K edge NEXAFS spectra of sulfur cathodes at different charging potentials. Compared to the obvious peak shift of S and Cl (Figure 3a and 3b), no peak shift is visible during charging process. These results indicate that the Al valence remains unchanged during cycling.
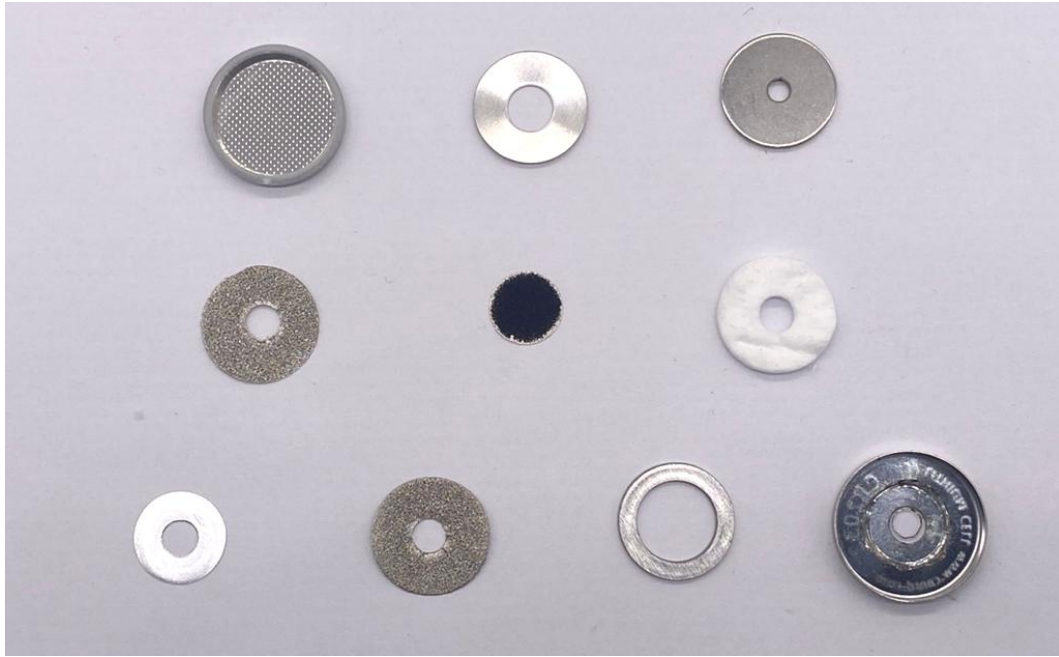
Supplementary Figure S11 The cell configurations for the *in-situ* Raman testing in Figure 4d.
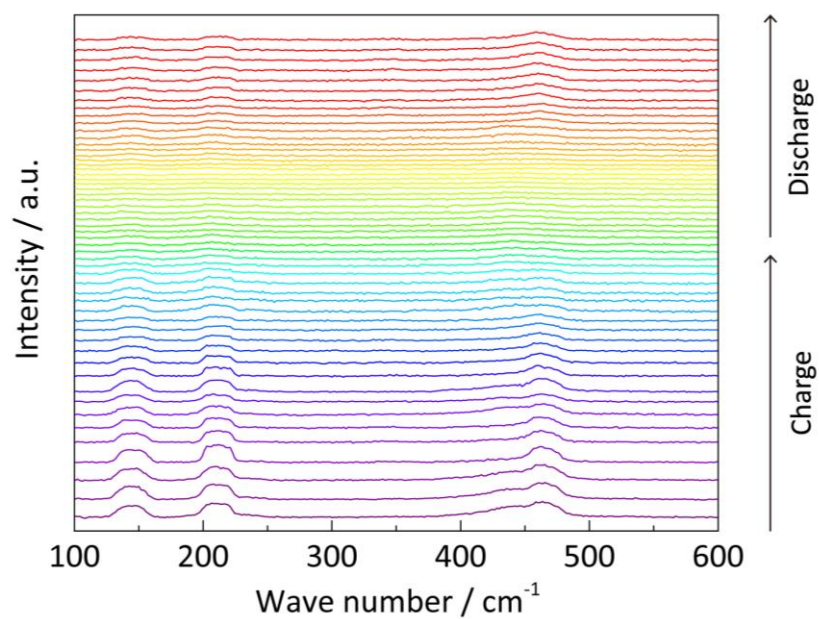
Supplementary Figure S12 The *in-situ* Raman spectra of sulfur cathode in Al−S battery. The decreased peak density of sulfur is visible during charging process, while the peaks emerge as the battery is discharged.
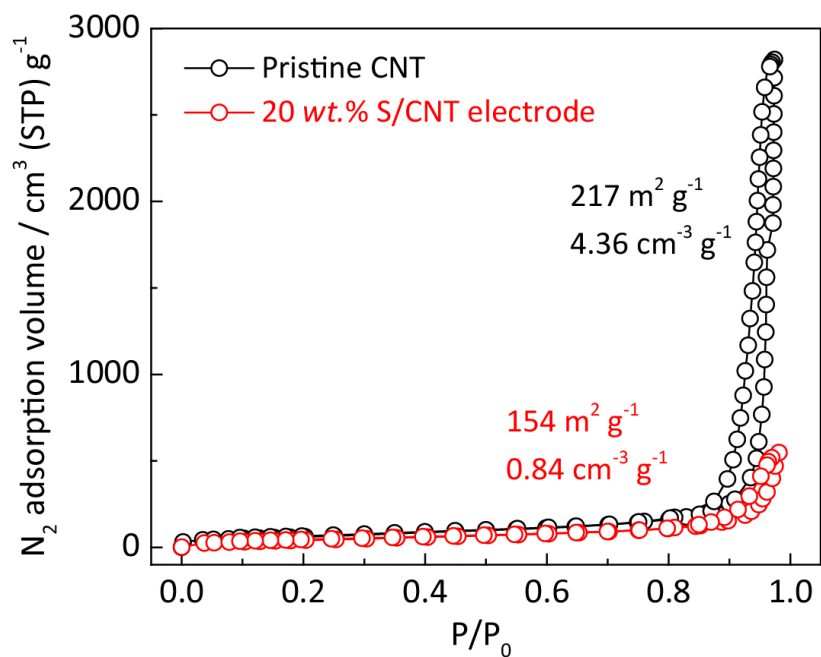
Supplementary Figure S13 N$_2$ adsorption-desorption isotherms (77 K) for pristine CNT and composite electrode with 20 *wt.*% sulfur in S/CNT. The pristine CNT shows a specific surface area of 217 m^2 g^{-1} with a pore volume of 4.36 cm^3 g^{-1}. After processing the S/CNT electrode with 20 *wt.*% sulfur, its specific surface area decreases to 154 m^2 g^{-1}, and meanwhile the pore volume decreases to 0.84 cm^3 g^{-1}. These decreases are attributed to the sulfur presence inside the CNT host.
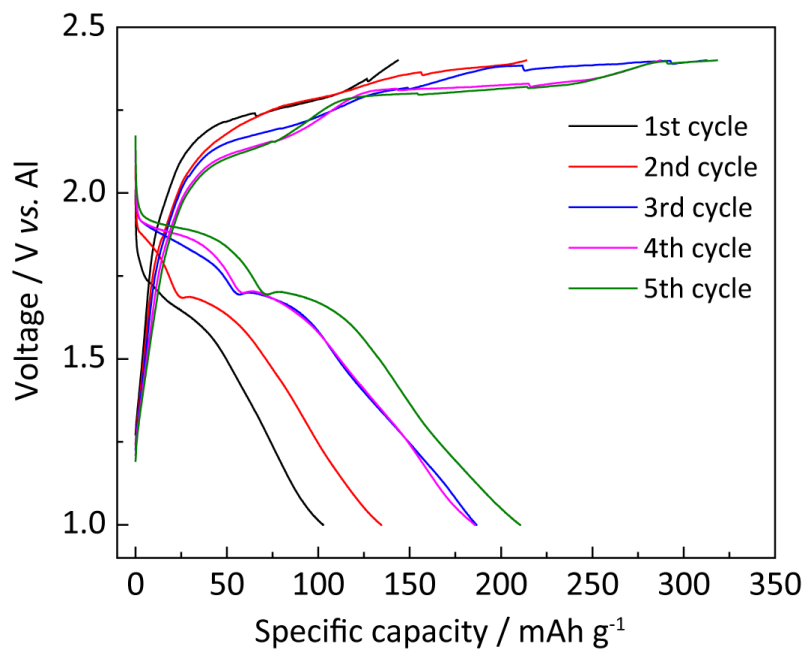
Supplementary Figure S14 The charge-discharge curves of Al−S batteries from 1st cycle to 5th cycle at 0.2 A g^{-1}. A pre-activation process with several electrochemical cycles is needed to activate the assembled fresh Al−S battery.

Supplementary Figure S15 Digital photos of sulfur cathode, separator and Al anode disassembled from the cycled Al−S batteries.
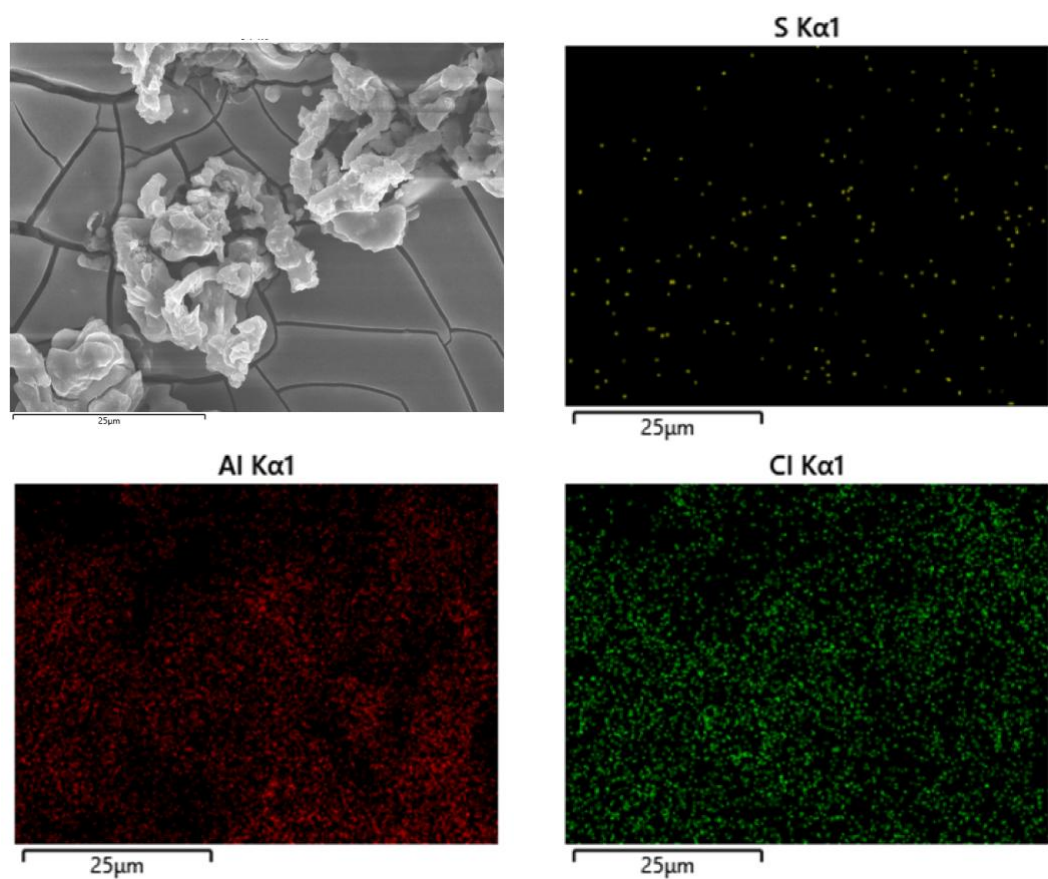
Supplementary Figure S16 The SEM image of cycled Al anode and its elemental mappings. There are obvious S and Cl signals for Al anode after cycling. This confirms the dissolution of SCl_3^+ and its migration to the anode side, leading to the capacity decay.
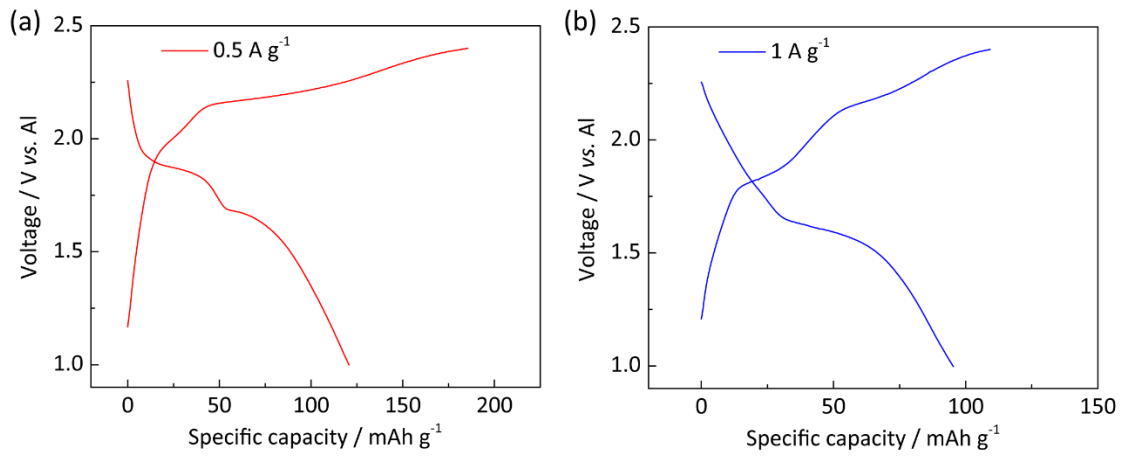
Supplementary Figure S17 Charge-discharge curves of Al−S batteries at 0.5 A g^{-1} and 1 A g^{-1}.
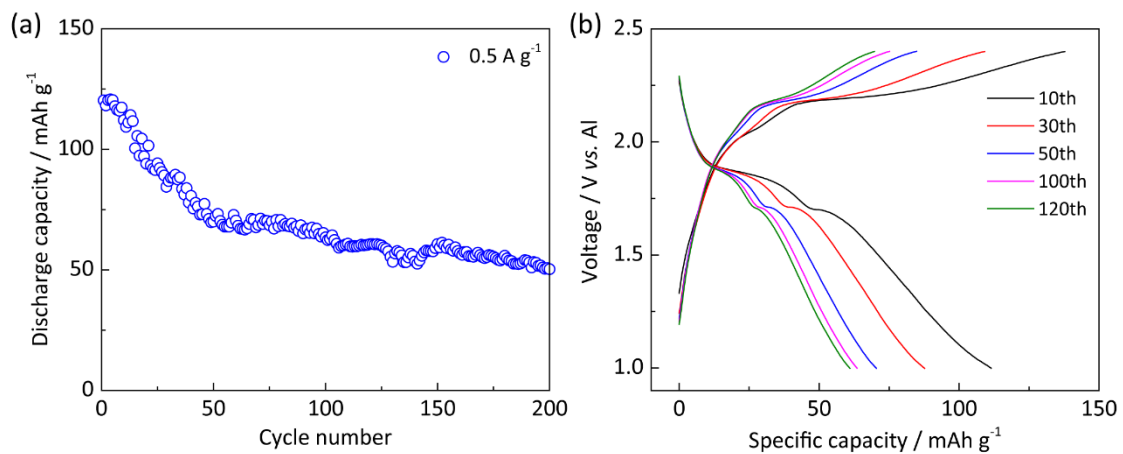
Supplementary Figure S18 (a) Cycling performance of Al−S battery at 0.5 A g⁻¹; (b) The charge-discharge curves at different cycles.
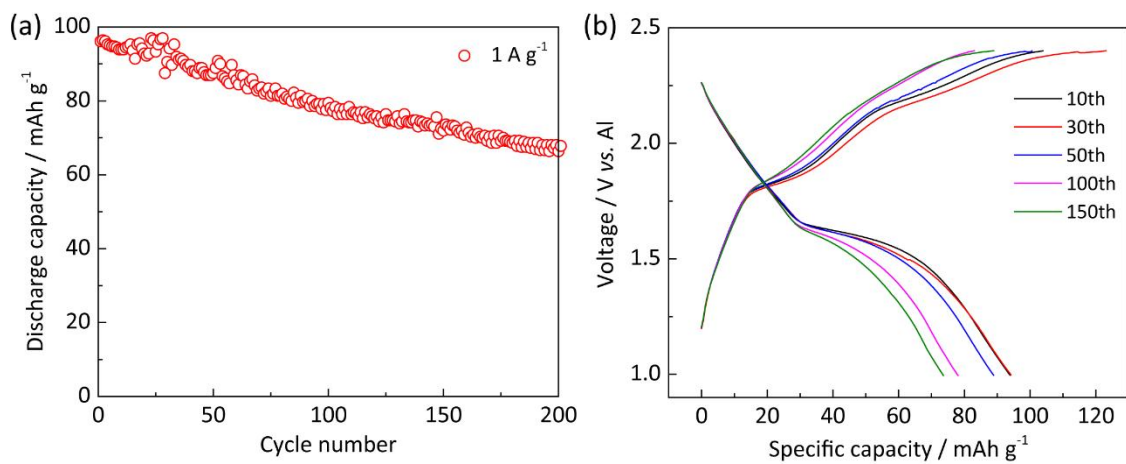
Supplementary Figure S19 (a) Cycling performance of Al−S battery at 1 A g^{-1}; (b) The charge-discharge curves at different cycles.
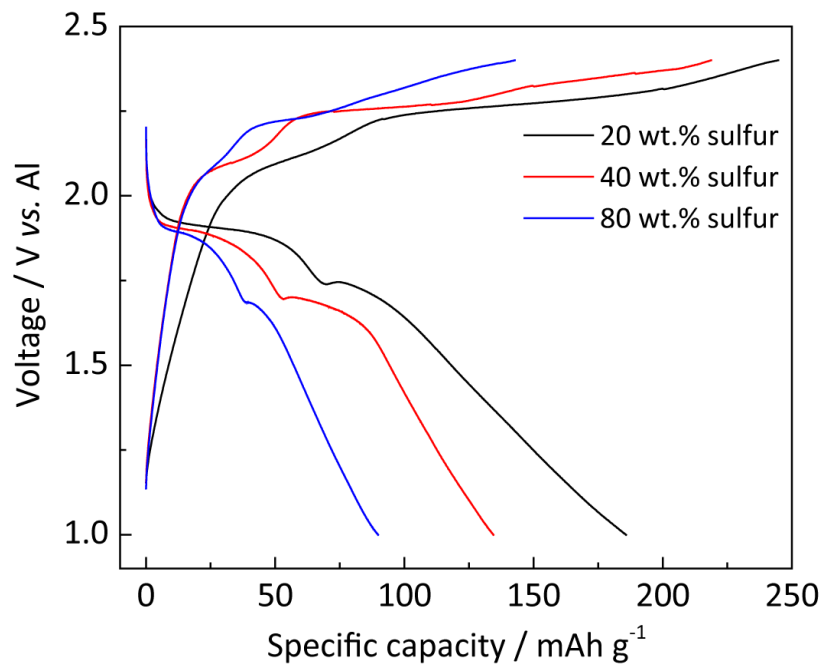
Supplementary Figure S20 Charge-discharge curves of Al−S batteries with different sulfur content

in S/CNT composites. The applied current density is 0.2 A g⁻¹.
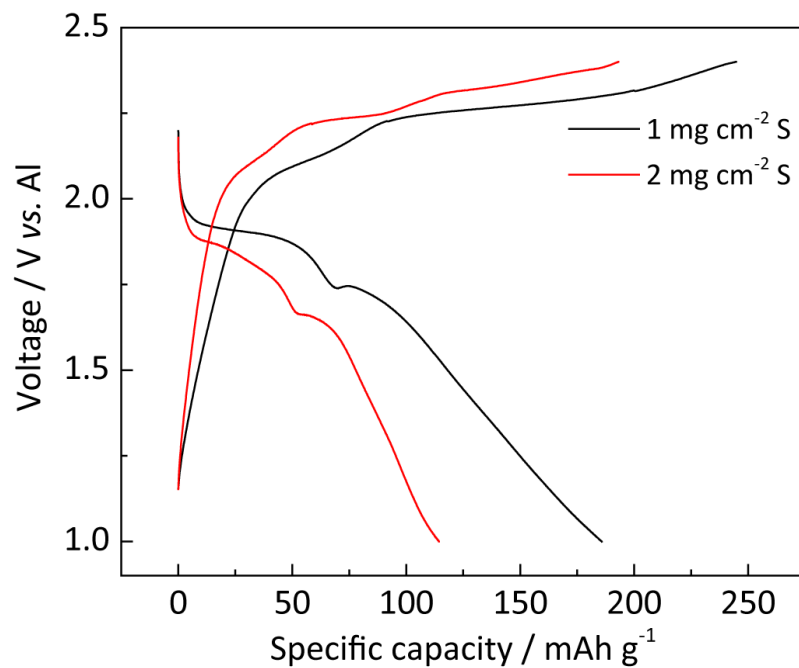
Supplementary Figure S21 Charge-discharge curves of Al−S batteries with different areal loadings of sulfur. The applied current density is 0.2 A g^{-1}.
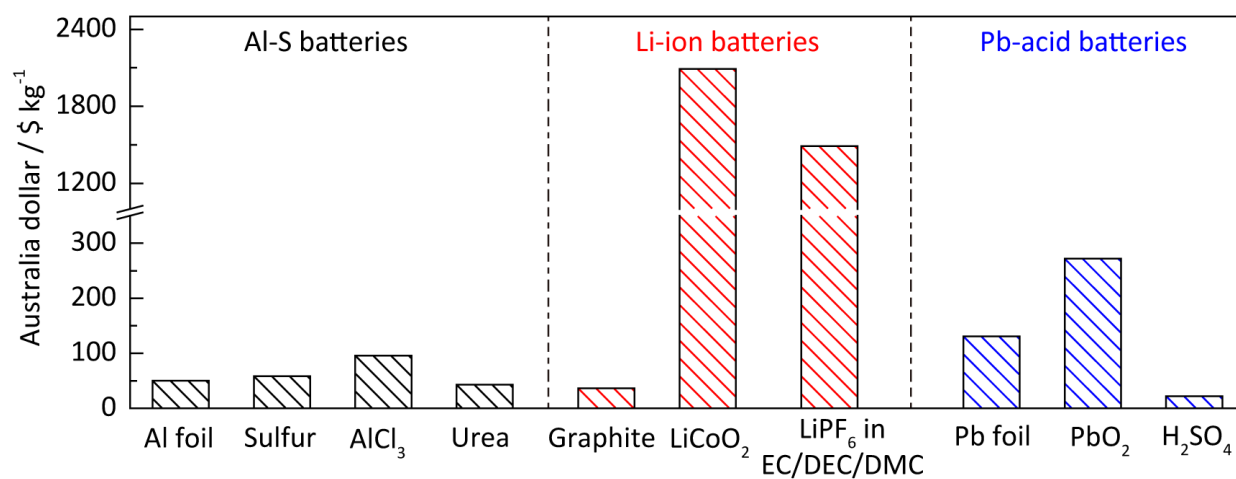
Supplementary Figure S22 The price comparison of electrode materials and electrolytes for Al−S, Li-ion and Pb-acid batteries.

Supplementary Table S1 The performance comparison with the reported cathode materials in ionic liquid electrolytes

Reported materials		Electrolyte	Discharge voltage / V	Specific capacity / mAh g^{-1}	Cycling life	Final capacity / mAh g^{-1}	Ref
Sulfur oxidation (This work)	S/CNT	AlCl$_3$/urea	~1.7 – 1.9 V	~225	200	~105	This work
Sulfur reduction	S/carbon cloth	AlCl$_3$/EmImCl	~ 0.6 V	~1300	20	~1000	1
	S/CNF paper	Li$^+$-AlCl$_3$/EmImCl	~ 0.75 V	~1000	50	~600	2
	S/CMK-3	AlCl$_3$/NBMPBr	~ 0.2 – 0.6 V	~1400	20	~600	3
	S/Co+C	AlCl$_3$/EmImCl	~ 0.1 – 0.8 V	~1600	200	~500	4
	S/CNF+coated separator	AlCl$_3$/EmImCl	~ 0.95 V	~1250	10	~600	5
Metal oxides	Binder-free V$_2$O$_5$	AlCl$_3$/BmImCl	~ 0.5 – 0.7 V	~240	5	~180	6
	V$_2$O$_5$ nanowires	AlCl$_3$/EmImCl	~ 0.55 V ~ 0.2 V	~305	20	~273	7
	Anatase TiO$_2$	AlCl$_3$/EmImCl	~ 0.5 V	~120	N/A	N/A	8
	Co$_3$O$_4$	AlCl$_3$/EmImCl	~ 0.2 – 0.7 V	~490	100	~122	9
Metal sulfides	Co$_3$S$_4$	AlCl$_3$/EmImCl	~ 0.7 V	~290	150	~90	10
	Mo$_6$S$_8$	AlCl$_3$/BmImCl	~ 0.55 V, ~0.38 V	~167	50	~70	11
	CuS	AlCl$_3$/EmImCl	~ 0.1 – 1.0 V	~250	100	~100	12
	MoS$_2$	AlCl$_3$/EmImCl	~ 0.4 – 0.8 V	~253	100	~67	13
Metal chlorides	VCl$_3$	AlCl$_3$/EmImCl	~ 1.0 V	~76	10	~10	14
Polymers	polypyrrole	AlCl$_3$/EmImCl	N/A	~70	100	~50	15
	polythiophene		~ 0.8 – 1.2 V	~90	100	~70	
Graphitic carbons	3D graphitic foam	AlCl$_3$/EmImCl	~ 1.5 – 2.2 V	~60	7500	~60	16
	Carbon paper	AlCl$_3$/EmImCl	~ 1.6 – 2.0 V	~85	50	~85	17
	Graphene nanoribbons	AlCl$_3$/EmImCl	~ 1.6 – 2.0 V	~110	10000	~123	18

Supplementary Table S2 The DFT-based energy (EDFT), zero-point energy (ZPE), entropy (TS) and Gibbs free energy (G) of different solids and ions

	Al	$AlCl_4^-$	$Al_2Cl_7^-$	$AlSCl_7$	Al_2S_3	S	Al^{3+}	SCl_3^+	Cl^-
E_{DFT}	-3.75	-22.43	-37.97	-28.1	-25.18	-4.13	-0.27	-3.54	-5.05
ZPE	0.032	0.12	0.27	0.315	0.25	0.041	0	0.04	0
TS	0.055	0.44	0.73	0.89	0.35	0.085	0.14	0.34	0.08
G	-3.77	-22.76	-38.43	-28.67	-25.28	-4.17	-0.42	-3.84	-5.13

Supplementary Table S3 The price list of electrode materials for Al−S, Li−ion and Pb−acid batteries based on the   Sigma-Aldrich and Alfa Aesar catalogs.

Battery	Components	Product	SKU-pack size	Price / AUS$ kg^{-1}
Al-S battery	anode	Al foil	Z185140-1EA	50.2
	cathode	sulfur	13825-1KG-R	58.4
	electrolyte	AlCl$_3$	11019-6KG	96
		urea	U5128-5KG	43
Li-ion battery	anode	graphite	332461-12KG	36.4
	cathode	LiCoO$_2$	442704-100G-A	2090
	electrolyte	LiPF$_6$ in EC/DEC/DMC	901685-500ML	1490
Pb-acid battery	anode	Pb foil	GF03246465-2EA	131
	cathode	PbO$_2$	AC217530025 (from Alfa Aesar)	272
	electrolyte	H$_2$SO$_4$	1603131000	22

Supplementary References

1   Gao, T. *et al.* A rechargeable Al/S battery with an ionic-liquid electrolyte. *Angew. Chem. Int. Ed.* **55**, 9898-9901 (2016).

2   Yu, X., Boyer, M. J., Hwang, G. S. & Manthiram, A. room-temperature aluminum-sulfur batteries with a lithium-ion-mediated ionic liquid electrolyte. *Chem* **4**, 586-598 (2018).

3   Yang, H. *et al.* An aluminum-sulfur battery with a fast kinetic response. *Angew. Chem. Int. Ed.* **57**, 1898-1902 (2018).

4   Guo, Y. *et al.* Rechargeable aluminium-sulfur battery with improved electrochemical performance by cobalt-containing electrocatalyst. *Angew. Chem. Int. Ed.* **59**, 22963-22967 (2020).

5   Yu, X. & Manthiram, A. Electrochemical energy storage with a reversible nonaqueous room-temperature aluminum-sulfur chemistry. *Adv. Energy Mater.* **7**, 1700561 (2017).

6   Wang, H. *et al.* Binder-free V_2O_5 cathode for greener rechargeable aluminum battery. *ACS Appl. Mater. Interfaces* **7**, 80-84 (2015).

7   Jayaprakash, N., Das, S. K. & Archer, L. A. The rechargeable aluminum-ion battery. *Chem. Commun.* **47**, 12610-12612 (2011).

8   Koketsu, T. *et al.* Reversible magnesium and aluminium ions insertion in cation-deficient anatase TiO_2. *Nat. Mater.* **16**, 1142-1150 (2017).

9   Liu, J., Li, Z., Huo, X. & Li, J. Nanosphere-rod-like Co_3O_4 as high performance cathode material for aluminium ion batteries. *J. Power Sources* **422**, 49-56 (2019).

10   Li, H. *et al.* A highly reversible Co_3S_4 microsphere cathode material for aluminum-ion batteries. *Nano Energy* **56**, 100-108 (2019).

11   Geng, L., Lv, G., Xing, X. & Guo, J. Reversible electrochemical intercalation of aluminum in Mo_6S_8. *Chem. Mater.* **27**, 4926-4929 (2015).

12   Wang, S. *et al.* High-performance aluminum-ion battery with CuS@C microsphere composite cathode. *ACS Nano* **11**, 469-477 (2017).

13   Li, Z. Y., Niu, B. B., Liu, J., Li, J. L. & Kang, F. Y. Rechargeable aluminum-ion battery based on MoS_2 microsphere cathode. *ACS Appl. Mater. Interfaces* **10**, 9451-9459 (2018).

14   Suto, K. *et al.* Electrochemical properties of Al/vanadium chloride batteries with $AlCl_3$-1-ethyl-3-methylimidazolium chloride electrolyte. *J. Electrochem. Soc.* **163**, A742-A747

(2016).

15 Hudak, N. S. Chloroaluminate-doped conducting polymers as positive electrodes in rechargeable aluminum batteries. *J. Phy. Chem. C* **118**, 5203-5215 (2014).

16 Lin, M.-C. *et al.* An ultrafast rechargeable aluminium-ion battery. *Nature* **520**, 324-328 (2015).

17 Sun, H. B. *et al.* A new aluminium-ion battery with high voltage, high safety and low cost. *Chem. Commun.* **51**, 11892-11895 (2015).

18 Yu, X., Wang, B., Gong, D., Xu, Z. & Lu, B. Graphene nanoribbons on highly porous 3D graphene for high-capacity and ultrastable Al-ion batteries. *Adv. Mater.* **29**, 1604118 (2017).

Chapter 5: Activity origin and design of catalysts for sulfur reduction electrocatalysis

5.1 Introduction and significance

The sulfur reduction reaction (SRR) is important in metal−sulfur batteries. Effective catalysts are often based on transition-metals, or compounds of them. However activity origins remain unclear, and there is therefore an absence of a quantitative guide for catalyst design. Here we formulate for the first time, design principles to boost SRR activity by controlling the Gibbs free energy of polysulfide species in a group of *3d* unary and binary transition-metal clusters. SRR reactivity trend is established through a quantitative correlation of *3d*-orbital charges with Gibbs free energy and catalytic activity. The design principles and reactivity trend are 1) readily applied to boost SRR activity through adjustment of natural material property, and 2) appear universal for rational design of more-efficient catalysts. Findings are therefore a significant conceptual advance that will be of immediate benefit in improved catalyst design for sulfur reduction electrocatalysis in metal−sulfur batteries. The highlights of this work include:

➢ We formulate new design principles for optimization of SRR catalytic activity, based on targeted control of the Gibbs free energy of polysulfide species on the material surface and findings from activity origins in a group of *3d* unary and binary clusters.

➢ We establish SRR reactivity trends by correlating the *3d*-orbital charges of transition-metal clusters, Gibbs free energy of polysulfides and SRR catalytic activity, to rationally design efficient SRR catalysts by adjusting natural material properties.

➢ We demonstrate practical application of an optimized CoZn cluster catalyst that exhibited a high SRR exchange current density of 0.63 mA cm^{-2}. This high activity is shown to highly significantly boost battery performance, especially at high current rate and high areal sulfur loading. As a result, the Li−S battery retained a high specific capacity of 820 mAh g^{-1} at 1.0 C current rate with an areal sulfur loading of 5 mg cm^{-2}. The battery worked steadily with a low 0.05 % capacity decay per cycle.

5.2 Activity origin and design of catalysts for sulfur reduction electrocatalysis

This Chapter is included as it appears as a journal paper submitted by **Huan Li**, Rongwei Meng, Anton Tadich, Yan Jiao, Chao Ye, Xiao Chen, Qinfen Gu, Bernt Johannessen, Kenneth Davey and Shi-Zhang Qiao*. Activity origin and design of catalysts for sulfur reduction electrocatalysis, **To be submitted**.

Statement of Authorship

Title of Paper	Activity origin and design of catalysts for sulfur reduction electrocatalysis
Publication Status	☐ Published ☐ Accepted for Publication ☐ Submitted for Publication ☑ Unpublished and Unsubmitted work written in manuscript style
Publication Details	Huan Li, Rongwei Meng, Anton Tadich, Yan Jiao, Chao Ye, Xiao Chen, Qinfen Gu, Bernt Johannessen, Kenneth Davey and Shi-Zhang Qiao*. To be submitted.

Principal Author

Name of Principal Author (Candidate)	Huan Li
Contribution to the Paper	Conducted material synthesis, carried out electrochemical tests and wrote the paper
Overall percentage (%)	70
Certification:	This paper reports on original research I conducted during the period of my Higher Degree by Research candidature and is not subject to any obligations or contractual agreements with a third party that would constrain its inclusion in this thesis. I am the primary author of this paper.
Signature	Date 14 June 2022

Co-Author Contributions

By signing the Statement of Authorship, each author certifies that:

    i.   the candidate's stated contribution to the publication is accurate (as detailed above);

    ii.   permission is granted for the candidate in include the publication in the thesis; and

    iii.   the sum of all co-author contributions is equal to 100% less the candidate's stated contribution.

Name of Co-Author	Rongwei Meng
Contribution to the Paper	Carried out battery tests and rotating disk electrode tests for sulfur reduction
Signature	Date 14 June 2022

Name of Co-Author	Anton Tadich
Contribution to the Paper	Helped with synchrotron soft X-ray spectra
Signature	Date 14 June 2022

Name of Co-Author	Yan Jiao			
Contribution to the Paper	Helped with theoretical computations			
Signature			Date	14 June 2022

Name of Co-Author	Chao Ye			
Contribution to the Paper	Helped with design of sulfur cathode			
Signature			Date	14 June 2022

Name of Co-Author	Xiao Chen			
Contribution to the Paper	Captured microscopic images			
Signature			Date	14 June 2022

Name of Co-Author	Qinfen Gu			
Contribution to the Paper	Helped with in-situ synchrotron X-ray diffraction characterizations			
Signature			Date	14 June 2022

Name of Co-Author	Bernt Johannessen			
Contribution to the Paper	Helped with synchrotron X-ray adsorption spectra			
Signature			Date	14 June 2022

Name of Co-Author	Kenneth Davey			
Contribution to the Paper	Revised the manuscript			
Signature			Date	14 June 2022

Name of Co-Author	Shi-Zhang Qiao			
Contribution to the Paper	Supervised the research project			
Signature			Date	14 June 2022

Please cut and paste additional co-author panels here as required.

Name of Co-Author	Shi-Zhang Qiao
Contribution to the Paper	Supervised the research project

Activity origin and design of catalysts for sulfur reduction electrocatalysis

Huan Li[1†], Rongwei Meng[2†], Anton Tadich[3], Yan Jiao[1], Chao Ye[1], Xiao Chen[4], Qinfen Gu[3], Bernt Johannessen[3], Kenneth Davey[1] and Shi-Zhang Qiao*[1]

[1]School of Chemical Engineering and Advanced Materials, The University of Adelaide, Adelaide, SA 5005, Australia; [2]Nanoyang Group, State Key Laboratory of Chemical Engineering, School of Chemical Engineering and Technology, Collaborative Innovation Center of Chemical Science and Engineering (Tianjin), Tianjin University, Tianjin 300072, China; [3]Australian Synchrotron, ANSTO, 800 Blackburn Rd, Clayton, VIC 3168, Australia; [4]Beijing Key Laboratory of Green Reaction Engineering and Technology, Department of Chemical Engineering, Tsinghua University, Beijing, China; [†]These authors contributed equally to this work.

* Corresponding E-mail: s.qiao@adelaide.edu.au

The sulfur reduction reaction (SRR) is important in metal−sulfur batteries. Effective catalysts are often based on transition-metals, or compounds of them. However activity origins remain unclear, and there is therefore an absence of a quantitative guide for catalyst design. Here we formulate for the first time, design principles to boost SRR activity by controlling the Gibbs free energy of polysulfide species in a group of *3d* unary and binary transition-metal clusters. SRR reactivity trend is established through a quantitative correlation of *3d*-orbital charges with Gibbs free energy and catalytic activity. The design principles and reactivity trend are 1) readily applied to boost SRR activity through adjustment of natural material property, and 2) appear universal for rational design of more-efficient catalysts. Findings are therefore a significant conceptual advance that will be of immediate benefit in improved catalyst design for sulfur reduction electrocatalysis in metal−sulfur batteries.

Electrocatalytic sulfur reduction reaction (SRR) is a fundamental but complex process in metal−sulfur batteries. In Li−S batteries, it involves consecutive reductions from S_8 ring molecules to soluble lithium polysulfides (Li_2S_x, x = 2~8), and soluble polysulfides into insoluble Li_2S solid ($S_8 \rightarrow Li_2S_x \rightarrow Li_2S$).[1-10] The use of SRR catalysts can increase energy density and life-span of Li−S batteries because it concomitantly promotes kinetics of sulfur reduction, and suppresses shuttle effects of Li_2S_x.[11, 12] To limit loss of sulfur, conventional design of sulfur hosts are based on ultra-high binding energy with polysulfides. A consequence is that SRR catalysts are often transition metals or compounds of them.[13-17] Although these are known to improve SRR activity, an understanding of activity origin is limited. As a result, present catalysts are proposed in the absence of rational principles. Therefore, a quantitative understanding of activity origin and reactivity trend is necessary for rational design and optimization of SRR catalysts.

The apparent activity of SRR is widely described by experimental parameters including, exchange current density and overpotential. However, the intrinsic electronic structures that are related to catalytic activity have been overlooked. Rational design and any optimization of SRR performance of catalysts therefore require an increased understanding of relation between apparent SRR activity and intrinsic electronic structure of catalysts. Density function theory (DFT) theoretical computations are widely used to investigate adsorption energetics, reaction thermodynamics and electronic structures.[18-22] By correlating these parameters with experimentally measured catalytic activities, the reactivity trend can give insight into activity origin of a group of catalysts, and importantly, a quantitative relation to optimize catalytic activity via adjustment of natural properties of the catalyst.[23-25] The reactivity trend has been established for other electrocatalytic reactions, such as oxygen reduction.[25] However because SRR has not received significant research attention, there is a present, limited understanding of catalysis mechanisms that restricts rational design of more-efficient catalysts.

Here through combined experimental and theoretical investigation of activity origin of a series of

3d transition-metal clusters including, Fe, Co, Ni, Cu, Zn and corresponding binary clusters, we formulate rational design principles to boost SRR activity via controlling the Gibbs free energy of polysulfide species on the catalyst surface. The CoZn cluster for example, outperforms others, as evidenced by the proper Gibbs free energy of Li_2S_x on its surface, with experimentally greater catalytic activity. Following screening of several electronic-structural parameters, the *3d*-orbital charges are found to be quantitatively correlated with the Gibbs free energies of Li_2S_x and therefore determine SRR activity. SRR activity is quantitatively correlated with the performance of Li−S batteries. High SRR activity boosts battery performance, especially at high current rate and high areal sulfur loading. We show therefore that a Li−S battery with CoZn cluster as a cathode catalyst retains a high specific capacity of 820 mAh g^{-1} at 1.0 C current rate with an areal sulfur loading of 5 mg cm^{-2}. The battery is demonstrated to work steadily with just 0.05 % capacity decay per cycle. Findings appear universal and will therefore be of immediate benefit in understanding SRR mechanisms and in practically advancing optimized design of metal-sulfur batteries.

Results

Failure of adsorption energy as a determinant for SRR. The ultra-high adsorption energy of Li_2S_x on the catalyst surface has been widely used in an attempt to explain high SRR activity.[11, 12] However typical catalysis includes not only the adsorption step, but also following conversion and desorption. Ultra-high adsorption energy therefore appears not to be a sufficient explanatory determinant for SRR activity. An investigation was undertaken therefore to determine whether SRR activity increased with increasing adsorption energy.

To determine the effect of adsorption strength of Li_2S_x on catalytic activity, we synthesized Co and Zn clusters loading on graphene substrate (details in **Experimental Section**). Through control of Co precursors, Co atoms tend to form clusters dominated with 6-aggregated atoms and an average Co−Co bond length of ∼ 2.25 Å (**Figs. 1a** and **1b**).[27, 28] Zn cluster is discussed in **Supplementary Fig. 1**. Synchrotron X-ray adsorption spectra confirmed Co−Co bonds in these clusters, **Fig. 1d** and
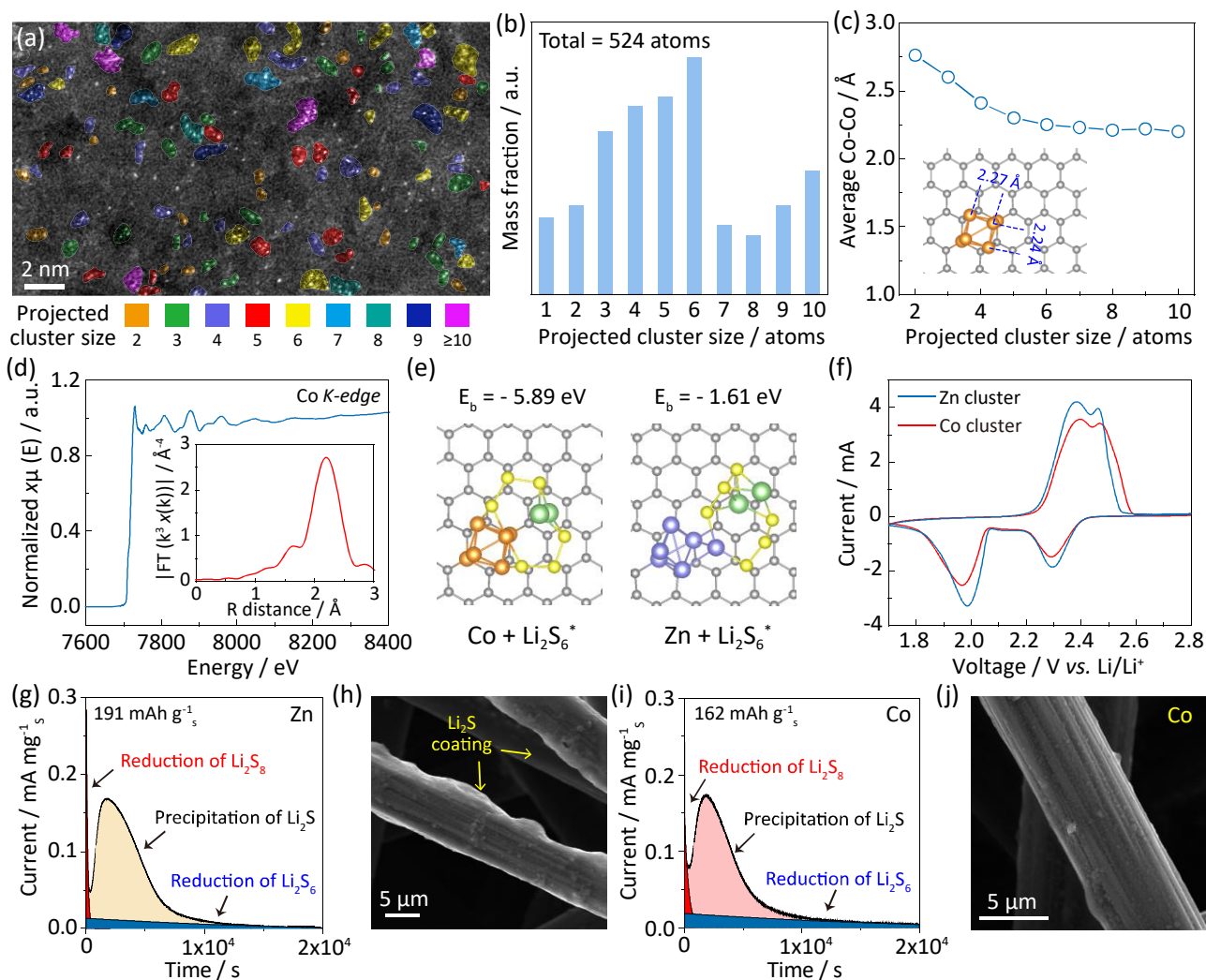
Figure 1 Strong binding energy with low catalytic activity. (a) STEM image of Co clusters on graphene substrate. The colors present the numbers of metal atoms in a cluster; (b) corresponding mass fraction histogram of identified clusters, and (c) average Co−Co distance in these clusters; (d) Synchrotron X-ray adsorption spectra for Co K-edge of Co clusters; (e) Schematic of binding energies for $Li_2S_6^*$ on Co and Zn clusters. Orange, purple, grey, green and yellow-color represent, respectively, Co, Zn, C, Li and S atoms; (f) Cyclic voltammetry curves for assembled Li−S battery with Co and Zn sulfur hosts; (g, i) Potential-static discharge curves for Li_2S deposition on Zn and Co and (h, j) SEM images following Li_2S deposition.

Supplementary Fig. 2. **Fig. 1e** simulates the optimized structures of $Li_2S_6^*$ binding with Co and Zn clusters on graphene substrates. The Co clusters exhibit a significantly greater binding energy of − 5.89 eV compared with that of − 1.61 eV for Zn clusters with $Li_2S_6^*$. Despite the high binding energy for Co clusters, a slower redox kinetic for polysulfide conversion is seen in the lower peak current

density in the cyclic voltammetry curve, **Fig. 1f** and **Supplementary Fig. 3**. Too strong an adsorption restricts polysulfide desorption from the catalyst surface. This restriction results in occupying active sites and lowering conversion kinetics. To test the greater catalytic activity of Zn clusters to regulate Li_2S precipitation, potential-static discharge was carried out by loading Co and Zn clusters on carbon fiber paper.[29] The Zn electrode exhibited a significantly greater Li_2S precipitation capacity of 191 mAh g^{-1} compared with 162 mAh g^{-1} for Co, **Figs. 1g** and **1i**. Increased Li_2S nucleates and precipitates on the Zn surface are seen in the SEM images of **Figs. 1h and 1j**. These findings demonstrate the greater catalytic activity of Zn to convert polysulfides into Li_2S products. Higher adsorption energy with Li_2S_x on Co clusters will not always result in greater SRR activity. Therefore a new determinant instead of adsorption energy is needed to explain SRR activity.

Catalyst design principles. We hypothesize that control of the Gibbs free energy (G) of Li_2S_x on the catalyst surface will impact SRR activity. This is because free energy involves both adsorption energetics and reaction thermodynamics. We extended this to additional $3d$ transition-metal clusters, Fe, Co, Ni, Cu and Zn together with corresponding binary clusters, and interactions with polysulfides in 165 models (**Supplementary Table 1**). Considering amounts of polysulfide intermediates are involved in SRR, it is therefore worth investigating if the free energy of these reaction intermediates is correlated or not. **Fig. 2a** presents the change in Gibbs free energy (ΔG) for $Li_2S_6^*$, $Li_2S_4^*$ and $Li_2S_2^*$ whilst binding with unary and binary clusters. It is seen that ΔG values for $Li_2S_8^*$, $Li_2S_6^*$, $Li_2S_4^*$ and $Li_2S_2^*$ are significantly correlated monotonically with the different metal clusters (**Supplementary Fig. 4**). These linear-relationships arise because all adsorbates bind to the surface through the metal−S bond. A similar linear-relationship is widely established for other electrocatalytic reactions, such as oxygen and nitrogen reduction.[25, 30, 31] The SRR free-energy diagram is plotted based on the main intermediates, $Li_2S_8^*$, $Li_2S_6^*$, $Li_2S_4^*$ and $Li_2S_2^*$ (details in **Computational Section**). ΔG value at equilibrium potential was computed from the sum of DFT-computed energy together with vdW corrections (ΔE), zero-point energy (ΔZPE) and entropy -
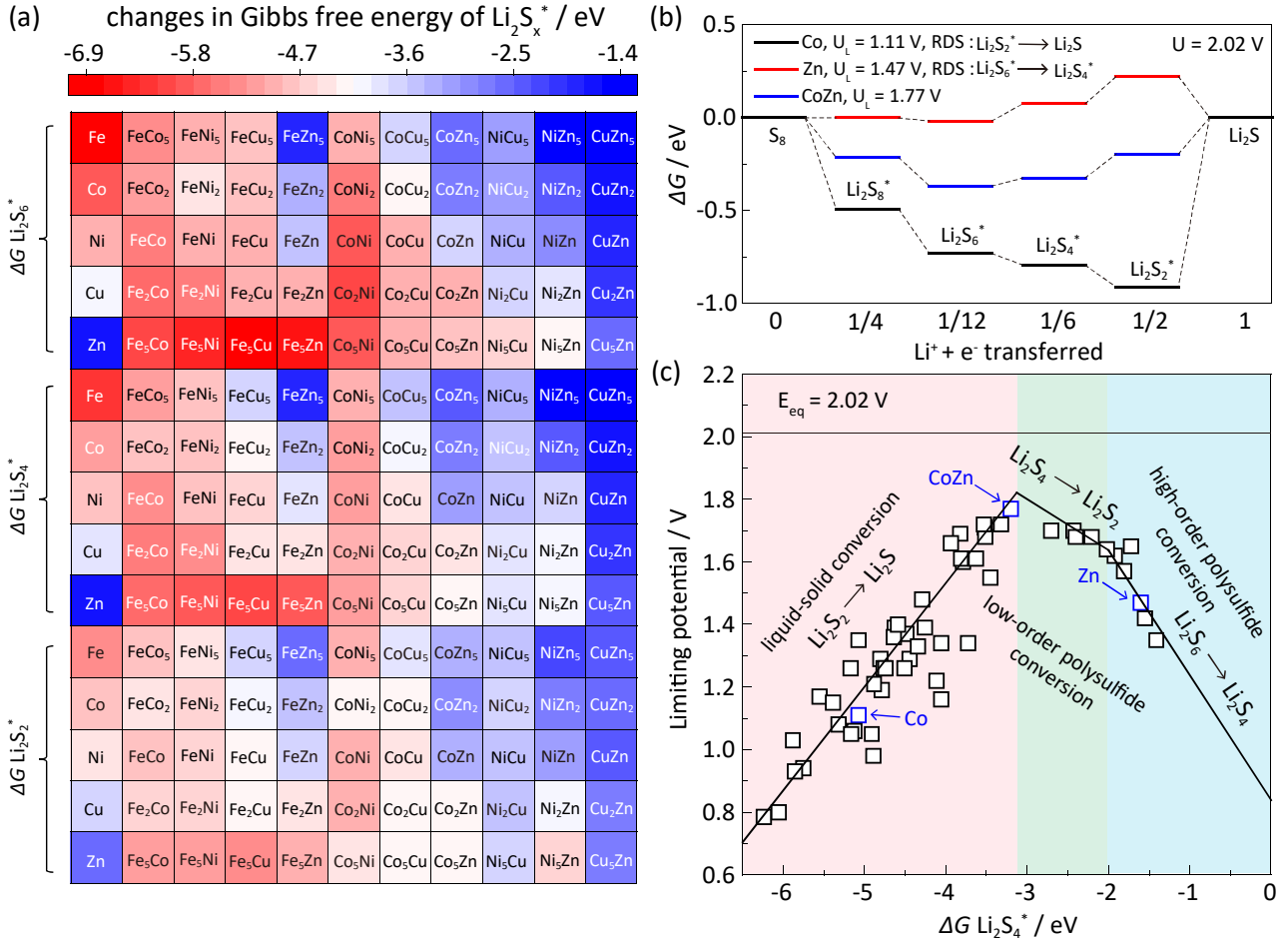
Figure 2 Catalyst design principles. (a) Change in Gibbs free energy (ΔG) for $Li_2S_6^*$, $Li_2S_4^*$ and $Li_2S_2^*$ on surface of Fe, Co, Ni, Cu and Zn-based unary and binary metal clusters; (b) SRR reaction pathways with Co, Zn and CoZn clusters; (c) Relationship between limiting potential and ΔG for $Li_2S_4^*$ for consecutive SRR. Activity trend for cluster catalysts can be identified from three rate-determining steps as is shown by blue, green and pink-color regions.

($T\Delta S$) (**Supplementary Table 2**).[23, 32] The limiting potential (U_L) is defined as the lowest negative potential at which the reaction pathway becomes exergonic,[25] and it is therefore an important parameter to describe the rate-determining step (RDS), and for evaluating intrinsic catalytic activity of any catalyst. A higher limited potential close to equilibrium potential (2.02 V) presents a greater SRR activity. **Fig. 2b** compares the reaction pathways for SRR on Co, Zn and CoZn surfaces (**Supplementary Fig. 5**). CoZn, Zn and Co exhibits U_L values of, respectively, 1.77, 1.47 and 1.11 V. This finding evidences the better SRR performance of Zn over Co clusters, **Fig. 1**. CoZn should, predictively, have the greatest SRR activity because of its significant limiting potential.

Fig. 2c presents the relationship between the limiting potential and ΔG for $Li_2S_4^*$, in which, each of the three-lines indicates one elementary step. Considering the consecutive nature of SRR, the activity trend of **Fig. 2c** is constructed by integrating multiple steps (details in **Supplementary Fig. 6**). The rate-determining steps are liquid-solid ($Li_2S_2^* \rightarrow Li_2S$), low-order polysulfide ($Li_2S_4^* \rightarrow Li_2S_2^*$) and high-order polysulfide ($Li_2S_6^* \rightarrow Li_2S_4^*$) conversions in, respectively, the pink-color, green and blue regions (**Supplementary Fig. 7**). In the pink-color region, the metal clusters bind the intermediates so strongly that desorption of $Li_2S_2^*$ to form Li_2S is restricted, for example, Fe, Co, Ni and corresponding binary clusters. For the right branch (blue-color region), the adsorption of high-order polysulfides ($Li_2S_6^*$) is weak. Therefore the conversion from $Li_2S_6^*$ to $Li_2S_4^*$ is hard to proceed, for example, Zn and CuZn. For design of boosted-catalysts, greater attention needs to be made in reaching the peak in **Fig. 2c**, where ΔG for $Li_2S_4^*$ is ~ -3.1 eV. Maximum SRR activity can be achieved if ΔG of polysulfides is purposefully tuned. It is concluded therefore that SRR activity of a catalyst is significantly effected by the Gibbs free energy of polysulfides on its surface. This must be carefully controlled however to optimize catalytic performance.

SRR activity and reaction kinetics. To experimentally test the activity of these catalysts, we synthesized unary, or binary metal clusters via pyrolyzing metal precursors on graphene substrates, including Fe, Co, Ni, Cu, Zn, CuZn and CoZn, **Fig. 3a** and **Supplementary Fig. 8**. CuZn and CoZn binary clusters were selected because polysulfide intermediates on all of Fe, Co, Ni, Cu and corresponding binary clusters exhibit ultra-high ΔG values, **Fig. 2c** (left branch). Integration of these pure metal clusters with Zn is efficient to tune the free energy of polysulfide intermediates on catalyst surface. The synthesis of these binary metal clusters is highly dependent on intrinsic alloying capability. This is readily deduced from the binary phase diagram, **Fig. 2b**.[33] Some binary clusters can be prepared facilely, including CoZn and CuZn. Some other binary clusters however cannot be synthesized such as FeCo and FeCu (**Supplementary Figs. 9 and 10**). To confirm synthesis of binary metal clusters, synchrotron-based near-edge X-ray adsorption fine structures (NEXAFS) was
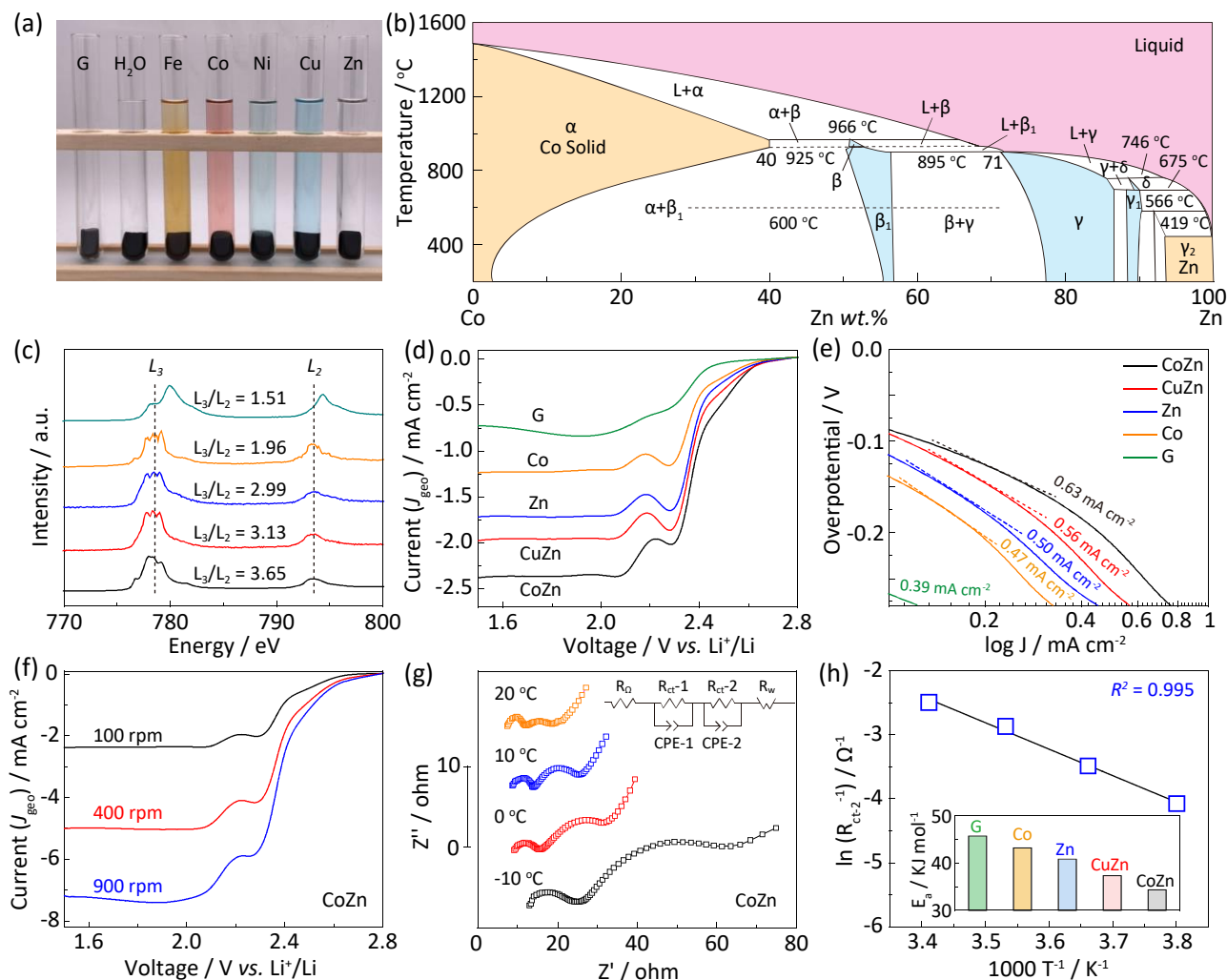
Figure 3 Electrocatalytic SRR activity and reaction kinetics. (a) Digital photograph of synthesis of metal clusters; (b) Binary phase diagrams for Co-Zn alloys. Co and Zn form binary clusters with each other at lower temperature (region in light blue-color region); (c) Co L-edge NEXAFS spectra for Co-foil, CoZn clusters, Co clusters, CoCl₂ and Co₃O₄; (d) LSV curves for CoZn, CuZn, Zn, Co and G at 20 mV s⁻¹ with 100 rpm and (e) corresponding Tafel-plot for determining exchange current density (J_0); (f) LSV curves for Cu-G with varying rotating rate using RDE; (g) EIS-plot for CoZn for varying temperature (h) Arrhenius-plot showing linear relationship between logarithmic value of reciprocal of charge transfer resistance and reciprocal of absolute temperature and activation energy for CoZn, CuZn, Zn, Co and G.

used. **Fig. 3c** shows the Co L-edge NEXAFS spectra for Co clusters and CoZn clusters referenced with Co-foil, CoCl₂ and Co₃O₄. L_3/L_2 peak intensity is reliably used to reveal the interactions between Co and Zn amongst the CoZn binary clusters.[34] A low value for L_3/L_2 confirms a

low-valence for Co. The L_3/L_2 value is 2.99 for Co unary cluster. However this increases to 3.13 for CoZn binary clusters and evidences an efficient electron transfer from Zn to Co, and therefore, the existence of CoZn binary clusters.

Fig. 3d shows the linear sweep voltammetry (LSV) curves for Co, Zn, CuZn and CoZn cluster catalysts together with pristine graphene (G) using a three-electrode system.[1, 3, 35] Different from oxygen reduction reactions, these catalysts exhibit two-step reaction characteristics. This is evident from the first small-peak, and following diffusion-limited current density (J_d). This corresponds to a two-step conversion, respectively, from S_8 to Li_2S_x, and then from Li_2S_x to Li_2S. The value of J_d for CoZn is greatest at ~ 2.37 mA cm^{-2}, confirming its superior catalytic activity. Tafel-plots were extracted from the LSV curves to determine the exchange current density (J_0) (details in **Supplementary Discussion**). As is shown in **Fig. 3e**, J_0 for CoZn is the greatest at 0.63 mA cm^{-2}. This evidences significantly accelerated reaction kinetics (**Supplementary Fig. 11**). Rotating disk electrode (RDE) measurements were made to compute the electron transfer numbers involved in SRR. **Fig. 3f** presents LSV curves for CoZn with rotation rates from 100 to 900 rpm. It is seen in the figure that all curves exhibit diffusion-controlled characteristics with clearly-determined J_d values. As a result, the Koutecky-Levich plot (J_d^{-1} vs $\omega^{-1/2}$) showed excellent linear-scaling. The slope of the curve gives the electron transfer number. CoZn has the highest electron transfer number of 7.8 e$^-$ (**Supplementary Fig. 12**). This finding underscores it driving reduction of S_8 molecules to solid-state products.

Activation energy is an important parameter that reveals the energy barrier to catalysis. It is usually obtained from the Arrhenius-equation.[36, 37] In SRR, the reaction rate is reflected in charge-transfer resistance. This can be obtained by fitting electrochemical impedance spectra (EIS)-plots.[7] EIS is a voltage-dependent characterization, in which applied voltage has a significant impact. Two semi-circles were observed at 2.1 V corresponding to the two-step conversions of polysulfide species (**Supplementary Fig. 13**). The fitted charge-transfer resistances related to the

first and second semi-circle are, respectively, abbreviated as R_{ct-1} and R_{ct-2}. **Fig. 3g** presents the EIS-plots for CoZn at -10, 0, 10 and 20 °C. The temperature-dependent R_{ct} values permit extraction of the activation energy (E_a) via the Arrhenius-equation. Through fitted R_{ct-2} values, CoZn exhibited the lowest activation energy amongst the catalysts of 34.3 kJ mol^{-1}, **Fig. 3h** and **Supplementary Figs. 14 and 15**). This value underscores superior conversion kinetics and catalytic activity. Importantly, these experimentally derived trends coincide with computational results. It is concluded therefore these findings validate our new design principles for SRR catalysts.

Validation of electrocatalytic sulfur reduction via *in-situ* spectra. To validate the high SRR activity of CoZn binary cluster, *in-situ* synchrotron powder X-ray diffraction (XRD) was used to track the dissolution of sulfur and evolution of Li$_2$S.[38-40] Additionally, *in-situ* ultra violet-visible spectroscopy (UV-vis) was carried out to quantify the polysulfide intermediates during SRR.[41]

Fig. 4a depicts the *in-situ* synchrotron powder X-ray diffraction test. This test is highly significantly sensitive in monitoring the minor crystal changes in sulfur and Li$_2$S during SRR. The diffraction peaks at 8.79°, 9.83°, 10.16°, 10.54° and 11.9° are assigned to sulfur, and the peak at 10.3° for Li$_2$S (**Supplementary Fig. 16**). The broad diffraction peak around 10° is due to the graphene substrate (**Fig. 4b**). **Figs. 4c** and **4d** present the time-dependent XRD pattern and discharge curve for sulfur cathode with CoZn cluster catalyst. During SRR the sulfur signal disappears quickly, and the Li$_2$S signal appears significantly earlier, **Figs. 4d** and **4e**. For the sulfur cathode without CoZn catalyst, crystallized sulfur remains for a lengthy period and a delayed Li$_2$S evolution is observed, **Fig. 4e** (lower contour) (**Supplementary Figs. 17 and 18**). This sharp contrast confirms the high activity of CoZn in driving sulfur dissolution and Li$_2$S evolution during SRR.

To quantify the changes in polysulfide intermediates, *in-situ* UV-vis spectra was carried out using a honeycomb working-electrode coupling with Au counter-electrode and organic Ag/Ag$^+$ reference, **Fig. 4f** and **Supplementary Fig. 19**. A linear scanning from −0.75 to −1.5 V was used to electrochemically drive the SRR (**Supplementary Fig. 20**). With CoZn catalyst, the polysulfide

peaks S_4^{2-} and S_6^{2-} appear gradually, followed by disappearance at lower voltage, **Fig. 4g**. This is
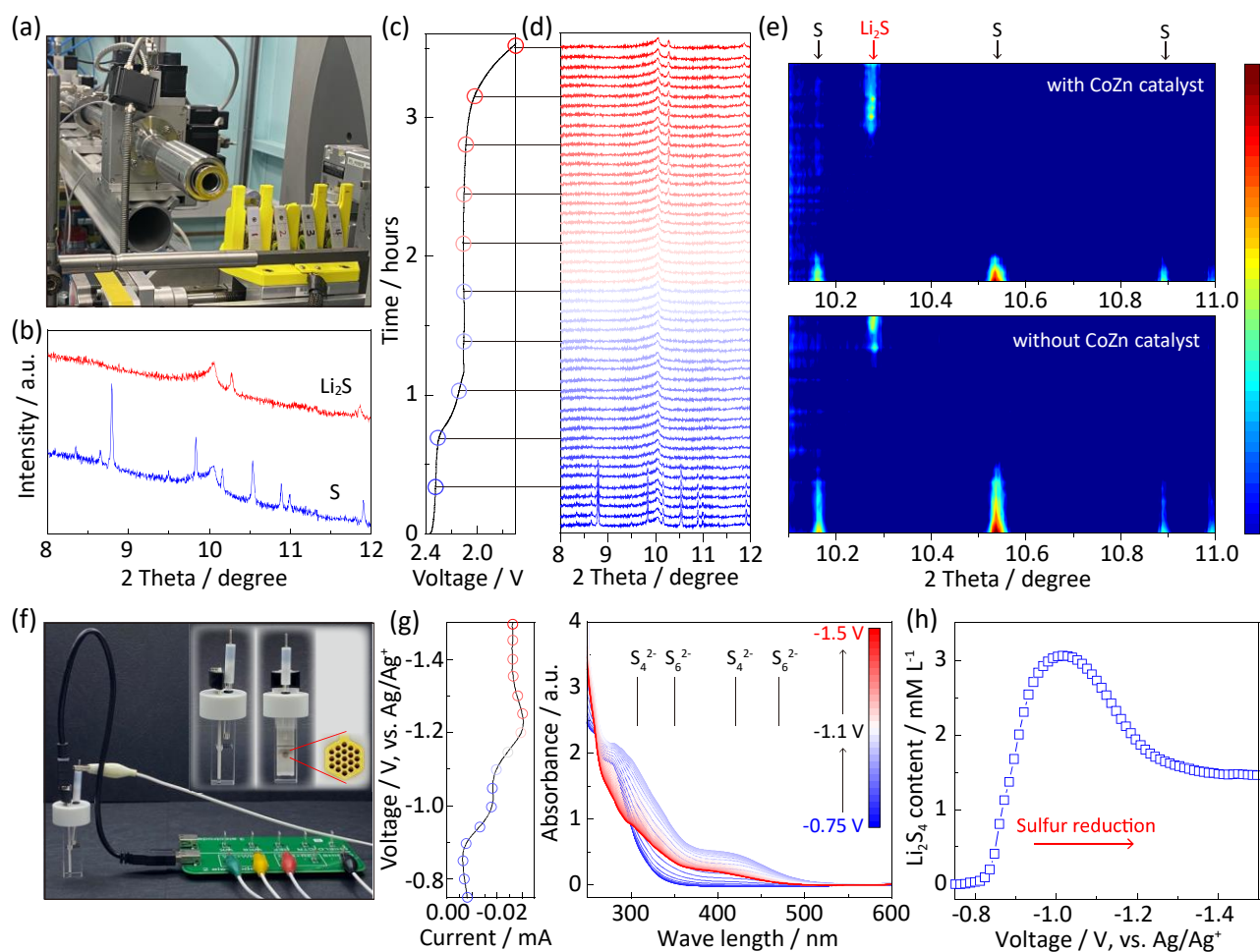
Figure 4 Validation of electrocatalytic sulfur reduction via *in-situ* spectra. (a) Digital photograph of *in-situ* synchrotron powder X-ray diffraction test; (b) Characteristic peaks for sulfur and Li_2S; (c) Galvanostatic discharge curve for sulfur cathode with CoZn catalyst during SRR; (d) Real-time stacked X-ray diffraction plots; (e) Contour patterns for sulfur cathode with/without CoZn catalyst; (f) Digital photograph of cell for *in-situ* UV-vis test; (g) LSV curve and corresponding stacked UV-vis plot; (h) Change in Li_2S_4 concentration during SRR.

because of the conversion from sulfur to soluble polysulfides, and subsequent reduction from polysulfides to Li_2S. As a result the maximum concentration of Li_2S_4 is 3 mmol L^{-1}, **Fig. 4h** and **Supplementary Figs. 21-24**. The weaker peaks without CoZn catalyst evidence a significantly lower concentration of polysulfides and, additionally, limited ability to drive further reduction from polysulfides to Li_2S. This is evidenced by the unchanged polysulfide concentrations (**Supplementary Figs. 25** and **26**).

Activity origin and reactivity trend. A present shortcoming in understanding SRR is a lack of any correlation between activity and intrinsic properties. It was considered essential therefore to determine activity origin of the metal clusters, and to establish the reactivity trend to guide catalyst design.

Fig. 5a presents the projected density of states (PDOS) for metal $3d$-orbital of the plane catalysts (Left, blue-color filling), and following $Li_2S_4^*$ adsorption (Right, red-color filling) (**Supplementary Fig. 27**). The $3d$-electron states of these metal clusters exhibit significant change following polysulfide adsorption. This finding highlights that the metal $3d$-orbital electrons are responsible for polysulfide interaction (**Supplementary Figs. 28 and 29**). To experimentally characterize the interaction between metal clusters and polysulfides, the synchrotron Co K-edge extended X-ray absorption fine structure (EXAFS) was used to confirm metal−sulfur bond by comparing pristine Co clusters with that soaked in a concentrated polysulfide solutions.[42] As shown in the R-space plots, **Fig. 5b**, Co clusters in polysulfides presents a clear peak shift compared with pristine Co clusters. The Co−S scattering length is ~ 1.9 Å whilst the Co−Co scattering in pristine Co clusters ~ 2.2 Å. As is seen in **Fig. 5c**, the wavelet transforms (WT) EXAFS oscillations underscores the Co−S bond between cluster catalyst and polysufides.

The catalytic activity of a material is determined fundamentally by its electronic structure. Therefore it is important to correlate one determinant related to metal $3d$-orbital with the Gibbs free energy of polysulfides, and apparent SRR activity.[43] To investigate the reactivity trend, several DOS-based descriptors for each metal cluster model was plotted against ΔG for $Li_2S_4^*$ (**Supplementary Fig. 30**).[24] As is shown in **Fig. 5d**, the $3d$-orbital charges show overall best-linear fit for all models. The interpretation of this relationship is that for a given metal catalyst, the smaller $3d$-orbital charge indicates stronger binding and greater Gibbs free energy of polysulfides. Because polysulfides are negatively charged, the S $3p$-orbital electrons tend to donate to the unoccupied $3d$-orbital of those metal clusters. This forms a strong metal−sulfur bond e.g. Co (**Fig. 5e**). In
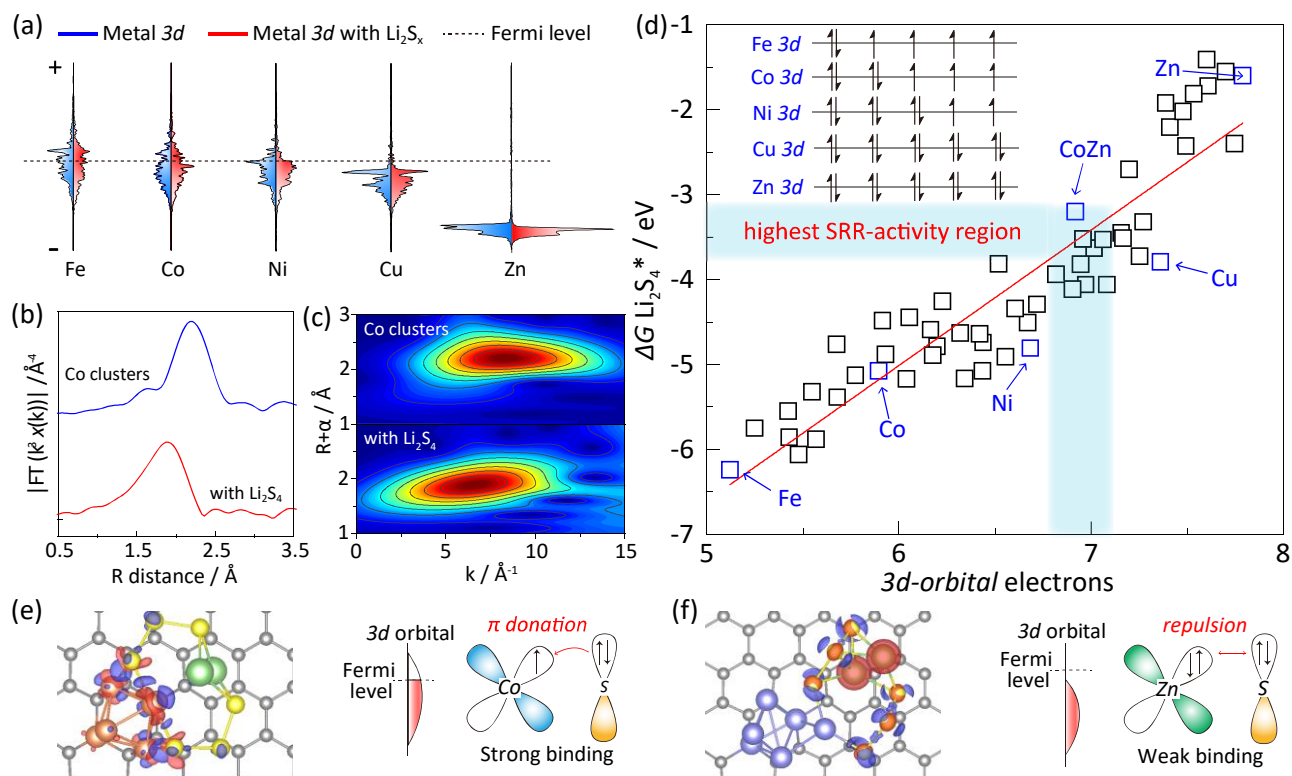
Figure 5 Activity origin and reactivity trend. (a) PDOS for metal *3d*-orbital before (blue-color pattern) and after (red pattern) $Li_2S_4^*$ adsorption; (b) EXAFS R-space plot for Co clusters with/without polysulfide adsorption; and (c) corresponding WT-transformed oscillations; (d) Fitted linear-relationship between change of free energy for $Li_2S_4^*$ and number of *3d*-orbital electrons for different metal clusters; Charge-transfer models (purple-color denotes electron accumulation and red, electron depletion) and schematic for effect of *3d*-orbital charges on free energy of (e) Co and (f) Zn.

contrast, more *3d*-orbital electrons in metal clusters will repulse the S *3p*-orbital of polysulfides. This leads to weak binding e.g. Zn. It is concluded therefore the *3d*-orbital charges are a significant determinant to correlate with Gibbs free energy of polysulfides and SRR activity. This quantitative correlation provides a comprehensive understanding of the impact of intrinsic property of catalysts on performance. The *3d*-orbital charges need to be precisely controlled for optimal catalysts, because this governs the Gibbs free energy of polysulfides and therefore SRR activity.

How high SRR activity benefits battery performance. To confirm the effect of SRR activity on battery performance, Li−S batteries with different catalysts were assembled and comparatively tested.[44-49] **Figs. 6a** and **6b** present the galvanostatic charge-discharge curves for Li−S batteries with

CoZn, CuZn, Zn, Cu, Ni, Co and Fe catalysts. There was no significant difference in specific capacity at low current rate with low sulfur loading, 0.2 C and 0.5 mg cm^{-2}, **Fig. 6a**. However there was significant dependence of capacity with different catalysts at a high current rate with high areal sulfur loading, 1 C and 5 mg cm^{-2}, **Fig. 6b**, **Supplementary Figs. 31-33**). The voltage hysteresis, defined as the subtraction between the charge and discharge voltage plateau, reflects well the activity difference of catalysts in batteries. Apparent changes in voltage hysteresis can also be identified at 1 C current rate with 5 mg cm^{-2} sulfur loadings, **Fig. 6c**. This evidences that a better SRR catalyst contributes to higher specific capacity and lower charge-discharge overpotential in Li−S batteries.[44-48]

Fig. 6d summarizes the relationship between the exchange current density of SRR and the specific capacities. The capacity increases with higher J_0 values as is expected. It is seen in the figure
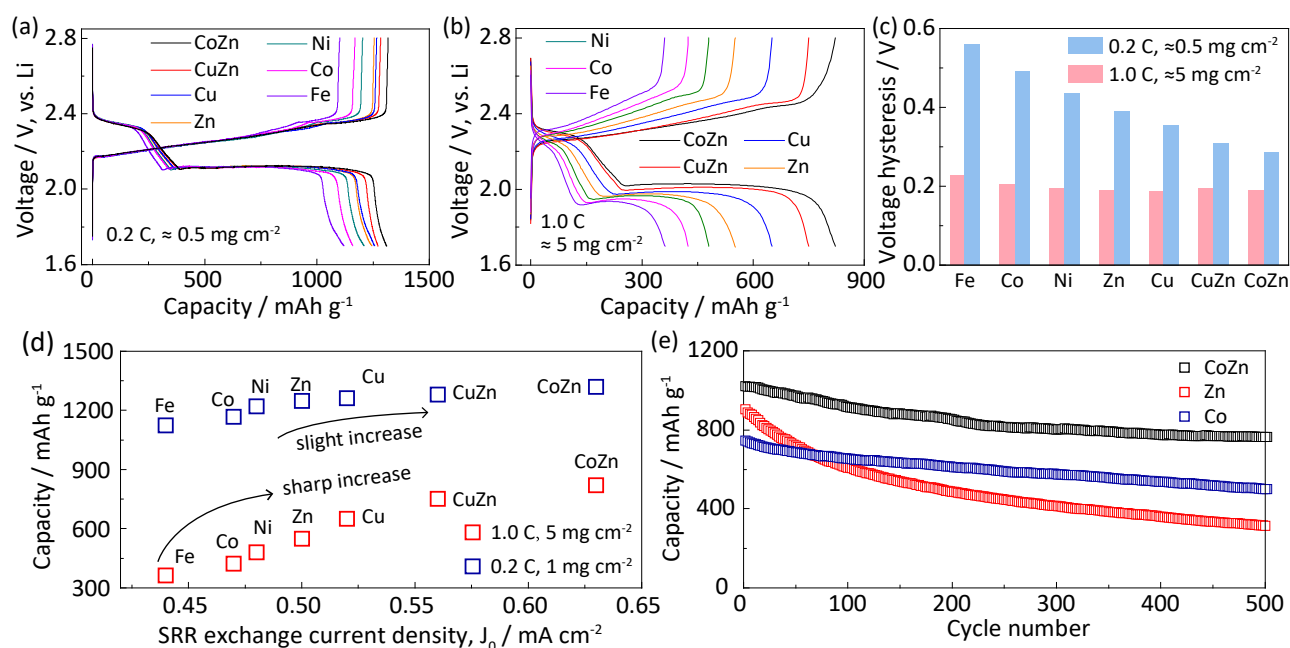
Figure 6 SRR catalysts for Li−S battery. Charge-discharge curves for Li−S batteries with CoZn, CuZn, Zn, Cu, Ni, Co and Fe catalyst at (a) 0.2 C current rate with 0.5 mg cm^{-2} areal sulfur loading; and (b) 1 C current rate with 5 mg cm^{-2} areal sulfur loading; (c) Voltage hysteresis comparison for different SRR catalysts; (d) Relationship between SRR exchange current density and specific capacity of sulfur cathode in Li−S battery; (e) Cycling performance at 1.0 C and 0.5 mg cm^{-2} of Li−S batteries with CoZn, Zn and Co catalysts.

that there is a significant increment with high current rate and high areal sulfur loading (red points of **Fig. 6d**). It can be concluded therefore that catalysts with high SRR activity largely benefit the battery performance, especially at higher current rate with high sulfur loadings. This is because of boosted sulfur utilization and conversion kinetics with catalysts. Then, we would like to discuss the effect of SRR activity on the cycling performance of Li−S batteries. It is found that the capacity retention is impacted by binding strength of metal catalysts with polysulfides. For example, despite the lowest SRR activity of the Co clusters, it exhibits excellent capacity retention of 67.2 % following 500 cycles. The Zn clusters with the weakest binding therefore exhibit poor cyclic stability, with just 35.3 % capacity retention following 500 cycles, **Fig. 6e**. This finding is attributed to the concentration-gradient driving of polysulfide shuttle effect. A stronger binding with polysulfides confines these to the cathode part, thereby resulting in a better cycling stability (**Supplementary Fig. 34**). The battery with CoZn catalyst exhibited both high specific capacity and excellent cyclic stability with just ~ 0.05 % capacity decay per cycle following 500 cycles (**Supplementary Fig. 35**). Importantly, the specific capacity, high-rate capacity retention and the cycling performance of Li−S batteries with CoZn catalysts outperform most–reported SRR catalysts as is demonstrated in the comparative summary of **Table S3**. Findings therefore evidence the practical benefits of an improved rational design of SRR catalyst to boost performance of Li−S batteries.

Conclusions

We have for the first time, formulated the design principles to rationally optimize SRR activity via controlling the Gibbs free energy of polysulfide species on the catalysts surface. SRR activity and its origin have been confirmed via series of electrochemical testing, theoretical computations, synchrotron-based analyses and *in-situ* spectroscopy. As a result, SRR reactivity trend is established by quantitatively correlating with *3d*-orbital charges of transition-metal clusters, Gibbs free energies of polysulfides and SRR catalytic activity. Optimized SRR catalyst significantly boosts battery performance, especially at high charge-discharge rate with high areal sulfur loadings. The

well-established relationship between apparent SRR activity, reaction thermodynamics and intrinsic electronic structure of materials, will benefit the understanding of SRR mechanism. Findings are therefore a significant conceptual advance that will be of immediate benefit in improved catalyst design for sulfur reduction electrocatalysis in metal−sulfur batteries.

Methods

Synthesis of metal-cluster catalysts. Graphite oxide (GO) was synthesized via modified Hummer's method. Typically, 20 mg GO was ultrasonicated in 20 mL deionized water for 2 h (1 mg mL^{-1}). 40 mg L-ascorbic acid sodium-salt was added to the GO suspension together with continuous stirring. The suspension was transferred to a glass vial and heated at 70 ^{o}C for 10 h to obtain a graphene hydrogel. This was washed with deionized water to remove sodium-salt. 3D graphene hydrogel was soaked in 20 mL solution containing 158 mg cobalt chloride (CoCl$_2$·6H$_2$O) for 24 h. The graphene hydrogel was freeze-dried overnight and heat treated at 600 ^{o}C in 5 vol.% H$_2$/Ar for 1.5 h. The mixture was washed with diluted hydrochloric acid (HCl), diluted nitric acid (HNO$_3$) and deionized water to remove larger particles. Synthesis of other metal clusters follows the same procedure with the same molar concentration (0.66 mmol) of the metal-chloride precursors, FeCl$_3$, NiCl$_2$, CuCl$_2$ and ZnCl$_2$. The binary metal cluster, e.g. CoZn was prepared by soaking the 3D graphene hydrogel in a mixed solution containing 0.33 mmol CoCl$_2$ and 0.33 mmol ZnCl$_2$. The same procedure was applied to synthesize other binary clusters such as CuZn.

Structural characterization. The morphology and structure of samples was characterized by scanning electron microscopy (SEM, Hitachi S4800, Japan). High-resolution STEM images were obtained under a Cs-corrected STEM (FEI Titan Cubed Themis G2 300) operated at 300 kV. Ultraviolet/visible (UV-vis) was carried out using a spectrometer (SHIMADZU UV-2600). X-ray diffraction (XRD) data were collected on a Rigaku Mini Flex 600 X-Ray Diffractometer. X-ray photoelectron spectra (XPS) was conducted with soft-X ray beamlines at the Australian Synchrotron (Clayton), part of ANSTO. The synchrotron-based near-edged X-ray absorption fine structure (NEXAFS) of Co L-edge was performed on the soft X-ray spectroscopy beamline at AS. The synchrotron-based X-ray absorption fine structure (XAFS) of Co K-edge was performed on the X-ray absorption beamline at AS. *In-situ* synchrotron XRD data were collected on the powder diffraction (PD) beamline at the Australian Synchrotron with a wavelength of 0.7903 Å. Data were collected continuously at 30 s intervals.

Electrochemical tests. For Li−S battery testing, the sulfur cathode was prepared by mixing 80 wt.%

S with 20 wt.% catalyst under 155 $^{\circ}$C for 12 h. The catalyst/S mixture was ball-milled with LA133 binder with a mass ratio 90:10. Total sulfur content in the cathode was 72 wt.%. Li−S batteries were assembled with CR2032 coin-cell in an Ar-filled glove box by coupling the Li-metal anode with 1 mol L^{-1} Bis(trifluoromethane)sulfonimide lithium salt (LiTfSi) in 1,3-Dioxolane (DOL)/1,2-Dimethoxyethane (DME) (1:1 volume ratio) with 0.2 mol L^{-1} LiNO$_3$ as the electrolyte. CV measurement was carried out from 1.7 to 2.8 V with a scan rate of 0.2 mV s^{-1}. For electrochemical testing of Li−S batteries including, rate and cycling performance, the batteries were galvanostatically charged and discharged at selected current rates (1C = 1675 mAh g^{-1}) and cycles.

For the Li$_2$S nucleation tests, the coin-cell was galvanostatically discharged to 2.06 V at 0.0785 mA, and then potentiostatically discharged at 2.02 V until the current was $< 10^{-5}$ A. In assembly of cells for Li$_2$S nucleation testing, the Li$_2$S$_8$ solution was prepared by combining nano-sulfur and Li$_2$S powder in a molar ratio of 7:1 in tetraglyme under vigorous stirring for 24 h. Carbon-fiber paper (CP) disks with a diameter of 12 mm were used as the substrates to load Co and Zn with 1 mg cm^{-2} to assemble the coin-cells. Li-foil was used as the counter electrode. 25 µL Li$_2$S$_8$ (0.25 mol L^{-1}) catholyte was added on the cathode and 20 µL blank electrolyte on the anode.

Electrocatalytic SRR activity was tested using a SP150 electrochemical workstation (Biologic Instruments) coupled with RDE technique (Pine Research Instrumentation). The three-electrode cell was sealed in an Ar-filled glovebox. RDE loaded with catalyst was used as working electrode, and two (2) pieces of Li-foil were used as, respectively, counter electrode and reference electrode. 2 mg catalyst was sonicated in 1 mL ethanol (Analytical Reagent) with 20 µl 5 wt.% Nafion solution to form a uniform catalyst-ink. 10 µL ink was drop-cast onto a freshly-polished glassy-carbon electrode of 0.196 cm^2. Electrolyte solution used for SRR tests was 4 mmol S$_8$ molecules dissolved in blank-electrolyte, 1 mol L^{-1} LiTFSI in DOL/DME. The catalyst film-electrode was activated in the blank electrolyte via cyclic voltammetry from 3.1 to 3.0 V. Linear sweep voltammetry (LSV) curves were recorded with a scan rate of 20 mV s^{-1} from 3.0 to 1.5 V at varying rates from 100 to 1600 rpm.

The temperature-dependant electrochemical impedance spectra (EIS) were obtained using the Li−S coin-cells in which both Li-metal anode and electrolyte were overloaded. The batteries were placed in an incubator with controlled temperature ranging from -10 to 30 $^{\circ}$C. The EIS tests were carried out with IVIUM workstation (Netherlands) at a frequency range of 100 kHz to 1 mHz.

Model optimization. Computations for this work were carried out using density functional theory (DFT) as implemented in VASP code. Electronic exchange-correlation energy was modeled using the Perdew-Burke-Ernzerhof (PBE) function within a generalized gradient approximation (GGA). The projector-augmented wave (PAW) method was used to describe the ionic cores. For the plane-wave

expansion a 450 eV kinetic energy cut-off was used following testing a series of different cut-off energies. A Monkhorst-Pack 2×2×1 k-point grid was used to sample the Brillouin zone. Convergence criterion for the electronic structure iteration was set to 10^{-4} eV, and that for geometry optimizations was 0.01 eV Å^{-1} on force. A Gaussian smearing of 0.1 eV was applied during geometry optimization and for total energy computations.

Computation of binding energy. Binding energy (E_b) in Fig. 1e was computed by subtracting the energy of substrate and absorbed molecular with the energy of whole system. For example, for $Li_2S_4^*$ on Co the binding energy is computed as follows:

$$E_b = E\,(Co+Li_2S_4) - E\,(Li_2S_4^*) - E\,(Co) \tag{1}$$

where $E\,(Co+Li_2S_4^*)$ is the DFT-based total energy of Li_2S_4 on Co, eV, $E\,(Li_2S_4^*)$ the energy of individual $Li_2S_4^*$ in the same supercell, eV, and $E\,(Co)$ the energy of Co, eV. A more negative value means stronger binding interaction.

Construction of SRR reaction pathway. In SRR S_8 is the reactant and Li_2S is product. To construct the reaction pathway the overall equilibrium potential from S_8 to Li_2S is computed because the equilibrium potential determines the initial and final energy states of SRR. The overall reaction is:

$$1/8\ S_8 + 2\ (Li^+ + e^-)\ \rightarrow\ Li_2S \tag{2}$$

It is necessary to solve for the energy of Li^++e^-. Given the definition for computational hydrogen electrode (CHE) proposed by Nørskov et al.[50] the potential at which a solvated Li^+ ion and an electron (e^-) in the electrode are in equilibrium with bulk $Li_{(s)}$ was set to zero, namely:

$$Li_{(s)} \rightarrow Li^+ + e^- \qquad \Delta G = 0\ eV\ at\ U = 0\ V \tag{3}$$
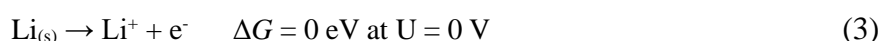
In this the free energy of a Li^++e^- pair at 0 V is defined as equal to the free energy of a single Li atom with a Li^+ concentration of 1 mol L^{-1}. This accords with other reports.[51] The equilibrium potential is therefore computed by the change in Gibbs free energy (ΔG) of S_8, (Li^++e^-) pair, and Li_2S crystal, as follows:

$$\Delta G = \Delta E + \Delta E_{ZPE} - T\Delta S \tag{4}$$

$$U_{eq} = \Delta G\,/\,e \tag{5}$$

where ΔE is the electronic energy difference obtained by DFT computation, ΔE_{ZPE} the change in zero-point energy (ZPE), T room temperature (298.15 K), and ΔS entropy change. ZPE and vibrational entropy of adsorbed species were obtained following frequency computations as is shown in **Supplementary Table 2**. During vibration analysis for intermediate states frequencies were computed by treating all 3N degrees of the adsorbates as vibrational in the harmonic oscillator approximation. U_{eq} is equilibrium potential computed as 2.02 V. This value is in very good

agreement with the experimental value in Li−S batteries.

Three lithium polysulfide intermediates, $Li_2S_8{}^*$, $Li_2S_6{}^*$ and $Li_2S_4{}^*$, are the commonly-accepted discharge products in Li−S chemistry.[1, 5] The specific reactions at each step are:

$$1/8 \ S_8 + 2 \ (Li^+ + e^-) \ \rightarrow \ 1/8 \ Li_2S_8{}^* + 7/4 \ (Li^+ + e^-) \tag{6a}$$

$$1/8 \ Li_2S_8{}^* + 7/4 \ (Li^+ + e^-) \ \rightarrow \ 1/6 \ Li_2S_6{}^* + 5/3 \ (Li^+ + e^-) \tag{6b}$$

$$1/6 \ Li_2S_6{}^* + 5/3 \ (Li^+ + e^-) \ \rightarrow \ 1/4 \ Li_2S_4{}^* + 3/2 \ (Li^+ + e^-) \tag{6c}$$

$$1/4 \ Li_2S_4{}^* + 3/2 \ (Li^+ + e^-) \ \rightarrow \ Li_2S \tag{6d}$$
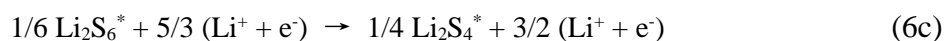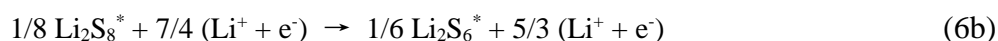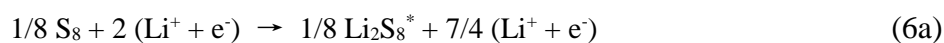
The free energy of each intermediate is a function of electrode potential. The free energy of an electron is assumed linearly-dependent on the electrode potential and shifted by −eU at a applied potential, U:

$$\Delta G(U) = \Delta G(0 \ V) - neU \tag{7}$$

ΔG(U) is the free energy introduced by changing electrode potential. The change of free energy at each step can be computed as follows:

$$\Delta G = \Delta E + \Delta E_{ZPE} - T\Delta S + \Delta G(U) \tag{8}$$

Data availability

Data supporting findings from this work are available within the article and Supplementary Information files. All other relevant data supporting findings are available from the corresponding author on request.

References

1   Peng, L. *et al.* A fundamental look at electrocatalytic sulfur reduction reaction. *Nat. Catal.* **3**, 762-770 (2020).

2   Zhao, C. *et al.* A high-energy and long-cycling lithium–sulfur pouch cell via a macroporous catalytic cathode with double-end binding sites. *Nat. Nanotech.* **16**, 166-173 (2020).

3   Zhao, C. X. *et al.* Semi-immobilized molecular electrocatalysts for high-performance lithium-sulfur batteries. *J. Am. Chem. Soc.* **143**, 19865-19872 (2021).

4   Zhou, G., Chen, H. & Cui, Y. Formulating energy density for designing practical lithium–sulfur batteries. *Nat. Energy* **7**, 312-319 (2022).

5   Li, G., Chen, Z. & Lu, J. Lithium–sulfur batteries for commercial applications. *Chem* **4**, 3-7 (2018).

6   Manthiram, A., Fu, Y., Chung, S. H., Zu, C. & Su, Y. S. Rechargeable lithium–sulfur batteries. *Chem. Rev.* **114**, 11751-11787 (2014).

7   Fang, R. *et al.* More reliable lithium–sulfur batteries: status, solutions and prospects. *Adv. Mater.* **29**, 1606823 (2017).

8   Pang, Q., Liang, X., Kwok, C. Y. & Nazar, L. F. Advances in lithium–sulfur batteries based on multifunctional cathodes and electrolytes. *Nat. Energy* **1**, 16132 (2016).

9   Tikekar, M. D., Choudhury, S., Tu, Z. Y. & Archer, L. A. Design principles for electrolytes and interfaces for stable lithium–metal batteries. *Nat. Energy* **1**, 16114-16120 (2016).

10   Yang, X., Luo, J. & Sun, X. Towards high-performance solid-state Li–S batteries: from fundamental understanding to engineering design. *Chem. Soc. Rev.* **49**, 2140-2195 (2020).

11   Yang, Y. *et al.* Electrocatalysis in lithium sulfur batteries under lean electrolyte conditions. *Angew. Chem. Int. Ed.* **57**, 15549-15552 (2018).

12   Song, Y. *et al.* Rationalizing electrocatalysis of Li–S chemistry by mediator design: progress and prospects. *Adv. Energy Mater.* **10**, 1901075 (2019).

13   Hua, W. *et al.* Selective catalysis remedies polysulfide shuttling in lithium–sulfur batteries. *Adv. Mater.* **33**, 2101006 (2021).

14   Zhong, Y. R. *et al.* Surface chemistry in cobalt phosphide-stabilized lithium–sulfur batteries. *J. Am. Chem. Soc.* **140**, 1455-1459 (2018).

15   Xue, W. *et al.* Intercalation-conversion hybrid cathodes enabling Li–S full-cell architectures with jointly superior gravimetric and volumetric energy densities. *Nat. Energy* **4**, 374-382 (2019).

16   Du, Z. *et al.* Cobalt in nitrogen-doped graphene as single-atom catalyst for high-sulfur content lithium–sulfur batteries. *J. Am. Chem. Soc.* **141**, 3977-3985 (2019).

17   Zhou, G. *et al.* Catalytic oxidation of Li_2S on the surface of metal sulfides for Li–S batteries. *Proc. Natl. Acad. Sci. U. S. A.* **114**, 840-845 (2017).

18   Seh, Z. W. *et al.* Combining theory and experiment in electrocatalysis: Insights into materials design. *Science* **355**, eaad4998 (2017).

19   Ross, M. B. *et al.* Designing materials for electrochemical carbon dioxide recycling. *Nat. Catal.* **2**, 648-658 (2019).

20   Seo, D. H. *et al.* The structural and chemical origin of the oxygen redox activity in layered and cation-disordered Li-excess cathode materials. *Nat. Chem.* **8**, 692-697 (2016).

21   Hwang, J. *et al.* Perovskites in catalysis and electrocatalysis. *Science* **358**, 751-756 (2017).

22   Tian, X. *et al.* Engineering bunched Pt-Ni alloy nanocages for efficient oxygen reduction in practical fuel cells. *Science* **366**, 850-856 (2019).

23   Jiao, Y., Zheng, Y., Jaroniec, M. & Qiao, S. Z. Design of electrocatalysts for oxygen- and hydrogen-involving energy conversion reactions. *Chem. Soc. Rev.* **44**, 2060-2086 (2015).

24   Jiao, Y., Zheng, Y., Davey, K. & Qiao, S.-Z. Activity origin and catalyst design principles for

electrocatalytic hydrogen evolution on heteroatom-doped graphene. *Nat. Energy* **1**, 16130 (2016).

25 Kulkarni, A., Siahrostami, S., Patel, A. & Norskov, J. K. Understanding catalytic activity trends in the oxygen reduction reaction. *Chem. Rev.* **118**, 2302-2312 (2018).

26 Qiao, Y., Jiang, K., Deng, H. & Zhou, H. A high-energy-density and long-life lithium-ion battery via reversible oxide–peroxide conversion. *Nat. Catal.* **2**, 1035-1044 (2019).

27 Sultan, S. *et al.* Single atoms and clusters based nanomaterials for hydrogen evolution, oxygen evolution reactions, and Full Water Splitting. *Adv. Energy Mater.* **9**, 1900624 (2019).

28 Liu, L. & Corma, A. Metal catalysts for heterogeneous catalysis: From single atoms to nanoclusters and nanoparticles. *Chem. Rev.* **118**, 4981-5079 (2018).

29 Fan, F. Y., Carter, W. C. & Chiang, Y. M. Mechanism and kinetics of Li_2S precipitation in lithium–sulfur batteries. *Adv. Mater.* **27**, 5203-5209 (2015).

30 Liu, X., Jiao, Y., Zheng, Y., Davey, K. & Qiao, S.-Z. A computational study on Pt and Ru dimers supported on graphene for the hydrogen evolution reaction: new insight into the alkaline mechanism. *J. Mater. Chem. A* **7**, 3648-3654 (2019).

31 Liu, X., Jiao, Y., Zheng, Y., Jaroniec, M. & Qiao, S. Z. Building up a picture of the electrocatalytic nitrogen reduction activity of transition metal single-atom catalysts. *J. Am. Chem. Soc.* **141**, 9664-9672 (2019).

32 Wang, L. *et al.* Design rules of a sulfur redox electrocatalyst for lithium–sulfur batteries. *Adv. Mater.* **34**, e2110279 (2022).

33 Massalski, T. B. O., H. Binary Alloy Phase Diagrams. *ASM International* (1990).

34 Kurata, H. & Colliex, C. Electron-energy-loss core-edge structures in manganese oxides. *Phys. Rev. B Condens Matter.* **48**, 2102-2108 (1993).

35 Lu, Y.-C., He, Q. & Gasteiger, H. A. Probing the lithium–sulfur redox reactions: A rotating-ring disk electrode study. *J. Phy. Chem. C* **118**, 5733-5741 (2014).

36 Li, Y. *et al.* Enabling high-areal-capacity lithium–sulfur batteries: designing anisotropic and low-tortuosity porous architectures. *ACS Nano* **11**, 4801-4807 (2017).

37 Shen, Z. *et al.* Rational design of a $Ni_3N_{0.85}$ electrocatalyst to accelerate polysulfide conversion in lithium–sulfur Batteries. *ACS Nano* **14**, 6673-6682 (2020).

38 Li, H. *et al.* Reversible electrochemical oxidation of sulfur in ionic liquid for high-voltage Al−S batteries. *Nat. Commun.* **12**, 5714 (2021).

39 Conder, J. *et al.* Direct observation of lithium polysulfides in lithium–sulfur batteries using operando X-ray diffraction. *Nat. Energy* **2**, 17069 (2017).

40 Li, H. *et al.* Revealing principles for design of lean-electrolyte lithium metal anode via in-situ spectroscopy. *J. Am. Chem. Soc.* **142**, 2012-2022 (2020).

41 Zou, Q. & Lu, Y. C. Solvent-dictated lithium sulfur redox reactions: an operando UV-vis spectroscopic study. *J. Phys. Chem. Lett.* **7**, 1518-1525 (2016).

42 Lin, F. *et al.* Synchrotron X-ray analytical techniques for studying materials electrochemistry in rechargeable batteries. *Chem. Rev.* **117**, 13123-13186 (2017).

43 Zhu, X. *et al.* Optimising surface *d* charge of AuPd nanoalloy catalysts for enhanced catalytic activity. *Nat. Commun.* **10**, 1428 (2019).

44 Liu, J. *et al.* Pathways for practical high-energy long-cycling lithium metal batteries. *Nat. Energy* **4**, 180-186 (2019).

45 Li, G. *et al.* Stringed "tube on cube" nanohybrids as compact cathode matrix for high-loading and lean-electrolyte lithium–sulfur batteries. *Energy Environ. Sci.* **11**, 2372-2381 (2018).

46 Jiao, S. *et al.* Stable cycling of high-voltage lithium metal batteries in ether electrolytes. *Nat. Energy* **3**, 739-746 (2018).

47 Gao, Y. *et al.* Polymer-inorganic solid-electrolyte interphase for stable lithium metal batteries under lean electrolyte conditions. *Nat. Mater.* **18**, 384-389 (2019).

48 Luo, C. *et al.* A chemically stabilized sulfur cathode for lean electrolyte lithium sulfur batteries. *Proc. Natl. Acad. Sci. U. S. A.* **117**, 14712-14720 (2020).

49 Niu, C. *et al.* Self-smoothing anode for achieving high-energy lithium metal batteries under realistic conditions. *Nat. Nanotech.* **14**, 594-601 (2019).

50 Norskov, J. K. *et al.* Origin of the overpotential for oxygen reduction at a fuel-cell cathode. *J. Phy. Chem. B* **108**, 17886-17892 (2004).

51 Xu, Y. & Shelton, W. A. O_2 reduction by lithium on Au(111) and Pt(111). *J. Chem. Phy.* **133**, 024703 (2010).

Acknowledgements

Author contributions

S.-Z. Q. conceived and supervised this research; H. L. designed and carried out experiments and DFT computations; R. M. carried out the synthesis of binary clusters and RDE electrochemical tests;

Y. J., assisted with DFT computations; W. H. tested Li−S battery performance; X. C. captured STEM images; C. Y. assisted with design of sulfur cathode; F. X. assisted with XAS data and fitting of EXAFS; Q. G. assisted with the *in-situ* synchrotron X-ray diffraction tests; A. T. assisted with the NEXAFS tests and related data analyses; B. J. carried out the XAS test and related data analyses; Q. Y. provided experimental conditions for H. L. during COVID-19 period in China; S.-Z. Q. and K. D. revised the manuscript. All authors discussed results and commented on the manuscript.

Competing interests

The authors declare no competing financial interests.

Additional information

Supplementary Information is available for this paper at http://www.nature.com/XXX

Correspondence and requests for materials should be addressed to S.Z. Q.

Reprints and permissions information is available at www.nature.com/reprints.

Publisher's note: Springer Nature remains neutral with regard to jurisdictional claims in published maps and institutional affiliations.

Activity origin and design of catalysts for sulfur reduction electrocatalysis

Huan Li[1†], Rongwei Meng[2†], Anton Tadich[3], Yan Jiao[1], Chao Ye[1], Xiao Chen[4], Qinfen Gu[3], Bernt Johannessen[3], Kenneth Davey[1] and Shi-Zhang Qiao*[1]

[1]School of Chemical Engineering and Advanced Materials, The University of Adelaide, Adelaide, SA 5005, Australia;

[2]Nanoyang Group, State Key Laboratory of Chemical Engineering, School of Chemical Engineering and Technology, Collaborative Innovation Center of Chemical Science and Engineering (Tianjin), Tianjin University, Tianjin 300072, China;

[3]Australian Synchrotron, ANSTO, 800 Blackburn Rd, Clayton, VIC 3168, Australia;

[4]Beijing Key Laboratory of Green Reaction Engineering and Technology, Department of Chemical Engineering, Tsinghua University, Beijing, China;

[†]These authors contributed equally to this work.

* Corresponding E-mail: s.qiao@adelaide.edu.au

Supplementary Results

Supplementary Figure 1 (a) SEM image of pristine graphene substrate; (b) STEM image of Zn metal clusters on graphene; Ten different colors below the figure present the projected cluster sizes ranging from 1 to 10; (c) corresponding cluster size distribution.
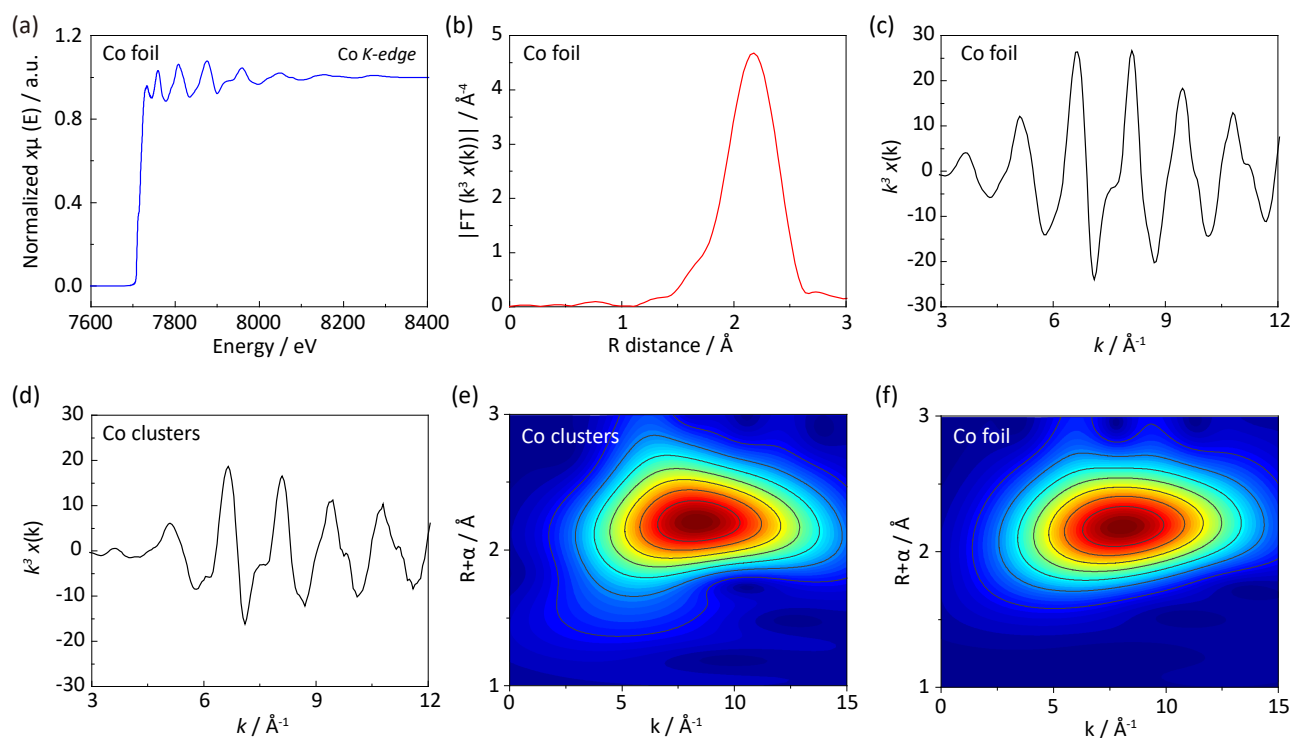
Supplementary Figure 2 (a) Normalized XAS plot for Co-foil, and transformed (b) R-space and (c) k-space curve; (d) k-space transformation for Co clusters; The wavelet-transformed contour for (e) Co clusters and (f) Co-foil. Co-Co bond can be identified from Co nano cluster catalysts.
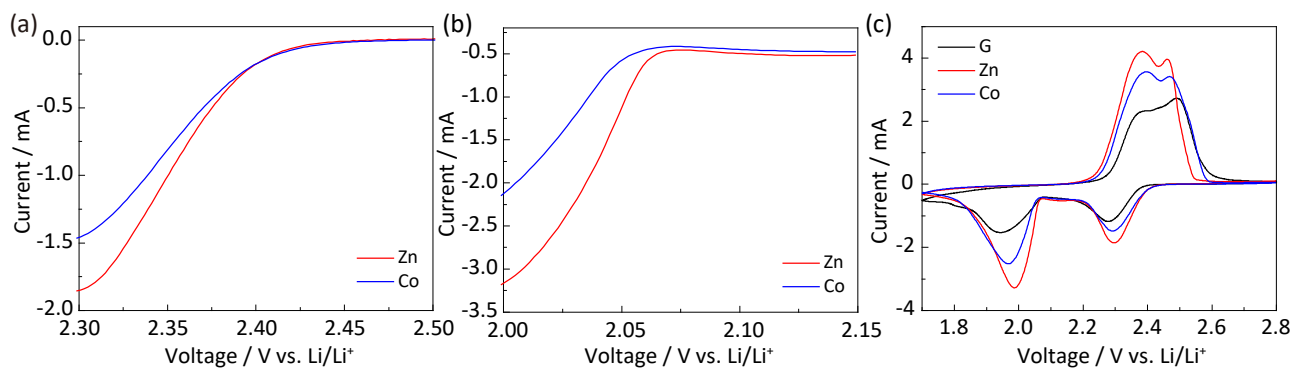
Supplementary Figure 3 Enlarged CV curve of Figure 1f at regions of (a) high-voltage sulfur reduction (from 2.50 to 2.30 V) and (b) low-voltage sulfur reduction (from 2.15 to 2.00 V); (c) CV curves for G, Co and Zn at 0.2 mV s^{-1}. These confirm a significantly lower catalytic activity for pristine graphene substrate.
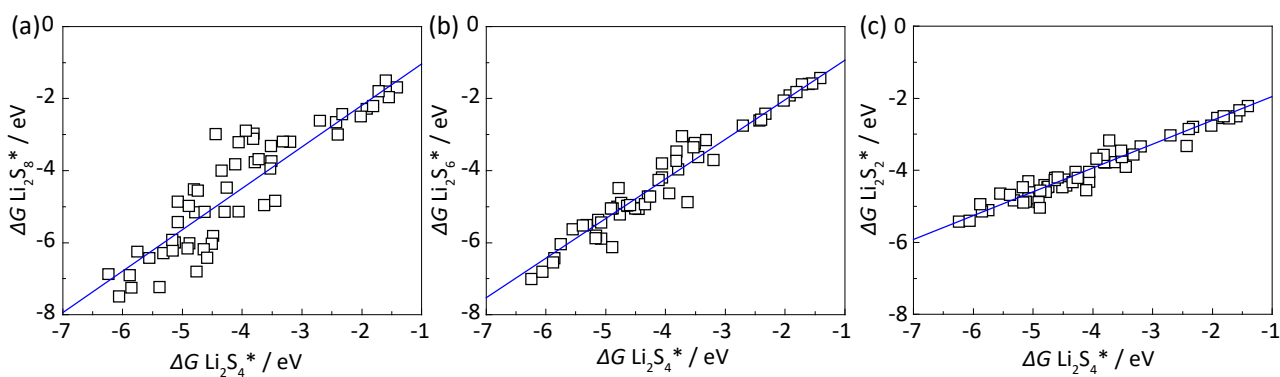
Supplementary Figure S4 Linear-scaling between change in Gibbs free energy (ΔG) for $Li_2S_4^*$ with (a) $Li_2S_8^*$, (b) $Li_2S_6^*$ and (c) $Li_2S_2^*$. In contrast to the double binding sites with both catalyst-sulfur and catalyst-lithium bonds, these transition-metal clusters bind only with polysulfide intermediates via metal-sulfur bonds. A linear-scaling can therefore be established similar to electrocatalytic reactions, such as oxygen reduction (ORR), hydrogen evolution (HER) and nitrogen reduction (NRR) reaction.
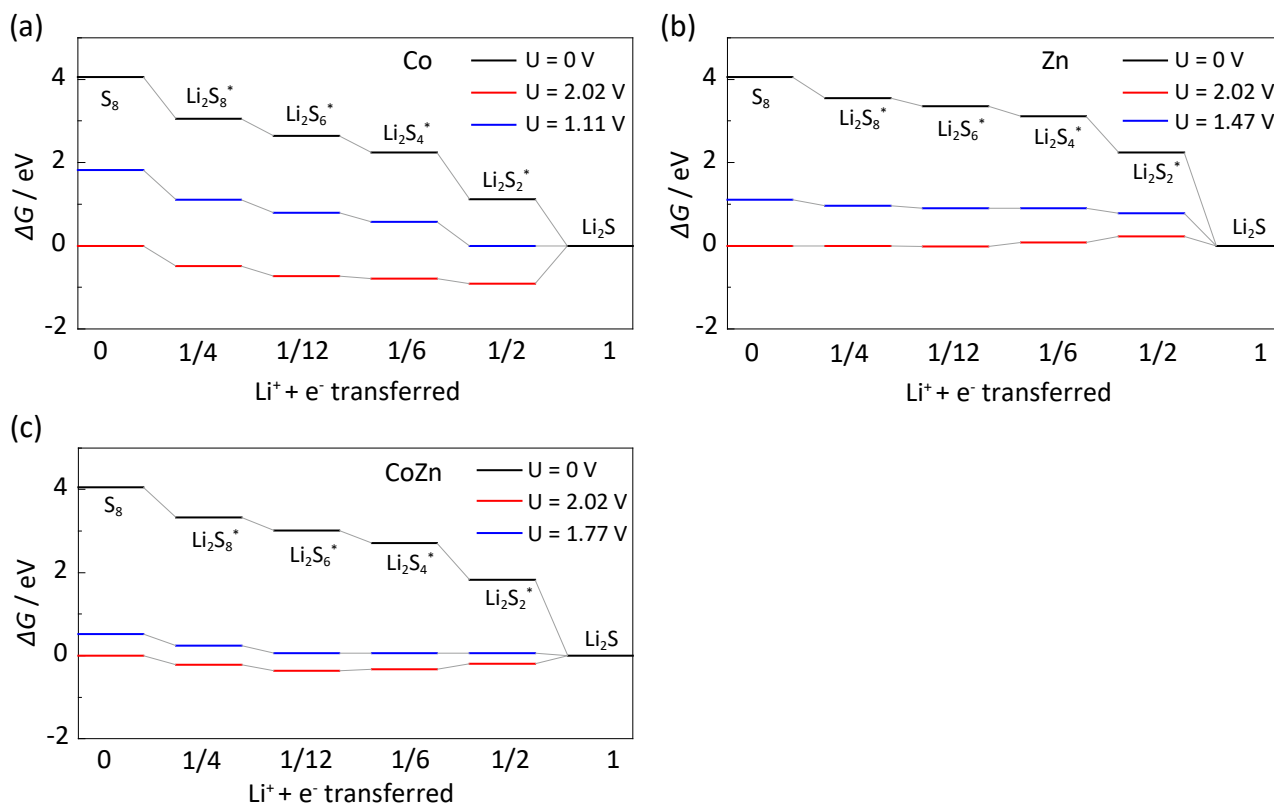
Supplementary Figure 5 SRR reaction pathways for (a) Co, (b) Zn and (c) CoZn at varying potential, 0 V, 2.02 V (equilibrium potential), and the limiting potential (respectively, 1.11, 1.47 and 1.77 V for Co, Zn and CoZn).
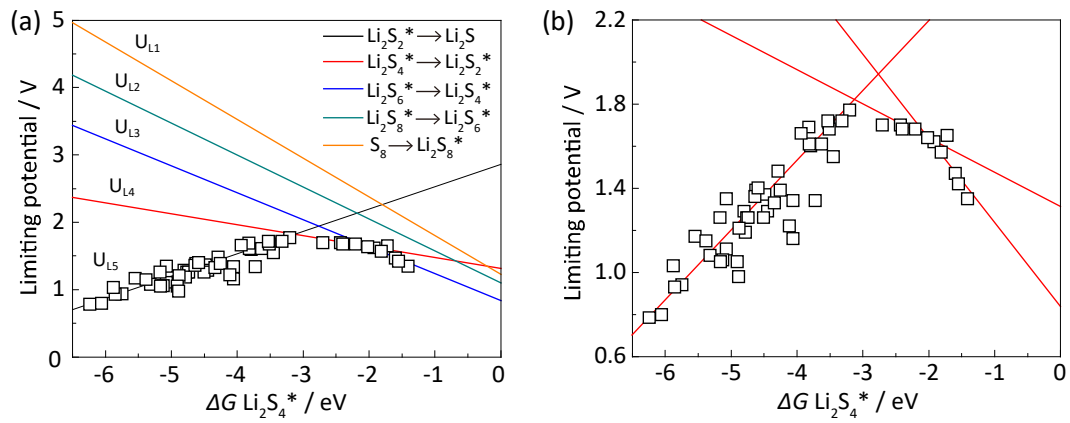
Supplementary Figure 6 (a) Limiting potential for each step, including U_{L1} for S_8 to $Li_2S_8^*$, U_{L2} for $Li_2S_8^*$ to $Li_2S_6^*$, U_{L3} for $Li_2S_6^*$ to $Li_2S_4^*$, U_{L4} for $Li_2S_4^*$ to $Li_2S_2^*$ and U_{L5} for $Li_2S_2^*$ to Li_2S; (b) Details to build reactivity trend of Figure 2c.
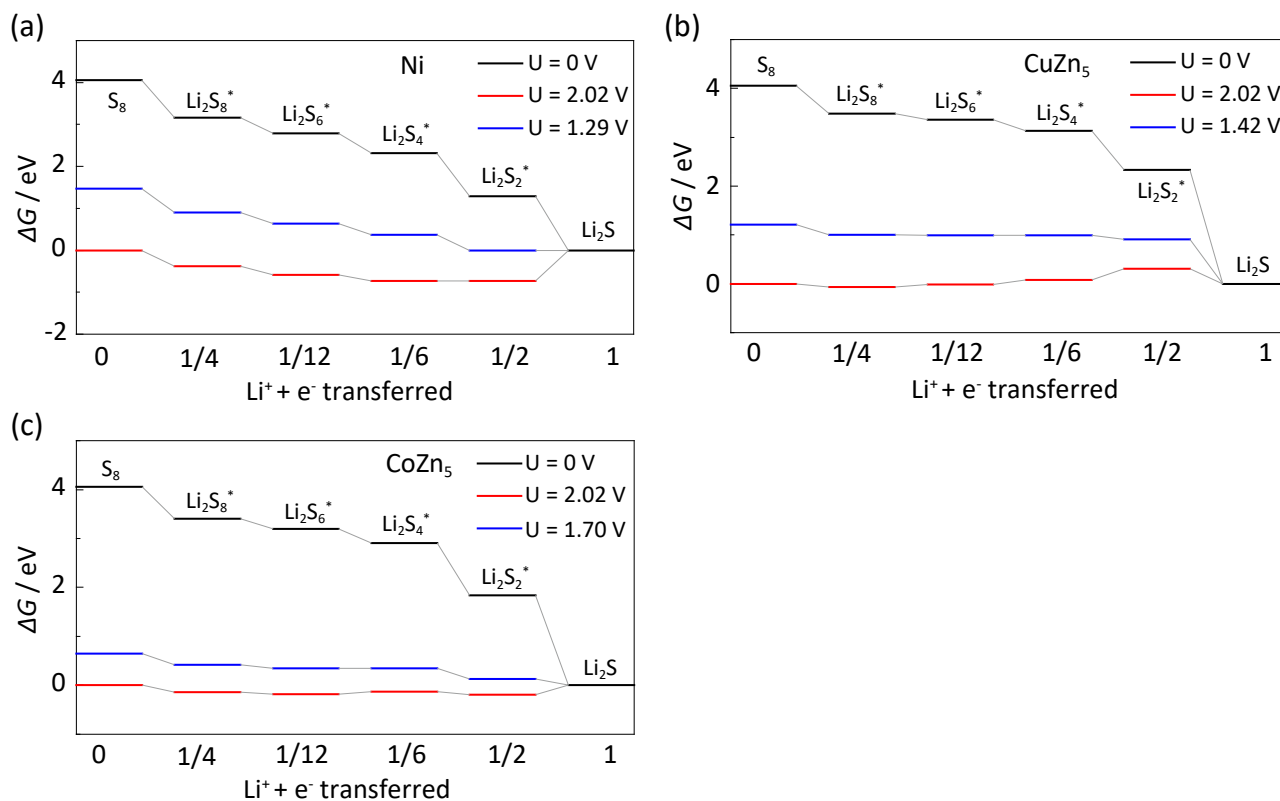
Supplementary Figure 7 Typical reaction pathways with different rate-determining steps. (a) Ni catalyst controlled by conversion from $Li_2S_2^*$ to Li_2S; (b) $CuZn_5$ catalyst controlled by conversion from $Li_2S_6^*$ to $Li_2S_4^*$ and (c) $CoZn_5$ catalyst controlled by conversion from $Li_2S_4^*$ to $Li_2S_2^*$.
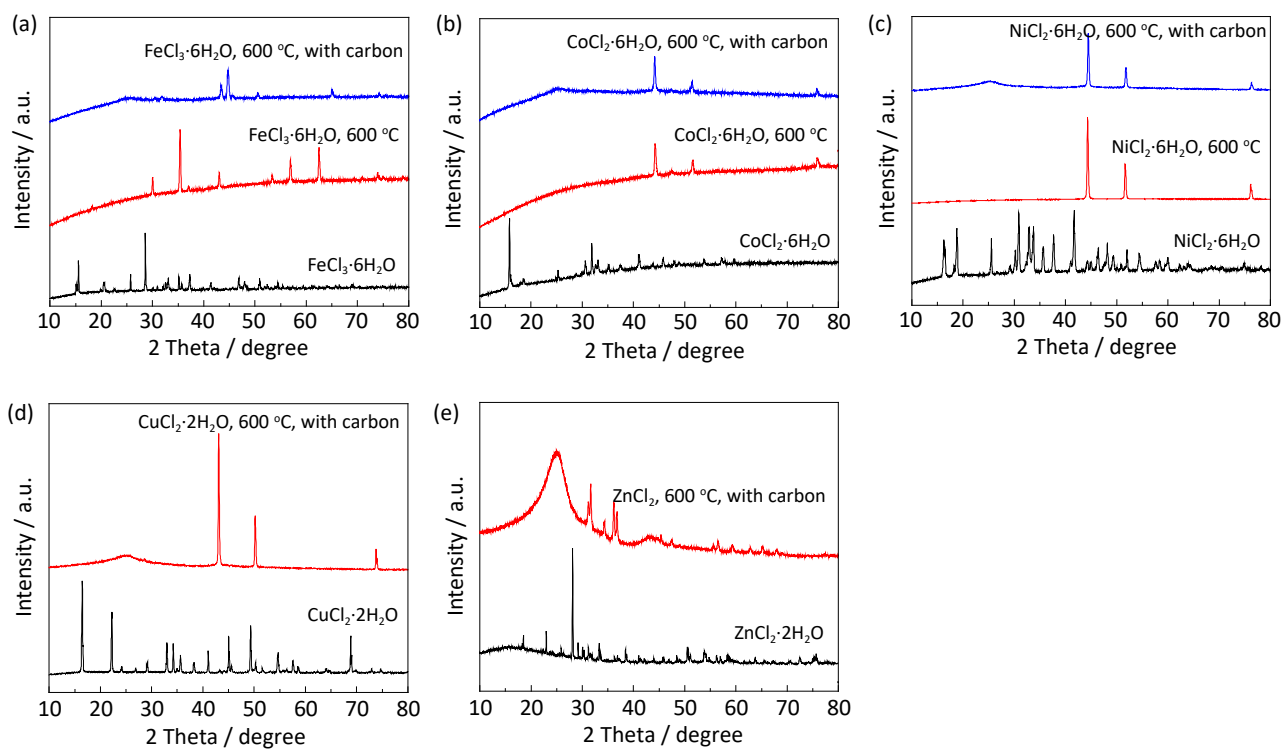
Supplementary Figure 8 XRD patterns for metal precursors following heat treatment at 600 °C in 5 vol% H_2. (a) $FeCl_3$ (b) $CoCl_2$ (c) $NiCl_2$ (d) $CuCl_2$ and (e) $ZnCl_2$. Metal-oxide and metal mixtures formed following heat treatment, and the metal clusters, are synthesized following removal of these large particles. Metal clusters are identified from high-resolution STEM images and synchrotron X-ray analyses.
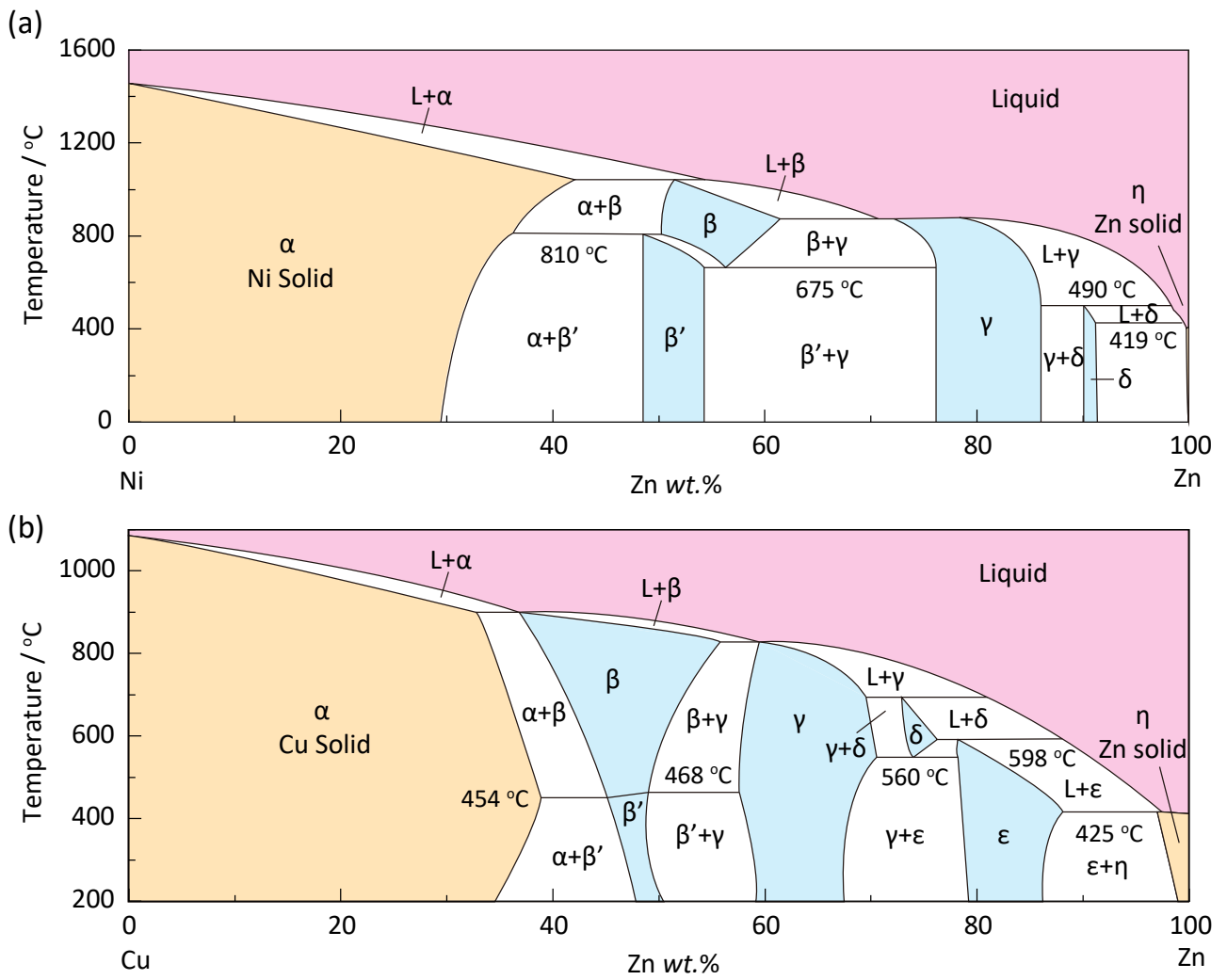
Supplementary Figure 9 Binary phase diagrams of (a) Ni-Zn and (b) Cu-Zn alloy. These metals tend to form binary alloys or, clusters with each other, at lower temperature (light blue-color area).
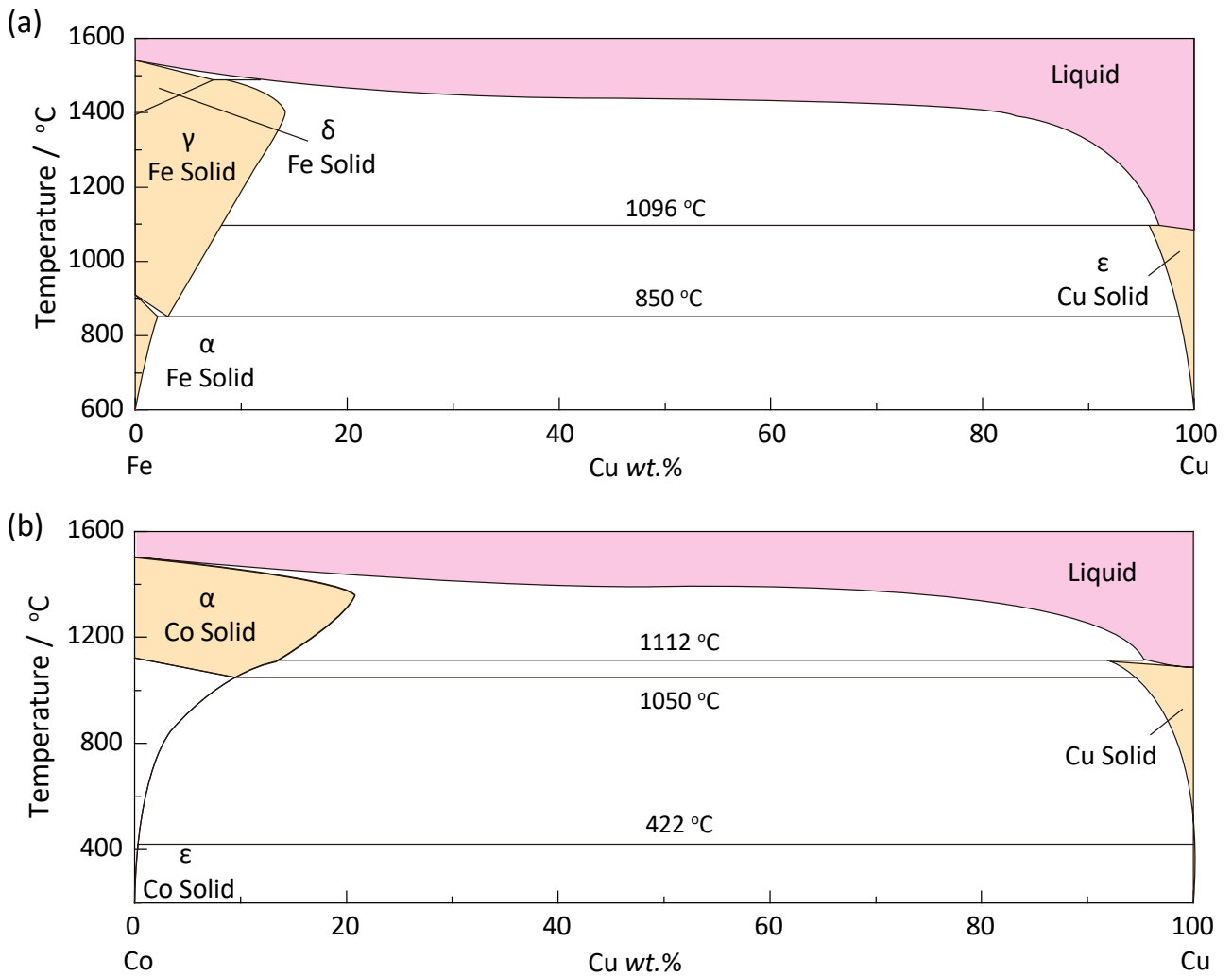
Supplementary Figure 10 Binary phase diagrams of (a) Fe-Cu and (b) Co-Cu alloy. These metals do not tend to form binary alloys, or clusters with each other, at lower temperatures.
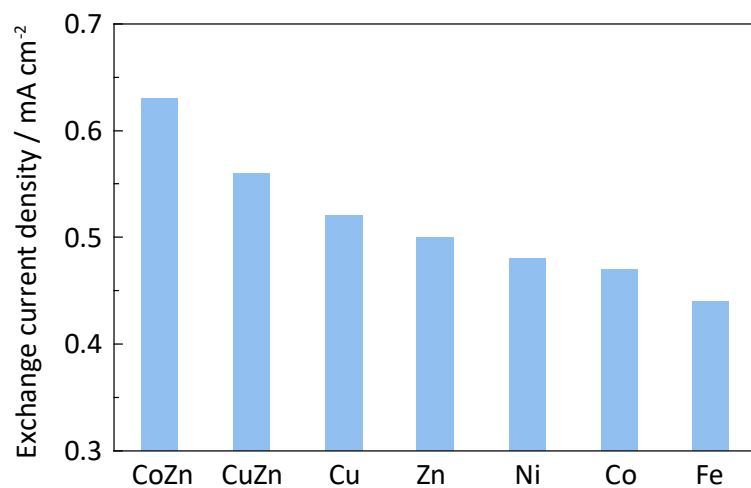
Supplementary Figure 11 Summary of exchange current density for CoZn, CuZn, Cu, Zn, Ni, Co and Fe catalyst.
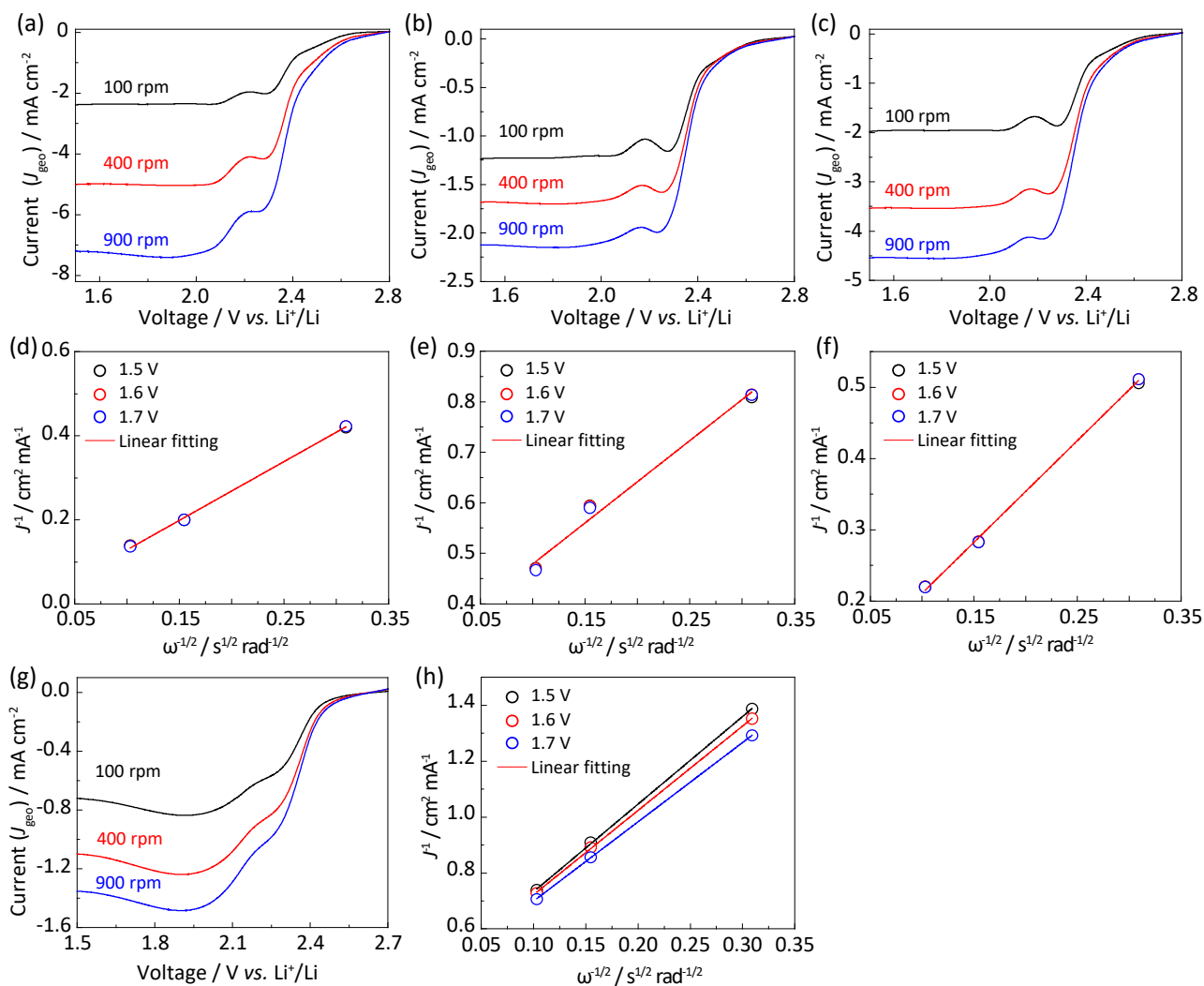
Supplementary Figure 12 LSV curves for (a) CoZn, (b) Zn and (c) CuZn at 100, 400 and 900 rpm and corresponding K-L linear-fitting (d-f). LSV curves for (g) pristine G substrate and K-L linear-fitting. Electron-transfer number is 7.8, 7.4, 6.6, 3.4 e⁻ for, respectively, CoZn, CuZn, Zn and G.
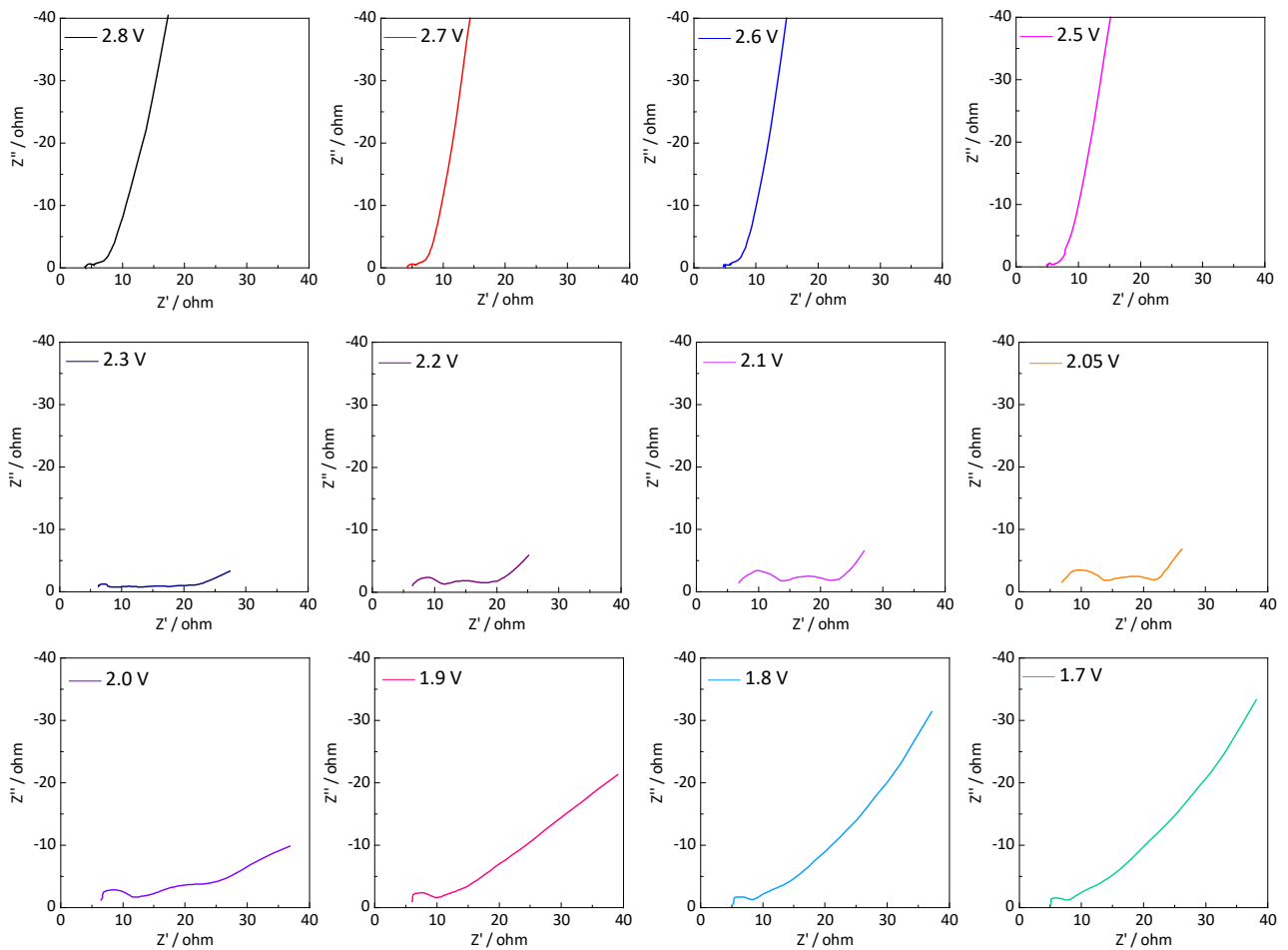
Supplementary Figure 13 EIS-plot for Li−S batteries from 1.7 to 2.8 V. It is seen that from 2.8 to 2.5 V there are no semi-circles. Near-vertical lines in low-frequency region highlight capacitive behavior without redox reactions. Two semi-circles are seen from 2.3 to 2.0 V. This finding highlights a two-step redox conversion. From 1.9 to 1.7 V, one semi-circle is seen, and two semi-circles disappear. This result underscores the difficulty for redox reactions in this voltage range. It was concluded therefore the EIS-plot with two semi-circles be selected to determine the activation energy.
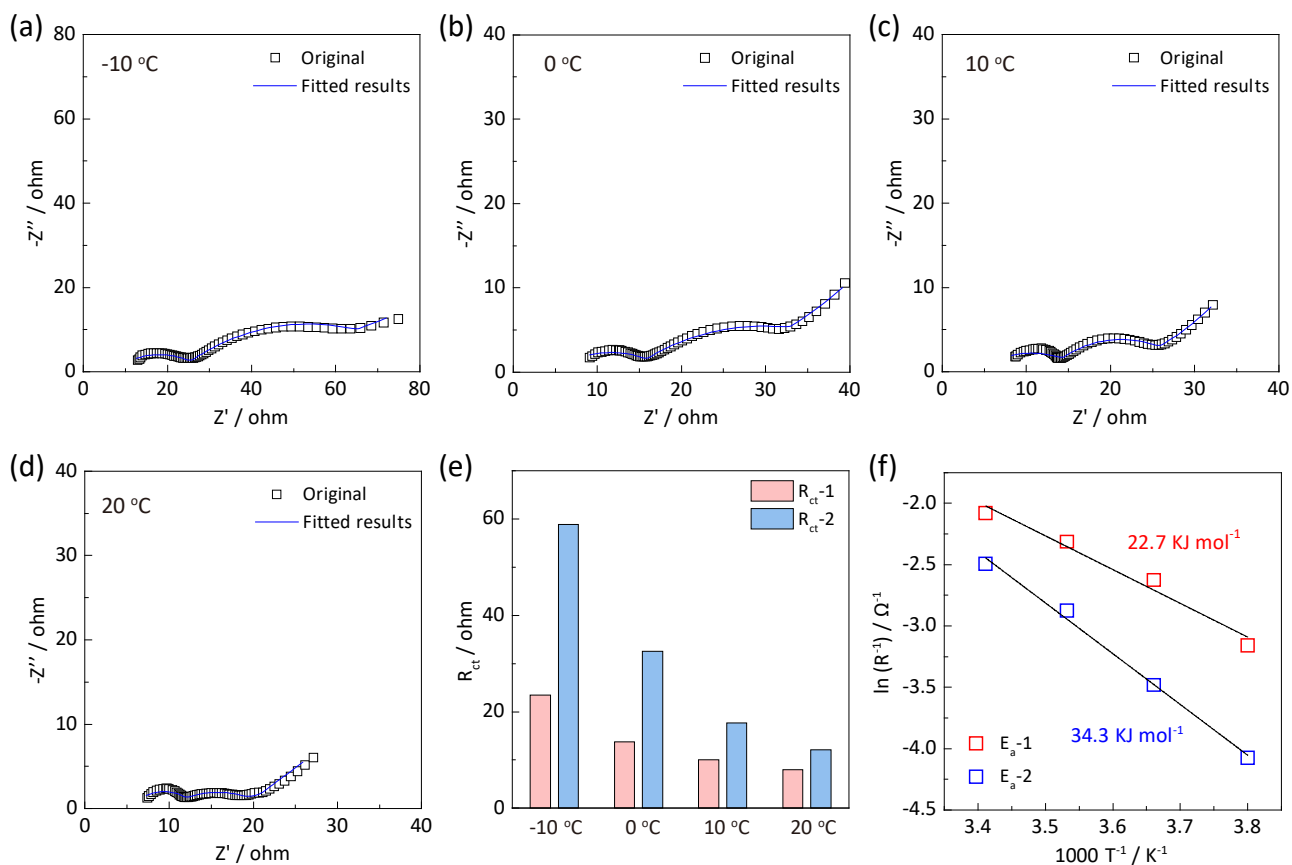
Supplementary Figure 14 Original and fitted data for CoZn catalyst for sulfur reduction electrocatalysis in Li-S batteries from (a) -10 $^{\circ}$C, (b) 0 $^{\circ}$C, (c) 10 $^{\circ}$C and (d) 20 $^{\circ}$C. Fitted values for charge-transfer resistances (R_{ct}) for the first and second semi-circles, are denoted R_{ct-1} and R_{ct-2} respectively; (f) Corresponding Arrhenius linear-fit of value of R_{ct-1} and R_{ct-2} to determine activation energy. E_{a-1} and E_{a-2} are, respectively, for conversion from S_8 to high-order Li_2S_x and high-order Li_2S_x to Li_2S.
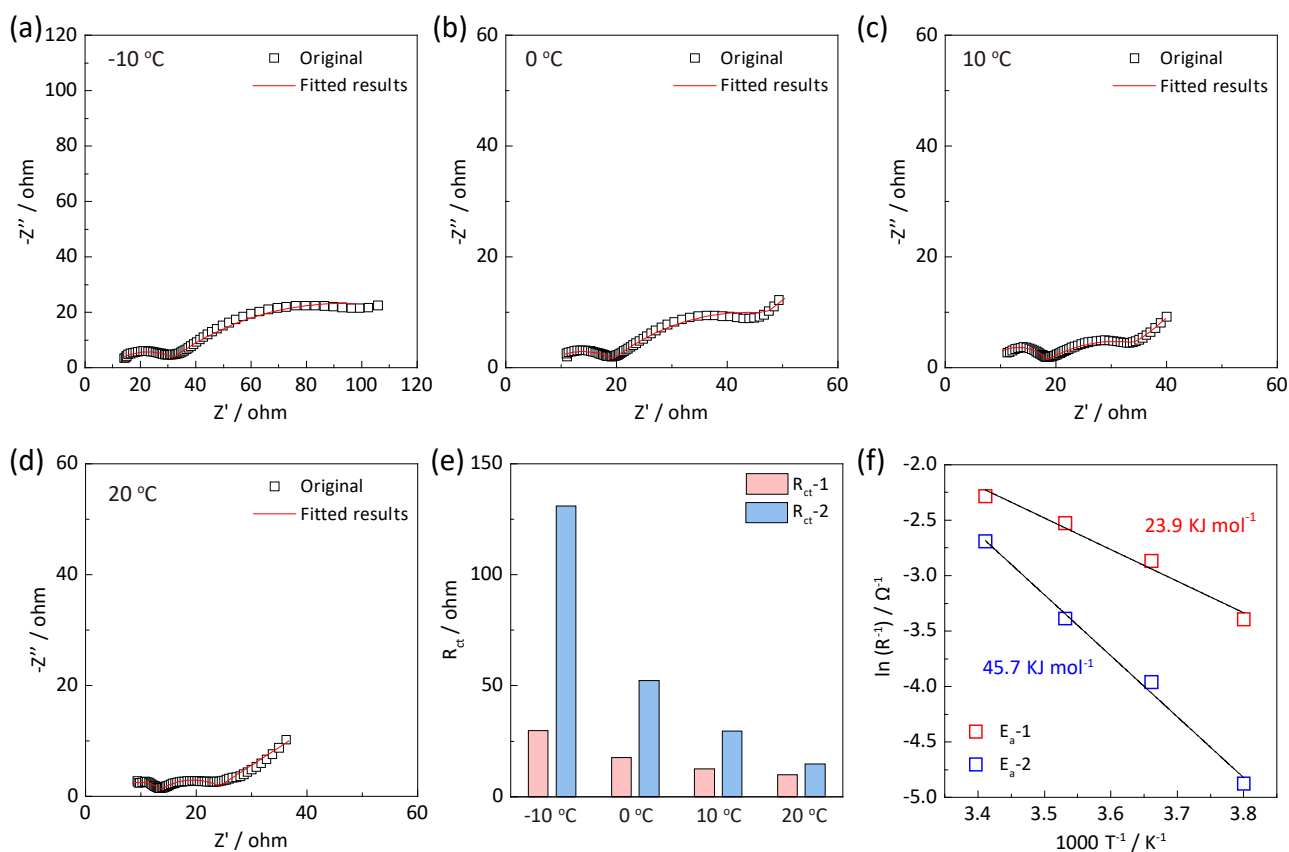
Supplementary Figure 15 Original and fitted data for G catalyst for sulfur reduction electrocatalysis in Li-S batteries from (a) -10 °C, (b) 0 °C, (c) 10 °C and (d) 20 °C. Fitted values of charge-transfer resistances (R_{ct}) for the first and second semi-circles, are denoted R_{ct-1} and R_{ct-2} respectively; (f) Corresponding Arrhenius linear-fitted of values of R_{ct-1} and R_{ct-2} to determine activation energy. E_{a-1} and E_{a-2} are, respectively, for conversion from S_8 to high-order Li_2S_x and high-order Li_2S_x to Li_2S.
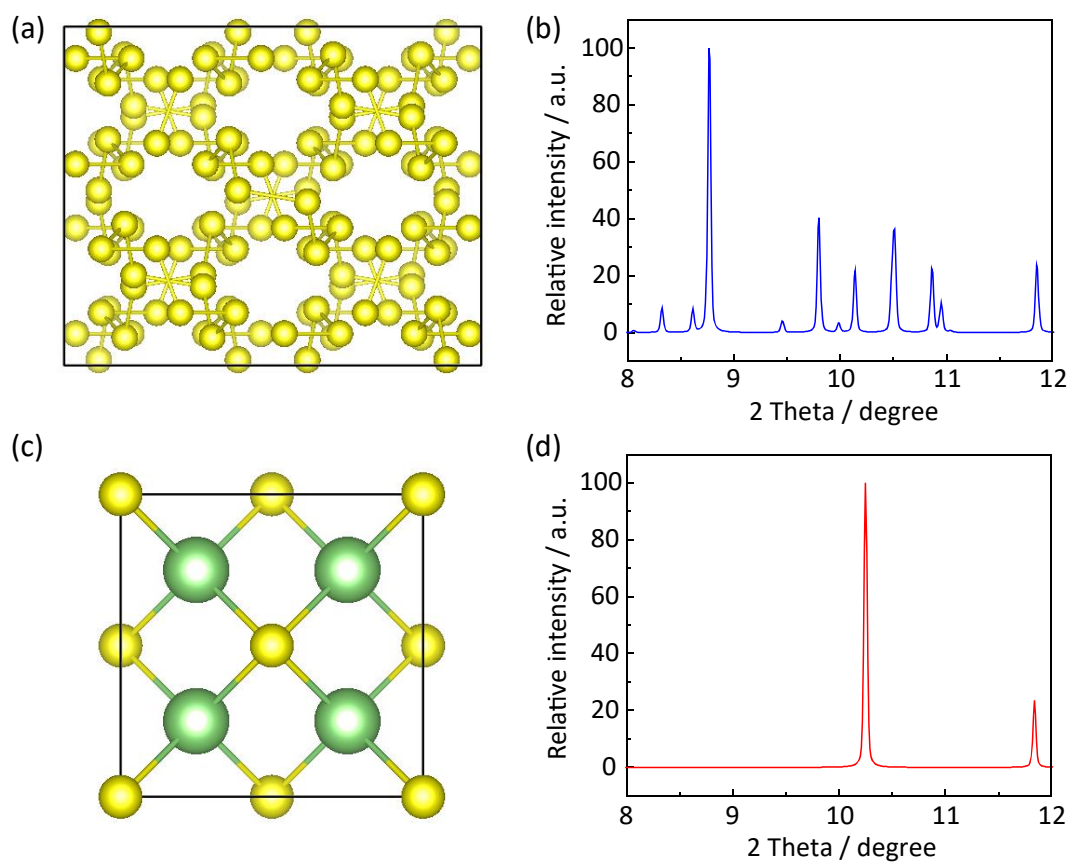
Supplementary Figure 16 Computed model for (a) sulfur and (b) simulated XRD patterns. Model for (c) Li_2S and (d) simulated XRD patterns. Wavelength is 0.5903 nm. The peak positions agree well with in-situ synchrotron X-ray diffraction.
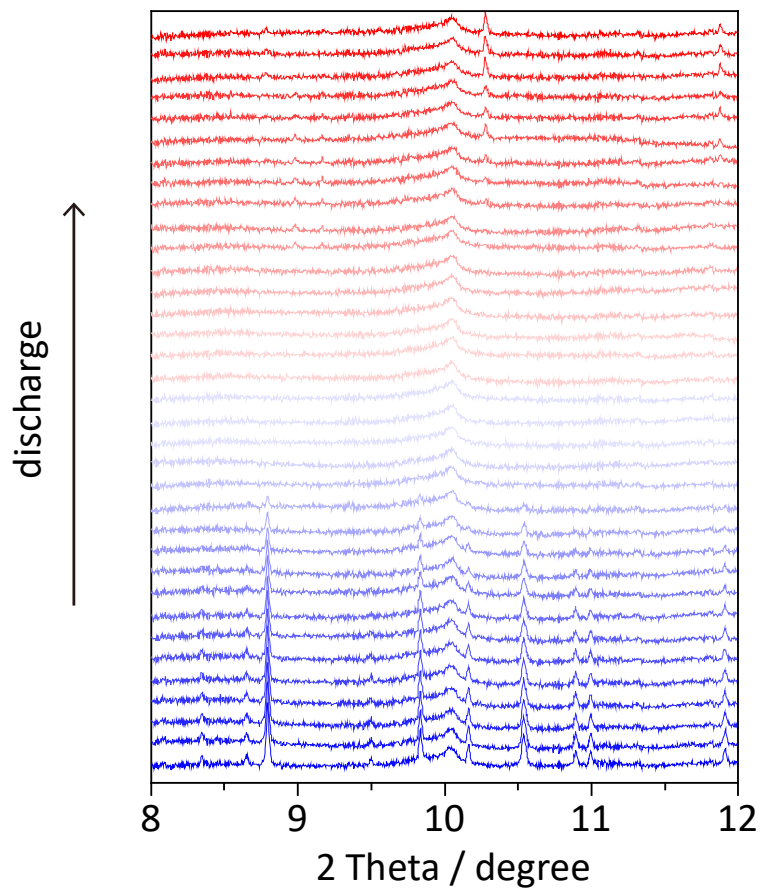
Supplementary Figure 17 In-situ synchrotron XRD pattern for sulfur cathode with pristine G host during discharge.
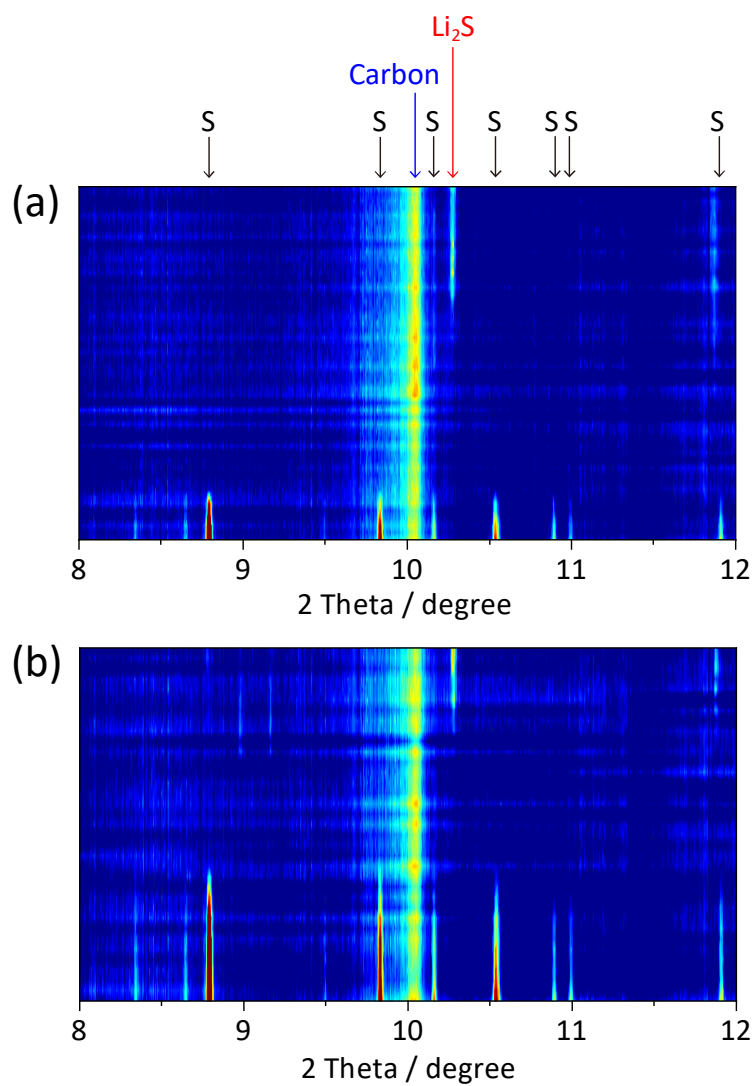
Supplementary Figure 18 In-situ synchrotron XRD contour pattern for sulfur cathodes with (a) CoZn catalyst and (b) pristine G host during discharge.
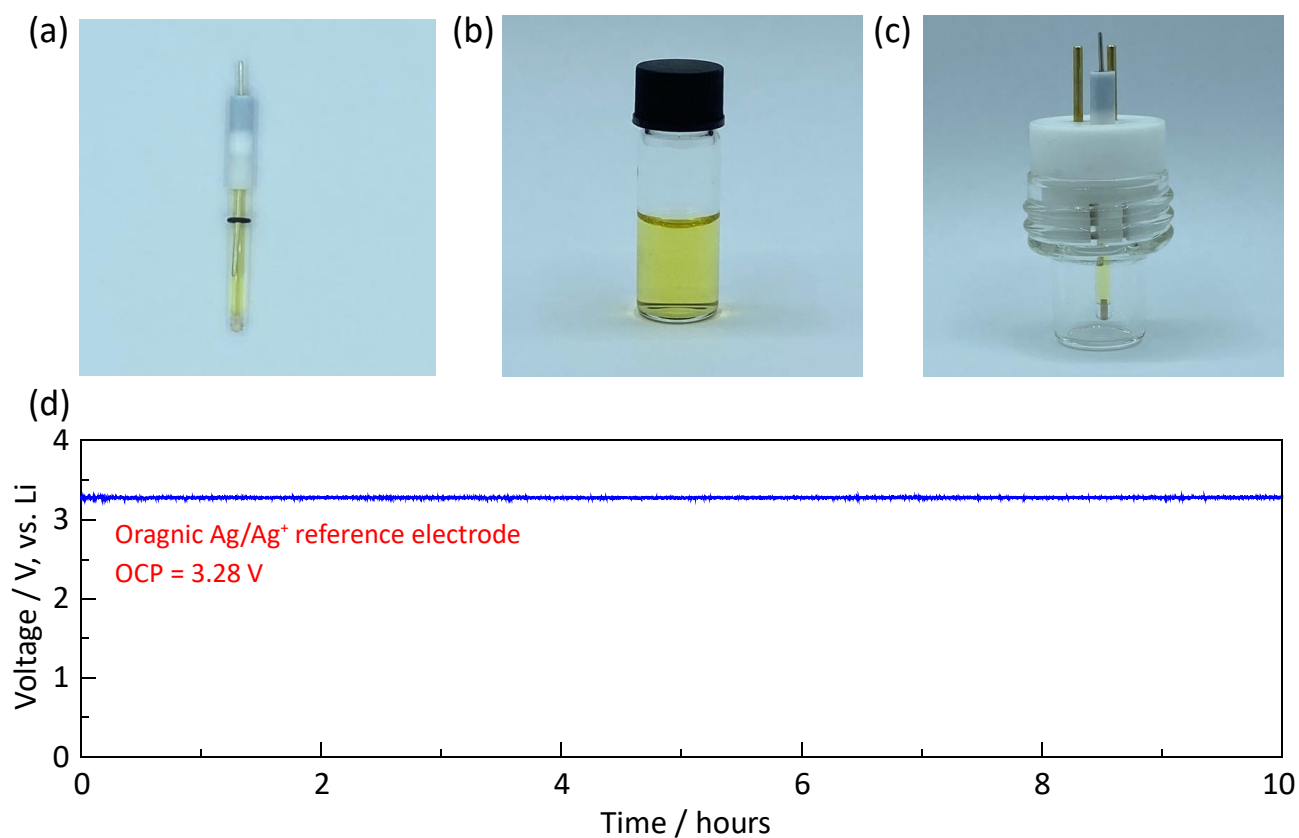
Supplementary Figure 19 Digital photograph of (a) organic Ag/Ag⁺ reference electrode with (b) 10 mmol L^{-1} silver nitrate (AgNO$_3$) in acetonitrile (CH$_3$CN) with 100 mM tetrabutylammonium perchlorate (NBu$_4^+$ClO$_4^-$) electrolyte; (c) Cell used to determine open circuit potential (OCP) of organic Ag/Ag⁺ reference electrode versus Li-metal anode; (d) Time-voltage curve of reference electrode with Li-anode in 1 mol L^{-1} LiTFSI in DOL/DME electrolyte. The OCP is stable at 3.28 V versus Li.
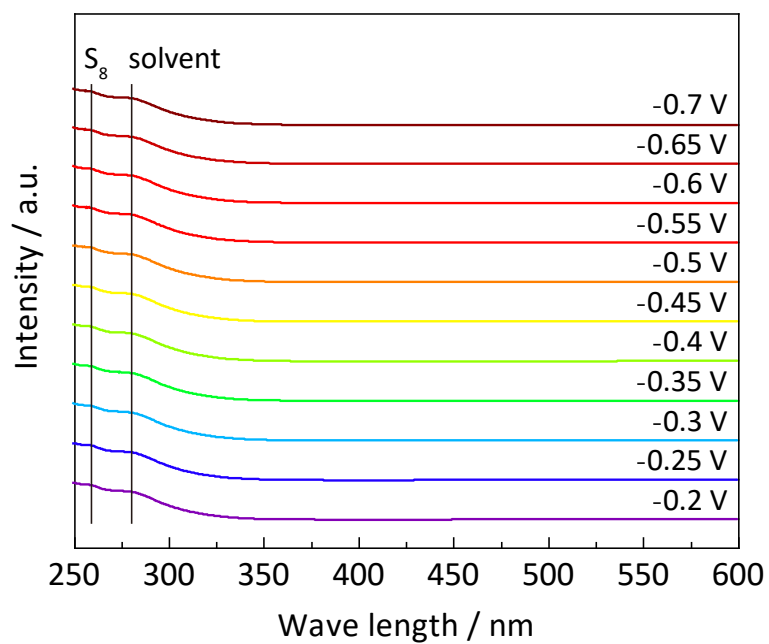
Supplementary Figure 20 UV-VIS absorbance plot from -0.2 to -0.7 V at a scan of 0.2 mV s^{-1}. Peaks at ~ 256 and ~ 274 nm are assigned to dissolved S$_8$ and DOL/DME solvent. No polysulfide signals were detected in this voltage region.
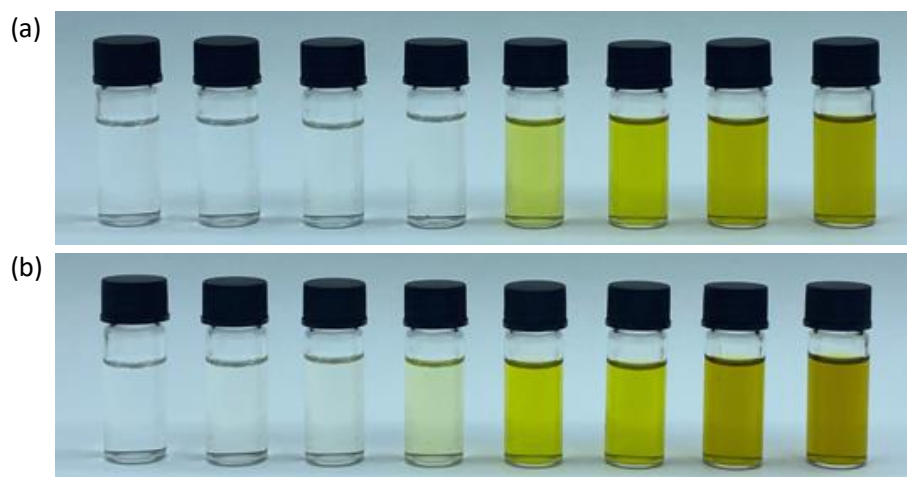
Supplementary Figure 21 Digital photograph of (a) Li_2S_4 and (b) Li_2S_6 standard solutions in 1 mol L^{-1} LiTFSI in DOL/DME electrolyte. Concentrations are from left to right, respectively, 0.2, 0.53, 0.8, 1, 2, 3, 4 and 5 mmol L^{-1}.
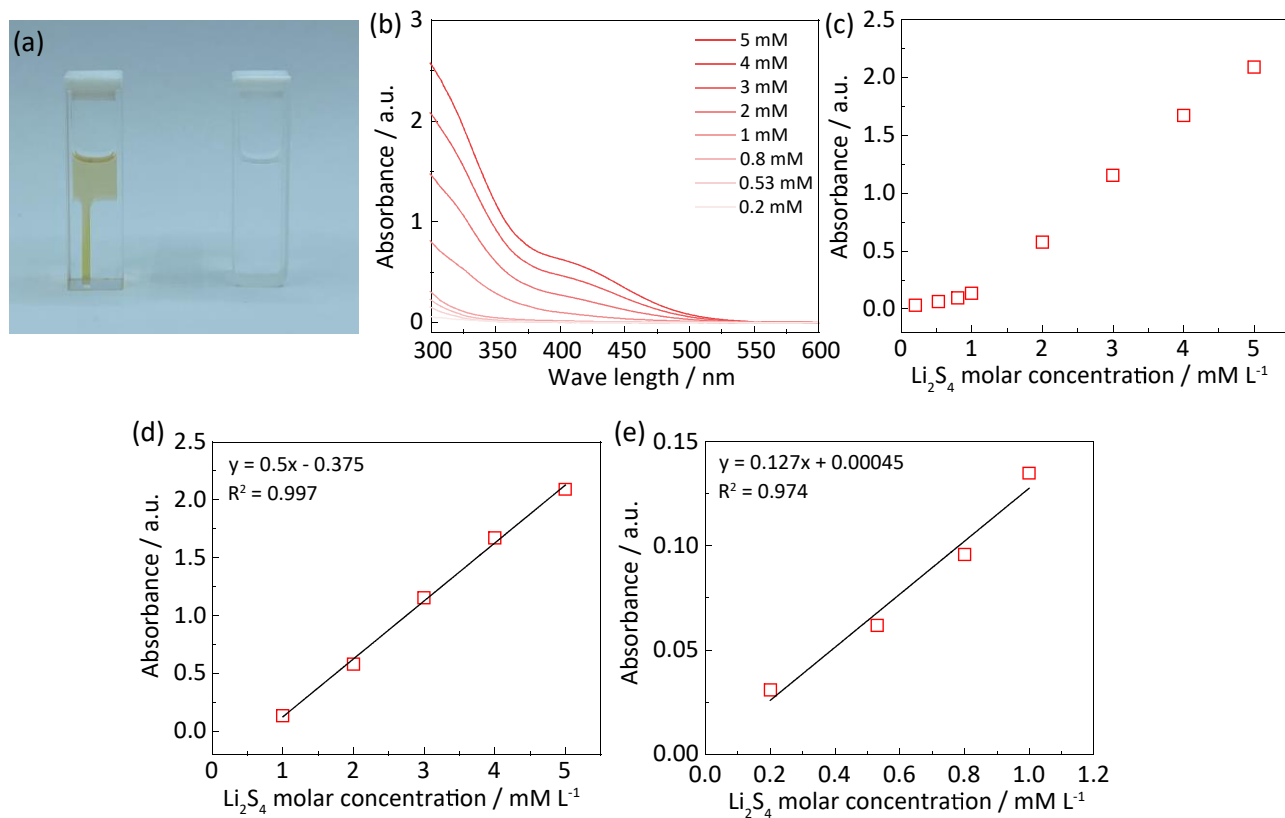
Supplementary Figure 22 Digital photograph of (a) Li_2S_4 standard solution in quartz cuvette for UV-VIS test; (b) UV-VIS absorbance curves for Li_2S_4 in 1 mol L^{-1} LiTFSI in DOL/DME electrolyte with Li_2S_4 concentration from 0.2 to 5 mmol L^{-1}; (c) Relationship between Li_2S_4 molar concentration and UV-VIS absorbance; Linear fit of Li_2S_4 molar concentration to UV-VIS absorbance in, (d) ultra-low, and (e) greater concentration region.
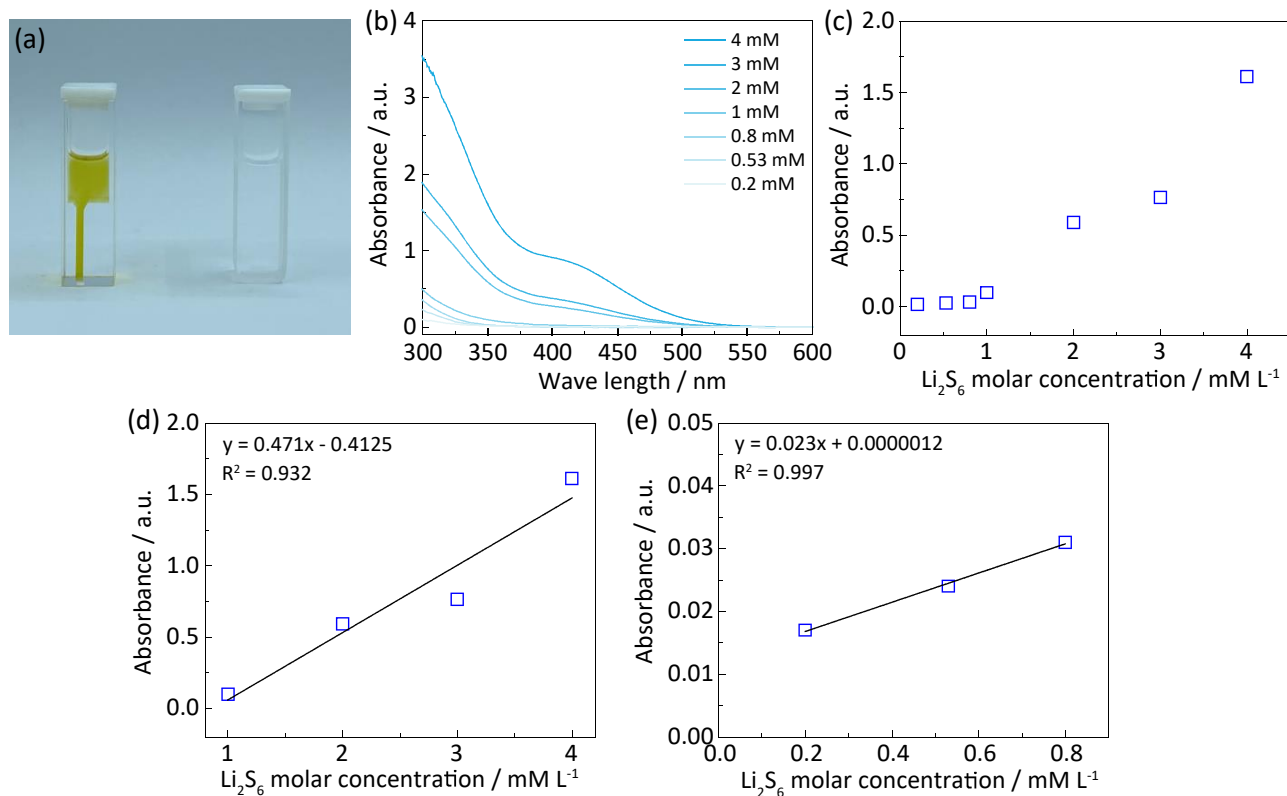
Supplementary Figure 23 Digital photograph of (a) Li_2S_6 standard solution in quartz cuvette for UV-VIS test; (b) UV-VIS absorbance curves for Li_2S_6 in 1 mol L^{-1} LiTFSI in DOL/DME electrolyte with Li_2S_6 concentration from 0.2 to 5 mmol L^{-1}; (c) Relationship between Li_2S_6 molar concentration and UV-VIS absorbance; Linear fit of Li_2S_6 molar concentration to UV-VIS absorbance in, (d) ultra-low and (e) greater concentration region.
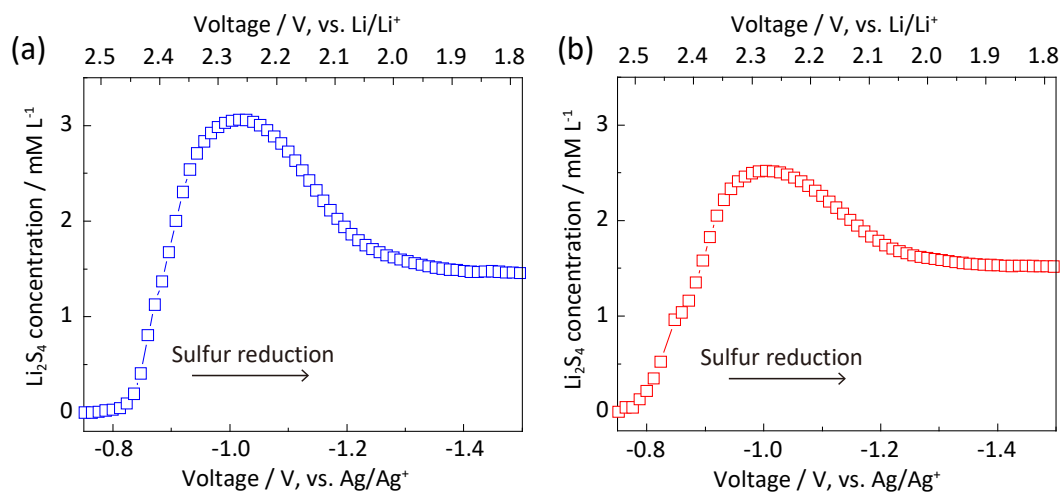
Supplementary Figure 24 Change in (a) Li_2S_4 and (b) Li_2S_6 concentration with CoZn catalyst at differing voltages based on in-situ UV-VIS test.
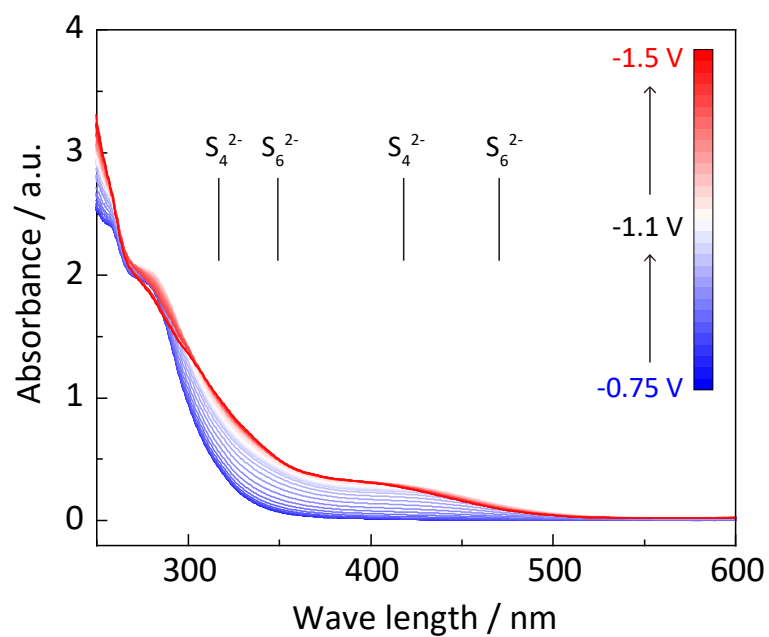
Supplementary Figure 25 In-situ UV-VIS curves from -0.75 to -1.5 V without CoZn catalyst exhibiting weaker peak intensity for S_4^{2-} and S_6^{2-}, and confirming limited SRR activity.
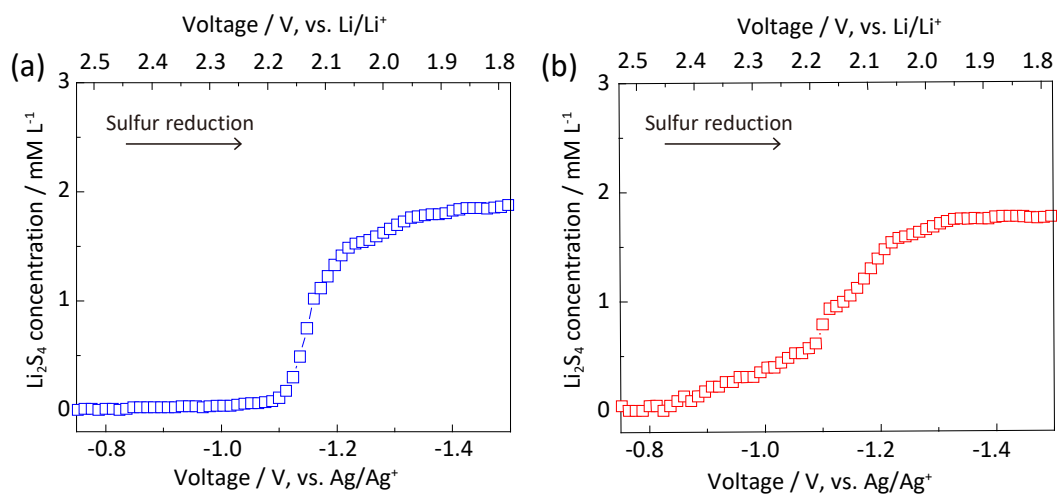
Supplementary Figure 26 Change in (a) Li_2S_4 and (b) Li_2S_6 concentration with pristine G catalyst at differing voltage based on in-situ UV-VIS test.
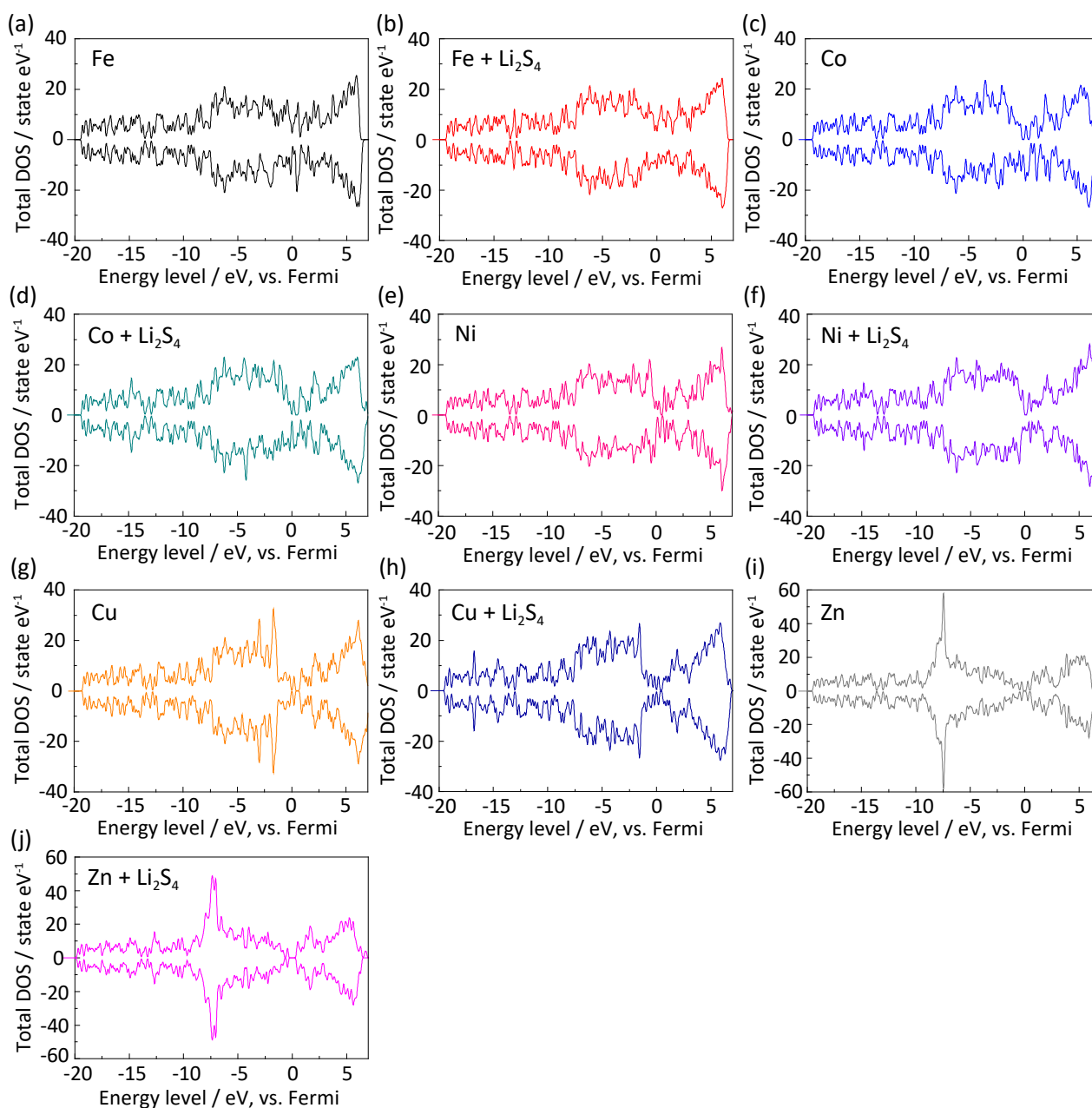
Supplementary Figure 27 Total density of state (DOS) for (a) Fe, (b) Fe+Li_2S_4, (c) Co, (d) Co+Li_2S_4, (e) Ni, (f) Ni+Li_2S_4, (g) Cu, (h) Cu+Li_2S_4, (i) Zn and (j) Zn+Li_2S_4.
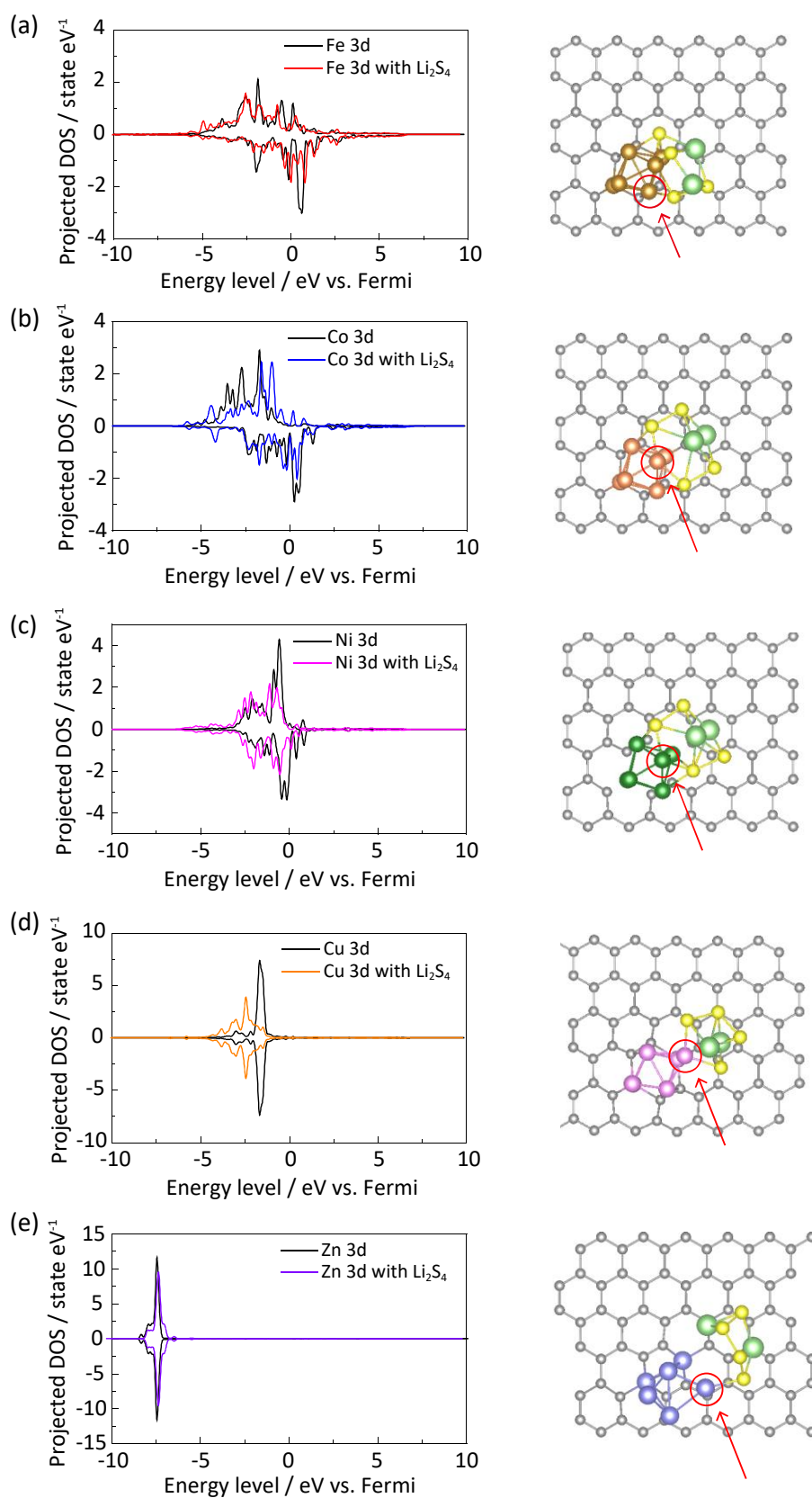
Supplementary Figure 28 Projected DOS for *3d*-orbital of selected metals before and following Li₂S₄* adsorption. (a) Fe, (b) Co, (c) Ni, (d) Cu and (e) Zn. Change in metal *3d* electron density confirms efficient metal-sulfur binding between metal cluster and polysulfides.
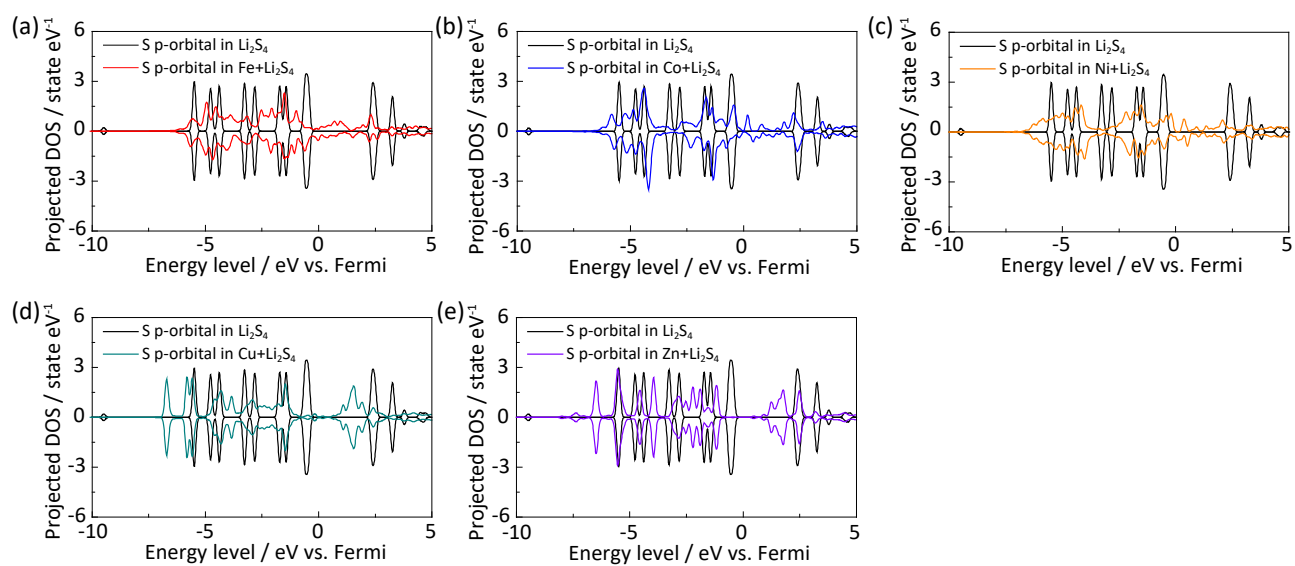
Supplementary Figure 29 Projected DOS for *p*-orbital for Li_2S_4 on different metal clusters, (a) Fe, (b) Co, (c) Ni, (d) Cu and (e) Zn. Significant change in S *p*-orbital electron density confirms metal-sulfur binding between metal clusters and polysulfides.
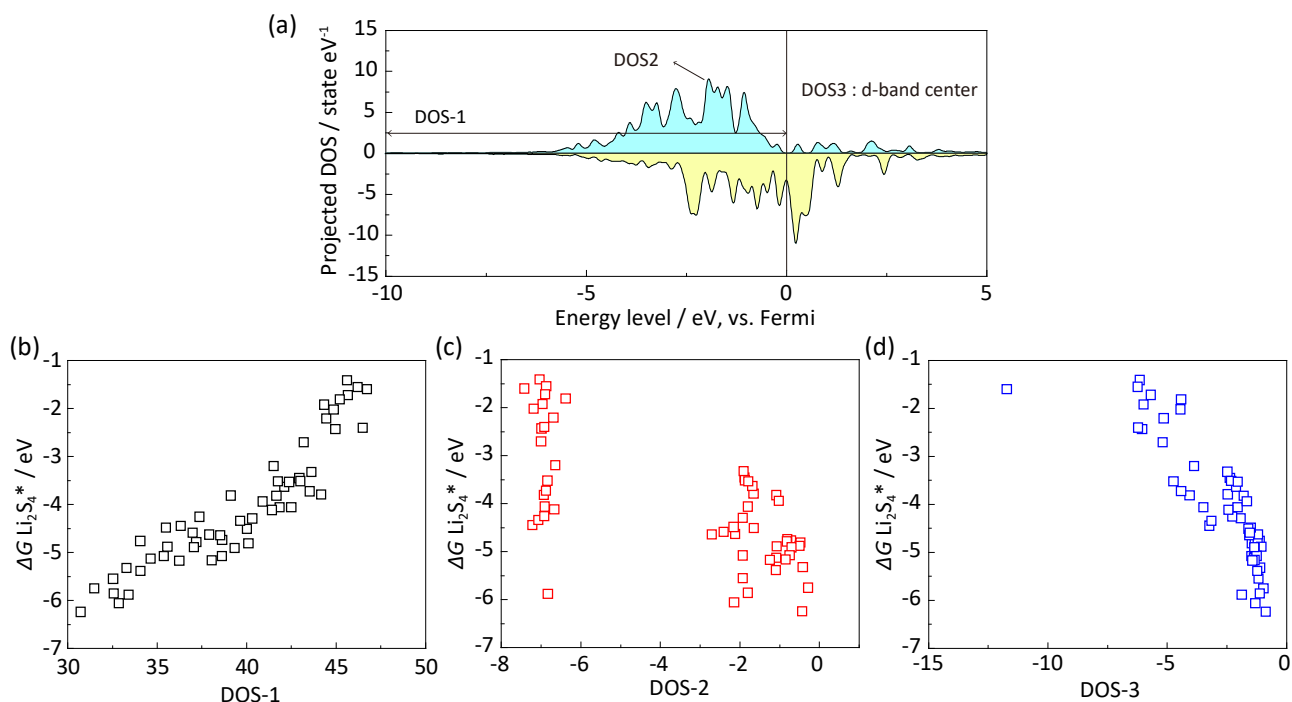
Supplementary Figure 30 Screening of DOS-based descriptors to correlate with Gibbs free energy for $Li_2S_4^*$. (a) Projected metal $3d$ DOS pattern for plane catalyst. Inset shows definition of DOS-1, DOS-2 and DOS-3. Relationship between Gibbs free energy for $Li_2S_4^*$ with (b) DOS-1 (c) DOS-2 and (d) DOS-3. In (a) can be seen a fitted linear-scaling relationship for the plane catalyst. DOS-1 refers to the total numbers $3d$-orbital electrons. It is concluded therefore that $3d$-orbital electrons can be used as a reliable descriptor to associate with free energy of $Li_2S_4^*$.
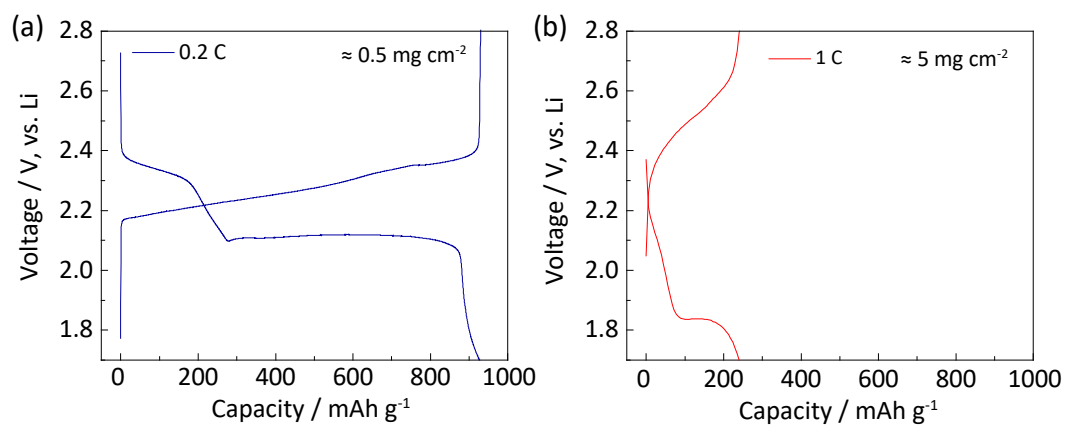
Supplementary Figure 31 Charge-discharge curve for sulfur cathode with pristine G host at (a) 0.2 C with areal sulfur loading of ~ 0.5 mg cm^{-2} and (b) 1.0 C with areal sulfur loading of ~ 5 mg cm^{-2}.
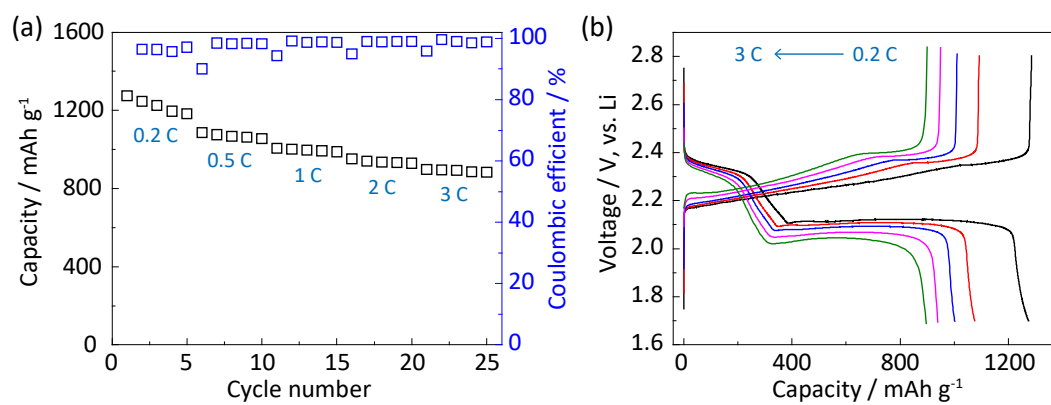
Supplementary Figure 32 (a) Rate performance of Li-S batteries with CoZn cathode catalyst, and (b) corresponding charge-discharge curves from 0.2 C to 3 C. The sulfur loading is ~ 0.5 mg cm^{-2}.
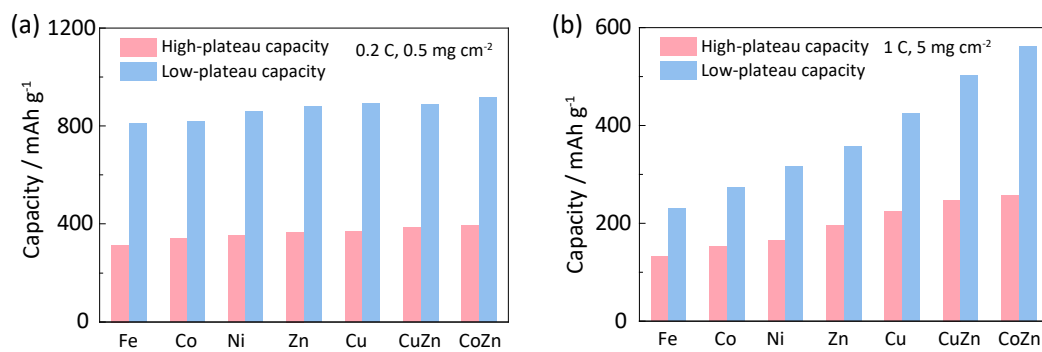
Supplementary Figure S33 High-plateau and low-plateau capacity for sulfur cathodes using differing catalyst. (a) 0.2 C charge-discharge and areal sulfur loading of 0.5 mg cm^{-2}, (b) 1 C charge-discharge and areal sulfur loading of 5 mg cm^{-2}.
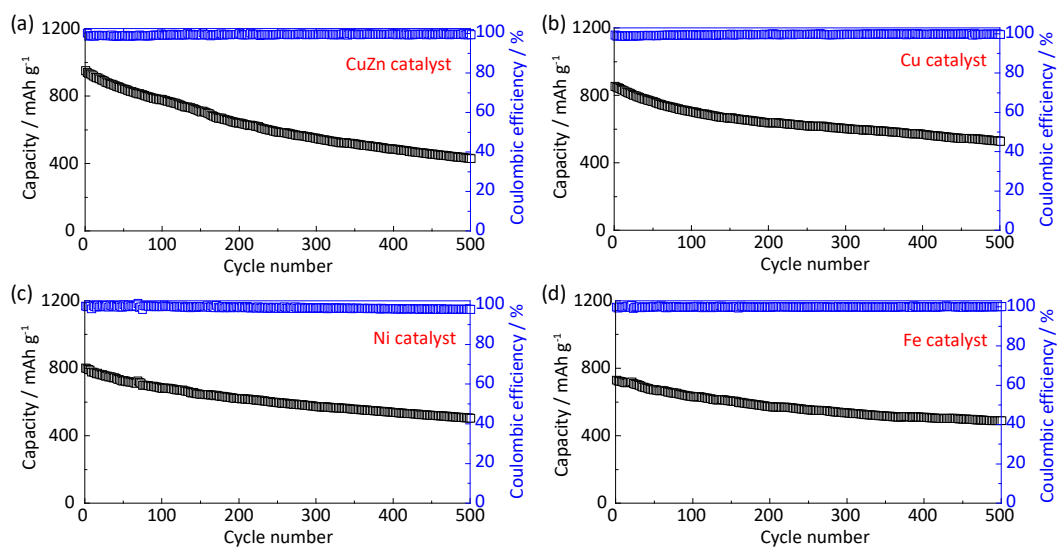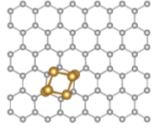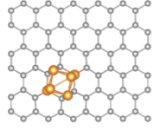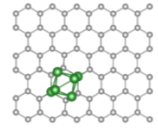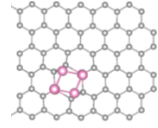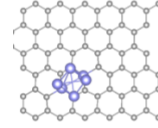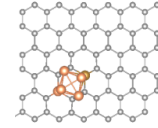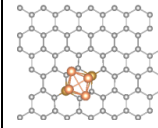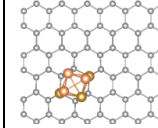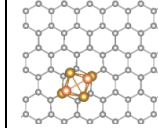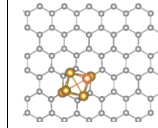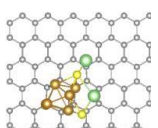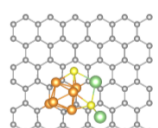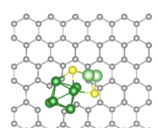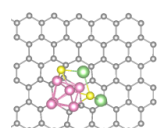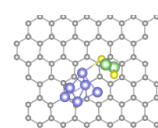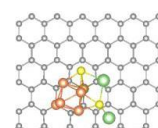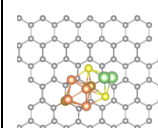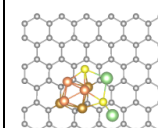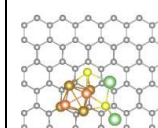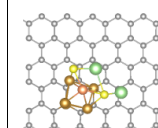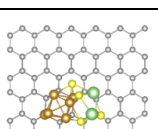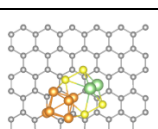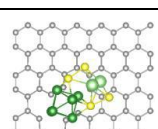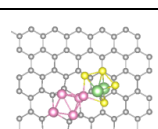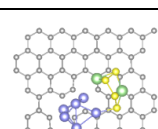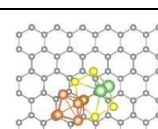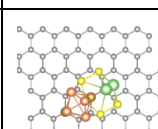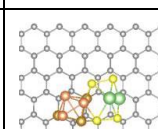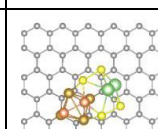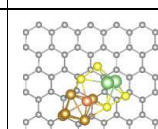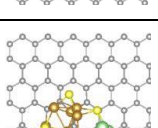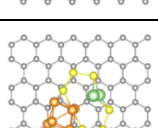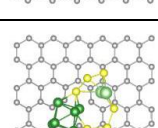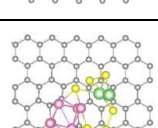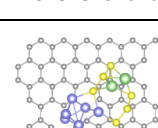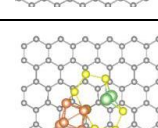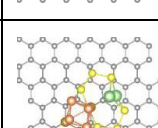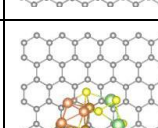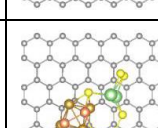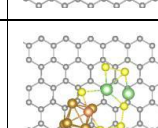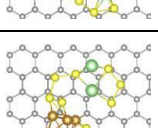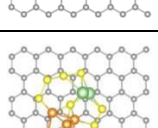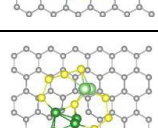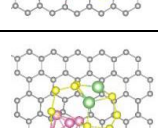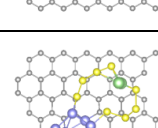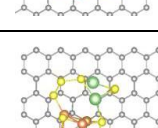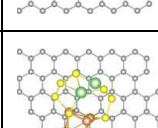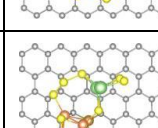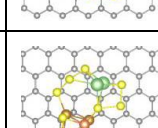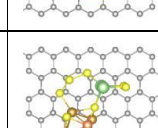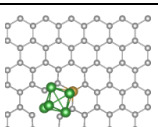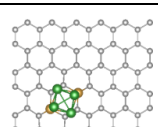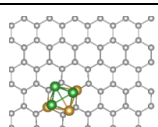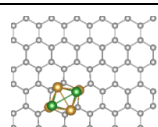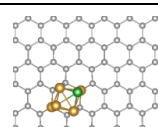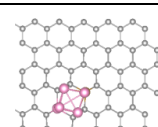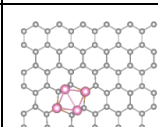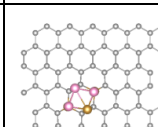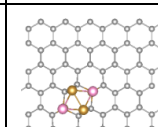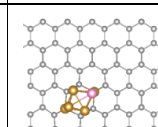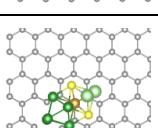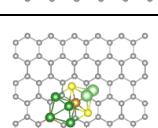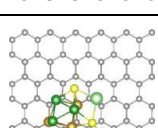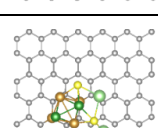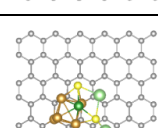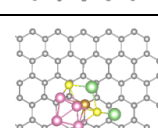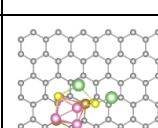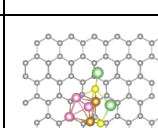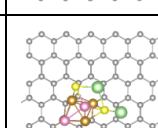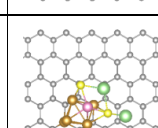
Supplementary Figure S34 Cycling performance of Li-S batteries with (a) CuZn, (b) Cu, (c) Ni and (d) Fe catalysts. The sulfur loading is ~ 0.5 mg cm^{-2} and the charge-discharge current density is 1 C.
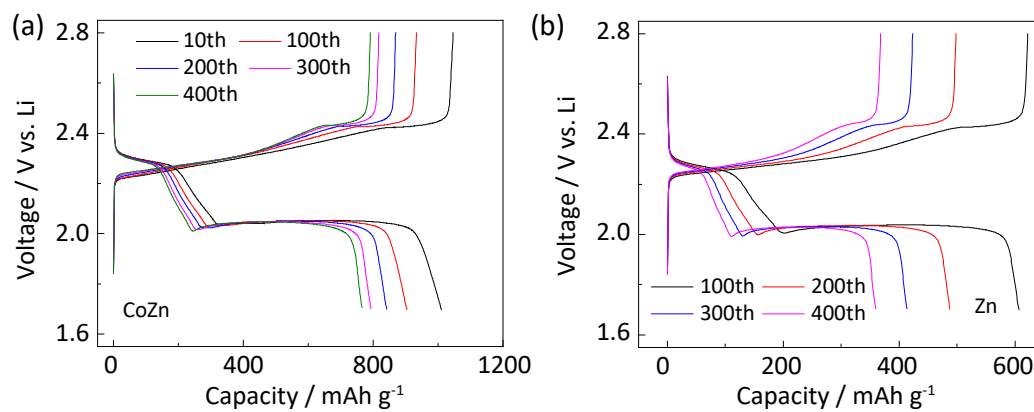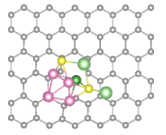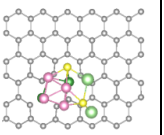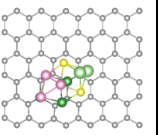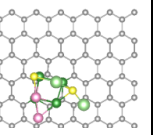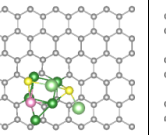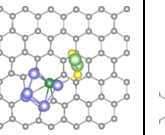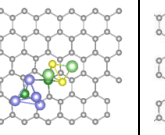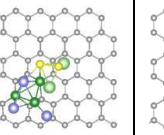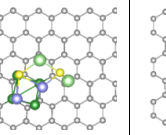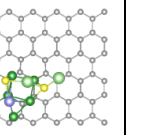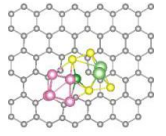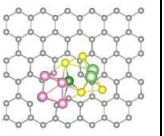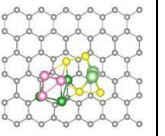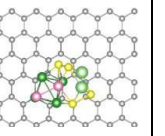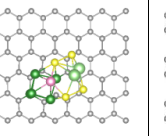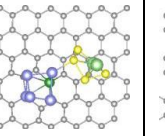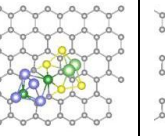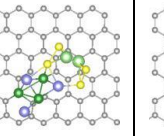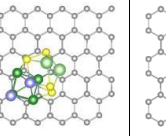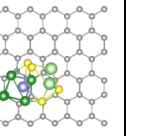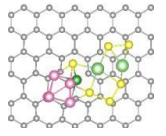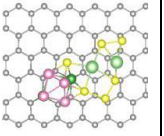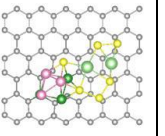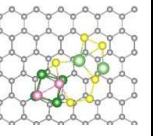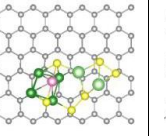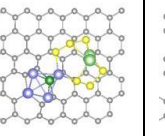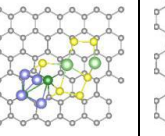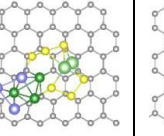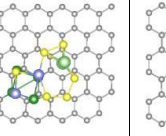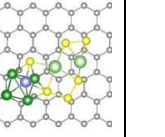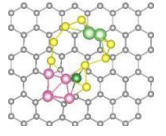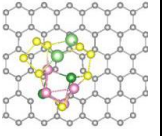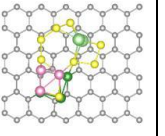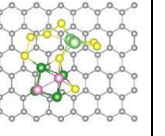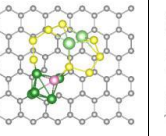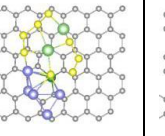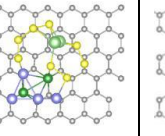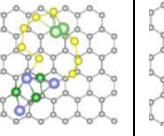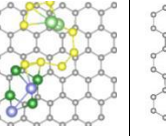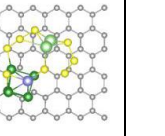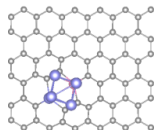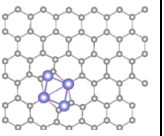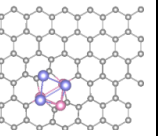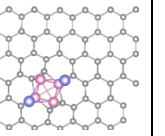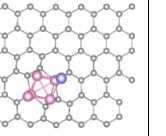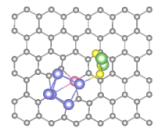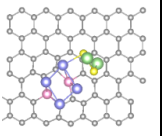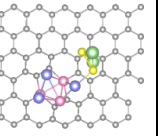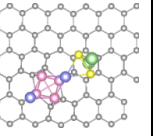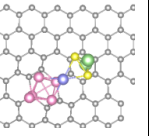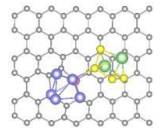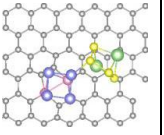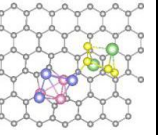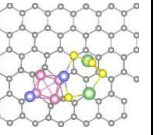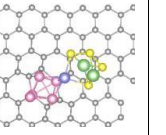
Supplementary Figure S35 Charge-discharge curve for sulfur cathode with (a) CoZn and (b) Zn catalyst at differing cycles.

Table S1 Optimized structure of polysulfide intermediates on the surface of metal clusters

	Fe	Co	Ni	Cu	Zn	FeCo$_5$	FeCo$_2$	FeCo	Fe$_2$Co	Fe$_5$Co
Clean										
Li$_2$S$_2$*										
Li$_2$S$_4$*										
Li$_2$S$_6$*										
Li$_2$S$_8$*										
	FeNi$_5$	FeNi$_2$	FeNi	Fe$_2$Ni	Fe$_5$Ni	FeCu$_5$	FeCu$_2$	FeCu	Fe$_2$Cu	Fe$_5$Cu
Clean										
Li$_2$S$_2$*										

	FeZn$_5$	FeZn$_2$	FeZn	Fe$_2$Zn	Fe$_5$Zn	CoNi$_5$	CoNi$_2$	CoNi	Co$_2$Ni	Co$_5$Ni

Li$_2$S$_4$*

Li$_2$S$_6$*

Li$_2$S$_8$*

Clean

Li$_2$S$_2$*

Li$_2$S$_4$*

Li$_2$S$_6$*

Li$_2$S$_4$*										
Li$_2$S$_6$*										
Li$_2$S$_8$*										
	FeZn$_5$	FeZn$_2$	FeZn	Fe$_2$Zn	Fe$_5$Zn	CoNi$_5$	CoNi$_2$	CoNi	Co$_2$Ni	Co$_5$Ni
Clean										
Li$_2$S$_2$*										
Li$_2$S$_4$*										
Li$_2$S$_6$*										

Li$_2$S$_6$*					
Li$_2$S$_8$*					

Table S2 Zero-point energy (ΔZPE) and entropy (TΔS) of polysulfide intermediates on the surface of metal clusters

	ΔZPE / eV				TΔS / eV			
	$Li_2S_2^*$	$Li_2S_4^*$	$Li_2S_6^*$	$Li_2S_8^*$	$Li_2S_2^*$	$Li_2S_4^*$	$Li_2S_6^*$	$Li_2S_8^*$
Fe	0.15	0.21	0.29	0.32	0.16	0.2	0.29	0.25
Co	0.14	0.21	0.27	0.33	0.16	0.2	0.26	0.32
Ni	0.16	0.23	0.26	0.35	0.15	0.26	0.23	0.34
Cu	0.16	0.22	0.29	0.35	0.18	0.24	0.29	0.34
Zn	0.15	0.22	0.27	0.33	0.16	0.2	0.27	0.32
FeCo$_5$	0.15	0.22	0.28	0.33	0.16	0.21	0.25	0.28
FeCo$_2$	0.16	0.21	0.27	0.35	0.16	0.24	0.27	0.31
FeCo	0.14	0.22	0.27	0.34	0.16	0.24	0.28	0.34
Fe$_2$Co	0.14	0.23	0.29	0.34	0.17	0.25	0.29	0.33
Fe$_5$Co	0.15	0.23	0.26	0.33	0.16	0.2	0.25	0.29
FeNi$_5$	0.16	0.22	0.28	0.33	0.17	0.21	0.26	0.3
FeNi$_2$	0.16	0.21	0.28	0.34	0.15	0.22	0.25	0.31
FeNi	0.15	0.22	0.29	0.35	0.16	0.25	0.28	0.35
Fe$_2$Ni	0.16	0.23	0.27	0.33	0.17	0.22	0.29	0.34
Fe$_5$Ni	0.16	0.23	0.29	0.35	0.16	0.26	0.28	0.34
FeCu$_5$	0.13	0.22	0.26	0.35	0.16	0.22	0.27	0.33
FeCu$_2$	0.16	0.20	0.27	0.33	0.18	0.23	0.27	0.33
FeCu	0.15	0.23	0.28	0.32	0.16	0.24	0.29	0.32
Fe$_2$Cu	0.16	0.23	0.27	0.34	0.18	0.25	0.28	0.33

Fe₅Cu	0.14	0.22	0.27	0.34	0.16	0.2	0.26	0.28
FeZn₅	0.14	0.22	0.28	0.35	0.15	0.22	0.28	0.33
FeZn₂	0.16	0.21	0.26	0.35	0.17	0.23	0.27	0.32
FeZn	0.15	0.22	0.27	0.35	0.16	0.21	0.25	0.35
Fe₂Zn	0.14	0.23	0.27	0.35	0.16	0.24	0.27	0.34
Fe₅Zn	0.15	0.23	0.29	0.32	0.15	0.25	0.27	0.27
CoNi₅	0.15	0.21	0.28	0.34	0.16	0.26	0.26	0.29
CoNi₂	0.15	0.22	0.28	0.33	0.16	0.25	0.26	0.31
CoNi	0.14	0.21	0.27	0.34	0.15	0.23	0.25	0.32
Co₂Ni	0.16	0.22	0.26	0.35	0.18	0.22	0.29	0.31
Co₅Cu	0.16	0.23	0.27	0.35	0.17	0.22	0.28	0.34
CoCu₅	0.14	0.22	0.28	0.34	0.16	0.24	0.27	0.34
CoCu₂	0.15	0.22	0.29	0.33	0.15	0.23	0.26	0.35
CoCu	0.14	0.21	0.28	0.33	0.17	0.24	0.28	0.34
Co₂Cu	0.15	0.23	0.27	0.33	0.16	0.25	0.29	0.35
Co₅Cu	0.16	0.22	0.27	0.34	0.18	0.23	0.28	0.33
CoZn₅	0.15	0.21	0.29	0.34	0.15	0.24	0.28	0.32
CoZn₂	0.16	0.22	0.26	0.33	0.16	0.24	0.26	0.32
CoZn	0.15	0.23	0.28	0.34	0.15	0.23	0.27	0.34
Co₂Zn	0.15	0.21	0.28	0.35	0.16	0.25	0.27	0.33
Co₅Zn	0.14	0.22	0.27	0.34	0.18	0.23	0.26	0.3
NiCu₅	0.16	0.23	0.27	0.33	0.16	0.23	0.28	0.29

NiCu$_2$	0.14	0.22	0.28	0.34	0.16	0.24	0.25	0.3
NiCu	0.15	0.21	0.29	0.33	0.15	0.25	0.24	0.31
Ni$_2$Cu	0.14	0.23	0.27	0.34	0.18	0.22	0.24	0.32
Ni$_5$Cu	0.16	0.22	0.27	0.35	0.16	0.22	0.25	0.31
NiZn$_5$	0.16	0.23	0.29	0.35	0.17	0.24	0.26	0.31
NiZn$_2$	0.14	0.21	0.27	0.33	0.18	0.23	0.26	0.32
NiZn	0.16	0.22	0.26	0.34	0.16	0.24	0.27	0.33
Ni$_2$Zn	0.16	0.23	0.27	0.33	0.16	0.23	0.28	0.34
Ni$_5$Zn	0.14	0.21	0.28	0.33	0.17	0.22	0.27	0.31
CuZn$_5$	0.15	0.23	0.26	0.34	0.15	0.24	0.25	0.32
CuZn$_2$	0.16	0.21	0.27	0.33	0.15	0.24	0.27	0.34
CuZn	0.15	0.23	0.29	0.35	0.18	0.24	0.28	0.32
Cu$_2$Zn	0.15	0.22	0.27	0.33	0.16	0.25	0.29	0.35
Cu$_5$Zn	0.15	0.22	0.28	0.33	0.16	0.22	0.26	0.34

Table S3 Performance comparison of reported catalysts in Li-S batteries

	Catalyst	S areal loading mg cm^{-2}	Sulfur content %	Initial discharge capacity mAh g^{-1}	Capacity decay %, per cycle	Rate C	Reference
Heterogeneous catalysis	MgB$_2$	9.3	60	850	0.22 % 100 cycles	0.2	S1
	MoN-VN	3	58.5	708	0.068 % 500 cycles	2	S2
	MoP	6	61	~ 850	0.05 % 50 cycles	0.08	S3
	Ni$_3$FeN	4.8	63	1000	1.67 % 15 cycles	0.1	S4
	TiO$_2$-TN	4.3	64	~ 500	0.016 % 2000 cycles	1	S5
	Black P	8	60	~ 610	0.06 % 200 cycles	0.1	S6
	TiO$_2$-Ti$_3$C$_2$T$_x$	5.1	75	~ 700	0.035 % 200 cycles	0.5	S7
	VS$_2$	1.3	56	830	0.052 % 300 cycles	0.5	S8
	SAV	2	68	780	0.073 % 400 cycles	0.5	S9
	ReS$_2$	4.8	62	~ 400	0.22 % 131 cycles	0.05	S10
	Co-N/G	6	67.5	850	0.029 % 100 cycles	0.2	S11
Homogeneous catalysis	CoCp$_2$	4.8	63	1150	1.52 % 20 cycles	0.05	S12
	DMDS	4	49	1320	0.97 % 25 cycles	0.03	S13
	NiCl$_2$-DME	1	56	750	0.13 % 100 cycles	0.5	S14
	CoZn	0.5	72	1311		0.2	This work
		0.5		1021	0.05 % 500 cycles	1.0	
		5		821	0.21 % 200 cycles	1.0	

Supplementary Discussion

Exchange current density computed from Tafel-equation. Exchange current density refers to the reaction rate at zero overpotential obtained from:[S15]

$$\eta = A \times \log (J/J_0) \tag{1}$$

in which η, A, J, J_0 are, respectively, overpotential, Tafel-slope, measured current density, and exchange current density. The exchange current density is computed based on linear-fitting, namely, $\eta \sim \log J$.

Electron-transfer numbers computed from Koutecký-Levich (K-L) equation. The electron-transfer numbers for a specific reaction are determined from the Koutecký-Levich (K-L) equation.[S16] This is a measures of electric current from an electrochemical reaction in relation to kinetic activity and mass transport of reactants. The K-L equation is:

$$\frac{1}{J} = \frac{1}{J_k} + \frac{1}{J_D} = \frac{1}{J_k} + \frac{1}{B\omega^{1/2}} \tag{2}$$

where J, J_k, and J_D, are respectively, measured, kinetic-limited, and diffusion-limited current density. J_k is assumed constant at a particular potential. J_D is proportional to the square-root of angular velocity (ω) as applied in RDE. The proportionality coefficient, B, is given by:

$$B = 0.62 \, D^{2/3} \, \nu^{-1/6} \, nFC \tag{3}$$

in which D is the diffusion coefficient of the reactant, ν the kinematic viscosity of electrolyte, F the Faraday constant, and C concentration of reactant in bulk electrolyte.

Therefore n can be readily deduced from slope of the linear-plot of J^{-1} vs $\omega^{-1/2}$ (K-L plot) using reported parameters.[S16]

Computation of activation energy. Activation energy is determined via the Arrhenius-equation:

$$K = Ae^{-\,E_a/RT} \tag{4}$$

in which k is reaction rate, illustrated by the charge-transfer resistance (R_{ct}) obtained from fitted EIS-plots, E_a the activation energy, A pre-exponential factor, R gas constant and T temperature. Therefore E_a can be computed from slope of the linear-plot of ln R_{ct} vs 1/T.[S15]

References

1   Pang, Q., Kwok, C. Y., Kundu, D., Liang, X. & Nazar, L. F. Lightweight metallic MgB_2 mediates polysulfide redox and promises high-energy-density lithium–sulfur batteries. *Joule* **3**, 136-148 (2019).

2   Ye, C. *et al.* 2D MoN-VN heterostructure to regulate polysulfides for highly efficient lithium-sulfur batteries. *Angew. Chem. Int. Ed.* **57**, 16703-16707 (2018).

3   Yang, Y. *et al.* Electrocatalysis in lithium sulfur batteries under lean electrolyte conditions. *Angew. Chem. Int. Ed.* **57**, 15549-15552 (2018).

4   Zhao, M. *et al.* Activating inert metallic compounds for high-rate lithium–sulfur batteries through in-situ etching of extrinsic metal. *Angew. Chem. Int. Ed.* **58**, 3779-3783 (2019).

5   Zhou, T. *et al.* Twinborn TiO_2–TiN heterostructures enabling smooth trapping–diffusion–conversion of polysulfides towards ultralong life lithium–sulfur batteries. *Energy Environ. Sci.* **10**, 1694-1703 (2017).

6   Xu, Z.-L. *et al.* Exceptional catalytic effects of black phosphorus quantum dots in shuttling-free lithium sulfur batteries. *Nat. Commun.* **9**, 4164 (2018).

7   Jiao, L. *et al.* Capture and catalytic conversion of polysulfides by in-situ built TiO_2-MXene heterostructures for lithium–sulfur batteries. *Adv. Energy Mater.* **9**, 1900219 (2019).

8   Zhou, G. *et al.* Catalytic oxidation of Li_2S on the surface of metal sulfides for Li–S batteries. *Proc. Natl. Acad. Sci. U. S. A.* **114**, 840-845 (2017).

9   Zhou, G. *et al.* Theoretical calculation guided design of single-atom catalysts toward fast kinetic and long-life Li–S batteries. *Nano Lett.* **20**, 1252-1261 (2020).

10   He, J., Bhargav, A., Yaghoobnejad Asl, H., Chen, Y. & Manthiram, A. 1T '-ReS_2 nanosheets in-situ grown on carbon nanotubes as a highly efficient polysulfide electrocatalyst for stable Li-S batteries. *Adv. Energy Mater.* **10**, 2001017 (2020).

11   Du, Z. *et al.* Cobalt in nitrogen-doped graphene as single-atom catalyst for high-sulfur content lithium-sulfur batteries. *J. Am. Chem. Soc.* **141**, 3977-3985 (2019).

12   Zhao, M. *et al.* Dictating high-capacity lithium-sulfur batteries through redox-mediated lithium sulfide growth. *Small Methods* **4**, 1900344 (2020).

13   Chen, S. *et al.* High capacity of lithium-sulfur batteries at low electrolyte/sulfur ratio enabled by an organosulfide containing electrolyte. *Nano Energy* **31**, 418-423 (2017).

14   Luo, C. *et al.* An organic nickel salt-based electrolyte additive boosts homogeneous catalysis for lithium-sulfur batteries. *Energy Storage Mater.* **33**, 290-297 (2020).

15   Peng, L. *et al.* A fundamental look at electrocatalytic sulfur reduction reaction. *Nat. Catal.* **3**, 762-770 (2020).

16   Lu, Y.-C., He, Q. & Gasteiger, H. A. Probing the Lithium–Sulfur Redox Reactions: A Rotating-Ring Disk Electrode Study. *J. Phy. Chem. C* **118**, 5733-5741 (2014).

Chapter 6: Unraveling the catalyst-solvent interactions in lean-electrolyte sulfur reduction electrocatalysis in Li−S batteries

6.1 Introduction and significance

Sulfur is often an industrial waste. Its catalytic reduction is important for metal−sulfur batteries. However, the reported electrocatalysts generally exhibit high activity only with a large excess of electrolyte. Herein, we have proposed a general rule to boost lean-electrolyte sulfur reduction by controlling the catalyst-solvent interactions. As evidenced by synchrotron-based analysis, in-situ spectroscopy and theoretical computations, the catalyst-solvent binding strength plays a crucial role in lean-electrolyte performance. Benefitting from the strong interaction between solvent molecules and cobalt catalyst, the lithium−sulfur battery achieves stable cycling with only 0.22% capacity decay per cycle under lean-electrolyte conditions. Compared to the battery with flooded electrolyte, the lean-electrolyte battery with an electrolyte/sulfur mass ratio of 4.2 maintains 79% capacity, which is the highest capacity retention among systems with lowest electrolyte dosages reported so far. This work presents a mechanistic insight into catalyst-solvent interactions to reduce electrolyte dosage for practical metal−sulfur batteries. The highlights of this work include:

➢ **The first demonstration of catalyst-solvent interaction in lean-electrolyte sulfur electrocatalysis.** The comparative study of *3d*, *4d*, *5d* metallic catalysts (Co, Rh, Pt) shows that the metal-solvent binding strength plays a decisive role in improving the lean-electrolyte performance.

➢ **Deep mechanistic insight into local solvation environment.** Solvent molecules bind with metal catalysts through metal-oxygen bond involving *d-2p* orbital hybridizations. Low

occupancy of anti-bonding O *2p* orbital electron states among solvents results in strong adsorption between solvent and catalysts.

➢ **Low electrolyte dosage for practical Li−S batteries.** Benefitting from the strong binding between solvent molecules and Co catalyst, the Li−S battery achieves stable cycling with only 0.22% capacity decay per cycle under lean-electrolyte conditions. Compared to the battery with flooded electrolyte, the lean-electrolyte battery with an electrolyte/sulfur mass ratio of 4.2 retains its 79% capacity, which is the highest capacity retention among batteries with the lowest electrolyte dosages reported so far.

6.2 Unraveling the catalyst-solvent interactions in lean-electrolyte sulfur reduction electrocatalysis in Li−S batteries

This Chapter is included as it appears as a journal paper submitted by **Huan Li**, Rongwei Meng, Yong Guo, Chao Ye, Debin Kong, Bernt Johannessen, Mietek Jaroniec and Shi-Zhang Qiao*. Unraveling the catalyst-solvent interactions in lean-electrolyte sulfur reduction electrocatalysis*, Angew Chemie International Edition*, **In revision**.

Statement of Authorship

Title of Paper	Unraveling the catalyst-solvent interactions in lean-electrolyte sulfur reduction electrocatalysis
Publication Status	☐ Published ☐ Accepted for Publication ☑ Submitted for Publication ☐ Unpublished and Unsubmitted work written in manuscript style
Publication Details	Huan Li, Rongwei Meng, Yong Guo, Chao Ye, Debin Kong, Bernt Johannessen, Mietek Jaroniec and Shi-Zhang Qiao*, Angew Chemie International Edition, In revision.

Principal Author

Name of Principal Author (Candidate)	Huan Li
Contribution to the Paper	Conducted material synthesis, carried out electrochemical tests and wrote the paper
Overall percentage (%)	70
Certification:	This paper reports on original research I conducted during the period of my Higher Degree by Research candidature and is not subject to any obligations or contractual agreements with a third party that would constrain its inclusion in this thesis. I am the primary author of this paper.
Signature		Date	14 June 2022

Co-Author Contributions

By signing the Statement of Authorship, each author certifies that:

i. the candidate's stated contribution to the publication is accurate (as detailed above);

ii. permission is granted for the candidate in include the publication in the thesis; and

iii. the sum of all co-author contributions is equal to 100% less the candidate's stated contribution.

Name of Co-Author	Rongwei Meng
Contribution to the Paper	Carried out electrochemical tests and nuclear magnetic resonance
Signature		Date	14 June 2022

Name of Co-Author	Yong Guo
Contribution to the Paper	Helped with X-ray photoelectron spectra
Signature		Date	14 June 2022

Name of Co-Author	Chao Ye		
Contribution to the Paper	Helped with design of sulfur cathode		
Signature		Date	14 June 2022

Name of Co-Author	Debin Kong		
Contribution to the Paper	Helped with microscopic images		
Signature		Date	14 June 2022

Name of Co-Author	Bernt Johannessen		
Contribution to the Paper	Helped with synchrotron X-ray adsorption spectra		
Signature		Date	14 June 2022

Name of Co-Author	Mietek Jaroniec		
Contribution to the Paper	Revised the manuscript		
Signature		Date	14 June 2022

Name of Co-Author	Shi-Zhang Qiao		
Contribution to the Paper	Supervised the research project		
Signature		Date	14 June 2022

Please cut and paste additional co-author panels here as required.

Unraveling the catalyst-solvent interactions in lean-electrolyte sulfur reduction electrocatalysis for Li−S batteries

Huan Li [a], Rongwei Meng [b], Yong Guo [b], Chao Ye [a], Debin Kong [c], Bernt Johannessen [d], Mietek Jaroniec [e], and Shi-Zhang Qiao *[a]

[a] H. Li, Dr. C. Ye, Prof. S.-Z. Qiao
School of Chemical Engineering & Advanced Materials, The University of Adelaide, Adelaide, SA 5005, Australia
E-mail: s.qiao@adelaide.edu.au;
[b] R. Meng, Y. Guo
School of Chemical Engineering and Technology, Tianjin University, Tianjin 300350, China
[c] Prof. D. Kong
College of New Energy, China University of Petroleum (East China), Qingdao 266580, China
[d] Dr. Bernt Johannessen
Australian Synchrotron, ANSTO, 800 Blackburn Rd, Clayton, VIC 3168, Australia
[e] Prof. Mietek Jaroniec
Department of Chemistry and Biochemistry & Advanced Materials and Liquid Crystal Institute, Kent State University, Kent, OH 44242, USA

Abstract: *Lean-electrolyte condition is important for high-energy Li−S batteries, but sulfur cathode undergoes sluggish reduction kinetics with low electrolyte dosage. This demands efficient catalyst design to promote lean-electrolyte sulfur reduction. However, most of the reported electrocatalysts focus on the catalyst-polysulfide interactions, and these undertakings generally exhibit high activity only with a large excess of electrolyte. Therefore, a mechanistic insight into catalyst design targeted at lean-electrolyte sulfur reduction is still lacking. Herein, we have proposed a general rule to boost lean-electrolyte sulfur reduction by controlling the catalyst-solvent interactions. As evidenced by synchrotron-based analysis, in-situ spectroscopy, theoretical computations and electrochemical tests, the catalyst-solvent binding strength plays a crucial role in lean-electrolyte catalytic activity, electrolyte consumption and battery stability. Strong catalyst-solvent interaction greatly enhances the catalytic activity and battery performance, which is only obvious under lean-electrolyte conditions. Benefitting from the strong interaction between solvent molecules and cobalt catalyst, the Li−S battery achieves stable cycling with only 0.22% capacity decay per cycle under lean-electrolyte conditions. Compared to the battery with flooded electrolyte, the lean-electrolyte battery with an electrolyte/sulfur mass ratio of 4.2 maintains 79% capacity, which is the highest capacity retention among systems with low electrolyte dosages reported so far.*

Introduction

The practical energy density of Li-S battery still remains far from its theoretical value due to excessive use of electrolytes.[1] The electrolyte occupies a large percentage of weight and volume among the whole device, decreasing the actual energy density.[1a, 1b] Therefore, it is important to reduce electrolyte dosage for Li-S batteries. However under lean-electrolyte conditions, the sulfur cathode usually undergoes sluggish reduction kinetics, leading to a low output capacity of battery.[2] This demands efficient catalyst design to promote lean-electrolyte sulfur reduction kinetics. However, most of the reported electrocatalysts exhibit high activity when a large excess of electrolyte is used.[3] The design of catalysts working well under lean electrolyte conditions is still lacking. Although some catalysts were proposed to facilitate sulfur reduction in lean electrolyte,[4] it has been unnoticed that the

operation of Li-S battery is concomitant with electrolyte consumption. The battery gradually runs off electrolyte followed by capacity decay, finally leading to battery failure.[5] These problems are exacerbated especially when the usage of electrolyte decreases. Therefore, a general design rule of catalysts is needed to boost the lean-electrolyte sulfur reduction activity and simultaneously restrain electrolyte loss to increase cycling stability.

Sulfur reduction reaction (SRR) undergoes consecutive reduction from sulfur to polysulfides, and then from polysulfides to sulfide. The conversion efficiency of polysulfide intermediates determines the energy output during SRR.[1i, 6] These polysulfides are solvated by solvent molecules and are electrochemically reduced on the surface of catalyst.[7] Therefore, the local solvent environment of catalyst is critical for polysulfide conversions, which is determined by solvent affinity toward catalysts. Ether solvents are mostly used in Li–S batteries, for example, 1,3-dioxolane (DOL), 1,2-dimethoxyethane (DME).[1a, 1b, 2b] The oxygen atoms in these solvent molecules expose 2p-orbital electrons, which tend to hybridize with d-orbital of metal catalysts.[8] During the operation of Li–S batteries, the shuttle of solvated polysulfides from cathode to anode leads to the consumption of both active sulfur species and solvent molecules. The reported solutions to this problem are often based on the control of catalyst-polysulfide interactions.[1a, 1h, 2b, 2c] However, the catalyst-solvent interactions for lean-electrolyte Li–S batteries have not been studied. The catalyst surface with more adsorbed solvent molecules is expected to promote polysulfide conversion and restrain electrolyte loss. Therefore it is essential to unravel the role of local solvent environments on the catalyst surface for lean-electrolyte sulfur reduction.

In this work, we present a general rule to boost lean-electrolyte sulfur reduction by controlling the catalyst-solvent interactions. Co, Rh, Pt are selected as comparative model catalysts because these metals are typical 3d, 4d and 5d catalysts which are chemically stable during SRR.[9] It is found that the strength of catalyst-solvent interaction plays a decisive role on lean-electrolyte SRR activity, electrolyte consumption and battery stability. Synchrotron-based X-ray adsorption fine structures are used to confirm metal-oxygen binding between catalyst and solvent molecules. Theoretical computation further reveals that
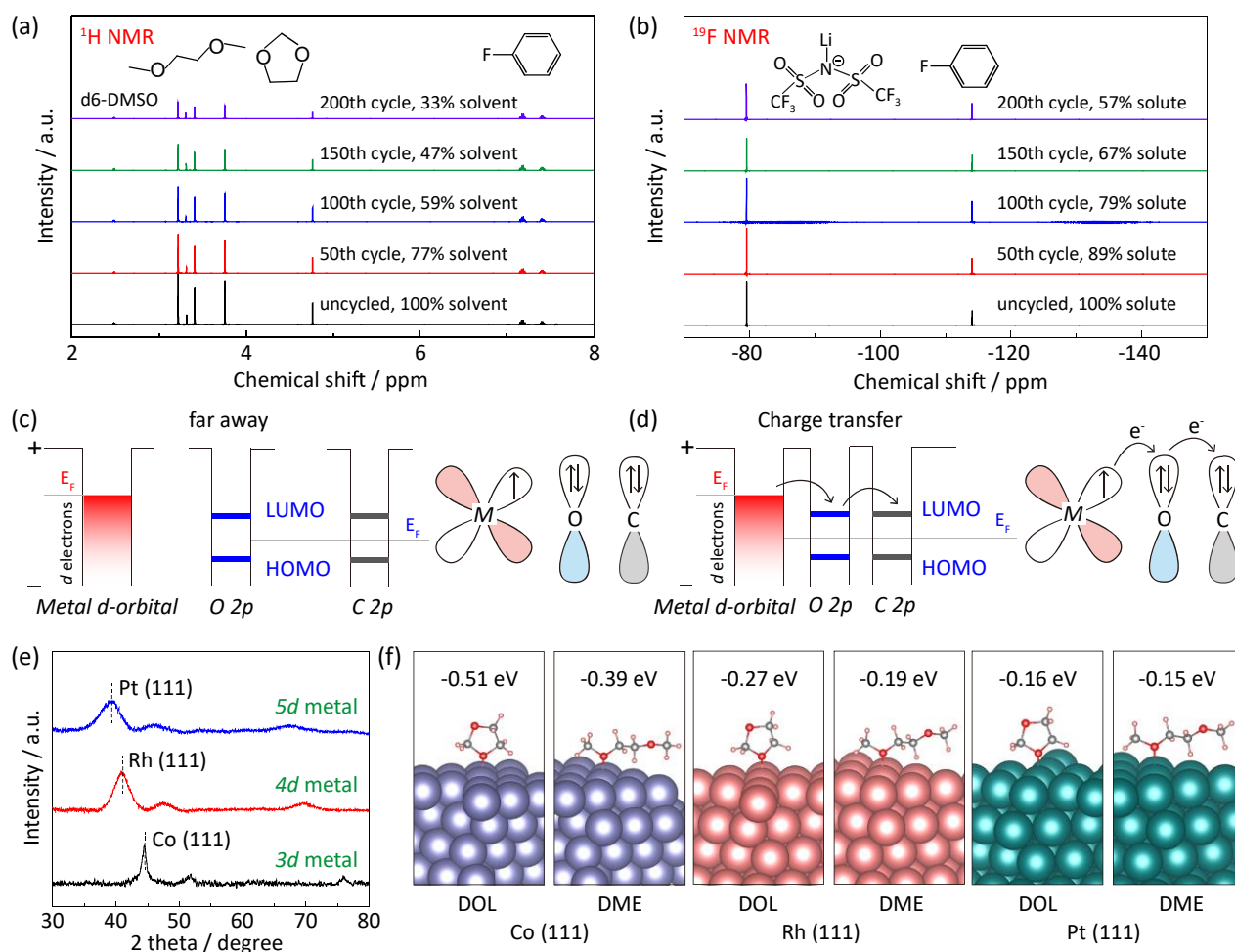
Figure 1 Consumption of solvents and demonstration of catalyst-solvent interactions. (a) ^{1}H and **(b)** ^{19}F NMR spectra of electrolytes extracted from Li–S batteries at different cycles. [1]H spectra are used to quantify the content of DOL/DME solvent, and ^{19}F spectra are used to determine the amounts of LiTfSI solute. A known amount of fluorobenzene (0.1 M) is used as internal reference, and its peak area is normalized to 100%; Scheme of the energy levels of a metal (left) and a solvent molecule (right): **(c)** when they are far away from each other; **(d)** charge transfer; **(e)** XRD patterns of prepared Co, Rh, Pt metal catalysts on graphene substrates; **(f)** Optimized models of DOL/DME solvent molecules on the surface of Co (111), Rh (111) and Pt (111).

lower occupancy of anti-bonding O 2p orbital electron states of adsorbed solvent results in the stronger interaction. Compared to Rh and Pt catalysts, the greater SRR activity of Co catalyst is only obvious under lean electrolyte conditions, including higher kinetic current, lower Tafel slope and more Li_2S deposition. This highlights the significance of catalyst-solvent interactions to boost lean-electrolyte performance. As a result, the Li−S battery exhibits stable cycling while maintaining a high lean-electrolyte capacity with low electrolyte consumption.

Results and Discussion

Consumption of solvents and demonstration of catalyst-solvent binding. The electrolyte consumption during cycling of Li–S battery was quantified by nuclear magnetic resonance (NMR) spectra (**Fig. S1**).[5a, 10] ^{1}H and ^{19}F NMR spectra were respectively investigated for solvents and solute, because H and F signals come exclusively from the DOL/DME solvent and Lithium bis(trifluoromethane sulfonimide) solute (LiTfSI) (**Fig. S2**). The electrolyte consumption is mainly caused by polysulfide shuttle and anode corrosion. As shown in **Figs. 1a** and **1b**, the contents

of both solvent and solute gradually decrease during battery cycling. Only 33% of solvent remains after 200 cycles, in contrast 57% of original content of lithium salt solute is retained. This indicates the significant consumption of solvent during battery cycling, leading to the dramatic capacity decay and battery failure. Therefore, it is essential to restrain the solvent loss in Li–S batteries.

Considering that the oxygen 2p-orbital electrons among the solvent molecules are exposed to the outer shell, these electrons can be effectively used to bind these solvent molecules with metal catalysts through d-2p hybridization. **Fig. 1c** shows a schematic representation of the energy levels of a metal and a typical solvent molecule when they are separated from each other. When the solvent molecule contacts with the metal, the outer-shell s-orbital electrons of oxygen become more reactive and O-C bonds are impaired. The d-orbital electrons on the metal surface transfer through the unoccupied energy level of O 2p-orbital of solvent molecule, and finally are accumulated on the adjacent carbon atom (**Fig. 1d and Fig. S3**). As a result, the electronic density of solvent rearranges due to the charge transfer at the interface, forming metal- oxygen bond between metal catalysts and solvent molecules.
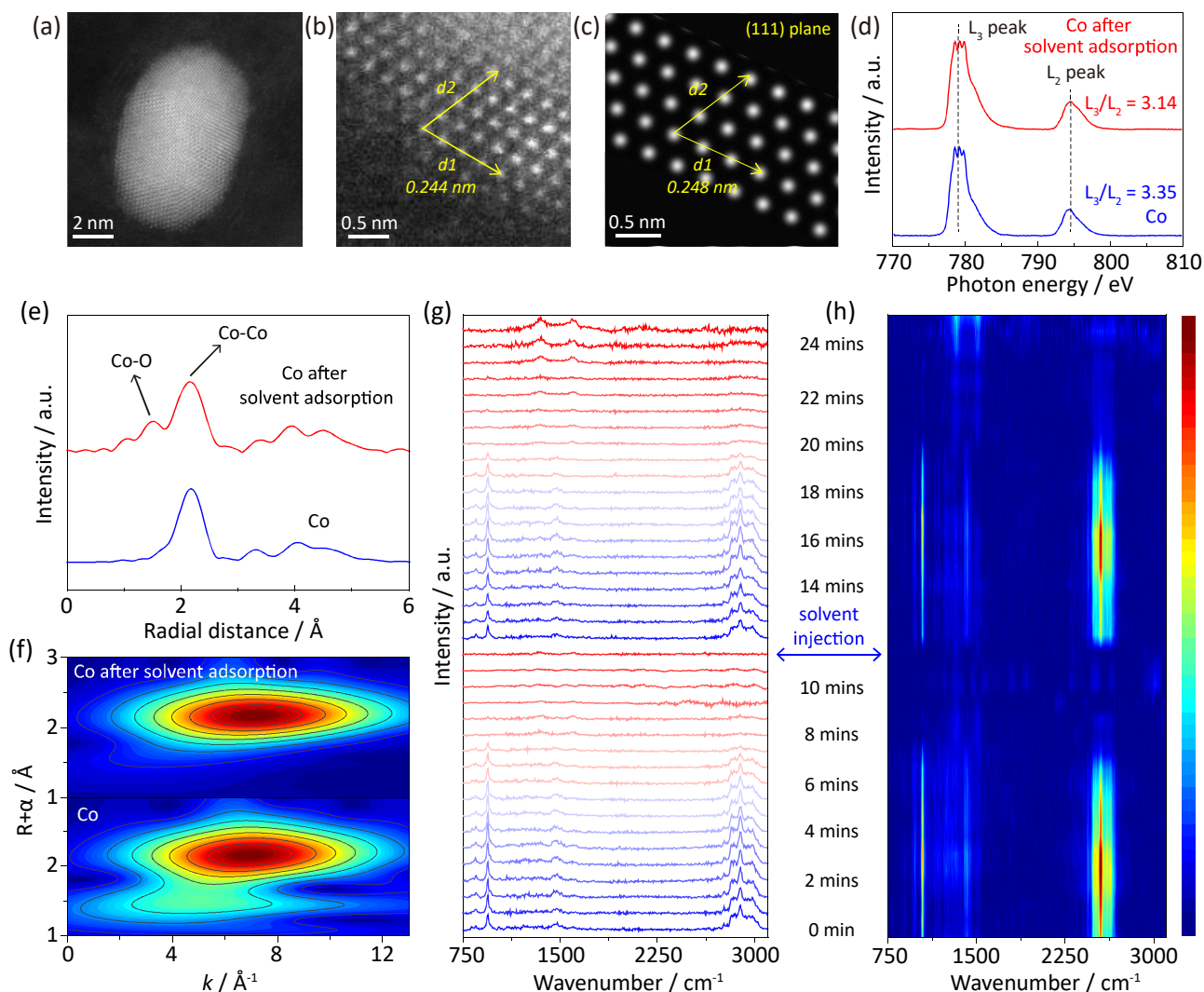
Figure 2 Spectroscopic confirmation of catalyst-solvent interaction. (a, b) High-resolution TEM images of Co catalyst; **(c)** Simulated image of Co (111) plane that coincides well with the experimental observations; **(d)** Co L-edge NEXAFS spectra and **(e)** Co K-edge EXAFS spectra with **(f)** corresponding wave-transform patterns of pristine Co catalyst and after solvent adsorption; *In-situ* Raman spectra revealing the local solvent environment on Co surface: **(g)** Time-dependent stacked plots and **(h)** contour pattern.

To investigate the binding strength of metal-oxygen bonds, typical 3d, 4d, 5d nanometal catalysts of Co, Rh, Pt are comparatively synthesized with dominating (111) crystal planes as evidenced by to the X-ray diffraction patterns (**Fig. 1e**, **Fig. S4**). Theoretical computations based on density functional theory (DFT) are used to model the interactions of DOL/DME molecules on the metal (111) surfaces. As shown in **Fig. 1f**, the DOL and DME molecules prefer to be adsorbed on the metal surfaces via vertical orientations (**Fig. S5**). All these metals bind with solvent molecules via metal-oxygen bonds, confirming the efficient catalyst-solvent binding at the interface. Co metal catalyst exhibits much stronger binding with DOL and DME molecules compared to those on Rh and Pt catalysts (**Fig. S6**). Therefore, Co metal catalyst is expected to demonstrate greater activity than Rh and Pt under lean electrolyte conditions.

Spectroscopic confirmation of catalyst-solvent interaction.
To experimentally unravel the catalyst-solvent binding, the synchrotron based near-edge X-ray adsorption fine-structure (NEXAFS), extended X-ray adsorption fine structure (EXAFS), and in-situ Raman spectra were used. As shown in **Fig. 2a** and

Fig. S7, Co nanoparticles are uniformly distributed on the 3D graphene network. The high-resolution transmission microscopy (TEM) image confirms the dominated (111) crystal plane (**Figs. 2b** and **2c**). The content of Co is 14.2 wt.% on graphene substrate (**Fig. S8**) and loading of other metal nanoparticles for Rh and Pt does not alter the properties of graphene (**Fig. S9**). The Co catalyst presents excellent properties toward surface wetting with solvents as suggested by the contact angles (**Fig. S10**). **Fig. 2d** shows the NEXAFS spectra of pristine Co catalyst and Co after solvent adsorption. The L_3/L_2 intensity decreases from 3.35 to 3.14 after solvent adsorption, indicating a higher valence of Co while binding with DOL/DME molecules (**Fig. S11**).[11] The Co K-edge EXAFS spectra are used to reveal the origin of higher valence of Co catalyst after solvent adsorption. As shown in **Fig. 2e**, an obvious scattering radial distance of ~1.8 Å is observed after adsorption of solvent, which belongs to the Co-O bond between catalyst and solvent molecules (**Figs. S12** and **S13**). The wavelet-transform contour in **Fig. 2f** confirms the Co-O bond by comparing with the spectrum of the CoO standard reference (**Fig. S14**). The X-ray photoelectron spectra (XPS) coincide well with the NEXAFS and EXAFS analysis (**Fig. S15**). In-situ Raman
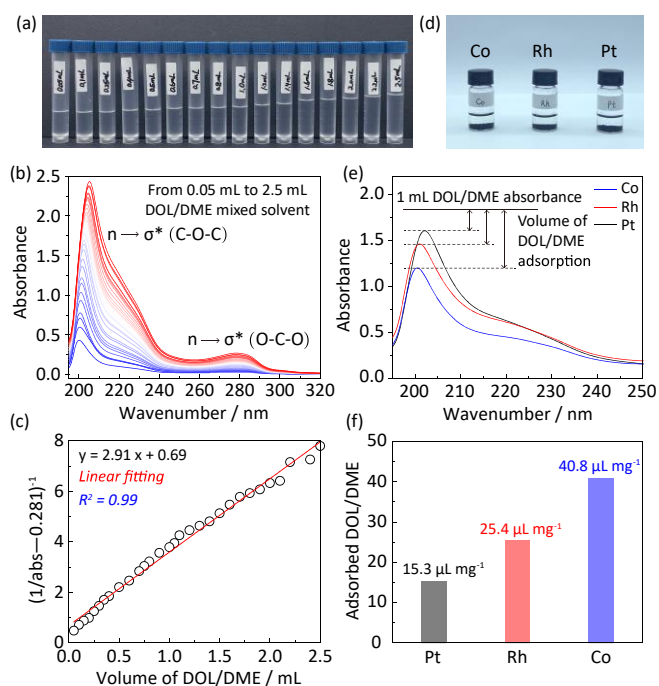
Figure 3 Quantifying the solvent adsorption on catalyst surfaces. (a) Digital photograph of standard solutions with 3 mL of ethanol and DOL/DME solvent ranging from 0.05 to 2.5 mL, which are used to plot the standard relation between the solvent volume and UV-vis absorbance; **(b)** The stacked UV-vis plots of solutions in (a); **(c)** Linear fitting between the UV-vis absorbance and DOL/DME volume; **(d)** Digital photograph of Co, Rh and Pt catalysts immersed in DOL/DME solvent. The supernatant is used to quantify the solvent adsorption; **(e)** UV-vis plots for 1 mL of DOL/DME solvent on Co, Rh and Pt catalysts; **(f)** The quantified adsorbed volume of solvent for Co, Rh and Pt catalysts.

spectra were used to characterize the local solvent environment and solvent retention on the catalyst surface.[12] The Co catalyst was loaded in an open cell with DOL/DME. Due to the volatile nature of DOL and DME, these solvent molecules tend to evaporate from the material surface. **Fig. 2g** presents the time-dependent Raman spectra on the surface of Co catalyst with DOL/DME adsorption, and its corresponding contour pattern is shown in **Fig. 2h**. The peaks at ~940, ~1460 and ~2900 cm^{-1} are assigned to DOL and DME molecules (**Fig. S16**). Due to the strong binding between Co catalyst and solvent, the solvent shows a long retention time of ~7 mins under atmosphere. In contrast, the solvent molecules can only retain for ~4 mins without Co catalyst (**Fig. S17**). The above results confirm the catalyst-solvent binding via Co-O bond, and Co catalysts exhibit better affinity and strong adsorption of solvent molecules.

Quantifying the solvent adsorption on catalyst surfaces. Both DOL and DME are ether molecules, and the C-O bonds demonstrate obvious absorbance in the ultraviolet region.[13] Therefore, ultraviolet–visible spectroscopy (UV-vis) is a good method to quantify the solvent adsorption on different catalysts.[7b] Prior to the quantification, a standard plot that correlates the UV-vis absorbance and DOL/DME volume should be made. Ethanol was selected to dissolve DOL/DME because ethanol shows different UV-vis peak positions and weak peak intensity as compared to DOL/DME (**Fig. S18**). **Fig. 3a** shows the digital photograph of standard solutions with 3 mL of ethanol and DOL/DME solvent ranging from 0.05 to 2.5 mL (**Fig. S19**). The

corresponding UV-vis curves are shown in **Fig. 3b**. Peaks at ~205 and ~280 nm are assigned to the C-O bonds in DOL/DME, which are caused by the electron transition to anti-bonding σ* orbital (**Fig. S20**). The dominated peak at ~205 nm is used to plot the standard relation between the solvent volume and UV absorbance. As a result, a well-fitted linear scaling relationship is seen in **Fig. 3c**, allowing to obtain the specified solvent volumes at different UV-vis absorbance (**Figs. S21** and **S22**). To compare the adsorption ability of catalysts, the Co, Rh, Pt catalysts were immersed in DOL/DME solvent (**Fig. 3d**). After adsorption, 1 mL of supernatant was taken out and mixed with 3 mL of ethanol for UV-vis test. As shown in **Fig. 3e**, the supernatant after adsorption on Co exhibits the lowest peak intensity around ~205 nm, confirming the strongest interaction of Co with solvent molecules. As a result, Co catalyst is quantified with solvent adsorption of 40.8 $\mu L\ mg^{-1}$, which is much higher than those of 25.4 and 15.3 $\mu L\ mg^{-1}$ for Rh and Pt catalysts, respectively (**Fig. 3f**).

Lean-electrolyte sulfur reduction electrocatalysis. To investigate the SRR activity under lean-electrolyte conditions, the cyclic voltammetry (CV) and potential-static Li_2S deposition were comparatively tested for Co, Rh and Pt catalysts. **Fig. 4a** compares the CV curves of Li–S batteries with Co, Rh and Pt catalysts at 0.2 mV s^{-1}, which were tested with an electrolyte to sulfur (E/S) ratio of 4.2 $\mu L\ mg^{-1}$. Two distinct peaks around 2.3 V and 2.05 V are attributed to the reduction from sulfur to polysulfides, and from polysufides to Li_2S. Co presents a much higher kinetic current for Li_2S deposition of ~2.0 A g^{-1} even with lean electrolyte. This suggests its superior catalytic activity for lean-electrolyte sulfur reduction (**Fig. S23**). **Figs. 4b** and **4c** present the Tafel plots of two reduction ranges for these catalysts. For the reduction from Li_2S_4 to Li_2S, Co exhibits the lowest Tafel slope of 52 mV dec^{-1} and the lowest overpotential of 110 mV (by considering 2.15 V as the equilibrium potential). These results confirm the higher electrocatalytic activity of Co under lean electrolyte conditions.

To confirm higher catalytic activity of Co catalysts to regulate Li_2S precipitation with lean electrolyte, the potential-static discharge was carried out by loading Co, Rh, Pt catalysts on carbon fiber paper with only 15 μL electrolyte addition.[14] The Co electrode exhibited a significantly greater Li_2S precipitation capacity of 151 mAh g^{-1} than Rh and Pt with 124 mAh g^{-1} and 98 mAh g^{-1}, respectively, **Figs. 4d**, **4e** and **4f**. Obviously, Li_2S nucleates and precipitates are seen on the Co-contained cathode surface in the scanning electron microscopy (SEM) image (**Fig. 4g**), which are more pronounced than those on the cathode surfaces with Rh and Pt catalysts (**Figs. 4h** and **4i**). These findings confirm higher activity of Co to catalyze polysulfides into Li_2S products under lean-electrolyte conditions.

Mechanistic insights into catalyst-solvent interaction. The relationship between the adsorption ability of a material and its electronic structure can be schematically explained by the underlying as illustrated in **Fig. 5a**.[15] When a solvent molecule from the electrolyte is adsorbed on the metal surface to form metal-oxygen bond, the electronic states of the metal interact with those of oxygen. Consequently, the hybridized energy levels split into two groups: one is the anti-bonding orbital (σ*) close to Fermi level (E_F), the other is the bonding orbital (σ) positioned far from Fermi level. The difference in the adsorption strength comes both from bonding states and anti-bonding states. A higher occupancy
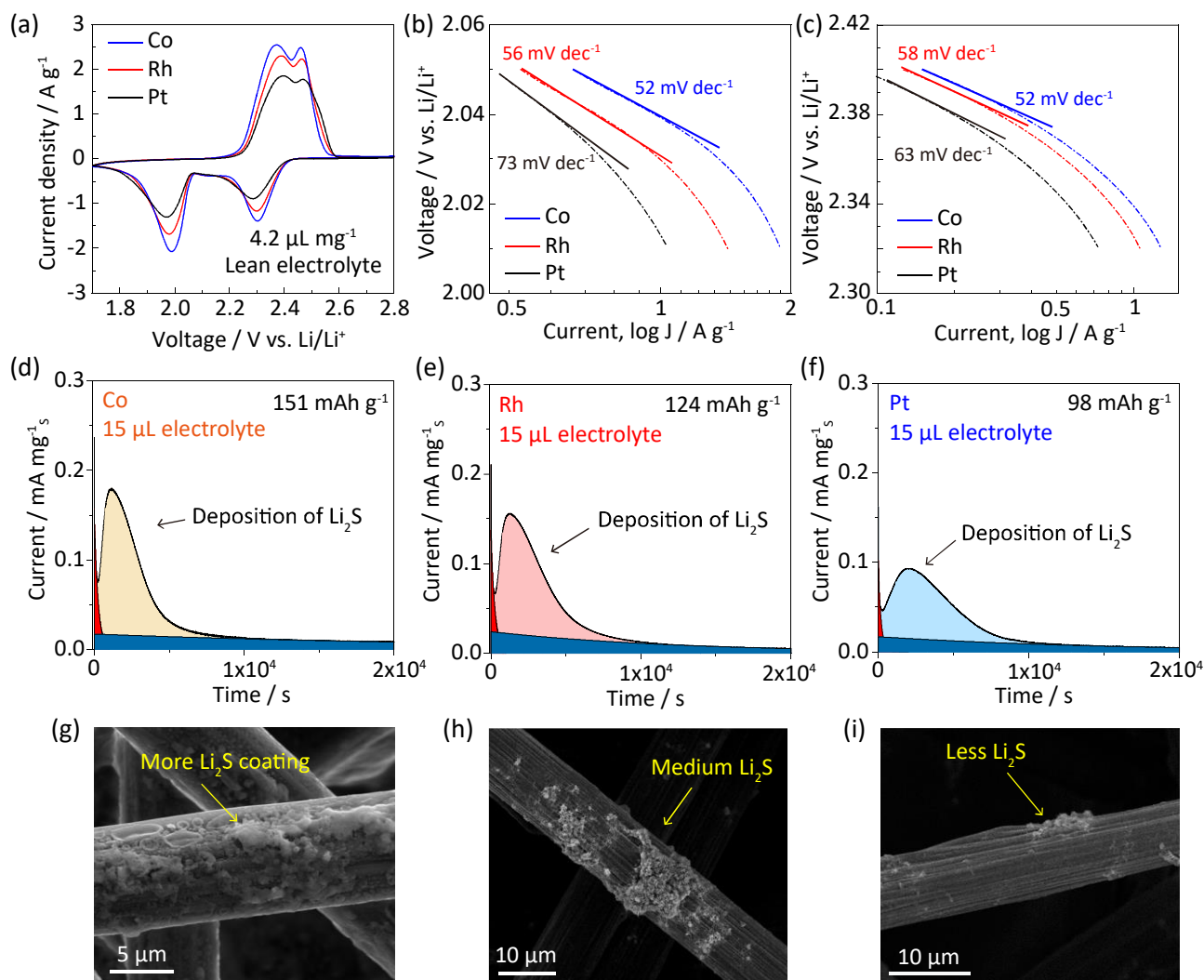
Figure 4 Lean-electrolyte sulfur reduction electrocatalysis. (a) CV curves of Li–S batteries with Co, Rh and Pt catalysts at 0.2 mV s^{-1} under lean electrolyte conditions (E/S = 4.2); Tafel plots for **(b)** the electrocatalytic reduction from polysulfides to Li$_2$S and **(c)** from sulfur to polysulfides; Potential-static discharge curves for Li$_2$S deposition from polysulfides in 15 µL of lean electrolyte with **(d)** Co, **(e)** Rh and **(f)** Pt catalysts; SEM images of Li$_2$S precipitation on carbon fibre using **(g)** Co, **(h)** Rh and **(i)** Pt catalysts.

of bonding states and a lower occupancy of anti-bonding states result in a stronger solvent-metal catalyst interaction. In this work, we introduced projected crystal orbital Hamilton population (pCOHP) to analyze the interaction between the metal catalysts and solvent molecules. We follow the usual way of displaying COHP, namely, drawing bonding contributions to the right and anti-bonding contribution to the left. As shown in **Fig. 5b**, the filling of bonding orbital populations increases from Pt, Rh to Co but the filling of anti-bonding orbital populations decreases. This explains the stronger interaction between Co catalysts and solvent molecules. In addition, we calculated the integrated COHP (ICOHP) by calculating the energy integral up to the highest occupied bands (below Fermi level, E$_F$), which directly gives more quantitative information on the bonding strength. As shown in **Fig. 5b and Fig. S24**, the ICOHP between oxygen atom among DOL molecule and metal atom are -1.01, -0.73 and -0.67 eV for Co, Rh and Pt respectively, and a more negative value of Co confirms its stronger binding with solvent molecules.

The binding strength can be also explained by the charge transfer of solvent molecules on metal surfaces. **Fig. 5c** depicts the charge-transfer patterns of DOL on Pt (111), Rh (111) and Co

(111), where red indicates electron accumulation and blue denotes electron depletion. DOL and DME on Co (111) demonstrates more electrons transferred at the interface compared to those on Rh (111) and Pt (111) (**Figs. 5c, S25 and S26**). The charge-transfer numbers can be further quantified with Bader charge analysis (**Fig. S27**). The surface Co atom shows higher electron depletion of -0.155 while adsorbed with DOL molecule. This depletion is much larger than those of -0.101 and -0.089 for DOL molecule on Rh and Pt. As a result, Co catalyst exhibits the strongest binding with DOL and DME molecules, which are -0.51 and -0.39 eV, respectively. These values are much higher than those on the Rh and Pt surfaces (**Fig. 5d**). These data indicate that the lower occupation of anti-bonding state of Co and efficient charge transfer result in a strong binding between Co and solvent molecules.

Lean-electrolyte electrocatalysis in Li−S batteries. To confirm the effect of lean-electrolyte SRR electrocatalysis on the battery performance, the Li−S batteries with different catalysts were assembled and comparatively 2tested. **Fig. 6a** presents the galvanostatic charge-discharge curves for Li−S batteries using Co,
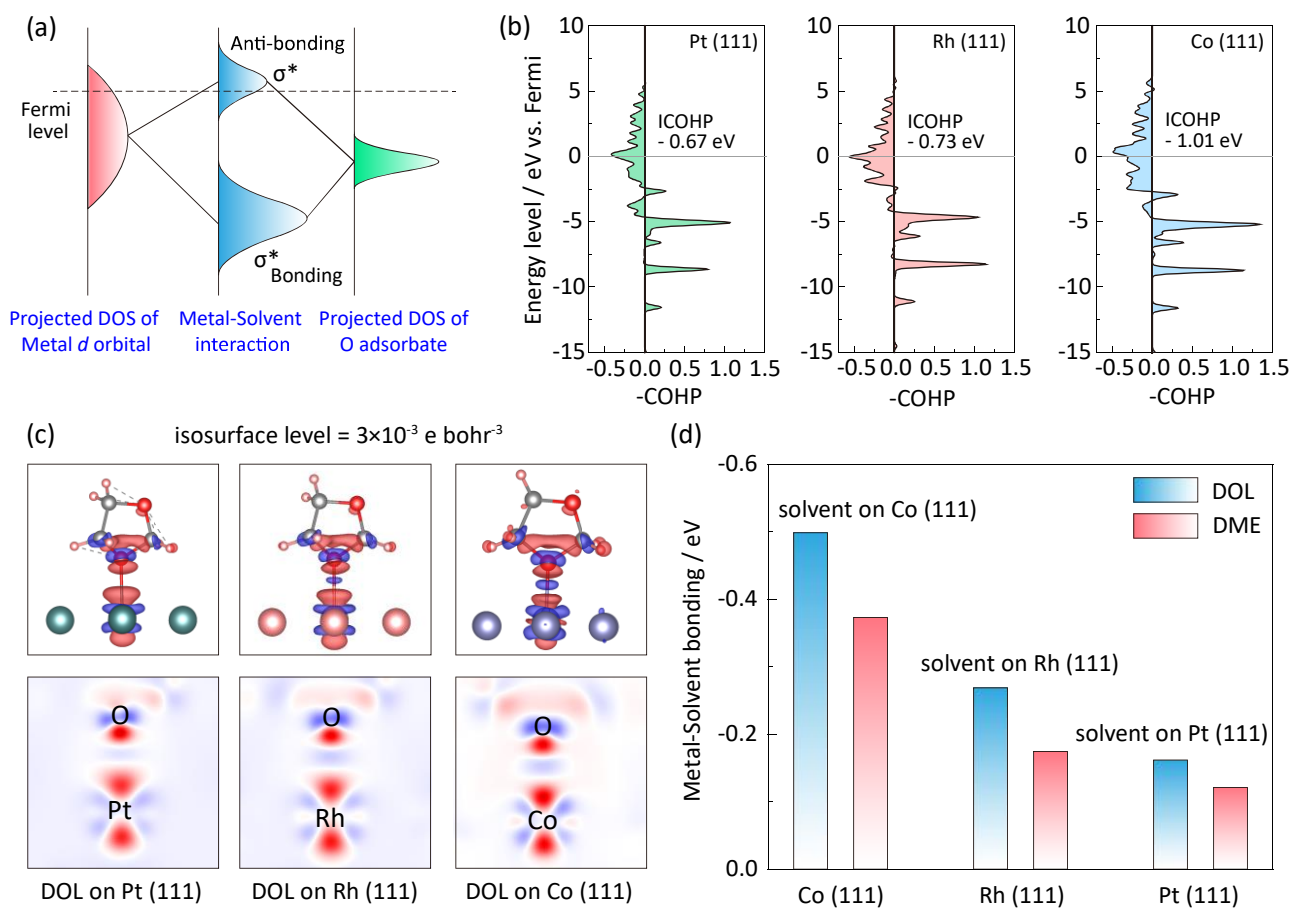
Figure 5 Mechanistic insights into catalyst-solvent interactions. (a) Energy level diagram showing orbital hybridization of metal active sites and solvent adsorbate. σ and σ* indicate bonding and anti-bonding states, respectively; **(b)** Projected crystal orbital Hamilton population (pCOHP) between the surface metal atom and the oxygen atom of DOL molecule. Green filling, Pt; Pink filling, Rh; Blue filling, Co. The insets present the integrated COHP (ICOHP) values; **(c)** Charge-transfer maps of DOL molecules on Pt (111), Rh (111) and Co (111). Red indicates electron accumulation and blue denotes electron depletion; **(d)** Summary of binding strength of DOL and DME molecules on different metal surfaces.

Rh and Pt catalysts with excessive electrolyte (E/S = 30). Co-catalyzed Li−S battery shows a slightly lower specific capacity of 1144 mAh g^{-1} due to the higher binding energy between polysulfides and Co (**Fig. S28**). Too strong binding energy would lead to a lower catalytic activity following Sabatier's principle.[1i] In contrast, Pt-catalyzed battery exhibits a higher capacity due to the greater catalytic activity of Pt (**Fig. S29**). However, under lean-electrolyte conditions (E/S = 4.2), the specific capacity of Pt-catalyzed Li−S battery dramatically decreases to 623 mAh g^{-1}, and the Co-catalyzed battery delivers the highest capacity of 900 mAh g^{-1} (**Fig. 6b**). Therefore, the greater SRR activity of Co catalyst is only obvious under lean electrolyte conditions. Compared to the battery with flooded electrolyte, the lean-electrolyte battery with Co catalyst maintains 79% capacity, which is the highest capacity retention among systems with low electrolyte dosages reported so far (**Table S1**). However, the lean-electrolyte battery with Pt catalyst only retains 45% of its capacity. Therefore, the activity of these catalysts is highly dependent on the electrolyte dosage, and a strong binding between catalyst and solvent contribute a high battery capacity under lean electrolyte conditions (**Fig. 6c, Fig. S30**). Additionally, the high lean-electrolyte catalytic activity of Co can be also confirmed by the lower charge-discharge overpotentials compared with those for the batteries with Rh and Pt, **Fig. S31**. The cycling performances are also compared with lean electrolyte

and flooded electrolyte. Prior to the cycling test, the battery was first charged-discharged at 0.1 C for pre-activation, and the following initial capacity is based on the discharge capacity at the second cycle under 0.2 C. Li−S batteries with Co, Rh and Pt catalysts are able to work steadily upon cycles. This suggests that these metal catalysts are electrochemically stable while used as SRR catalysts in Li−S batteries, coinciding with the previous reports.[9] In the excessive electrolyte, these catalysts show similar battery stability with about ~900 mAh g^{-1} initial capacity and ~60% capacity retention after 400 cycles at 1.0 C (**Fig. 6d**). In contrast, the Co catalyst greatly outperforms other catalysts under lean electrolyte conditions (E/S = 4.2, **Fig. 6e**). Specially, the battery with Co catalyst exhibits an initial capacity of ~900 mAh g^{-1} at 0.2 C, much higher than those of 736 mAh g^{-1} and 627 mAh g^{-1} for Rh- and Pt-catalyzed batteries. Additionally, the Co-catalyzed battery exhibits higher capacity retention during the following cycles. For example, the Co-catalyzed battery exhibits capacity retentions of 69%, 61% and 56% at the 100th, 150th and 200th cycles, respectively which are much higher than the corresponding values for the batteries with Rh and Pt catalysts. The Coulombic efficiency is near ~100% (**Fig. S32**). By comparison, due to the weak binding between Pt and solvent molecules, the battery with Pt catalyst only delivers an initial capacity of ~627 mAh g^{-1} with 41% capacity retention.

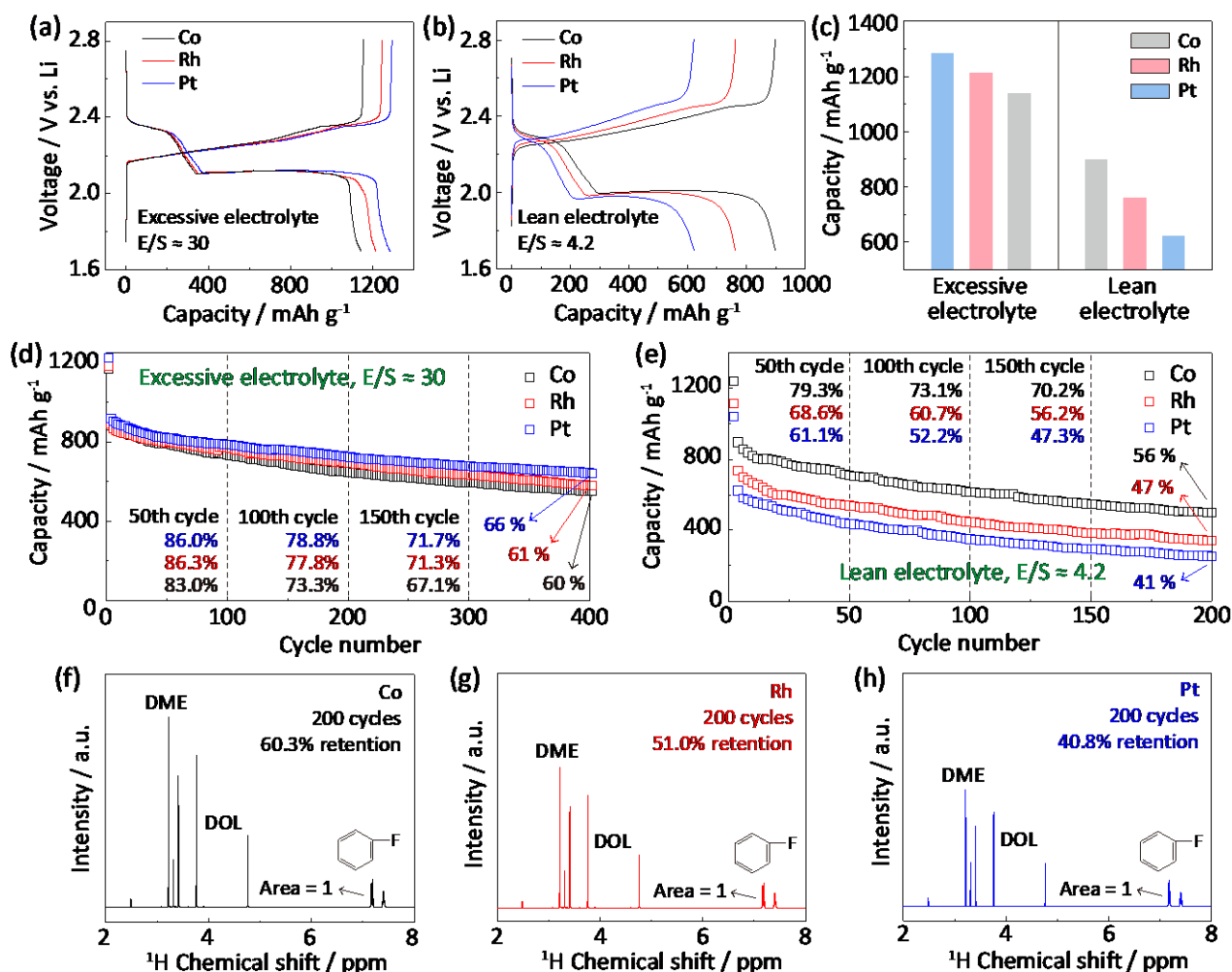After cycling of Li−S batteries, the electrolyte was extracted from

Figure 6 Lean-electrolyte electrocatalysis in Li−S batteries. Galvanostatic charge-discharge curves for Li−S batteries using Co, Rh and Pt catalysts at 0.2 C **(a)** with excessive electrolyte (E/S = 30) and sulfur loading of ~0.5 mg cm^{-2} and **(b)** lean electrolyte (E/S = 4.2) and sulfur loading of ~5 mg cm^{-2}; **(c)** Capacity comparison with Co, Rh and Pt catalysts under flooded and lean electrolyte conditions; Cycling performance for Li−S batteries with Co, Rh and Pt catalysts with **(d)** excessive electrolyte (E/S = 30) with sulfur loading of ~0.5 mg cm^{-2} at 1.0 C and **(e)** lean electrolyte (E/S = 4.2) with sulfur loading of ~5 mg cm^{-2} at 0.2 C; **(f-h)** The solvent retention after 200 cycles for Li−S batteries with Co, Rh and Pt catalysts.

the cell and used for NMR analysis to quantify the electrolyte consumption. Because of the known amount of an internal fluorobenzene reference (0.1 M), the integrated area of DOL and DME peaks can be used to quantify the electrolyte retention. The battery with Co catalyst retains 65% of electrolyte after 200 cycles (**Fig. 6f**), which is much higher than the corresponding values for Rh and Pt catalysts, 54% and 45% respectively (**Figs. 6g** and **6h**). The NMR-determined solvent retentions coincide well with the quantifications by high-performance liquid chromatography (HPLC) (**Fig. S33**). Additionally, chemical shift from 3.6 to 5.0 ppm corresponds to the H signal in DOL, and chemical shift from 3.0 to 3.6 ppm are assigned to DME (**Fig. S2**). The integrations of these regions can give quantitative information for respective retention for each DOL and DME solvent. For Co, Rh and Pt catalysts, the DOL retentions are 60%, 51%, 41% and the DME retentions are 69%, 58%, 50%, respectively (**Fig. S34**). The consumption of DOL is more severe than DME due to the ring-opening reactions of DOL molecules.[16] To quantify the retention of LiTfSI solute, Fourier-transform infrared spectroscopy with attenuated total reflectance mode (FTIR-ATR) was used to detect the -CF$_3$ group in the cycled electrolyte because the -CF$_3$ group comes exclusively from LiTfSI solute. Co-catalyzed batteries

show a retention of 71% for TfSI$^-$ anion, slightly higher than those of 67% and 65% for Rh and Pt catalysts (**Fig. S35**). Compared to the severe solvent consumption with lean electrolyte, the consumption of LiTfSI solute is less, coinciding with our previous findings (**Figs. 1a** and **1b**). This comparison confirms superior ability of Co catalyst to restrain solvent loss (**Table S2**). Therefore, the above results highlight the significance of catalyst-solvent binding on the battery performance under lean electrolyte conditions.

Conclusions

The presented comparative study of 3d, 4d, 5d metal catalysts demonstrates that the catalyst-solvent interaction determines the lean-electrolyte SRR activity, electrolyte consumption and battery stability. The lean-electrolyte performance of Li−S batteries can be boosted via strong catalyst-solvent interactions. This metal-oxygen interaction between metal catalysts and solvent molecules has been confirmed via a series of synchrotron-based analysis, in-situ spectroscopy and theoretical computations. The

strong interaction between Co catalyst and DOL/DME molecules greatly enhance the lean-electrolyte SRR activity such as higher kinetic current, lower Tafel slope and more Li_2S deposition. The greater SRR activity of Co catalyst over Rh and Pt is only obvious under lean-electrolyte conditions, which reveals the significance of strong catalyst-solvent interaction to boost lean-electrolyte SRR performance. As a result, the Li−S battery achieves stable cycling, high capacity retention and low electrolyte consumption under lean electrolyte conditions. The role understanding of thecatalyst-solvent interactions should be helpful for the design of electrocatalysts for lean-electrolyte metal−sulfur batteries.

Acknowledgements

Conflicts of interests

The authors declare no conflict of interest.

Keywords: Sulfur reduction reaction; Electrocatalysis; Catalyst-solvent interactions; Lean electrolyte condition; Li−S batteries

[1]   a) M. Zhao, B. Q. Li, H. J. Peng, H. Yuan, J. Y. Wei, J. Q. Huang, *Angew Chem. Int. Ed.* **2020**, *59*, 12636-12652; b) R. Fang, S. Zhao, Z. Sun, D. W. Wang, H. M. Cheng, F. Li, *Adv. Mater.* **2017**, *29*, 1606823; c) C. Zhao, G.-L. Xu, Z. Yu, L. Zhang, I. Hwang, Y.-X. Mo, Y. Ren, L. Cheng, C.-J. Sun, Y. Ren, X. Zuo, J.-T. Li, S.-G. Sun, K. Amine, T. Zhao, *Nat. Nanotech.* **2020**, *16*, 166-173; d) X. Yang, J. Luo, X. Sun, *Chem. Soc. Rev.* **2020**, *49*, 2140-2195; e) S.-H. Chung, A. Manthiram, *Adv. Mater.* **2019**, *31*, 1901125; f) G. Zhou, H. Chen, Y. Cui, *Nat. Energy* **2022**, *7*, 312-319; g) W. Xue, Z. Shi, L. Suo, C. Wang, Z. Wang, H. Wang, K. P. So, A. Maurano, D. Yu, Y. Chen, L. Qie, Z. Zhu, G. Xu, J. Kong, J. Li, *Nat. Energy* **2019**, *4*, 374-382; h) H. Chen, Z. Wu, M. Zheng, T. Liu, C. Yan, J. Lu, S. Zhang, *Mater. Today* **2022**, *52*, 364-388; i) L. Peng, Z. Wei, C. Wan, J. Li, Z. Chen, D. Zhu, D. Baumann, H. Liu, C. S. Allen, X. Xu, A. I. Kirkland, I. Shakir, Z. Almutairi, S. Tolbert, B. Dunn, Y. Huang, P. Sautet, X. Duan, *Nat. Catal.* **2020**, *3*, 762-770.

[2]   a) G. Li, S. Wang, Y. Zhang, M. Li, Z. Chen, J. Lu, *Adv. Mater.* **2018**, *30*, 1705590; b) Q. Pang, X. Liang, C. Y. Kwok, L. F. Nazar, *Nat. Energy* **2016**, *1*, 16132; c) Y. Song, W. Cai, L. Kong, J. Cai, Q. Zhang, J. Sun, *Adv. Energy Mater.* **2019**, *10*, 1901075.

[3]   a) W. Hua, H. Li, C. Pei, J. Xia, Y. Sun, C. Zhang, W. Lv, Y. Tao, Y. Jiao, B. Zhang, S. Z. Qiao, Y. Wan, Q. H. Yang, *Adv. Mater.* **2021**, *33*, 2101006; b) C. X. Zhao, X. Y. Li, M. Zhao, Z. X. Chen, Y. W. Song, W. J. Chen, J. N. Liu, B. Wang, X. Q. Zhang, C. M. Chen, B. Q. Li, J. Q. Huang, Q. Zhang, *J. Am. Chem. Soc.* **2021**, *143*, 19865-19872; c) Q. Pang, C. Y. Kwok, D. Kundu, X. Liang, L. F. Nazar, *Joule* **2019**, *3*, 136-148; d) L. Wang, W. Hua, X. Wan, Z. Feng, Z. Hu, H. Li, J. Niu, L. Wang, A. Wang,

J. Liu, X. Lang, G. Wang, W. Li, Q. H. Yang, W. Wang, *Adv. Mater.* **2022**, *34*, e2110279; e) Z. Du, X. Chen, W. Hu, C. Chuang, S. Xie, A. Hu, W. Yan, X. Kong, X. Wu, H. Ji, L. J. Wan, *J. Am. Chem. Soc.* **2019**, *141*, 3977-3985; f) Y. R. Zhong, L. C. Yin, P. He, W. Liu, Z. S. Wu, H. L. Wang, *J. Am. Chem. Soc.* **2018**, *140*, 1455-1459.

[4]   a) Y. Yang, Y. Zhong, Q. Shi, Z. Wang, K. Sun, H. Wang, *Angew Chem. Int. Ed.* **2018**, *57*, 15549-15552; b) M. Wang, L. Fan, X. Sun, B. Guan, B. Jiang, X. Wu, D. Tian, K. Sun, Y. Qiu, X. Yin, Y. Zhang, N. Zhang, *ACS Energy Letters* **2020**, *5*, 3041-3050; c) C. Lu, Y. Chen, Y. Yang, X. Chen, *Nano letters* **2020**, *20*, 5522-5530; d) Z. Ye, Y. Jiang, L. Li, F. Wu, R. Chen, *Adv. Mater.* **2020**, *32*, 2002168.

[5]   a) H. Li, D. Chao, B. Chen, X. Chen, C. Chuah, Y. Tang, Y. Jiao, M. Jaroniec, S.-Z. Qiao, *J. Am. Chem. Soc.* **2020**, *142*, 2012-2022; b) J. Chen, H. Zhang, H. Yang, J. Lei, A. Naveed, J. Yang, Y. Nuli, J. Wang, *Energy Storage Mater.* **2020**, *27*, 307-315.

[6]   a) J. Zheng, G. Ji, X. Fan, J. Chen, Q. Li, H. Wang, Y. Yang, K. C. DeMella, S. R. Raghavan, C. Wang, *Adv. Energy Mater.* **2019**, *9*, 1803774; b) G. Li, F. Lu, X. Dou, X. Wang, D. Luo, H. Sun, A. Yu, Z. Chen, *J. Am. Chem. Soc.* **2020**, *142*, 3583-3592.

[7]   a) Z. Li, H. Jiang, N.-C. Lai, T. Zhao, Y.-C. Lu, *Chem. Mater.* **2019**, *31*, 10186-10196; b) Q. Zou, Y. C. Lu, *J. Phys. Chem. Lett.* **2016**, *7*, 1518-1525.

[8]   Z. Han, S. Zhao, J. Xiao, X. Zhong, J. Sheng, W. Lv, Q. Zhang, G. Zhou, H. M. Cheng, *Adv. Mater.* **2021**, *33*, e2105947.

[9]   a) X. Song, D. Tian, Y. Qiu, X. Sun, B. Jiang, C. Zhao, Y. Zhang, L. Fan, N. Zhang, *Energy Storage Materials* **2021**, *41*, 248-254; b) H. Al Salem, G. Babu, C. V. Rao, L. M. R. Arava, *J. Am. Chem. Soc.* **2015**, *137*, 11542-11545.

[10]   Y. Gao, Z. Yan, J. L. Gray, X. He, D. Wang, T. Chen, Q. Huang, Y. C. Li, H. Wang, S. H. Kim, T. E. Mallouk, D. Wang, *Nat. Mater.* **2019**, *18*, 384-389.

[11]   H. Kurata, C. Colliex, *Phys Rev B Condens Matter* **1993**, *48*, 2102-2108.

[12]   H. Li, R. Meng, Y. Guo, B. Chen, Y. Jiao, C. Ye, Y. Long, A. Tadich, Q.-H. Yang, M. Jaroniec, S.-Z. Qiao, *Nat. Commun.* **2021**, *12*, 5714.

[13]   J. Zheng, X. Fan, G. Ji, H. Wang, S. Hou, K. C. DeMella, S. R. Raghavan, J. Wang, K. Xu, C. Wang, *Nano Energy* **2018**, *50*, 431-440.

[14]   F. Y. Fan, W. C. Carter, Y. M. Chiang, *Adv. Mater.* **2015**, *27*, 5203-5209.

[15]   a) C. Ye, H. Jin, J. Shan, Y. Jiao, H. Li, Q. Gu, K. Davey, H. Wang, S.-Z. Qiao, *Nat. Commun.* **2021**, *12*, 7195; b) B. Hammer, J. K. Norskov, *Nature* **1995**, *376*, 238-240.

[16]   a) X. Y. Li, S. Feng, M. Zhao, C. X. Zhao, X. Chen, B. Q. Li, J. Q. Huang, Q. Zhang, *Angew. Chem. Int. Ed.* **2022**, *61*, e202114671; b) F.-Q. Liu, W.-P. Wang, Y.-X. Yin, S.-F. Zhang, J.-L. Shi, L. Wang, X.-D. Zhang, Y. Zheng, J.-J. Zhou, L. Li, Y.-G. Guo, *Sci. Adv.* **2018**, *4*, eaat5383; c) H. Cheng, J. Zhu, H. Jin, C. Gao, H. Liu, N. Cai, Y. Liu, P. Zhang, M. Wang, *Mater. Today Energy* **2021**, *20*, 100623; d) D. Aurbach, E. Pollak, R. Elazari, G. Salitra, C. S. Kelley, J. Affinito, *J. Electrochem. Soc.* **2009**, *156*, A694-A702.

Entry for the Table of Contents
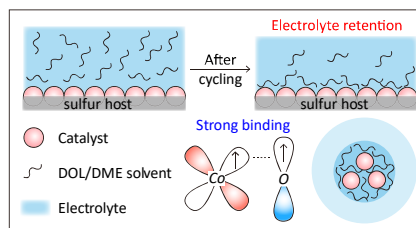
The catalyst-solvent interaction in Li−S batteries is found to determine the lean-electrolyte sulfur reduction activity, electrolyte consumption and battery stability. The catalyst-solvent interaction has been confirmed via a series of synchrotron-based analysis, in-situ spectroscopy and theoretical computations. Benefitting from the strong interaction between solvent molecules and cobalt catalyst, the Li−S battery achieves stable cycling, high capacity retention and low electrolyte consumption under lean electrolyte conditions.

Unraveling the catalyst-solvent interactions in lean-electrolyte sulfur reduction electrocatalysis for Li−S batteries

Huan Li, Rongwei Meng, Yong Guo, Chao Ye, Debin Kong, Bernt Johannessen, Mietek Jaroniec, and Shi-Zhang Qiao*

Experimental Procedures

Material Synthesis. Graphite oxide (GO) was synthesized via modified Hummer's method. Typically, 20 mg of GO was ultrasonicated in 20 mL of deionized water for 2 h (1 mg mL^{-1}). 40 mg of L-ascorbic acid sodium-salt was added to the GO suspension under continuous stirring. The suspension was transferred to a glass vial and heated at 70 $^{\circ}$C for 10 h to obtain a graphene hydrogel. The product was washed with deionized water to remove sodium-salt. 3D graphene hydrogel was soaked in 20 mL of solution containing 238 mg (1 mmol) of cobalt chloride (CoCl$_2$·6H$_2$O) for 24 h. The graphene hydrogel was freeze-dried overnight, and heated at 600 $^{\circ}$C in 5 vol.% H$_2$/Ar for 1.5 h. The mixture was repeatedly washed with diluted hydrochloric acid and deionized water to remove larger particles. Nanosized Co metal particles remain on the 3D graphene substrate. Synthesis of other metal nanoparticles follows the same procedure with the same molar concentration (1 mmol) of the chloride-based precursors. Rhodium chloride (RhCl$_3$) and chloroplatinic acid hexahydrate (H$_2$PtCl$_6$·6H$_2$O) were used to synthesize Rh and Pt nanoparticle catalysts, respectively.

Characterization Techniques. The morphology and structure of samples was characterized by scanning electron microscopy (SEM, Hitachi S4800, Japan). High-resolution STEM images were obtained under a Cs-corrected STEM (FEI Titan Cubed Themis G2 300) operated at 300 kV. Ultraviolet-visible (UV-vis) was carried out using a spectrometer (SHIMADZU UV-2600). X-ray diffraction (XRD) data were collected on a Rigaku Mini Flex 600 X-Ray Diffractometer. X-ray photoelectron spectra (XPS) were measured with the Thermo Fisher Scientific ESCALAB Xi+, Al Kα radiation. Raman spectra were collected with Labram HR Evolution (Horiba Scientific). Fourier-transform infrared spectroscopy with attenuated total reflectance mode (FTIR-ATR) was performed with a Thermo-Fisher Nicolet iS20 equipped with a liquid nitrogen-cooled HgCdTe (MCT) detector using a VeeMax III ATR accessory (Pike Technologies). The electrolyte is extracted and mixed with 500 μL of water for FTIR-ATR tests. High-performance liquid chromatography (HPLC) was performed with Waters LC system while using an Acclaim™ Polar Advantage II column with acetonitrile/water (20%/80%) mobile phase. The electrolyte was mixed with 10 mL of water, and then 100 μL of mixed solution was extracted to mix into 5 mL of water for HPLC tests. The synchrotron-based near-edged X-ray absorption fine structure (NEXAFS) of Co L-edge was performed on the soft X-ray spectroscopy beamline at Australian Synchrotron (Clayton), part of ANSTO. The synchrotron-based extended X-ray absorption fine structure (EXAFS) of Co K-edge was performed on the X-ray absorption beamline at Australian Synchrotron (Clayton), part of ANSTO.

Nuclear Magnetic Resonance (NMR) Analysis. The electrolyte component used in this work is 1 M bis(trifluoromethane)sulfonamide lithium salt (LiTfSI) in 1,3-dioxolane (DOL)/1,2-dimethoxyethane (DME) (1:1 volume ratio) with 0.4 M LiNO$_3$. For ^{1}H and ^{19}F NMR tests, the electrolyte from the cycled cells was extracted with 500 μL of deuterated dimethyl sulfoxide (d$_6$-DMSO). Fluorobenzene is selected as the internal reference for both ^{1}H and ^{19}F tests because its chemical shift is far from that of DOL/DME

solvent and TfSI⁻ anions in both ¹H and ¹⁹F spectra. Fluorobenzene is not included into the battery during cycling, and therefore it is not consumed. Its addition is 0.1 M for use as the reference for NMR quantifications. The ¹H and ¹⁹F peaks of fluorobenzene are normalized to 100%. Due to the known content of the internal reference, the electrolyte retention of both DOL/DME solvent or TfSI⁻ anions can be quantified by comparing the peak areas.

Electrochemical Tests. For Li−S battery testing, the sulfur cathode was prepared by mixing 80 wt.% of S with 20 wt.% of the catalyst. The catalyst/S mixture was ball-milled with LA-133 binder with a mass ratio 90:10. Total sulfur content in the cathode was 72 wt.%. Li−S batteries were assembled with CR2032 coin-cell in an Ar-filled glove box by coupling a piece of Li-metal anode with 1 mol L⁻¹ LiTfSI in DOL/DME (1:1 volume ratio) with 0.4 mol L⁻¹ LiNO$_3$ as the electrolyte. The cyclic voltammetry (CV) measurements were carried out from 1.7 to 2.8 V with a scan rate of 0.2 mV s⁻¹. For electrochemical test of Li−S batteries including rate and cycling performance, the batteries were galvanostatically charged and discharged at the selected current rates (1C = 1675 mAh g⁻¹) and cycles. The galvanostatic charge-discharge of all the batteries was carried out using Neware battery test system (CT-4008T-5V50mA-164, Shenzhen, China). For the Li$_2$S nucleation tests, the coin-cell was galvanostatically discharged to 2.06 V at 0.0785 mA, and then potentiostatically discharged at 2.02 V until the current was < 10⁻⁵ A. For Li$_2$S nucleation testing, the Li$_2$S$_8$ catholyte was prepared by combining sublimed sulfur and Li$_2$S powder in a molar ratio of 7:1 in LiTfSI/DOL/DME electrolyte under vigorous stirring for 24 h. Carbon-fiber paper (CP) disks with a diameter of 10 mm were used as the substrates to load Co, Rh and Pt catalysts with 1 mg cm⁻² to assemble the coin-cells. Li-foil was used as the counter electrode. 10 μL of Li$_2$S$_8$ (0.25 mol L⁻¹) catholyte was added on the cathode and 5 μL of blank electrolyte on the anode. Therefore, the Li$_2$S nucleation was tested under lean electrolyte (15 μL) conditions.

Computational details. Computations for this work were carried out using density functional theory (DFT) as implemented in Vienna ab-initio simulation package (VASP) code. Electronic exchange-correlation energy was modeled using the Perdew-Burke-Ernzerhof (PBE) function within a generalized gradient approximation (GGA). The projector-augmented wave (PAW) method was used to describe the ionic cores. For the plane-wave expansion a 450 eV kinetic energy cut-off was used following testing a series of different cut-off energies. A Monkhorst-Pack 2×2×1 k-point grid was used to sample the Brillouin zone. Convergence criterion for the electronic structure iteration was set to 10⁻⁵ eV, and that for geometry optimizations was 0.02 eV Å⁻¹ on force. A Gaussian smearing of 0.1 eV was applied during geometry optimization and for total energy computations.

Binding energy (E_b) was computed by subtracting the energy of substrate and absorbed molecule from the energy of whole system. For example, for DOL on Co metal surface, the binding energy is computed as follows:

$E_b = E$ (Co+DOL) − E (DOL) − E (Co)

where E (Co+DOL) is the DFT-based total energy of DOL on Co, eV, E (DOL) the energy of individual DOL in the same supercell, eV, and E (Co) the energy of Co, eV. A more negative value means stronger binding interaction.
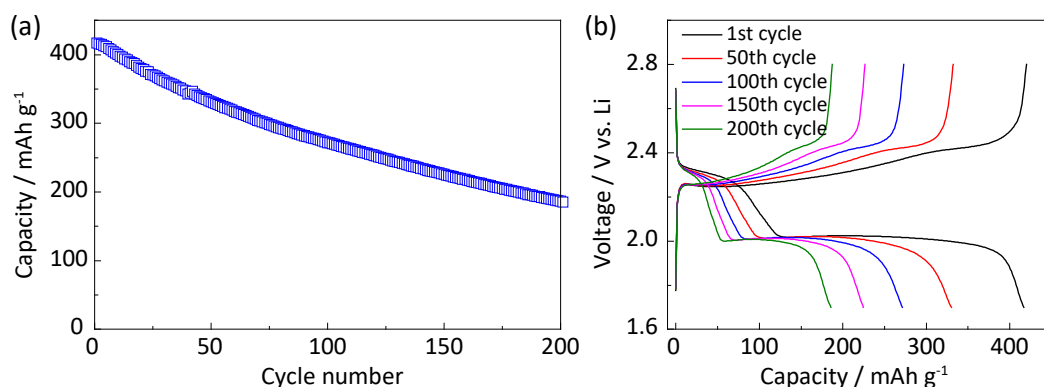
Figure S1. (a) Cycling performance of the Li−S battery, and (b) the corresponding charge-discharge curves at different cycles. The battery was assembled using graphene as sulfur host, and charged-discharged at 0.5 C. The electrolyte/sulfur (E/S) mass ratio is 5.
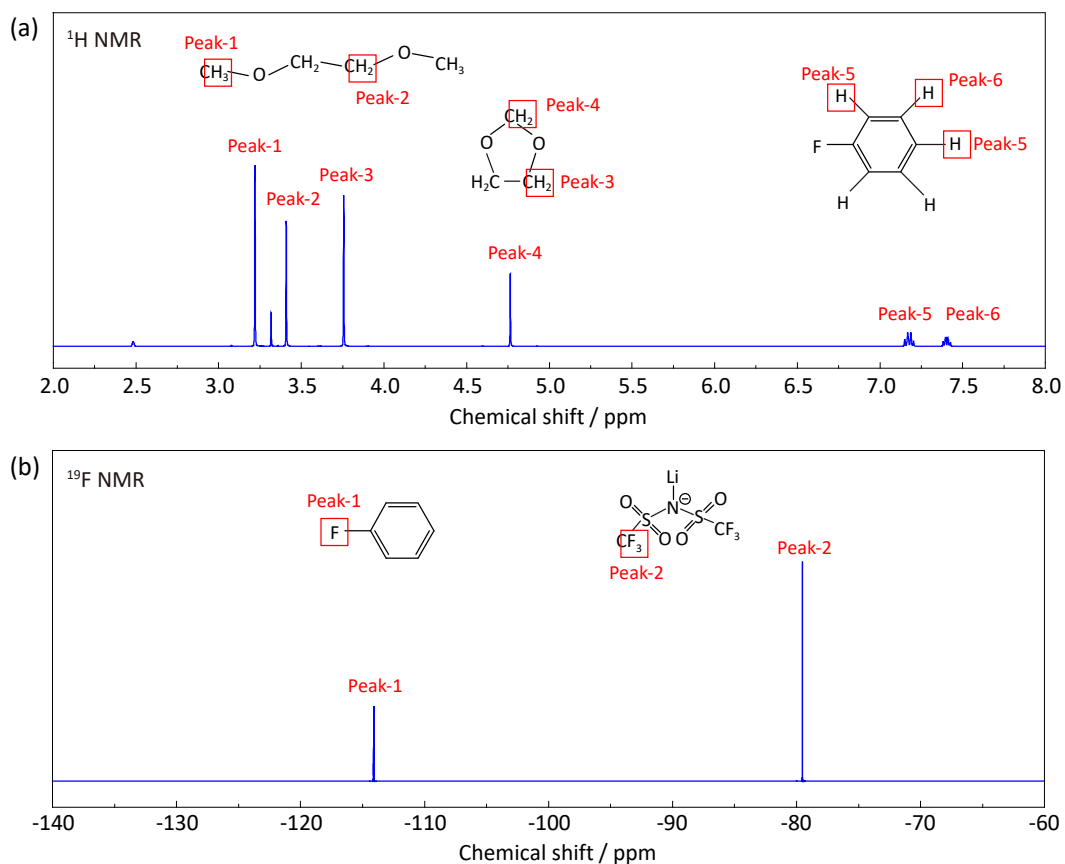

Figure S2. (a) ^{1}H and (b) ^{19}F NMR spectra of DOL, DME and LiTfSI. 0.1 M Fluorobenzene was used as an internal reference to quantify DOL/DME and LiTfSI contents. The insets in these figures present the detailed peak information of H and F with different chemical environments.
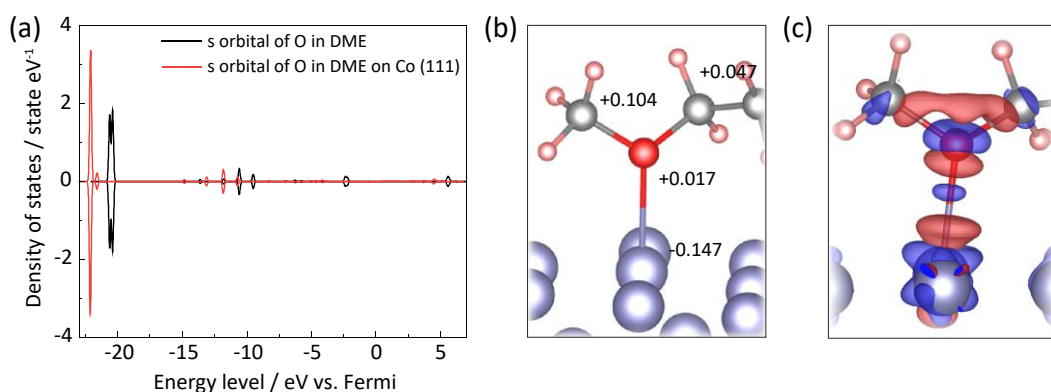
Figure S3. (a) Projected DOS changes of O s-orbital for pure DME and DME adsorbed on Co (111); (b) Bader charge analysis of DME on Co (111); (c) Charge-difference figure of DME on Co (111) wherein red indicates electron accumulation and blue denotes electron depletion.
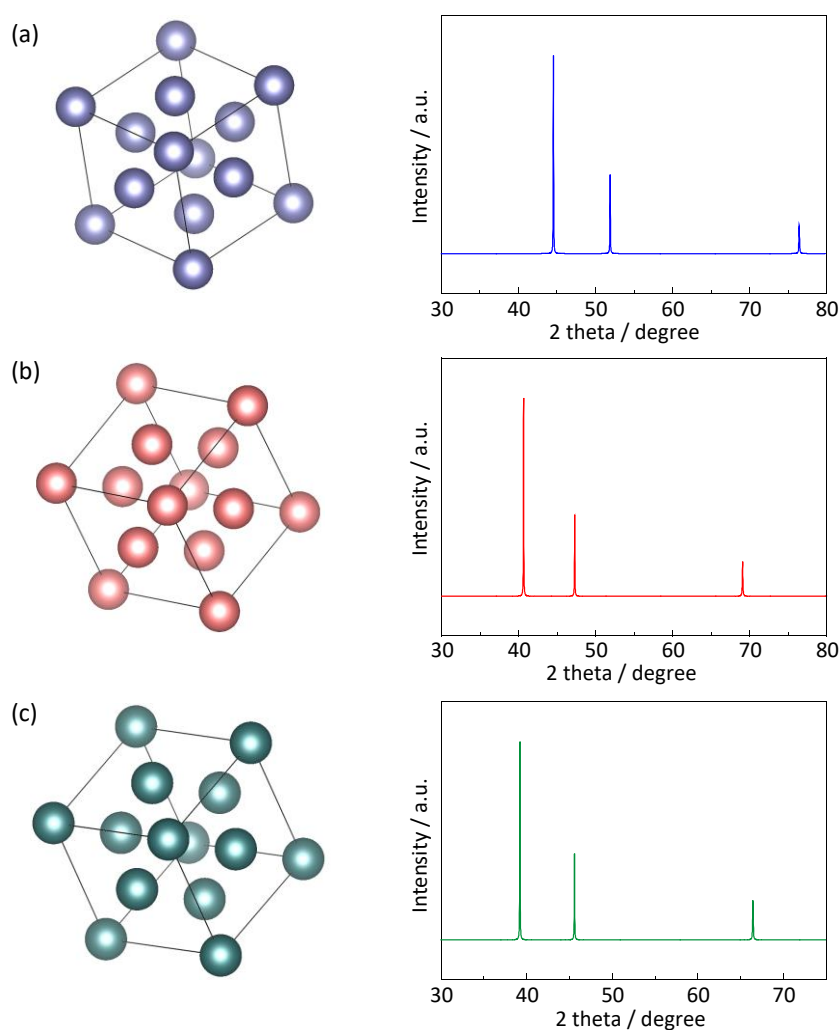

Figure S4. Crystal structures of (a) Co, (b) Rh, (c) Pt metals and the corresponding simulated XRD patterns. The results agree with the XRD results in Figure 1f.
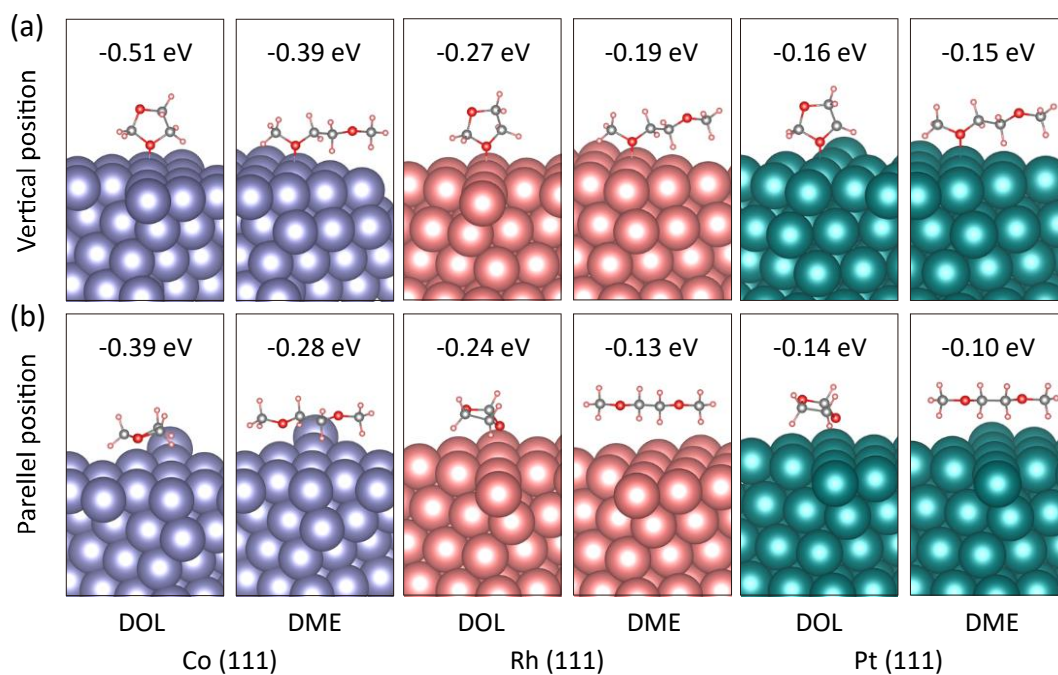
Figure S5. The optimized structures of DOL and DME molecules with (a) vertical position and (b) parallel position on Co (111), Rh (111) and Pt (111). The binding energies with vertical positions are higher than those with parallel positions. This suggests that the solvent molecules prefer to adsorb on the catalyst surface by vertical alignment. In the parallel case, the repulsion between surface metal atoms and edged hydrogen atoms leads to a weak binding.
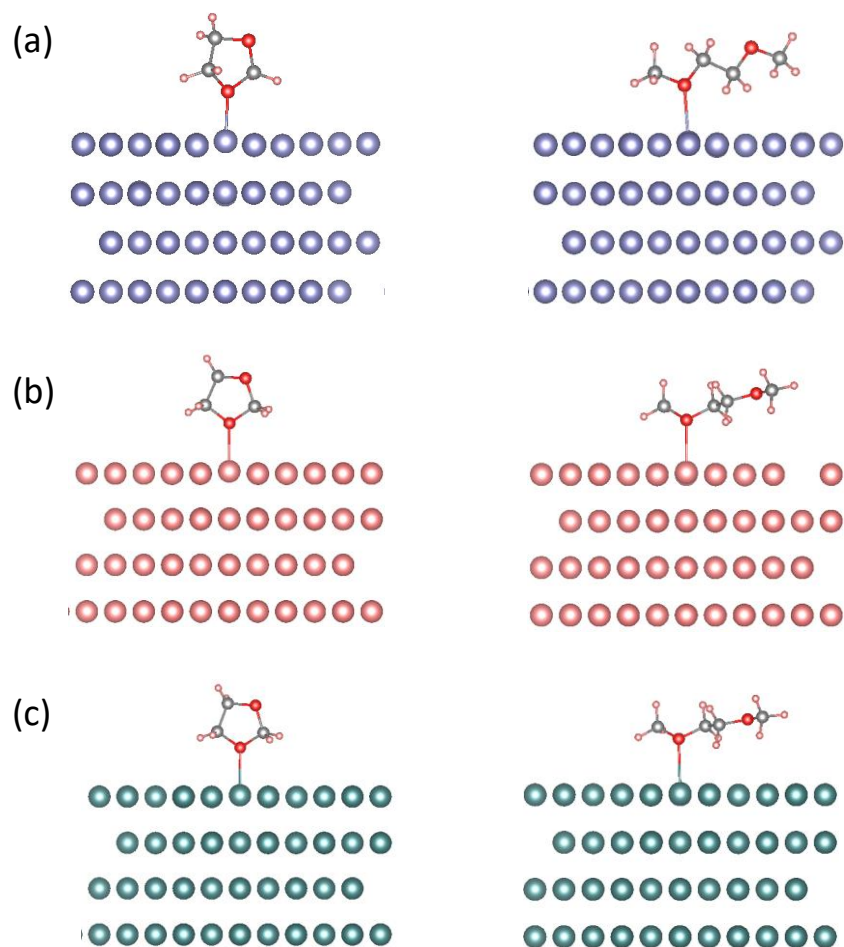
Figure S6. Optimized structures of DOL and DME on (a) Co (111), (b) Rh (111) and (c) Pt (111). Purple, light red, green atoms present Co, Rh, Pt, respectively. Grey, red, and pink atoms denote carbon, oxygen and hydrogen, respectively. Metal−oxygen bonds are identified based on these optimized models.
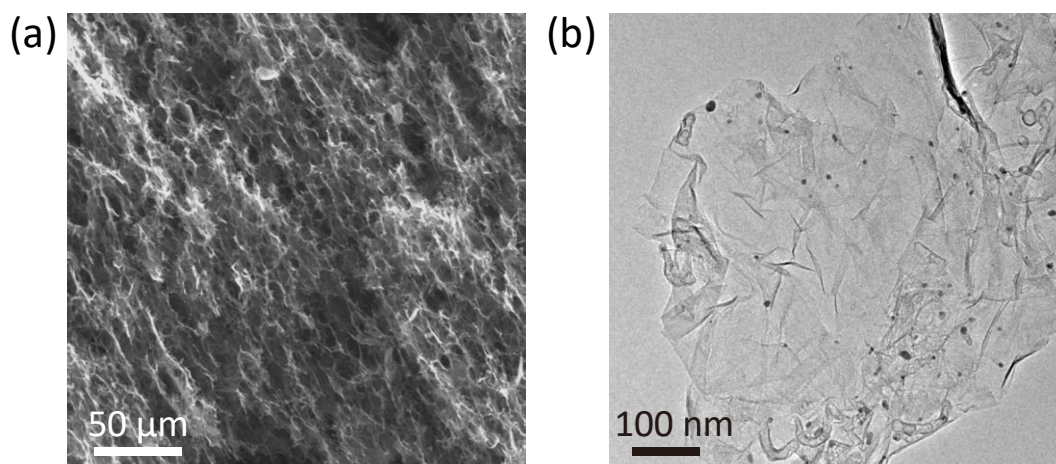

Figure S7. Microscopic images of graphene substrate and Co nanoparticles. (a) SEM image of graphene substrate. 3D interconnected graphene network is observed in this image; (b) TEM image of Co nanoparticles on graphene substrate.
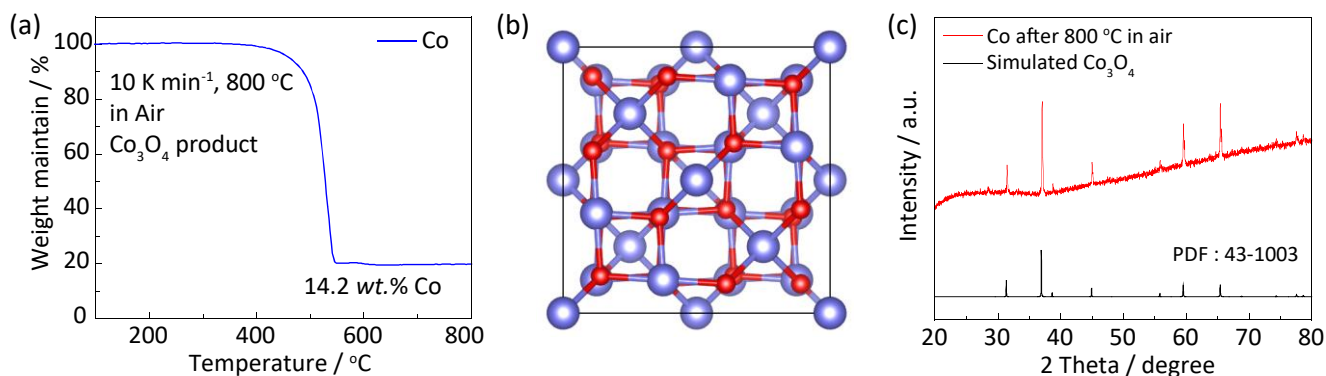
Figure S8. (a) Thermogravimetric analysis (TGA) of synthesized Co catalyst on graphene substrate in air; (b) The crystal structure of Co_3O_4 and (c) the experimental and simulated XRD patterns of Co_3O_4. This confirms the Co_3O_4 product after annealing Co nanoparticle at 800 °C in air. The Co content is 14.2 *wt.%*.
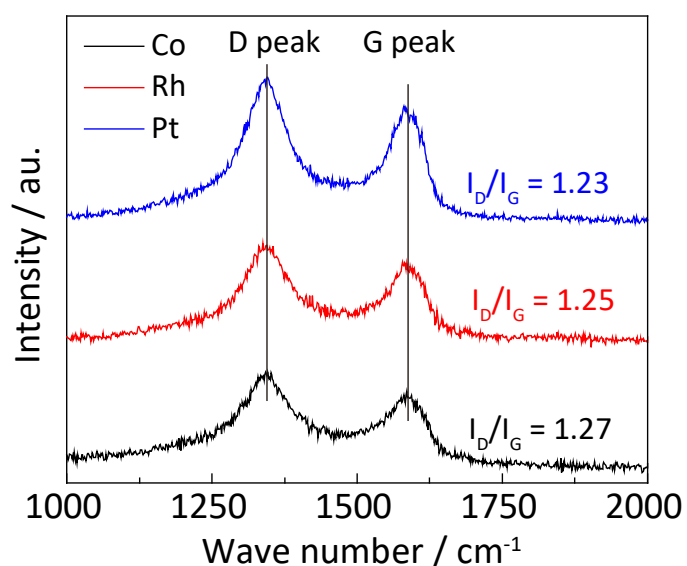

Figure S9. Raman spectra of graphene substrates with different metal loading. The I_D/I_G value does not change significantly. This suggests that the loading of Co, Rh and Pt does not alter the properties of graphene substrate.
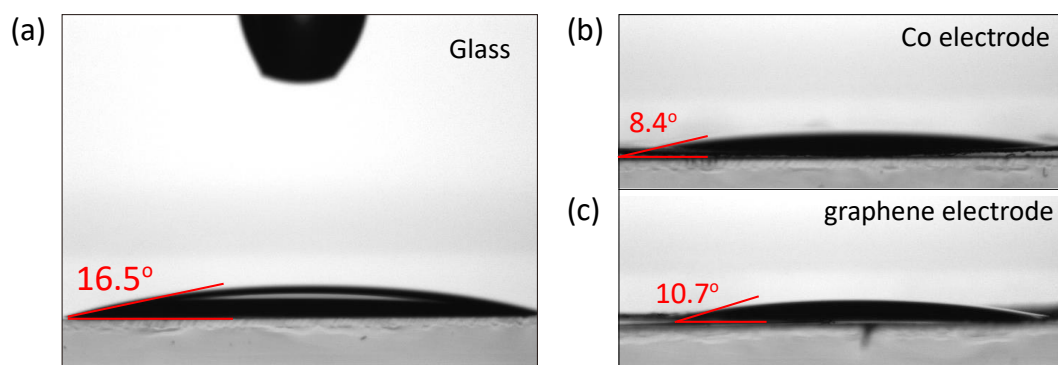
Figure S10. The contact angle of DOL/DME droplet on (a) glass, (b) Co-catalyst electrode, and (c) graphene electrode. The lower contact angle on the Co-catalyst electrode confirms higher affinity of electrolyte solvent toward Co surface.
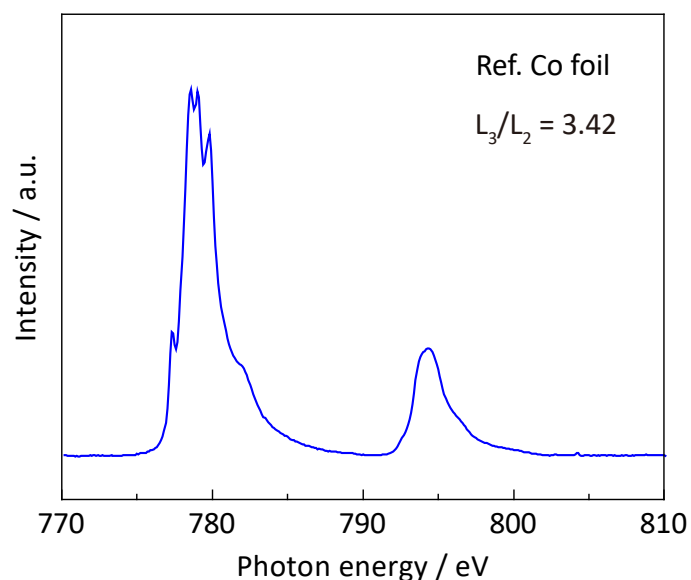

Figure S11. The Co L-edge near-edge X-ray adsorption fine structure (NEXAFS) of reference Co foil. The peak ratio of L_3/L_2 is 3.42.
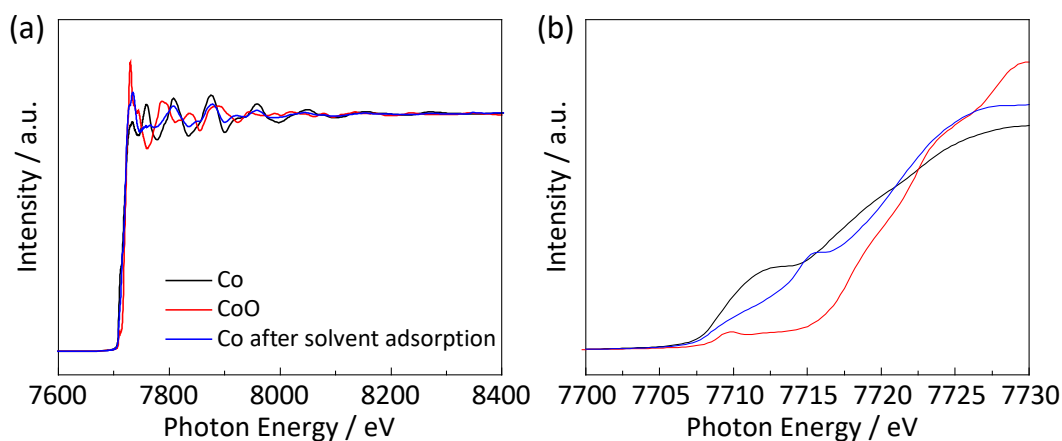
Figure S12. (a) The Co K-edge extended X-ray adsorption fine structures (EXAFS) of synthesized Co catalyst, CoO and Co catalyst after solvent adsorption; (b) The enlarged figure shows the white-line ranges of these samples.
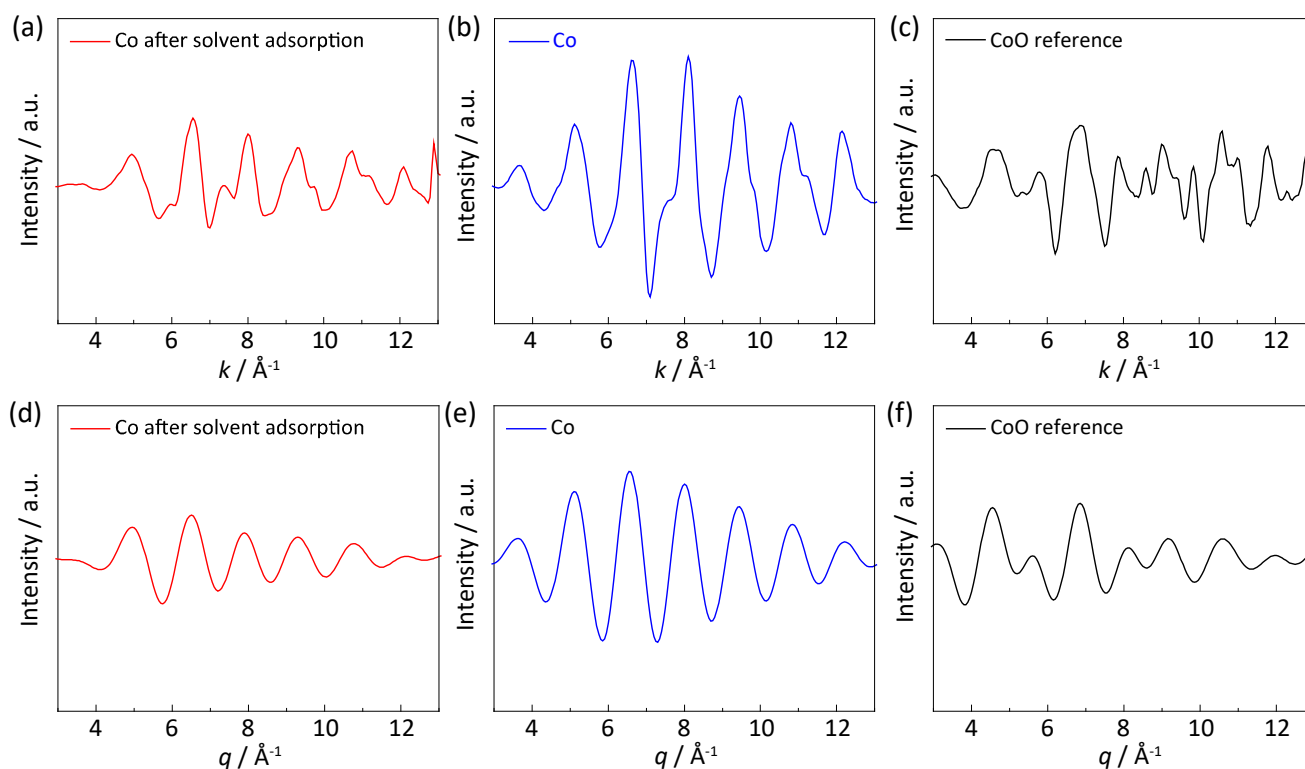

Figure S13. The k-space curves of (a) Co after solvent adsorption, (b) Co and (c) CoO reference; and the transformed q-space data of (d) Co after solvent adsorption, (e) Co and (f) CoO reference.
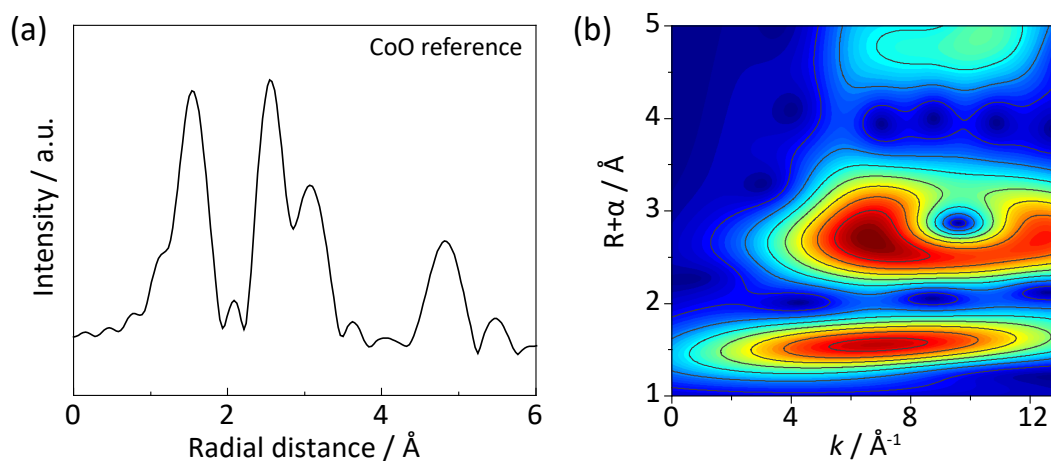
Figure S14. (a) The radial distance in R-space of CoO reference and (b) the corresponding wavelet-transformed contour pattern.
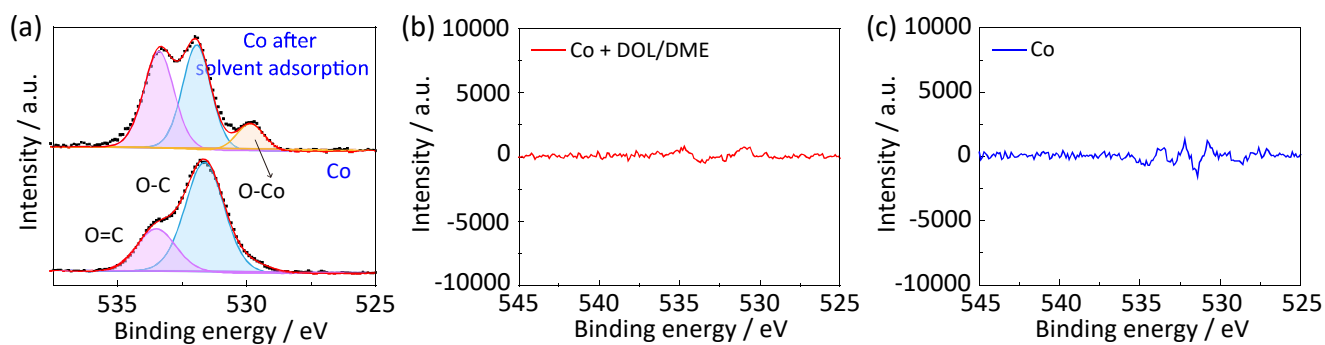

Figure S15. (a) XPS spectra of Co catalyst and Co after DOL/DME adsorption; and (b, c) the corresponding subtracted curves between the raw and fitting data for the spectra.
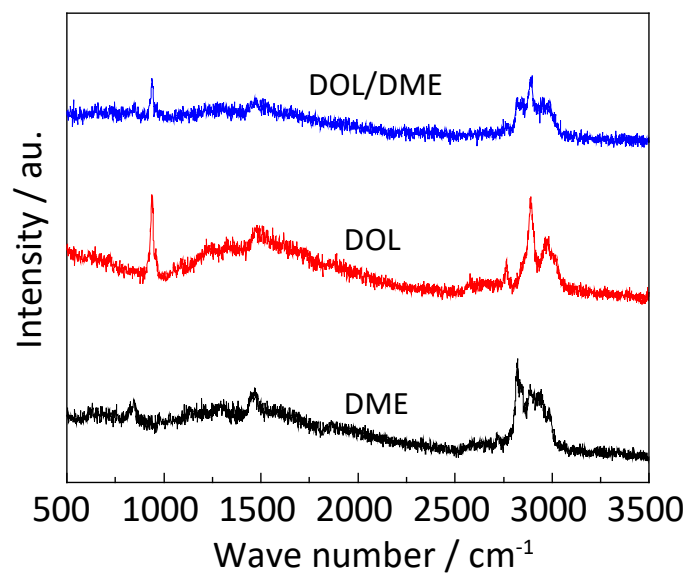
Figure S16. Raman spectra of pristine DOL, DME and DOL/DME mixed solvent.
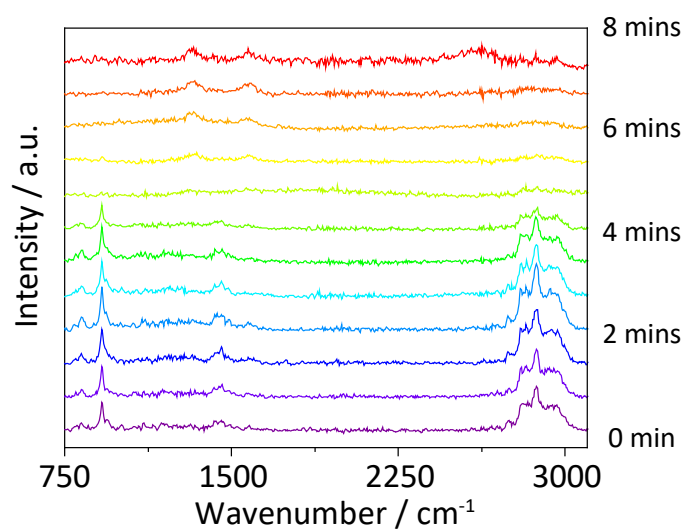
Figure S17. The time-dependent Raman spectra of DOL/DME solvent on pristine graphene substrate.
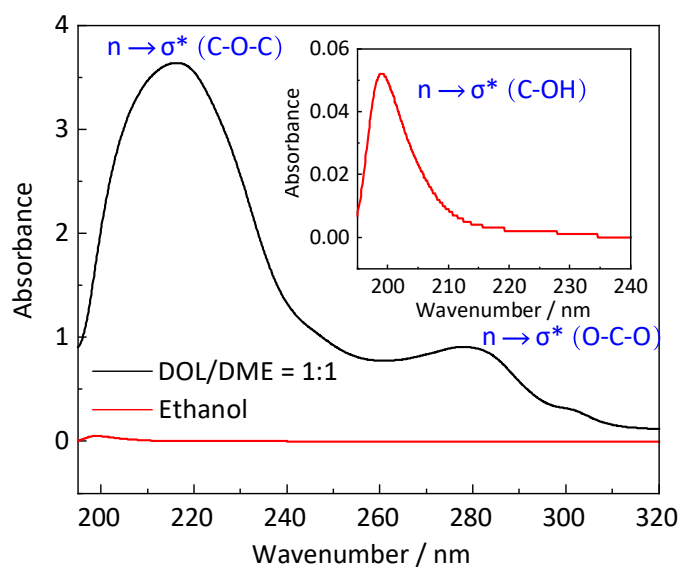
Figure S18. UV-vis absorption curves of DOL/DME and ethanol. The absorption peaks for C-OH, C-O-C and O-C-O functional groups are ~200 nm, ~210 nm and ~280 nm respectively. Besides, the peak for ethanol is very weak (inset Figure), and therefore ethanol is selected to dissolve different amounts of DOL/DME.
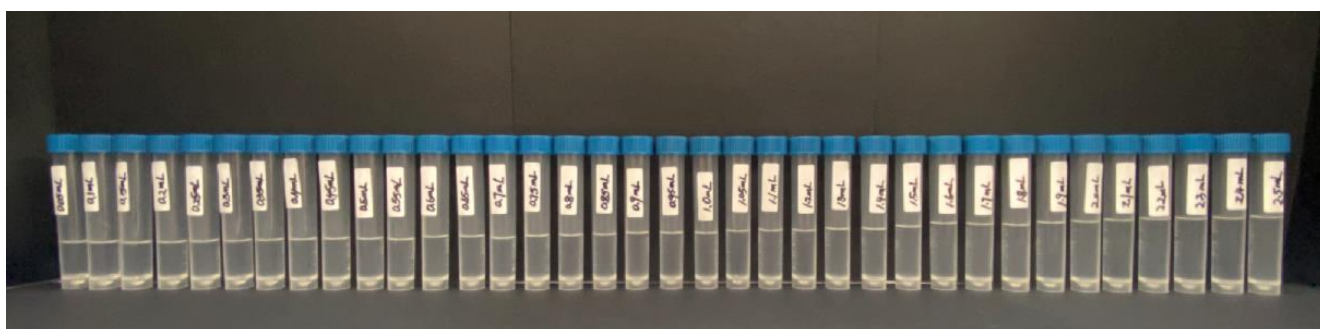
Figure S19. Digital photograph of DOL/DME in ethanol with different volume ratios. These standard solutions were used to obtain the relation between the UV-vis peak intensity and the volume concentration of DOL/DME mixed solvent.
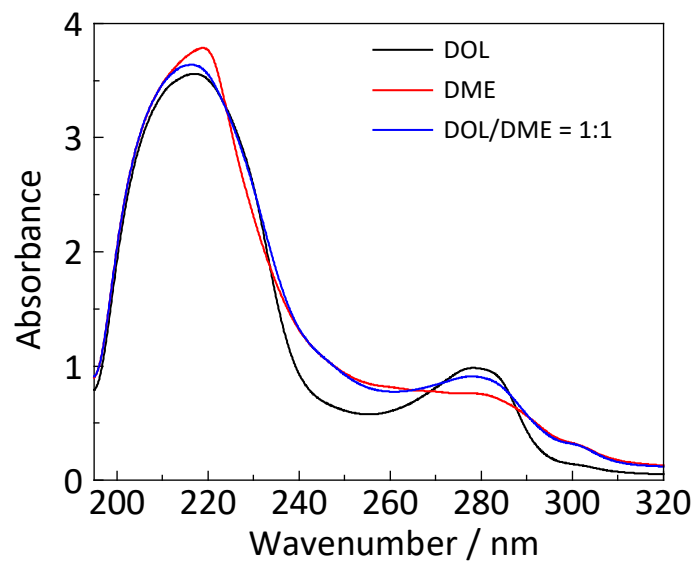
Figure S20. The UV-vis spectra of pure DOL, pure DME and DOL/DME mixed solvent.
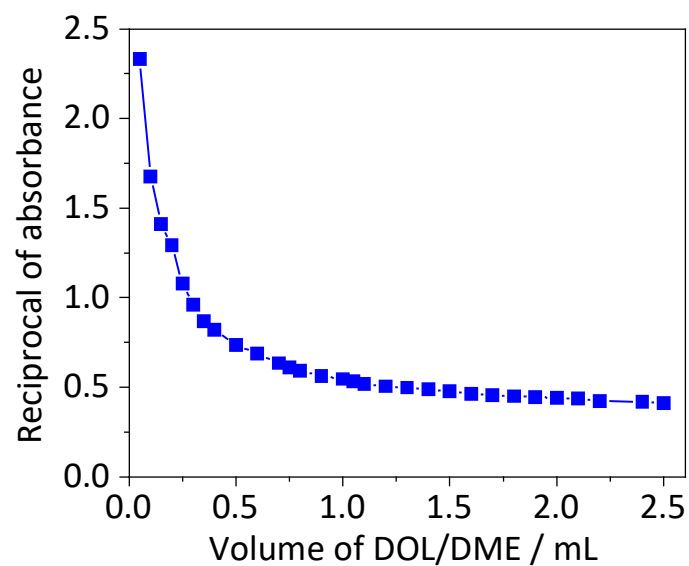
Figure S21. The relationship between the reciprocal of UV-vis absorbance and the volume of DOL/DME solvent.
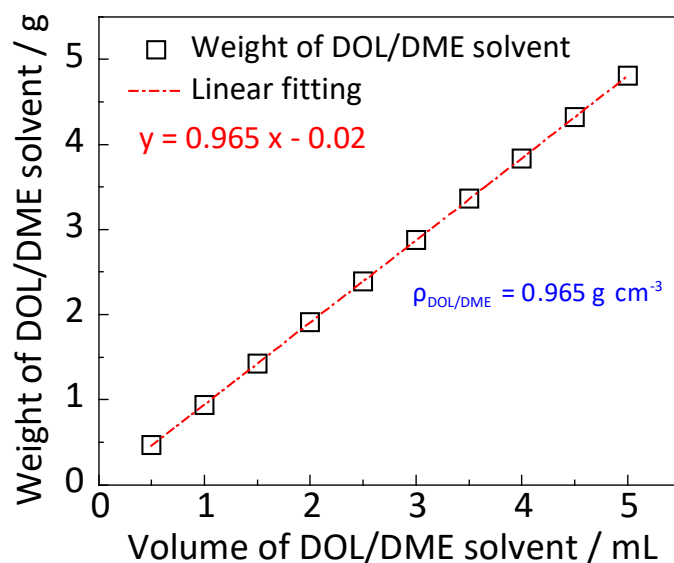
Figure S22. The relation between the weight and volume of DOL/DME mixed solvent. The density is calculated as 0.965 g cm^{-3} with the linear fitting.
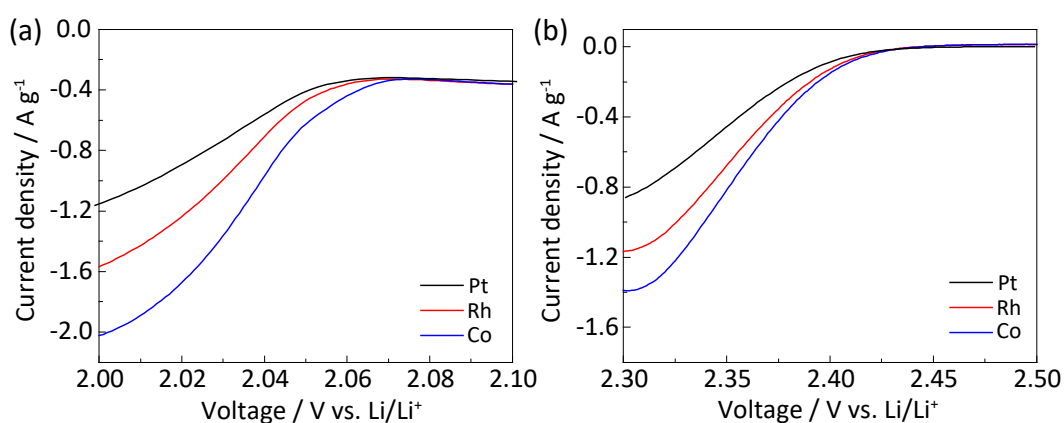
Figure S23. Enlarged CV curve of Figure 4a at regions of (a) high-voltage catalytic reduction from sulfur to polysulfides (2.50 to 2.30 V) and (b) low-voltage reduction from polysulfides to Li$_2$S (2.10 to 2.00 V).
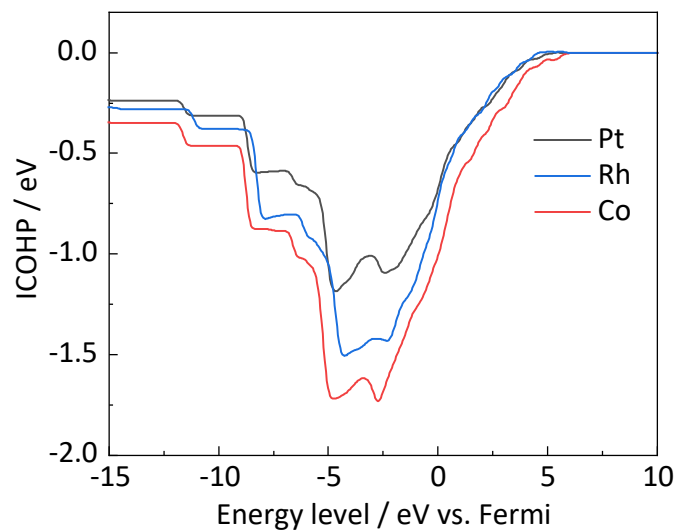
Figure S24. Integrated crystal orbital Hamilton population (ICOHP) between oxygen atom among DOL and the surface metal atoms. A more negative value at Fermi level suggests a stronger bonding between metal catalyst and solvent molecules.
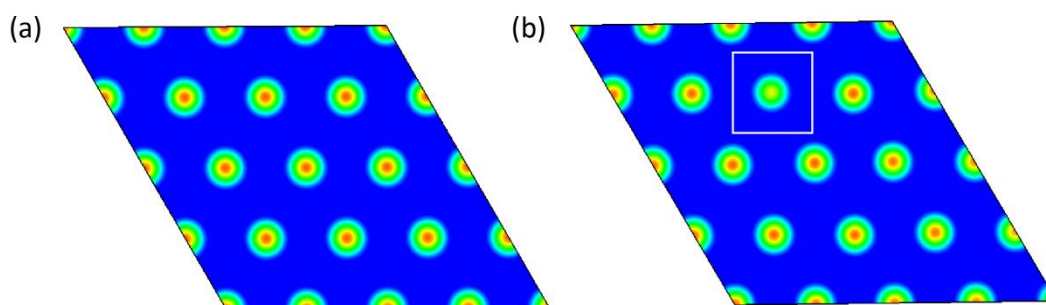
Figure S25. The charge density of (a) Co (111) surface and (b) Co (111) surface after DOL adsorption. The decreased density indicates the electron transfer from Co to DOL molecule (as marked by the while square in b).
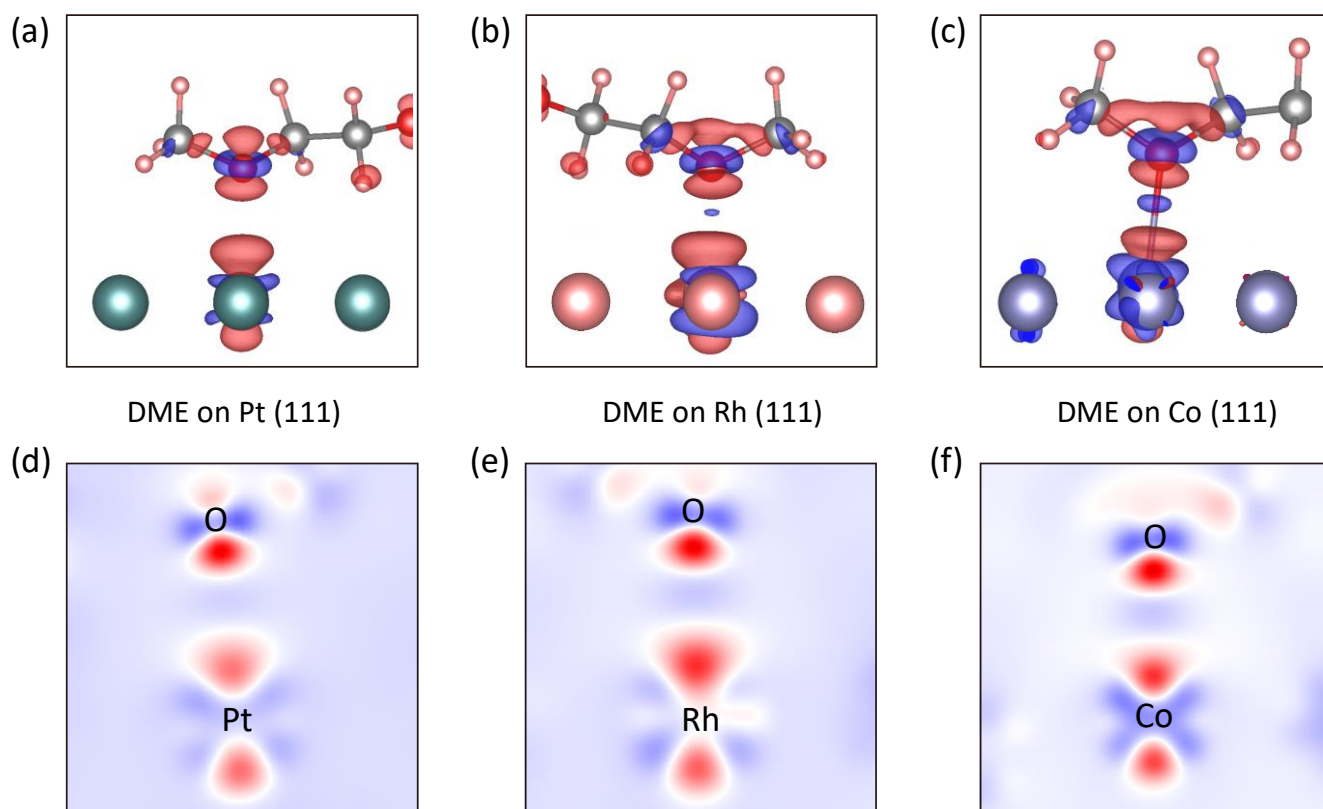
Figure S26. Charge differences of DME molecule on metal surfaces. 3D charge-difference figures of DME on (a) Pt (111), (b) Rh (111) and (c) Co (111); 2D sliced charge-difference figures of DME on (d) Pt (111), (e) Rh (111) and (f) Co (111). Red indicates electron accumulation and blue denotes electron depletion.
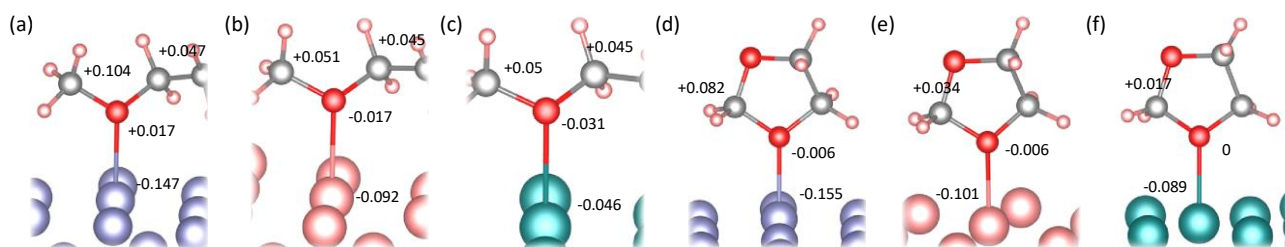
Figure S27. Bader charge analysis of adsorbed DOL/DME molecules on different metal surfaces. DME molecule on (a) Co (111), (b) Rh (111) and (c) Pt (111); DOL molecule on (d) Co (111), (e) Rh (111) and (f) Pt (111). The selected Co atom shows a higher value of electron depletion for both DOL and DME molecules. This confirms its strong binding with the solvent molecules.
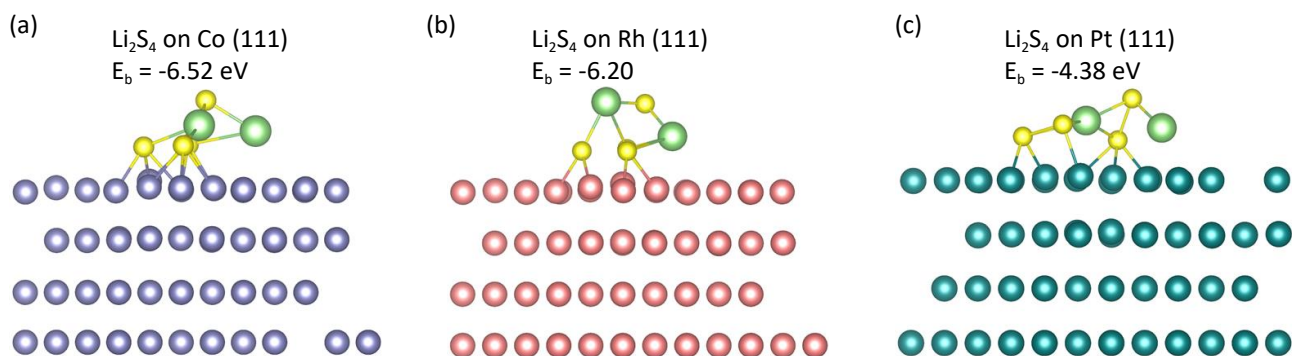
Figure S28. The optimized structures of Li_2S_4 on (a) Co (111), (b) Rh (111) and (c) Pt (111). The binding energies of $Li_2S_4^*$ on Co (111), Rh (111) and Pt (111) surface are -6.52 eV, -6.20 eV and -4.38 eV respectively. Too strong binding energy of Co would lead to a lower catalytic activity (**Figure 6a**).
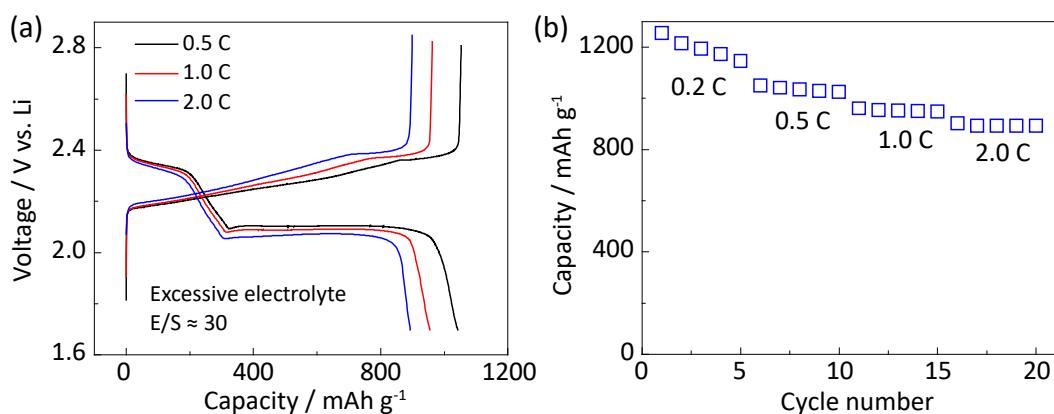
Figure S29. (a) Charge-discharge curves of Li−S batteries with Pt catalyst, and (b) capacity retention at different rates ranging from 0.2 to 2.0 C. The areal mass loading of sulfur is ≈ 0.5 mg cm^{-2} with excessive electrolyte. Pt demonstrates excellent battery performance with flooded electrolyte; however, its performance dramatically degrades under lean-electrolyte conditions.
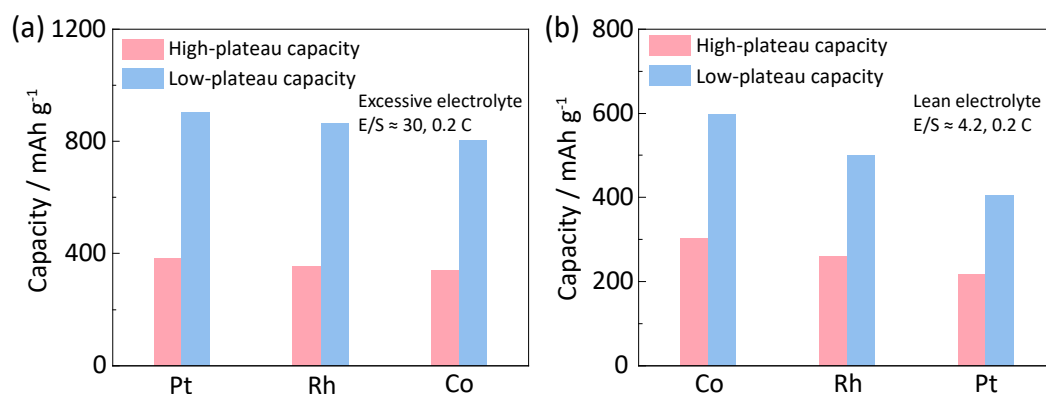
Figure S30. High-plateau and low-plateau capacity for sulfur cathodes using Co, Rh and Pt catalysts with (a) excessive electrolyte and (b) lean electrolyte. The capacity dramatically changes under lean electrolyte conditions.
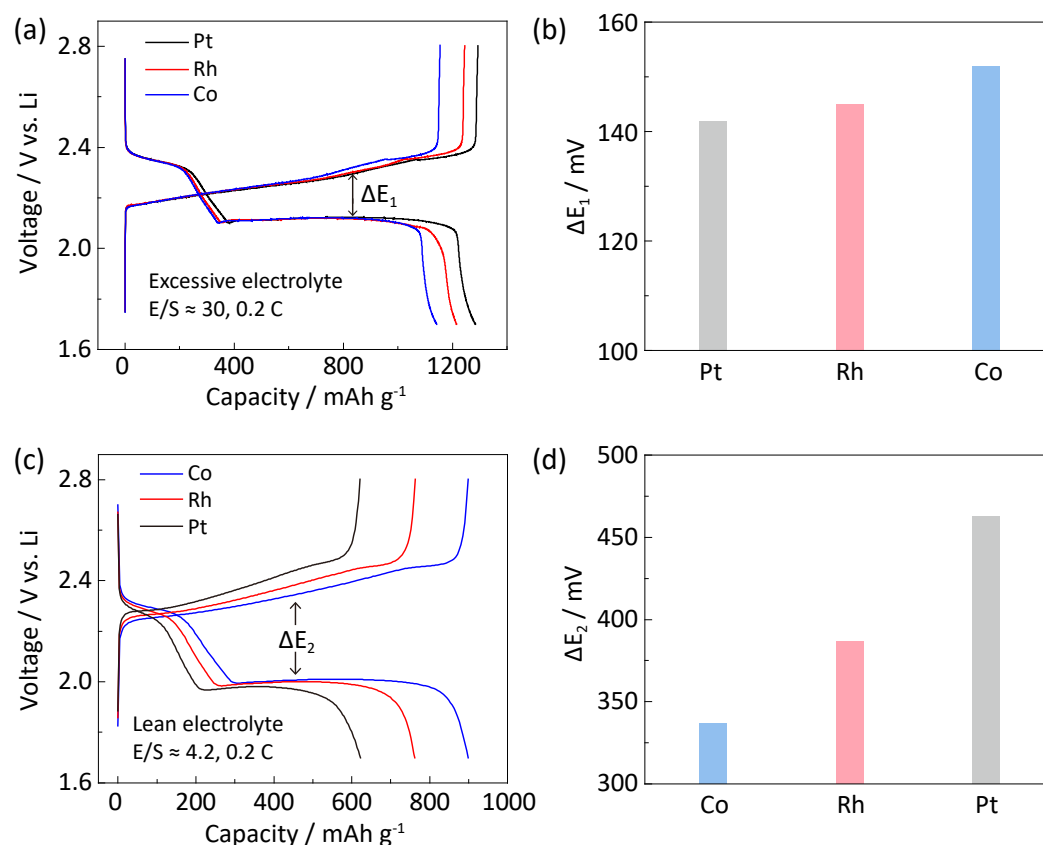
Figure S31. Charge-discharge curves of Li−S batteries using Co, Rh, Pt catalysts (a) with excessive electrolyte and (c) lean electrolyte; The corresponding charge-discharge overpotentials (b) with excessive electrolyte and (d) lean electrolyte. The charge-discharge overpotentials (ΔE) present a significant change under lean electrolyte conditions.
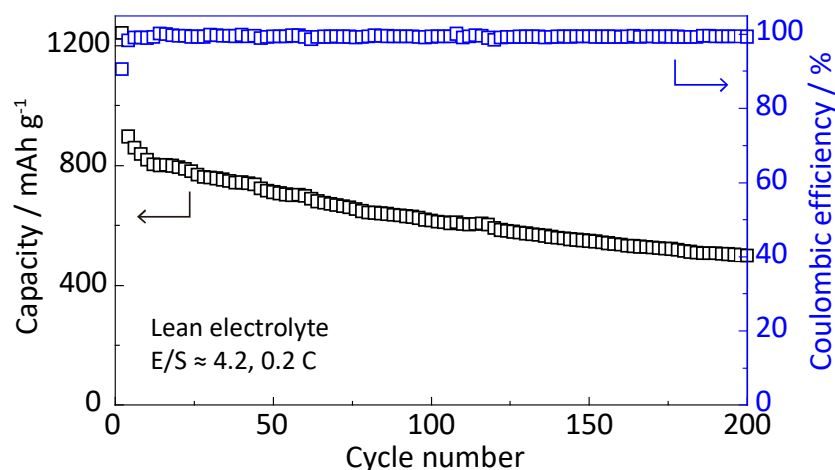
Figure S32. Cycling performance of Li−S battery with Co catalyst under lean electrolyte conditions shows a stable cycling with the Coulombic efficiency nearly 100%.
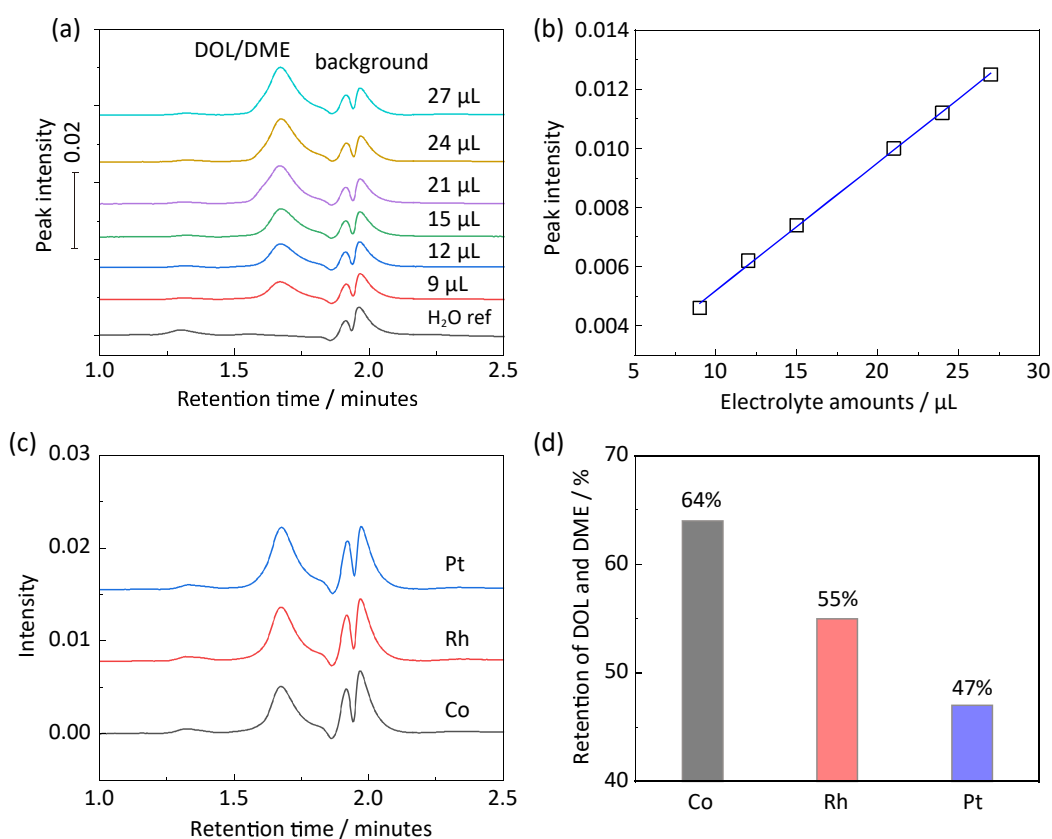
Figure S33. HPLC results to determine the retention of DOL and DME mixed solvent for the cycled electrolytes. (a) HPLC curves for the mixed solution with different electrolyte injection; (b) Standard relation between known amounts of electrolyte volume and HPLC peak intensity; (c) HPLC spectra for the cycled electrolyte with Co, Rh and Pt catalysts; (d) The retention of DOL and DME with Co, Rh and Pt catalysts.
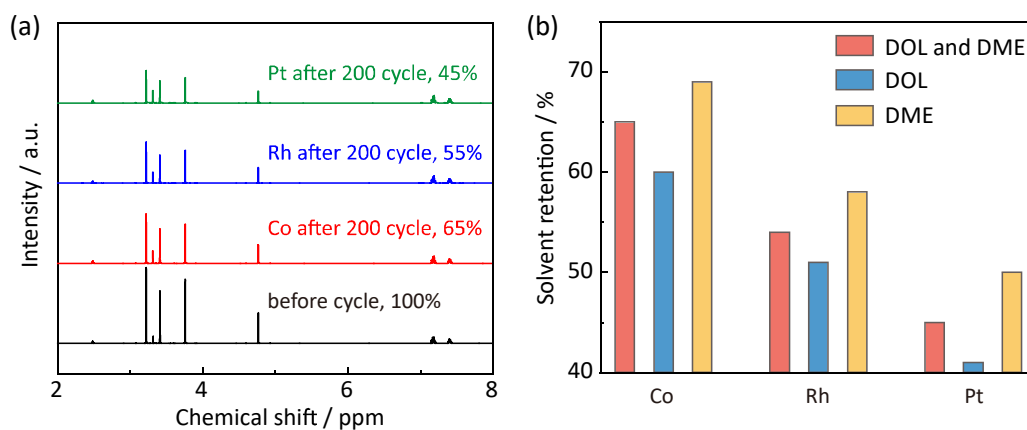
Figure S34. (a) ^{1}H NMR spectra of electrolytes extracted from un-cycled battery, and Co, Rh, Pt catalyzed Li−S batteries after 200 cycles. (b) the overall DOL and DME retentions are 65%, 54% and 45% for Co, Rh and Pt catalysts respectively. Among these catalysts, the DOL retentions are 60%, 51%, 41% and the DME retentions are 69%, 58%, 50%, respectively.
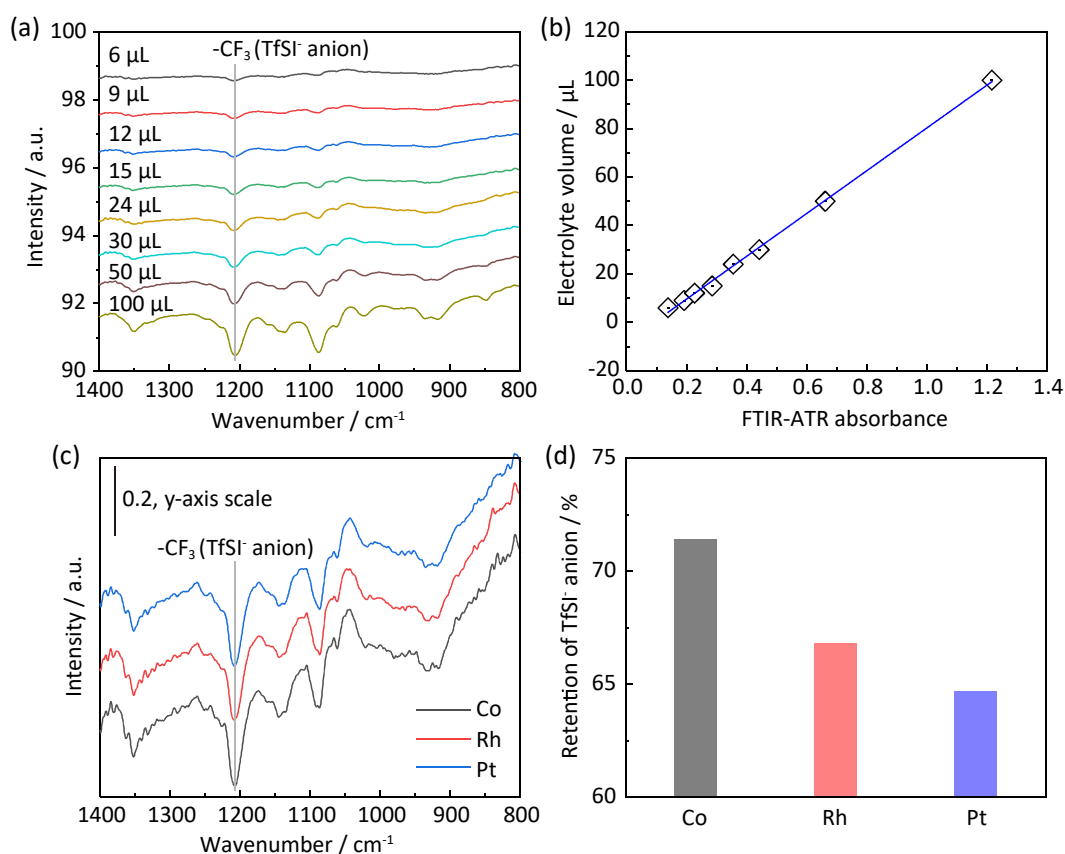
Figure S35. FTIR-ATR results to determine the retention of TfSI$^-$ anion for the cycled electrolytes. (a) FRIR-ATR spectra for the mixed solution with different electrolyte injection in 500 µL of water; (b) Standard relation between known amounts of TfSI$^-$ anion (electrolyte volume) and FRIR-ATR peak intensity; (c) FTIR-ATR spectra for the cycled electrolyte with Co, Rh and Pt catalysts; (d) The retention of TfSI$^-$ anion with Co, Rh and Pt catalysts.

Table S1 Performance comparison of lean-electrolyte Li-S batteries reported in this work and elsewhere

Reported Catalysts	Electrolyte dosage / μL mg^{-1}	Sulfur loading / mg cm^{-2}	Current density	Capacity (flooded electrolyte) / mAh g^{-1}	Capacity with (lean electrolyte) / mAh g^{-1}	Capacity retention	References
MoS$_2$ with EV(ClO$_4$)$_2$ mediator	5.0	5.6	0.5 mA cm^{-2}	~1320	~1022	77%	1
MoS$_2$	5.0	4.0	0.2 C	~700	~500	71%	2
Co-NC	8.3	3.8	0.2 C	~920	~450	49%	3
LDH	6.0	5.5	0.2 C	~1000	~727	73%	4
HPP	7.0	8.1	0.01 C	~1378	~981	72%	5
In$_2$O$_3$	4.6	5.9	0.1	~1320	~950	72%	6
Fe-Ni alloy	4.5	4.1	0.05 C	~1000 (0.2 C)	~600	60%	7
NiCl$_2$	5.0	N/A	0.5 C	~820	~630	77%	8
Ni$_3$FeN	4.7	4.8	0.2 C	~1150	~500	43.4%	9
NiSe$_2$	6.0	8.8	0.2 C	~1110	~852	77%	10
Fe-C$_3$N$_4$	3.8	N/A	0.2 C	~1270	~800	63%	11
MoP	4.0	6.0	0.8 mA cm^{-2}	N/A	~880	N/A	12
MgB$_2$	6.5	8.3	0.2 C	1250 (0.05 C)	~850	68%	13
MoB	7.0	6.1	0.2 C	~1200	~800	67%	14
Black P	6.5	4.0	0.1 C	~1280	~800	63%	15
Co	4.2	5.0	0.2 C	1142	900	79%	This work

Table S2 Retention of different electrolyte components after battery cycling

	LiTfSI retention (FTIR-ATR)	DOL and DME retention (HPLC)	DOL and DME retention (NMR)	DOL retention (NMR)	DME retention (NMR)
Co catalyst	71%	64%	65%	60%	69%
Rh catalyst	67%	55%	54%	51%	58%
Pt catalyst	65%	47%	45%	41%	50%

Supplementary References

[1] H. Ye, J. Sun, X. F. Lim, Y. Zhao, J. Y. Lee, *Energy Storage Mater.* **2021**, *38*, 338-343.

[2] Q. Wu, Z. Yao, X. Zhou, J. Xu, F. Cao, C. Li, *ACS Nano* **2020**, *14*, 3365-3377.

[3] H. Gao, S. Ning, Y. Zhou, S. Men, X. Kang, *Chem. Eng. J.* **2021**, *408*, 127323.

[4] C. Li, Y. Zhao, Y. Zhang, D. Luo, J. Liu, T. Wang, W. Gao, H. Li, X. Wang, *Chem. Eng. J.* **2021**, *417*, 129248.

[5] Z. Ye, Y. Jiang, L. Li, F. Wu, R. Chen, *Adv. Mater.* **2020**, *32*, 2002168.

[6] W. Hua, H. Li, C. Pei, J. Xia, Y. Sun, C. Zhang, W. Lv, Y. Tao, Y. Jiao, B. Zhang, S. Z. Qiao, Y. Wan, Q. H. Yang, *Adv. Mater.* **2021**, *33*, 2101006.

[7] J. He, A. Bhargav, A. Manthiram, *ACS Nano* **2021**, *15*, 8583-8591.

[8] C. Luo, X. Liang, Y. Sun, W. Lv, Y. Sun, Z. Lu, W. Hua, H. Yang, R. Wang, C. Yan, J. Li, Y. Wan, Q.-H. Yang, *Energy Storage Mater.* **2020**, *33*, 290-297.

[9] M. Zhao, H.-J. Peng, Z.-W. Zhang, B.-Q. Li, X. Chen, J. Xie, X. Chen, J.-Y. Wei, Q. Zhang, J.-Q. Huang, *Angew. Chem. Int. Ed.* **2019**, *58*, 3779-3783.

[10] A. H. Shao, X.-X. Zhang, Q.-S. Zhang, X. Li, Y. Wu, Z. Zhang, J. Yu, Z.-Y. Yang, *ACS Applied Energy Mater.* **2021**, *4*, 3431-3438.

[11] C. Lu, Y. Chen, Y. Yang, X. Chen, *Nano letters* **2020**, *20*, 5522-5530.

[12] Y. Yang, Y. Zhong, Q. Shi, Z. Wang, K. Sun, H. Wang, *Angew. Chem. Int. Ed.* **2018**, *57*, 15549-15552.

[13] Q. Pang, C. Y. Kwok, D. Kundu, X. Liang, L. F. Nazar, *Joule* **2019**, *3*, 136-148.

[14] J. He, A. Bhargav, A. Manthiram, *Adv. Mater.* **2020**, *32*, 2004741.

[15] Z.-L. Xu, S. Lin, N. Onofrio, L. Zhou, F. Shi, W. Lu, K. Kang, Q. Zhang, S. P. Lau, *Nat. Commun.* **2018**, *9*, 4164.

Author Contributions

Chapter 7: Operando unraveling the catalyst failure in sulfur reduction electrocatalysis

7.1 Introduction and significance

Many electrocatalysts have been used for sulfur reduction reaction (SRR). However, the failure mechanism of catalysts remains unclear. This is due to the instability of polysulfide intermediates under atmosphere, restricting the precise characterizations of SRR process. Therefore it is essential to investigate the catalyst-polysulfides interactions under operando conditions. Herein, we have for the first time, operando unraveled the catalyst failure caused by electrophilic substitution between polysulfides and catalyst. This leads to the surface vulcanization of catalyst and more severely, concomitant catalyst dissolution into electrolyte. Unlike other conventional electrocatalytic reactions, the failure of SRR catalyst does not depend on applied overpotentials. It is confirmed via a series of operando techniques including in-situ synchrotron X-ray diffraction, Infrared and ultraviolet–visible spectra together with theoretical computations. The proposed catalyst failure mechanism is universally extended to 3d, 4d and 5d (e.g. Co, Rh and Pt) metal catalysts. This work benefits further catalyst design for more-efficient sulfur reduction electrocatalysis. The highlights of this work include:

➢ **The first demonstration for the mechanism of catalyst failure in sulfur reduction electrocatalysis.** The failure mechanism of SRR catalysts is attributed to the electrophilic substitution between polysulfides and catalyst. This leads to the surface vulcanization of catalyst and more severely, the concomitant catalyst dissolution into electrolyte. Unlike other

conventional electrocatalytic reactions, the failure of SRR catalyst does not depend on applied voltage overpotentials.

➢ **Operando confirmation via a series of spectroscopic techniques.** Taking Pt catalyst as a typical example, the failure mechanism of catalyst is confirmed via a series of operando techniques including in-situ synchrotron X-ray diffraction, Infrared and ultraviolet–visible spectra together with theoretical computations. This enables us to track the precise information of catalyst-polysulfide interactions during SRR process.

➢ **A universal mechanism that extends to other catalysts.** The proposed catalyst failure mechanism appears as a universal principle, which can be extended to a group of 3d, 4d and 5d (e.g. Co, Rh and Pt) metal catalysts. This benefits further catalyst design for more-efficient sulfur reduction electrocatalysis.

7.2 Operando unraveling the catalyst failure in sulfur reduction electrocatalysis

This Chapter is included as it appears as a journal paper submitted by **Huan Li**, Yan Jiao, Jieqiong Shan, Junnan Hao, Chao Ye, Tao Ling, Qinfen Gu, Bernt Johannessen and Shi-Zhang Qiao[*]. Operando unraveling the catalyst failure in sulfur reduction electrocatalysis. **To be submitted**.

Statement of Authorship

Title of Paper	Operando unraveling the catalyst failure in sulfur reduction electrocatalysis
Publication Status	☐ Published ☐ Accepted for Publication ☐ Submitted for Publication ☑ Unpublished and Unsubmitted work written in manuscript style
Publication Details	Huan Li, Yan Jiao, Jieqiong Shan, Chao Ye, Junnan Hao, Tao Ling, Qinfen Gu, Bernt Johannessen and Shi-Zhang Qiao*, Unsubmitted.

Principal Author

Name of Principal Author (Candidate)	Huan Li		
Contribution to the Paper	Conducted material synthesis, carried out electrochemical tests and wrote the paper		
Overall percentage (%)	70		
Certification:	This paper reports on original research I conducted during the period of my Higher Degree by Research candidature and is not subject to any obligations or contractual agreements with a third party that would constrain its inclusion in this thesis. I am the primary author of this paper.		
Signature		Date	14 June 2022

Co-Author Contributions

By signing the Statement of Authorship, each author certifies that:

i. the candidate's stated contribution to the publication is accurate (as detailed above);

ii. permission is granted for the candidate in include the publication in the thesis; and

iii. the sum of all co-author contributions is equal to 100% less the candidate's stated contribution.

Name of Co-Author	Yan Jiao		
Contribution to the Paper	Helped with theoretical computations		
Signature		Date	14 June 2022

Name of Co-Author	Jieqiong Shan		
Contribution to the Paper	Helped with in-situ infrared spectra		
Signature		Date	14 June 2022

Name of Co-Author	Junnan Hao
Contribution to the Paper	Helped with X-ray adsorption spectra
Signature		Date	14 June 2022

Name of Co-Author	Chao Ye
Contribution to the Paper	Helped with design of sulfur cathode
Signature		Date	14 June 2022

Name of Co-Author	Tao Ling
Contribution to the Paper	Helped with nuclear magnetic resonance and Inductively coupled plasma mass spectrometry
Signature		Date	14 June 2022

Name of Co-Author	Qinfen Gu
Contribution to the Paper	Helped with in-situ synchrotron X-ray diffraction characterizations
Signature		Date	14 June 2022

Name of Co-Author	Bernt Johannessen
Contribution to the Paper	Helped with synchrotron X-ray adsorption spectra
Signature		Date	14 June 2022

Name of Co-Author	Shi-Zhang Qiao
Contribution to the Paper	Supervised the research project
Signature		Date	14 June 2022

Please cut and paste additional co-author panels here as required.

216

Operando unraveling the catalyst failure in sulfur reduction electrocatalysis

Huan Li[1], Yan Jiao[1], Jieqiong Shan[1], Junnan Hao[1], Chao Ye[1], Tao Ling[2], Qinfen Gu[3], Bernt Johannessen[3] and Shi-Zhang Qiao[*1]

[1]School of Chemical Engineering and Advanced Materials, The University of Adelaide, Adelaide, SA 5005, Australia;

[2]School of Materials Science and Engineering and Tianjin Key Laboratory of Composite and Functional Materials, Tianjin University, Tianjin 300350, China;

[3]Australian Synchrotron, ANSTO, 800 Blackburn Rd, Clayton, VIC 3168, Australia.

*Corresponding E-mail: s.qiao@adelaide.edu.au

Sulfur reduction reaction (SRR) is important in metal-sulfur batteries. Varies of electrocatalysts have been proposed, however, the failure mechanism of SRR catalysts has not been investigated. This is largely due to the instability of polysulfide intermediates under ambient atmosphere, restricting the precise characterizations of SRR process. Herein, we have for the first time, operando unraveled the catalyst failure caused by electrophilic substitution between polysulfides and catalyst. This leads to the surface vulcanization of catalyst and more severely, the concomitant catalyst dissolution into electrolyte. Unlike other conventional electrocatalytic reactions, the failure of SRR catalyst does not depend on applied overpotentials. It is confirmed via a series of operando techniques including in-situ synchrotron X-ray diffraction, Infrared and ultraviolet–visible spectra together with theoretical computations. The proposed catalyst failure mechanism appears to be universal that can be extended to a group of 3d, 4d and 5d (e.g. Co, Rh and Pt) metal catalysts. This work benefits further catalyst design for more-efficient sulfur reduction electrocatalysis.

Introduction

Electrocatalytic sulfur reduction reaction (SRR) is important in metal-sulfur batteries.[1-3] In Li−S batteries, it involves consecutive reductions from S_8 ring molecules to soluble lithium polysulfides (Li_2S_x, x = 2~8), and soluble polysulfides into insoluble Li_2S solid ($S_8 \rightarrow Li_2S_x \rightarrow Li_2S$).[4-10] The use of SRR catalysts can increase energy density and life-span of Li−S batteries because it concomitantly promotes kinetics of sulfur reduction, and suppresses shuttle effects of polysulfides.[11-12] Effective catalysts are often based on transition-metals, or compounds of them.[13-17] Although these catalysts are widely reported to improve SRR activity, the failure mechanism of these catalysts remains unclear. The failure mechanisms of catalysts have been widely investigated in other conventional electrocatalytic reactions such as O_2 reduction, CO_2 reduction, N_2 reduction, etc.[17-19] However, there is still an absence of mechanistic study on the catalyst failure for electrocatalytic sulfur reduction.[20, 21] During the SRR process, polysulfides intermediates undergo electrochemical reduction on the catalyst surface. Therefore, the real-time monitoring of catalyst-polysulfide interactions is imperative to track the local changes on catalyst surface. This would help deeply understand the underlying reasons of catalyst failure.

SRR process undergoes in an organic electrolyte.[1, 2, 22] The produced polysulfide intermediates are not stable in air due to their high reactivity with water and oxygen. This restricts the ambient characterizations of SRR catalysts absorbed with polysulfide intermediates. Therefore it is essential to develop real-time techniques that provide precise information of catalyst-polysulfide interfaces under operando conditions.[23-25] The operando protocols are capable of describing voltage-dependent variation of SRR catalysts with different electrochemical states. This allows us to track the change of catalysts during SRR process. Although some in-situ/operando spectroscopy have been developed for

metal-sulfur batteries, most of these undertaking aim at detecting polysulfide evolutions.[23] The change of catalysts has not been covered yet, restricting us to clarify how the catalyst fails during SRR.

In this work, we demonstrate that the electrophilic substitution between polysulfides and catalyst leads to the failure of SRR catalyst. Totally different from other electrocatalytic reactions, the electrophilic substitution between polysulfides and catalyst undergoes a slow chemical process, which does not depend on applied overpotentials. It leads to the surface vulcanization of catalyst and more severely, the concomitant catalyst dissolution into electrolyte. This is confirmed via a series of operando spectroscopic techniques including in-situ synchrotron X-ray diffraction, Infrared and ultraviolet–visible spectra together with theoretical computations. The proposed catalyst failure mechanism appears to be universal that can be extended to a group of 3d, 4d and 5d (e.g. Co, Rh and Pt) metal catalysts. This work clarifies the failure mechanism of SRR catalysts, and benefits further catalyst design for more-efficient sulfur reduction electrocatalysis.

Results and Discussion

Electrophilic substitution between polysulfides and catalysts. Figure 1a schematically shows the catalyst failure during SRR. Pt catalyst is taken as a typical example because it has been widely used for SRR catalyst. During the reduction of S_8 molecular, the lithium polysulfides (Li_2S_x) are produced and adsorbed on the surface of Pt catalyst. Then the electrophilic substitution occurs between Li_2S_x and Pt due to the interaction of Pt 5d and S 3p electron orbitals. This leads to the surface vulcanization of catalyst and the concomitant formation of $Li_2S_xPt_y$ intermediates that dissolved into electrolyte. **Figure 1b** and **1c** presents the transmission electron images (TEM) of synthesized Pt catalyst. The Pt nanoparticles are uniformly distributed on the carbon nanotubes (CNT), and (111)
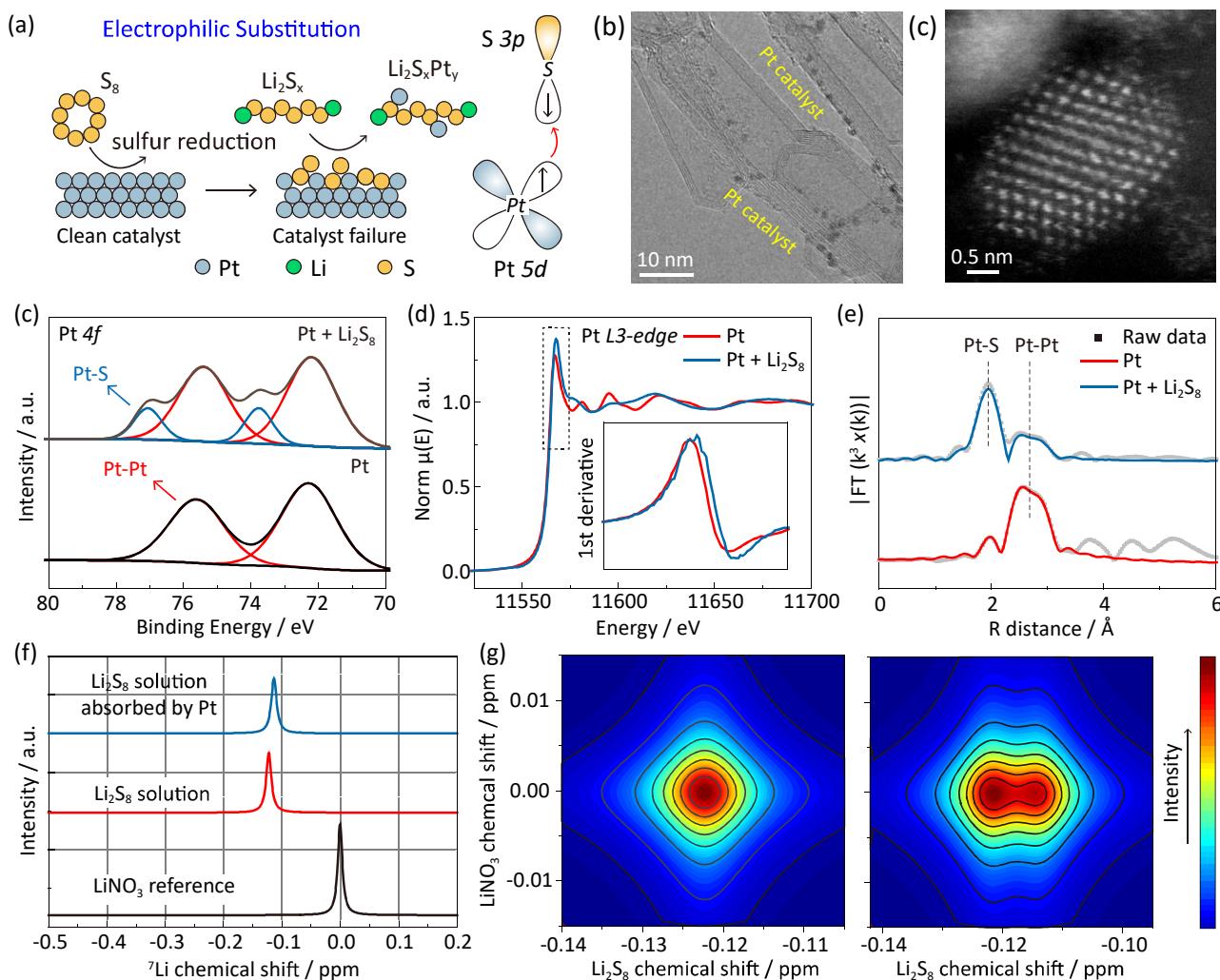
Figure 1 Electrophilic substitution between polysulfides and Pt. (a) Schematic for the electrophilic substitution during SRR; (b, c) TEM images of synthesized Pt catalyst on CNT substrates; (d) Pt 4f XPS spectra, (e) Pt L_3-edge XAS spectra, (f) R-space transformation of XAS spectra for pristine Pt catalyst and Pt after Li_2S_8 adsorption; (f) NMR spectra of Li2S8 solution and Li2S8 solution absorbed after Pt. $LiNO_3$ was used as a reference; (g) The contour NMR pattern showing the chemical shift of Li_2S_8 solution after Pt adsorption.

facet dominates in the Pt nanoparticles. The electrophilic substitution occurs between Li_2S_x and Pt is

a slow chemical process, which does not depend on the applied overpotentials. To prove this idea,

excessive Pt catalyst is immersed into a 5 mM Li_2S_8 solution, and the soaked Pt catalyst (namely

Pt+Li_2S_8) and the residue of Li_2S_8 solution were analyzed by X-ray photoelectron spectra (XPS),

X-ray adsorption spectra (XAS) and nuclear magnetic resonance (NMR). The surface vulcanization

of Pt catalyst is proved by XPS as shown in **Figure 1c**. Pt-Pt bond is only observed for pristine Pt

catalyst, in contrast, obvious Pt-S bond is seen after Li_2S_8 adsorption on Pt catalyst. Synchrotron

XAS analysis was further used to confirm the surface bonding states of Pt catalyst. **Figure 1d** depicts

the Pt L_3-edge XAS data for fresh Pt catalyst and Pt+Li_2S_8. There is an obvious shift to higher energy

states after Li_2S_8 adsorption, indicating a higher valence of Pt. This is attributed to the electron

transfer from Pt 5d to S 3p. The R-space transformation provides concise bond information as shown

in **Figure 1e**. An obvious scattering at ~ 2 Å is observed for Pt+Li_2S_8, which corresponds to the

formation of Pt-S bond on the catalyst surface (**Supplementary Figure 1** and **2**). To further confirm

the dissolution of $Li_2S_xPt_y$ intermediates, the residue of Li_2S_8 solution after Pt adsorption was

subjected for ^7Li NMR test. In the $Li_2S_xPt_y$ intermediates, both Pt and Li atoms are bonded with

sulfur. Therefore, the formation of Pt-S bond in $Li_2S_xPt_y$ intermediates should result in the change of

^7Li chemical shift. **Figure 1f** compares the NMR chemical shift of pristine Li_2S_8 solution and Li_2S_8

after Pt adsorption by referencing with $LiNO_3$.[26] The peak in NMR spectra of Li_2S_8 has an upshift

around -0.12 ppm after adsorbed by Pt catalyst. The upshift to low field is ascribed to deshielding

effect on ^7Li atom. To give a clear view on the chemical shift, the NMR data was transformed into

contour patterns by plotting the chemical shifts of Li_2S_8 and $Li_2S_xPt_y$ as x-axis and that of $LiNO_3$

reference as y-axix (**Figure 1g**). Compared to the pristine Li_2S_8, the solution after Pt adsorption

presents an obvious shift to higher values due to the formation of $Li_2S_xPt_y$ intermediates. These

results clearly demonstrate the failure mechanism of Pt catalyst. The surface vulcanization decreases

the catalytic activity of Pt, and the dissolution of $Li_2S_xPt_y$ intermediates leads to the loss of catalyst.

Identification of $Li_2S_xPt_y$ intermediates via operando spectroscopy. We further carried out the

in-situ IR spectra to indentify the formation of $Li_2S_xPt_y$ intermediates. S-S bond has obvious IR

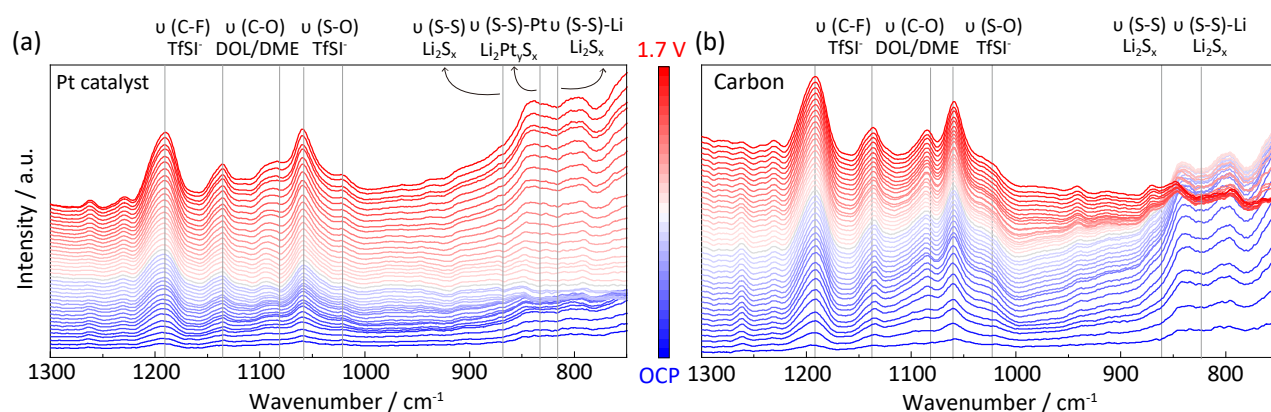**Figure 2 Identification of Li$_2$S$_x$Pt$_y$ intermediates via operando spectroscopy.** The stacked IR plots on the interface between sulfur cathode and electrolyte with (a) Pt catalyst and (b) carbon reference. The operation voltage is from OCP to 1.7 V.

adsorption signals due to the bond vibration (**Supplementary Figure 3**).[27] The IR signal should change while sulfur is binding to Pt atoms in Li$_2$S$_x$Pt$_y$ intermediates. To confirm this idea, in-situ IR spectra was carried out during SRR process (**Supplementary Figure 4**). **Figure 2a** and **2b** compare the in-situ IR stacked plots for Pt catalyst and carbon reference during SRR process. The voltage is from open circuit potential (OCP) to 1.7 V. P. Peak at ~860 cm^{-1} and ~820 cm^{-1} is assigned to the S-S bond in polysulfides (**Supplementary Figure 5**). With Pt catalyst, a new peak emerges at ~840 cm^{-1}. This is attributed to the evolution of Li$_2$S$_x$Pt$_y$ intermediates. The Pt-S bond causes the vibration change of S-S bond, and results in the appearance of new IR adsorption peaks (**Supplementary Figure 6**).

Catalyst failure revealed by in-situ synchrotron X-ray diffraction and ultraviolet-visible spectra. To quantify the molar ratio of S to Pt in Li$_2$S$_x$Pt$_y$ intermediates, we combined ultraviolet-visible spectra (UV-vis) and inductively coupled plasma–mass spectrometry (ICP-MS) to determine the S and Pt contents, respectively. As shown in **Figure 3a**, the concentration of polysulfides is correlated to the UV-vis absorbance, allowing us to calculate the S content after Pt adsorption (**Supplementary Figure 7-10**). Additionally, ICP-MS is effective to quantify trace
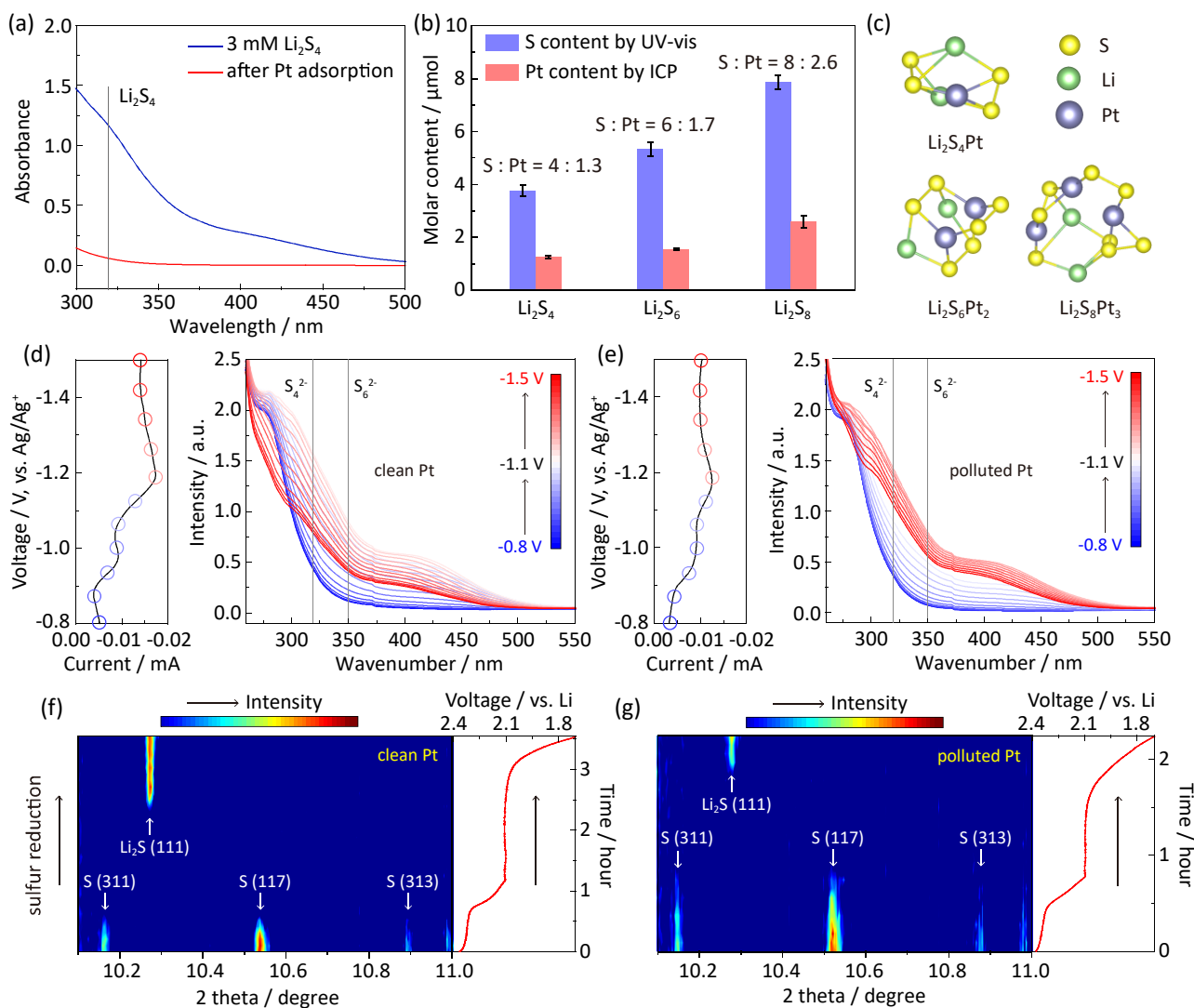
Figure 3 Catalyst failure revealed by in-situ synchrotron X-ray diffraction and ultraviolet-visible spectra. (a) UV-vis plots for 3 mM Li_2S_4 and 3 mM Li_2S_4 with Pt adsorption; (b) The determined molar ratio of S to Pt combined with UV-vis and ICP-MS tests; (c) The optimized structures of Li_2S_4Pt, $Li_2S_6Pt_2$ and $Li_2S_8Pt_3$; In-situ UV-vis plots during SRR for (d) clean Pt catalyst and (e) polluted Pt catalyst; In-situ synchrotron XRD contour patterns of sulfur cathode in Li-S batteries with (f) clean Pt catalyst and (g) polluted Pt catalyst.

amounts of metal elements, such as Pt. Typical polysulfide intermediates including Li_2S_4, Li_2S_6 and Li_2S_8 are taken as examples. The molar ratios of S to Pt in these solutions are determined as 4:1.3, 6:1.7 and 8:2.6, respectively (**Supplementary Figure 11**). **Figure 3c** shows the computational optimized structures of Li_2S_4Pt, $Li_2S_6Pt_2$ and $Li_2S_8Pt_3$ based on density functional theory (DFT).

These structures are quite stable by forming the S-Pt bonds.

To further verify the catalyst failure, in-situ UV-vis and in-situ synchrotron X-ray diffraction (XRD) are comparatively carried out for clean Pt catalyst and Pt catalyst soaked in polysulfides (namely polluted Pt).[28, 29] As shown in **Figure 3d** and **3e**, clean Pt and polluted Pt catalyst are capable to catalyze sulfur reduction to produce polysulfide intermediates as evidenced by the increased S_4^{2-} and S_6^{2-} peaks (blue to white plots) (**Supplementary Figures 12** and **13**). However, the polluted Pt has limited ability to catalyze further reduction from polysulfides to Li_2S_2/L_2S. In SRR, the reduction from polysulfides to Li_2S_2/L_2S is the rate-determined steps. For polluted Pt, it still remains a high-intensity of polysulfides absorbance even the applied voltage is as low as -1.5 V (vs. Ag/Ag^+), white to red plots (**Supplementary Figure 14**). This confirms the limited ability of polluted Pt catalyst in catalyzing SRR. To further track the dissolution of sulfur and evolution of Li_2S, in-situ synchrotron XRD was carried out for sulfur cathodes with clean and polluted Pt catalysts. This test is highly significantly sensitive in monitoring the minor crystal changes in sulfur and Li_2S during SRR. The diffraction peaks at 8.79 °, 9.83 °, 10.16 °, 10.54 ° and 11.9 ° are assigned to sulfur, and the peak at 10.3 ° for Li_2S (**Supplementary Figures 15** and **16**). **Figure 3f** and **3g** present the time-dependent XRD pattern and discharge curve for sulfur cathode with clean Pt and polluted Pt catalysts. In **Figure 3f**, during SRR the sulfur signal disappears quickly, and the Li_2S signal appears significantly earlier. In contrast with polluted Pt catalyst, crystallized sulfur remains for a lengthy period and a delayed Li_2S evolution is observed, **Figure 3g** (**Supplementary Figure 17**). This sharp contrast confirms the decreased catalytic activity of polluted Pt catalyst in driving sulfur dissolution and Li_2S evolution during SRR (**Supplementary Figure 18**). The above results confirm the decreased catalytic activity caused by electrophilic substitution (**Supplementary Figure 19**).
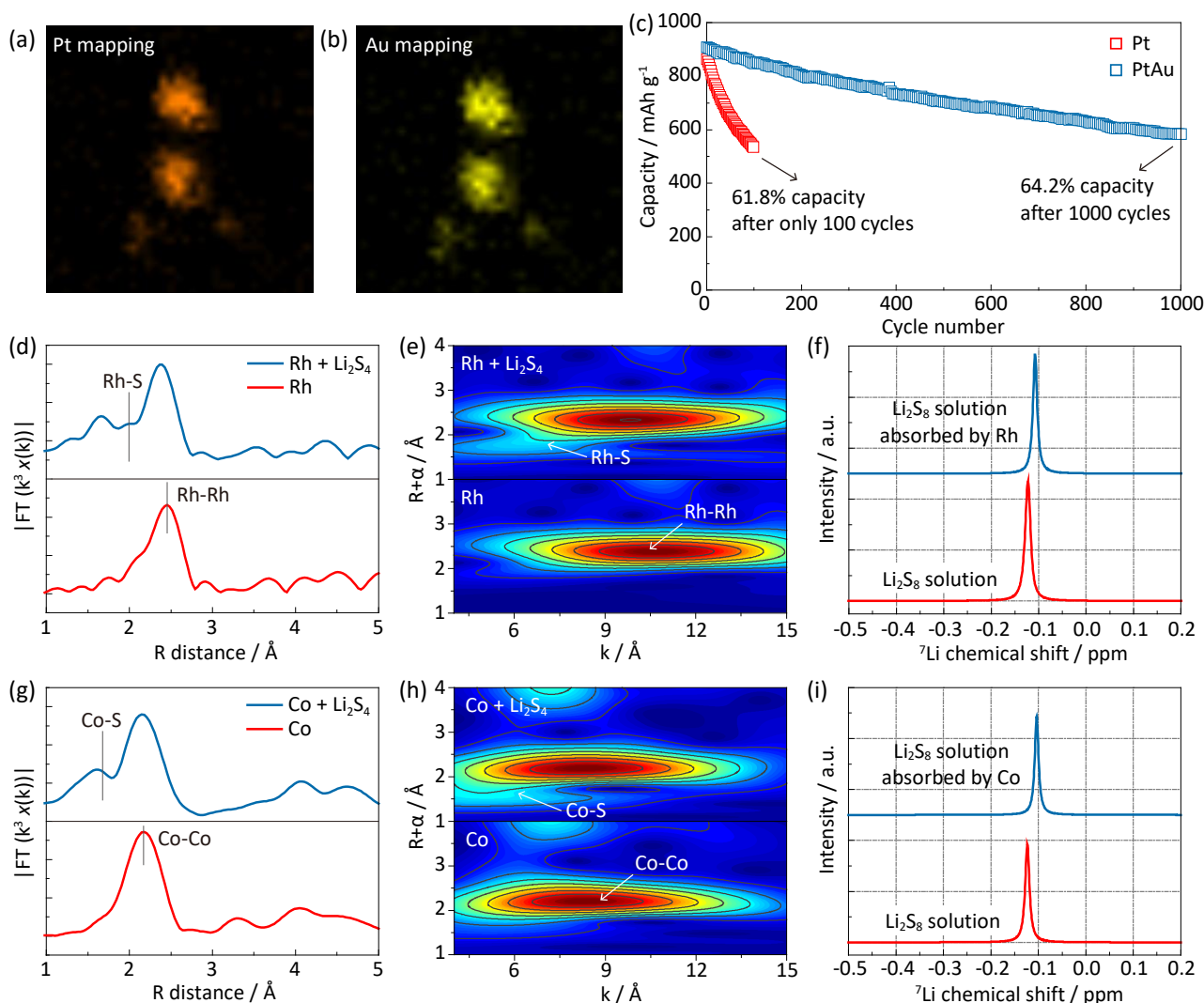
Figure 5 A universal failure mechanism extended to other catalysts. Elemental mapping of (a) Pt and (b) Au elements in PtAu alloy; (c) The cycling performance of Li-S batteries using PtAu and Pt catalysts; (d) R-space transformation of XAS spectra, (e) WT transformation of XAS spectra, (f) NMR spectra for pristine Rh catalyst and Rh after polysulfide adsorption; (g) R-space transformation of XAS spectra, (h) WT transformation of XAS spectra, (i) NMR spectra for pristine Co catalyst and Co after polysulfide adsorption.

A universal failure mechanism extended to other catalysts. The electrophilic substitution between polysulfides and Pt is attributed to the charge transfer from Pt 5d to S 3p orbital. Therefore it is essential to fill the Pt 5d orbital electrons to restrain the electrophilic substitution. Au is full of 5d-orbital electrons and therefore the Au-alloying with Pt would partly fill the Pt 5d-orbital electrons

in the most outer shell. The PtAu catalysts by microwaving the Pt- and Au- precursors (details in the experimental section), and Pt and Au elements are uniformly distributed (**Figure 4a**, **4b**, and **Supplementary Figure 20**). As expected, the Li-S battery with PtAu catalyst is workable over 1000 cycles with a high capacity retention of 64.2%. In contrast, the Pt-catalyzed Li-S battery exhibits a significantly capacity decay just only 100 cycles. This comparison suggests the effectiveness to restrain the catalyst failure by suppressing the electrophilic substitution between polysulfides and catalysts.

To prove the electrophilic substitution as a universal mechanism for catalyst failure, other typical 4d and 3d metal catalyst are then investigated. **Figure 4d** shows the R-space transformation of XAS plots for Rh catalyst with and without polysulfide reactions. An obvious Rh-S bond is observed on the catalyst surface while adsorbed with Li_2S_4. The wave-transform (WT) contour pattern further verifies the formation of Rh-S bond (**Figure 4e** and **Supplementary Figure 21**). **Figure 4f** compares the NMR chemical shift of pristine Li_2S_8 solution and Li_2S_8 after Rh adsorption. The upshift of ^7Li peak is ascribed to the evolution of $Li_2S_xRh_y$ intermediates. Similar to Rh and Pt catalyst, Co-S bond is observed on the Co surface after adsorbed with polysulfides (**Figure 4g**, **4h** and **Supplementary Figure 22**). The evolution of $Li_2S_xRh_y$ intermediate is also confirmed by the NMR chemical shift (**Figure 4i**). The above results confirm the electrophilic substitution for a group of 3d, 4d and 5d metal catalyst, appealing as a universal mechanism for catalyst failure.

Conclusions

We clarify the failure mechanism of SRR catalysts caused by electrophilic substitution between polysulfides and catalyst. This leads to the surface vulcanization of catalyst and more severely, the concomitant catalyst dissolution into electrolyte. Totally different from other electrocatalytic

reactions, the electrophilic substitution between polysulfides and catalyst undergoes a slow chemical process, which does not depend on applied voltage overpotentials. The catalyst failure is confirmed via a series of operando spectroscopic techniques including in-situ synchrotron X-ray diffraction, Infrared and ultraviolet–visible spectra together with theoretical computations. The proposed catalyst failure mechanism appears to be universal that can be extended to a group of 3d, 4d and 5d (e.g. Co, Rh and Pt) metal catalysts. This work proposes the failure mechanism of SRR catalysts, and benefits further catalyst design for more-efficient sulfur reduction electrocatalysis.

Methods

Synthesis of Pt, Rh, Co and PtAu catalysts. Carbon nanotubes (CNT) were used as substrate for the metal catalysts. For the synthesis of Pt catalyst, 20 mg CNT was mixed and milling with 9.4 mg chloroplatinic acid hexahydrate (H_2PtCl_6 $6H_2O$). Then the mixture was added to a transparent quartz crucible and placed in an 800 W microwave reactor under Ar. No obvious effect was observed for $\approx$ 10 s, after which there was a violent thermal reaction (flashes, the powder turned red, and a large amount of grey smoke was produced) that lasted for nearly 50 s until no smoke was produced. After cooling down, the mixture was washed with de-ionized water and diluted hydrochloric acid to remove the residues. Finally, Pt catalyst on CNT was obtained after drying the products. Synthesis of other metal nanoparticles follows the same procedure with the same mass concentration of metals in chloride-based precursors. Rhodium chloride ($RhCl_3$) and cobalt chloride ($CoCl_2$) were used to synthesize Rh and Co nanoparticle catalysts, respectively. For synthesis of PtAu catalyst, 20 mg CNT was mixed and milling with 5.8 mg chloroplatinic acid hexahydrate and 3.6 mg gold chloride tetrahydrate followed by the same procedure.

Structural characterization. The morphology and structure of samples was characterized by scanning electron microscopy (SEM, Hitachi S4800, Japan). High-resolution STEM images were obtained under a Cs-corrected STEM (FEI Titan Cubed Themis G2 300) operated at 300 kV. Ultraviolet/visible (UV-VIS) was carried out using a spectrometer (SHIMADZU UV-2600). X-ray diffraction (XRD) data were collected on a Rigaku Mini Flex 600 X-Ray Diffractometer. X-ray photoelectron spectra (XPS) were measured with the Thermo Fisher Scientific ESCALAB Xi+, Al Kα radiation. Raman spectra were collected with Labram HR Evolution (Horiba Scientific). The synchrotron-based near-edged X-ray absorption fine structure (NEXAFS) of Co L-edge was

performed on the soft X-ray spectroscopy beamline at Australian Synchrotron (Clayton), part of ANSTO. The synchrotron-based X-ray absorption fine structure (XAFS) was performed on the X-ray absorption beamline at Australian Synchrotron (Clayton), part of ANSTO.

Electrochemical tests. For Li−S battery testing, the sulfur cathode was prepared by mixing 80 wt.% of S with 20 wt.% of the catalyst. The catalyst/S mixture was ball-milled with LA133 binder with a mass ratio 90:10. Total sulfur content in the cathode was 72 wt.%. Li−S batteries were assembled with CR2032 coin-cell in an Ar-filled glove box by coupling the Li-metal anode with 1 mol L^{-1} LiTfSi in DOL/DME (1:1 volume ratio) with 0.4 mol L^{-1} LiNO$_3$ as the electrolyte. The CV measurements were carried out from 1.7 to 2.8 V with a scan rate of 0.2 mV s^{-1}. For electrochemical testing of Li−S batteries including, rate and cycling performance, the batteries were galvanostatically charged and discharged at the selected current rates (1C = 1675 mAh g^{-1}) and cycles.

Model optimization. Computations for this work were carried out using density functional theory (DFT) as implemented in VASP code. Electronic exchange-correlation energy was modeled using the Perdew-Burke-Ernzerhof (PBE) function within a generalized gradient approximation (GGA). The projector-augmented wave (PAW) method was used to describe the ionic cores. For the plane-wave expansion a 450 eV kinetic energy cut-off was used following testing a series of different cut-off energies. A Monkhorst-Pack 2×2×1 k-point grid was used to sample the Brillouin zone. Convergence criterion for the electronic structure iteration was set to 10^{-4} eV, and that for geometry optimizations was 0.02 eV Å^{-1} on force. A Gaussian smearing of 0.1 eV was applied during geometry optimization and for total energy computations.

Data availability

Data supporting findings from this work are available within the article and Supplementary Information files. All other relevant data supporting findings are available from the corresponding author on request.

References

1 Peng, L. *et al.* A fundamental look at electrocatalytic sulfur reduction reaction. *Nat. Catal.* **3**, 762-770 (2020).

2 Zhao, C. *et al.* A high-energy and long-cycling lithium–sulfur pouch cell via a macroporous catalytic cathode with double-end binding sites. *Nat. Nanotech.* **16**, 166-173 (2020).

3 Zhao, C. X. *et al.* Semi-Immobilized Molecular Electrocatalysts for High-Performance Lithium-Sulfur Batteries. *J. Am. Chem. Soc.* **143**, 19865-19872 (2021).

4   Zhou, G., Chen, H. & Cui, Y. Formulating energy density for designing practical lithium–sulfur batteries. *Nat. Energy* **7**, 312-319 (2022).

5   Li, G., Chen, Z. & Lu, J. Lithium-Sulfur Batteries for Commercial Applications. *Chem* **4**, 3-7 (2018).

6   Manthiram, A., Fu, Y., Chung, S. H., Zu, C. & Su, Y. S. Rechargeable lithium-sulfur batteries. *Chem Rev* **114**, 11751-11787 (2014).

7   Fang, R. *et al.* More Reliable Lithium-Sulfur Batteries: Status, Solutions and Prospects. *Adv. Mater.* **29**, 1606823 (2017).

8   Pang, Q., Liang, X., Kwok, C. Y. & Nazar, L. F. Advances in lithium-sulfur batteries based on multifunctional cathodes and electrolytes. *Nat. Energy* **1**, 16132 (2016).

9   Tikekar, M. D., Choudhury, S., Tu, Z. Y. & Archer, L. A. Design principles for electrolytes and interfaces for stable lithium-metal batteries. *Nat. Energy* **1**, 16114 (2016).

10   Yang, X., Luo, J. & Sun, X. Towards high-performance solid-state Li-S batteries: from fundamental understanding to engineering design. *Chem. Soc. Rev.* **49**, 2140-2195 (2020).

11   Yang, Y. *et al.* Electrocatalysis in Lithium Sulfur Batteries under Lean Electrolyte Conditions. *Angew. Chem. Int. Ed.* **57**, 15549-15552 (2018).

12   Song, Y. *et al.* Rationalizing Electrocatalysis of Li–S Chemistry by Mediator Design: Progress and Prospects. *Adv. Energy Mater.* **10**, 1901075 (2019).

13   Hua, W. *et al.* Selective Catalysis Remedies Polysulfide Shuttling in Lithium-Sulfur Batteries. *Adv. Mater.*, **33** (38), 2101006 (2021).

14   Zhong, Y. R. *et al.* Surface Chemistry in Cobalt Phosphide-Stabilized Lithium-Sulfur Batteries. *J. Am. Chem. Soc.* **140**, 1455-1459 (2018).

15   Xue, W. *et al.* Intercalation-conversion hybrid cathodes enabling Li–S full-cell architectures with jointly superior gravimetric and volumetric energy densities. *Nature Energy* **4**, 374-382 (2019).

16   Du, Z. *et al.* Cobalt in Nitrogen-Doped Graphene as Single-Atom Catalyst for High-Sulfur Content Lithium-Sulfur Batteries. *J. Am. Chem. Soc.* **141**, 3977-3985 (2019).

17   Shao, M., Chang, Q., Dodelet, J. P. & Chenitz, R. Recent Advances in Electrocatalysts for Oxygen Reduction Reaction. *Chem. Rev.* **116**, 3594-3657 (2016).

18   Liu, D. *et al.* Development of Electrocatalysts for Efficient Nitrogen Reduction Reaction under Ambient Condition. *Adv. Funct. Mater.* **31**, 2008983 (2020).

19 Zheng, Y. *et al.* Understanding the Roadmap for Electrochemical Reduction of CO_2 to Multi-Carbon Oxygenates and Hydrocarbons on Copper-Based Catalysts. *J. Am. Chem. Soc.* **141**, 7646-7659 (2019).

20 Al Salem, H., Babu, G., Rao, C. V. & Arava, L. M. R. Electrocatalytic Polysulfide Traps for Controlling Redox Shuttle Process of Li-S Batteries. *J. Am. Chem. Soc.* **137**, 11542-11545 (2015).

21 Chen, H. *et al.* Catalytic materials for lithium-sulfur batteries: mechanisms, design strategies and future perspective. *Mater. Today* **52**, 364-388 (2022).

22 Lu, Y.-C., He, Q. & Gasteiger, H. A. Probing the Lithium–Sulfur Redox Reactions: A Rotating-Ring Disk Electrode Study. *J. Phys. Chem. C* **118**, 5733-5741 (2014).

23 Zhang, L. *et al.* In situ optical spectroscopy characterization for optimal design of lithium-sulfur batteries. *Chem. Soc. Rev.* **48**, 5432-5453 (2019).

24 Li, M. *et al.* In Situ Techniques for Developing Robust Li-S Batteries. *Small Methods* **2** (11), 1800133 (2018).

25 Li, H. *et al.* Revealing Principles for Design of Lean-Electrolyte Lithium Metal Anode via In Situ Spectroscopy. *J. Am. Chem. Soc.* **142**, 2012-2022 (2020).

26 Xiao, J. *et al.* Following the Transient Reactions in Lithium-Sulfur Batteries Using an In Situ Nuclear Magnetic Resonance Technique. *Nano letters* **15**, 3309-3316 (2015).

27 Dillard, C., Singh, A. & Kalra, V. Polysulfide Speciation and Electrolyte Interactions in Lithium–Sulfur Batteries with In Situ Infrared Spectroelectrochemistry. *J. Phys. Chem. C* **122**, 18195-18203 (2018).

28 Li, H. *et al.* Reversible electrochemical oxidation of sulfur in ionic liquid for high-voltage Al−S batteries. *Nat. Commun.* **12**, 5714 (2021).

29 Zou, Q. & Lu, Y. C. Solvent-Dictated Lithium Sulfur Redox Reactions: An Operando UV-vis Spectroscopic Study. *J. Phys. Chem. Lett.* **7**, 1518-1525 (2016).

Acknowledgements

spectroscopy beamline, and XAS beamline at the Australian Synchrotron, Clayton, Victoria, a part of ANSTO.

Author contributions:

S.-Z. Q. conceived and supervised this research; H. L. designed and carried out experiments and DFT computations; Y. J. assisted with the DFT computations; J. S. helped with the in-situ IR test; J. H. assisted with the synchrotron XAS test; C. Y. assisted with the design of sulfur cathode; T. L. helped with the NMR and ICP-MS tests; Q. G. helped with the in-situ synchrotron XRD; B. J. carried out the XAS test and related data analyses; S.-Z. Q. edited the manuscript. All authors discussed results and commented on the manuscript.

Competing interests

The authors declare no competing financial interests.

Additional information

Supplementary Information is available for this paper at http://www.nature.com/XXX

Correspondence and requests for materials should be addressed to S.Z. Q.

Reprints and permissions information is available at www.nature.com/reprints.

Publisher's note: Springer Nature remains neutral with regard to jurisdictional claims in published maps and institutional affiliations.

Supplementary Information

Operando unraveling the catalyst failure in sulfur reduction electrocatalysis

Huan Li[1], Yan Jiao[1], Jieqiong Shan[1], Junnan Hao[1], Chao Ye[1], Tao Ling[2], Qinfen Gu[3], Bernt Johannessen[3] and Shi-Zhang Qiao[*1]
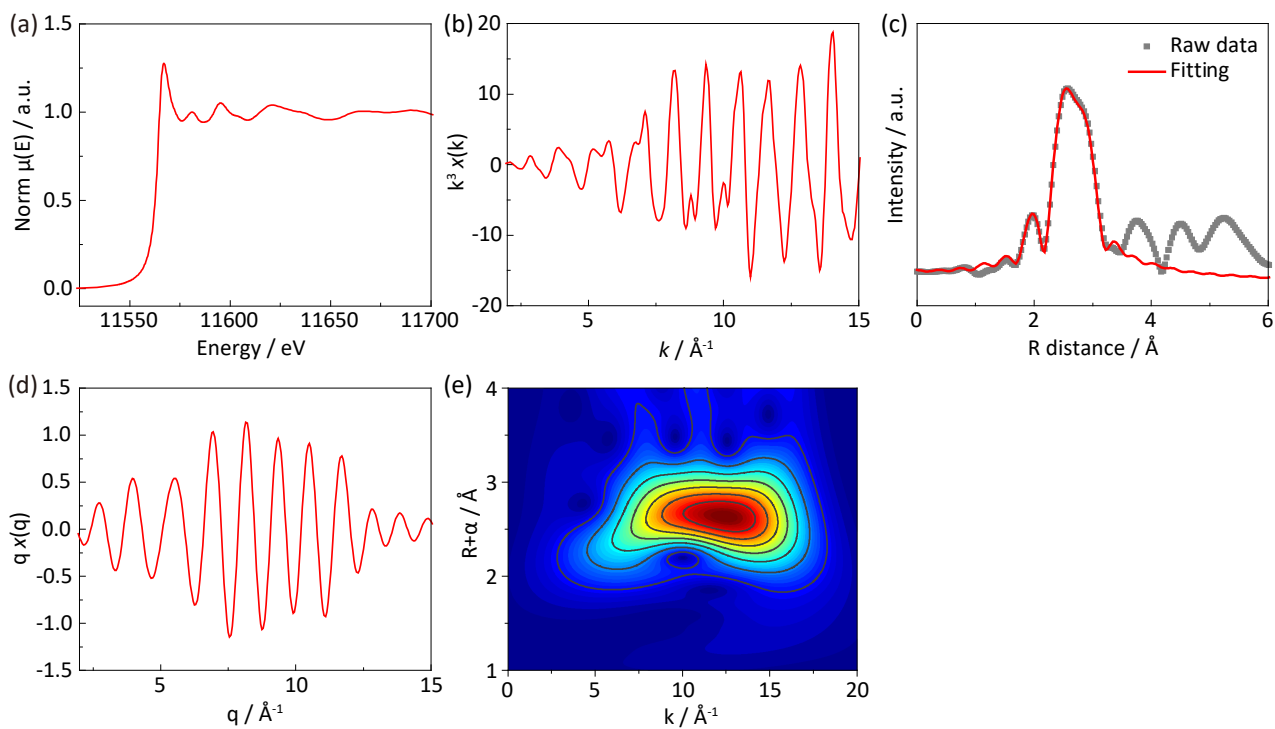
[1]School of Chemical Engineering and Advanced Materials, The University of Adelaide, Adelaide, SA 5005, Australia;

[2]School of Materials Science and Engineering and Tianjin Key Laboratory of Composite and Functional Materials, Tianjin University, Tianjin 300350, China;

[3]Australian Synchrotron, ANSTO, 800 Blackburn Rd, Clayton, VIC 3168, Australia.

***Corresponding E-mail: s.qiao@adelaide.edu.au

Supplementary Results

Supplementary Figure 1 (a) Normalized Pt L_3-edge X-ray adsorption spectra for Pt foil; (b) k-space curve, (c) R-space fitting and (d) q-space curve for Pt foil; (e) The wavelet-transformed contour pattern for Pt foil.
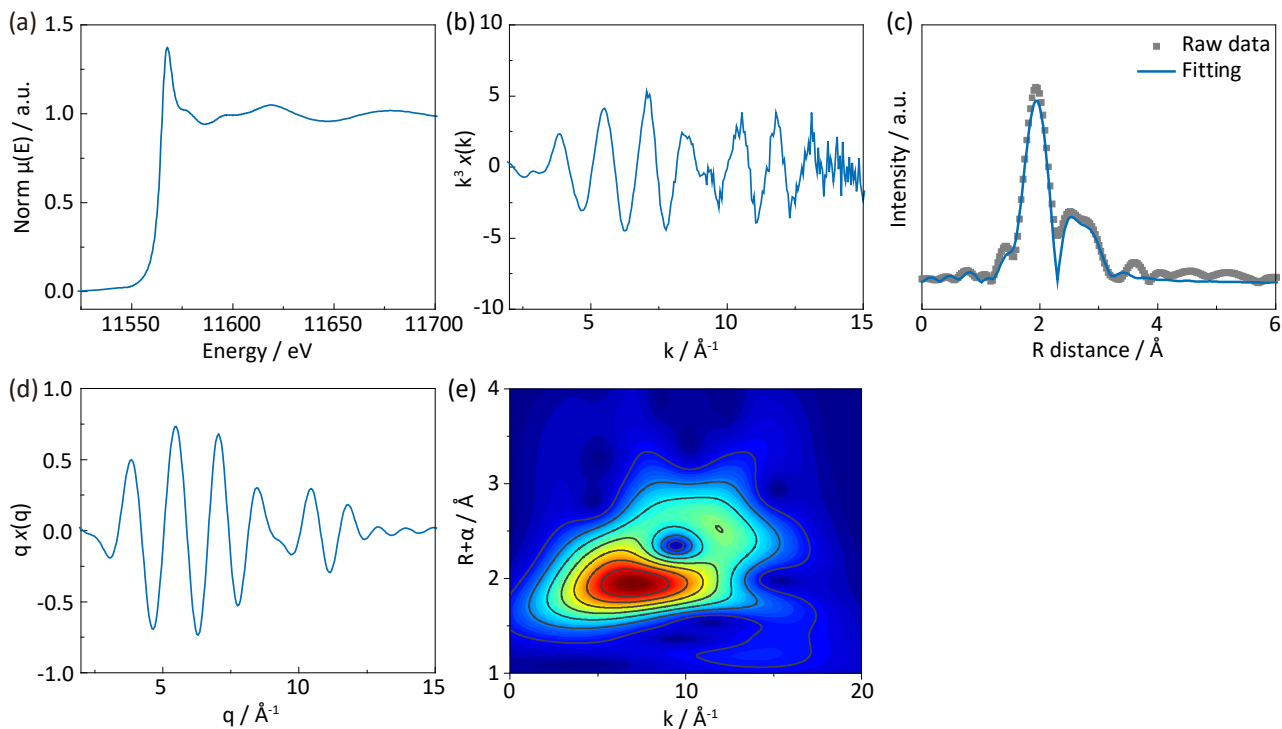
Supplementary Figure 2 (a) Normalized Pt L$_3$-edge X-ray adsorption spectra for Pt catalyst after polysulfide adsorption; (b) k-space curve, (c) R-space fitting and (d) q-space curve for Pt catalyst after polysulfide adsorption; (e) The corresponding wavelet-transformed contour pattern.
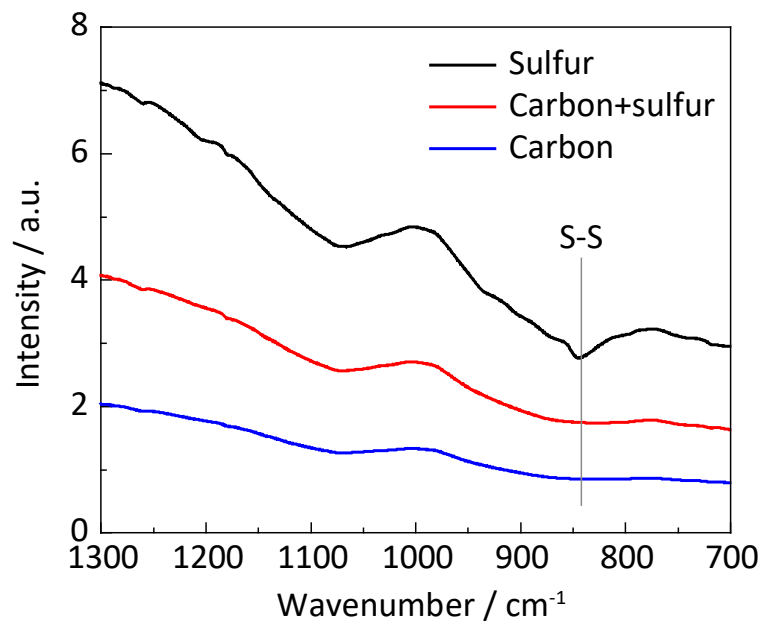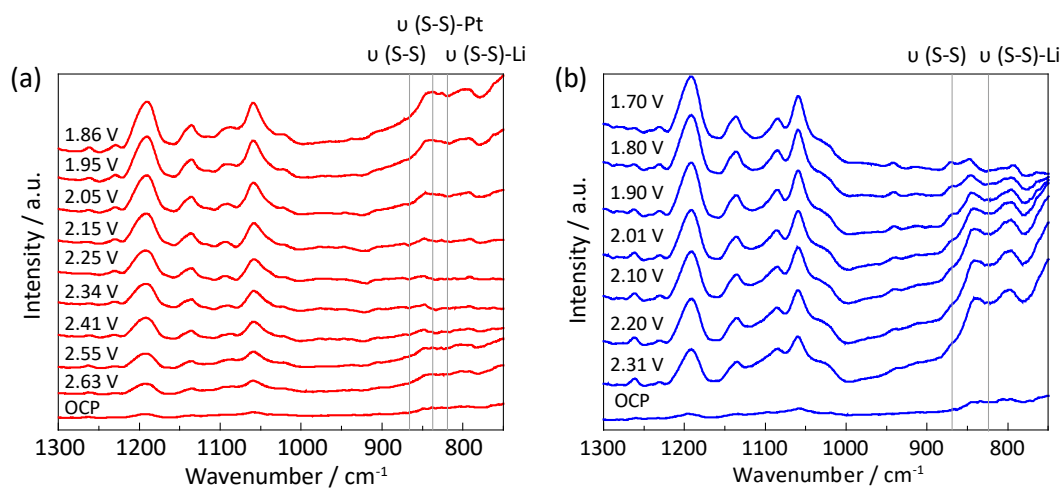
Supplementary Figure 3 FTIR spectra of sulfur, carbon/sulfur and carbon powders. The powders were mixed with KBr with a mass ratio of 1:99. Peak at 844 cm^{-1} is assigned to S-S bond in sulfur.
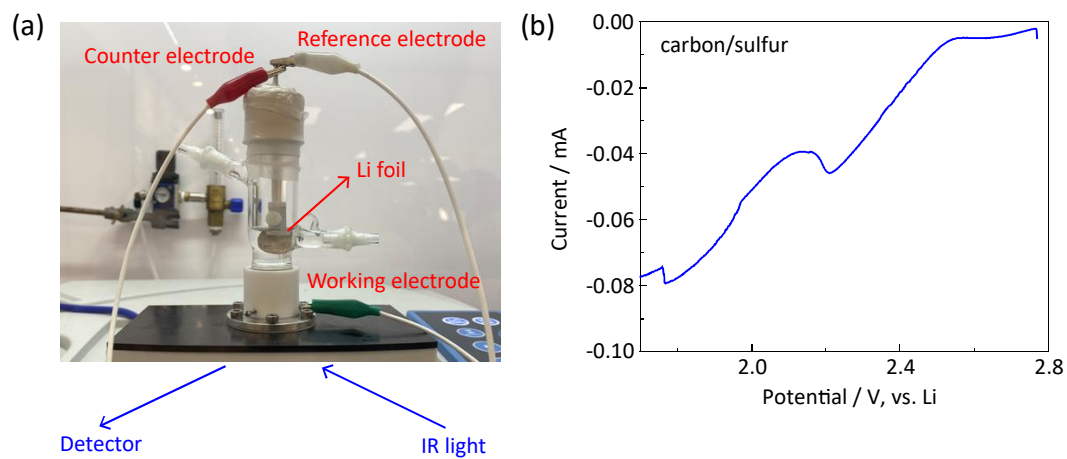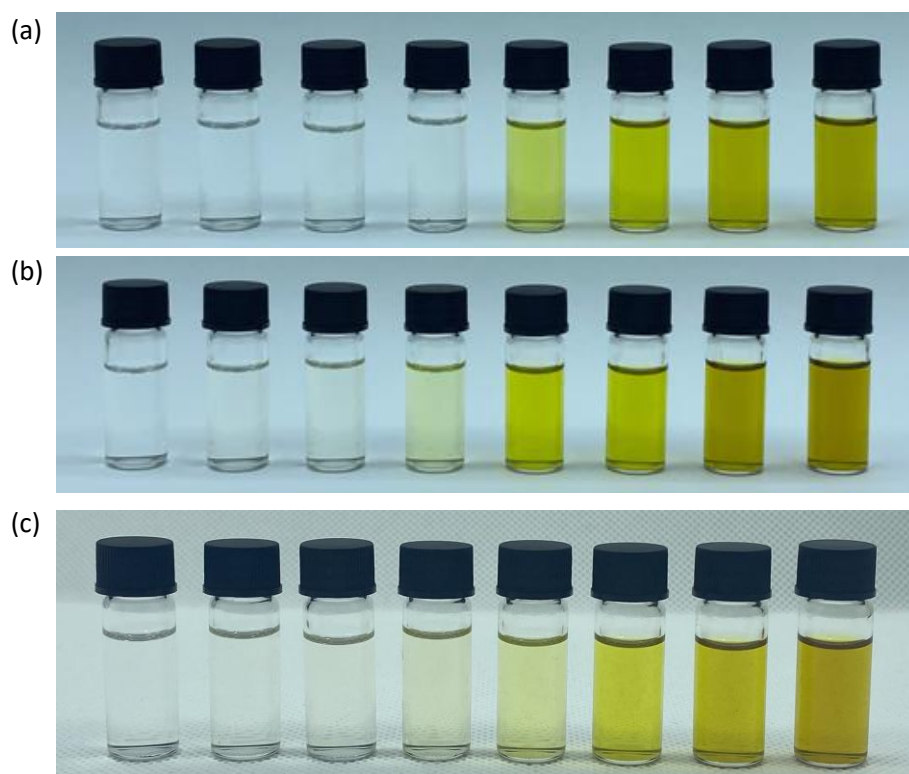
Supplementary Figure 4 (a) Digital photograph of cell for *in-situ* ATR-IR test; (b) Linear scanning voltammetry (LSV) curves of carbon/sulfur cathode from open circuit potential (OCP) to 1.7 V.
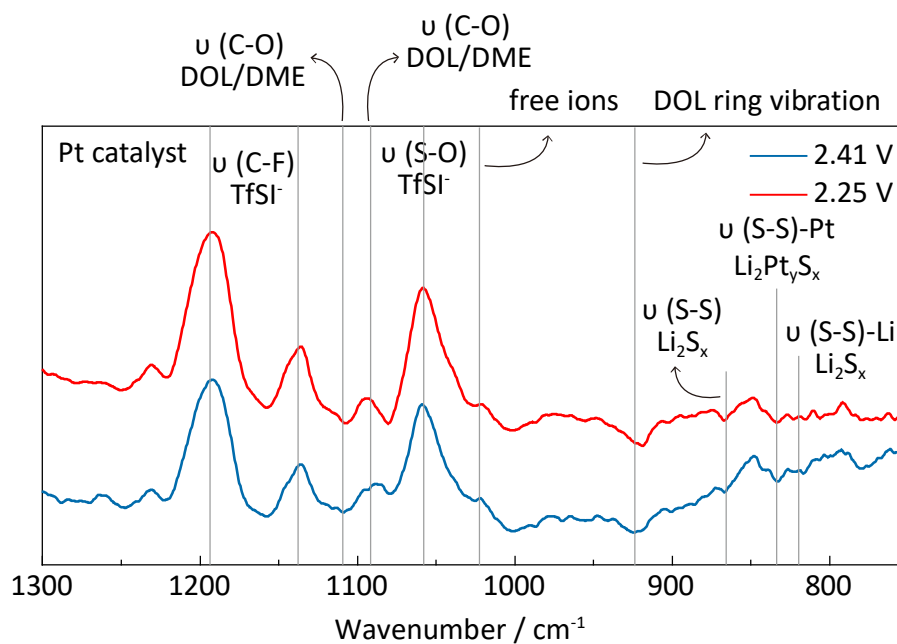
Supplementary Figure 5 Peak assignment of ATR-IR spectra for Pt/S cathode. The spectra include peaks of both polysulfide intermediates and electrolyte components.

Supplementary Figure 6 *In-situ* ATR-IR spectra of sulfur cathodes with (a) Pt catalyst and (b) carbon reference at different voltages. Obvious polysulfide signals are detected from both spectra. $Li_2Pt_yS_x$ signal are seen at 833 cm^{-1} in (a).

**Supplementary Figure 7** Digital photograph of (a) Li$_2$S$_4$, (b) Li$_2$S$_6$ and (c) Li$_2$S$_8$ standard solutions in 1 mol L^{-1} LiTFSI in DOL/DME electrolyte. For Li$_2$S$_4$ and Li$_2$S$_6$, concentrations are from left to right, respectively, 0.2, 0.53, 0.8, 1, 2, 3, 4 and 5 mmol L^{-1}. For Li$_2$S$_8$, concentrations are 0.2, 0.4, 0.6, 0.8, 1, 2, 3, 4 mmol L^{-1} from left to right.
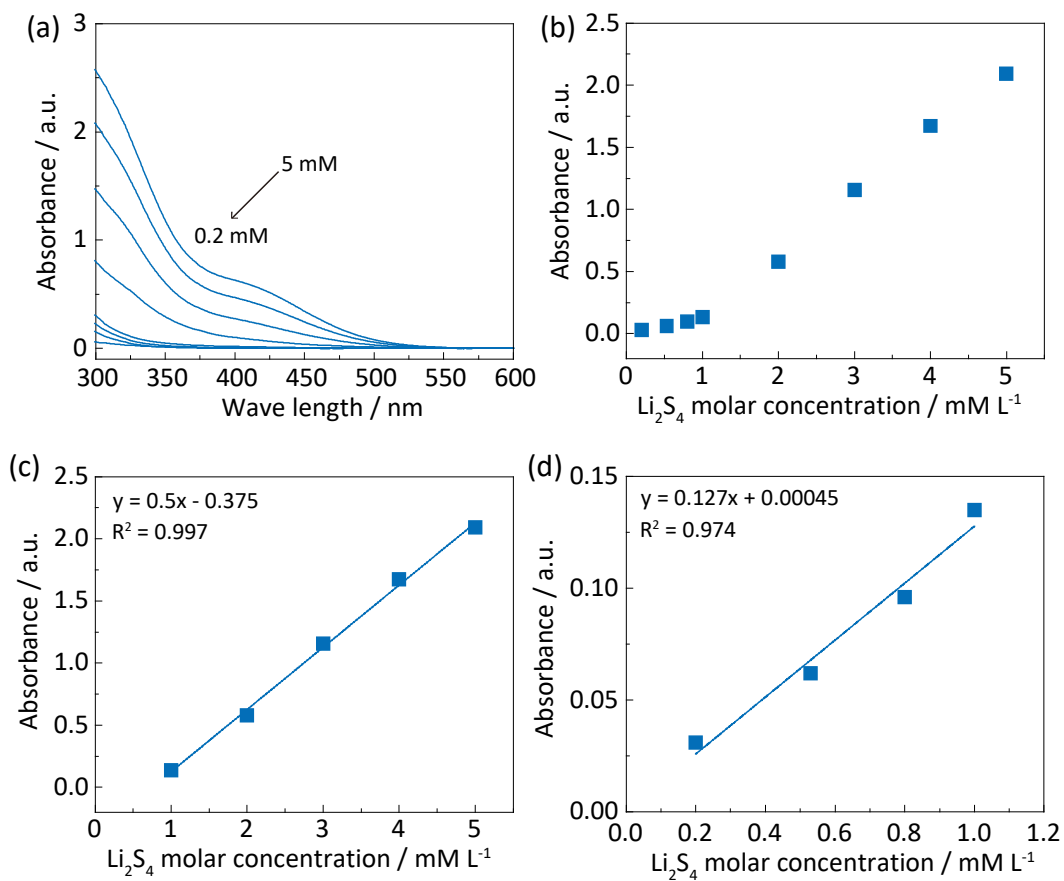
Supplementary Figure 8 (a) UV-vis absorbance curves for Li_2S_4 in 1 mol L^{-1} LiTFSI in DOL/DME electrolyte with Li_2S_4 concentration from 0.2 to 5 mmol L^{-1}; (b) Relationship between Li_2S_4 molar concentration and UV-vis absorbance; Linear fit of Li_2S_4 molar concentration to UV-vis absorbance in, (c) ultra-low, and (d) greater concentration region.
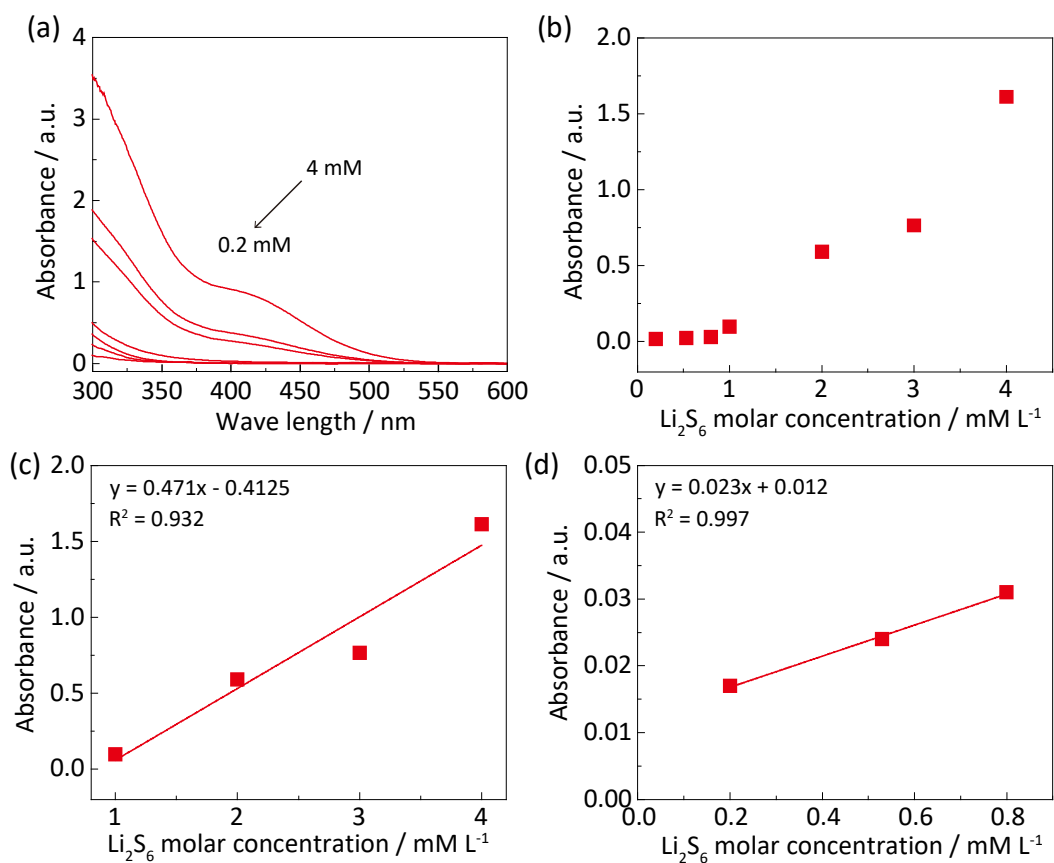
Supplementary Figure 9 (a) UV-vis absorbance curves for Li_2S_6 in 1 mol L^{-1} LiTFSI in DOL/DME electrolyte with Li_2S_6 concentration from 0.2 to 4 mmol L^{-1}; (b) Relationship between Li_2S_6 molar concentration and UV-vis absorbance; Linear fit of Li_2S_6 molar concentration to UV-vis absorbance in, (c) ultra-low, and (d) greater concentration region.
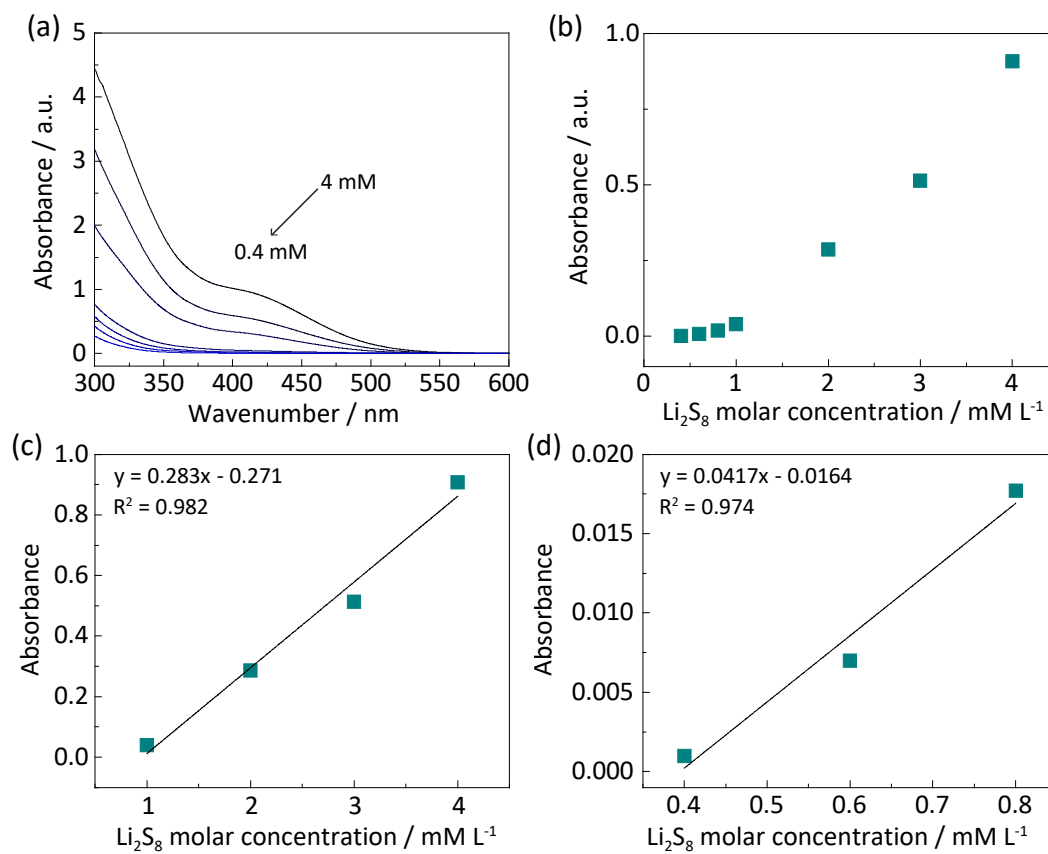
Supplementary Figure 10 (a) UV-vis absorbance curves for Li_2S_8 in 1 mol L^{-1} LiTFSI in DOL/DME electrolyte with Li_2S_8 concentration from 0.4 to 4 mmol L^{-1}; (b) Relationship between Li_2S_8 molar concentration and UV-vis absorbance; Linear fit of Li_2S_8 molar concentration to UV-vis absorbance in, (c) ultra-low, and (d) greater concentration region.
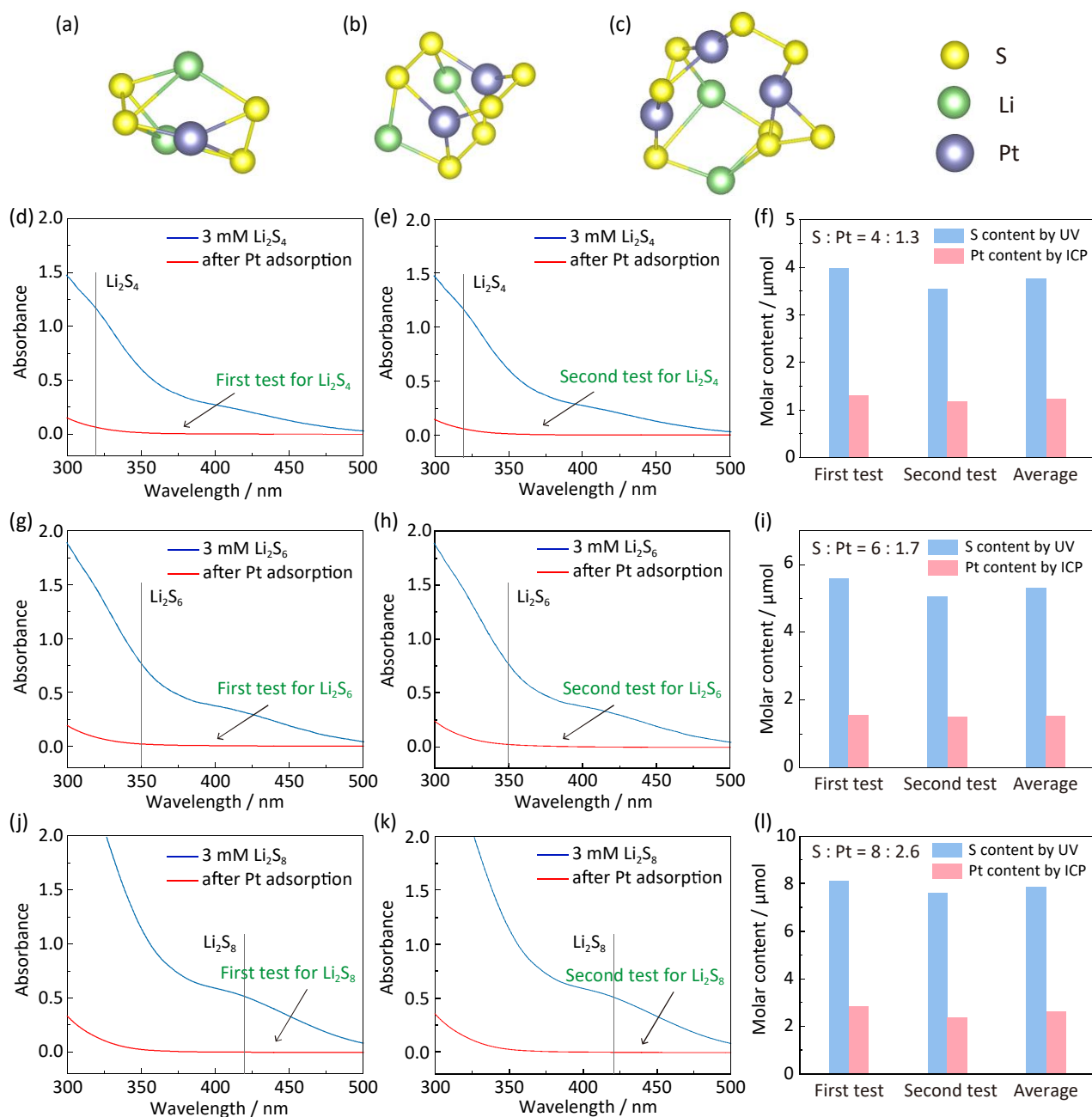
Supplementary Figure 11 Details to determine the molar ratio of Pt to S. Sulfur contents were calculated by UV-vis plots and Pt contents are determined by inductively coupled plasma–mass spectrometry (ICP-MS) test. Optimized structures (a) $Li_2Pt_1S_4$, (b) $Li_2Pt_2S_6$ and (c) $Li_2Pt_3S_8$; UV-vis plots of 3 mM Li_2S_4 and after Pt adsorption, (d) the first test and (e) second test; (f) The molar ratio of S to Pt is 4:1.3 in $Li_2Pt_yS_4$ solution; UV-vis plots of 3 mM Li_2S_6 and after Pt adsorption, (g) the first test and (h) second test; (i) The molar ratio of S to Pt is 6:1.7 in $Li_2Pt_yS_6$ solution; UV-vis plots of 3 mM Li_2S_8 and after Pt adsorption, (j) the first test and (k) second test; (l) The molar ratio of S to Pt is 8:2.6 in $Li_2Pt_yS_8$ solution;
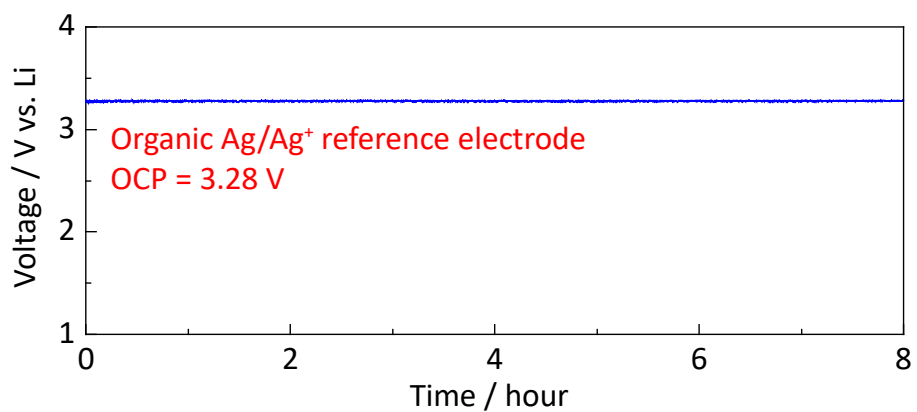
Supplementary Figure 12 Time-voltage curve of reference electrode with Li-anode in 1 mol L^{-1} LiTFSI in DOL/DME electrolyte. The organic Ag/Ag$^+$ reference electrode includes 10 mmol L^{-1} silver nitrate (AgNO$_3$) in acetonitrile (CH$_3$CN) with 100 mM tetrabutylammonium perchlorate (NBu$_4^+$ClO$_4^-$) electrolyte. The open circuit potential (OCP) is stable at 3.28 V versus Li.
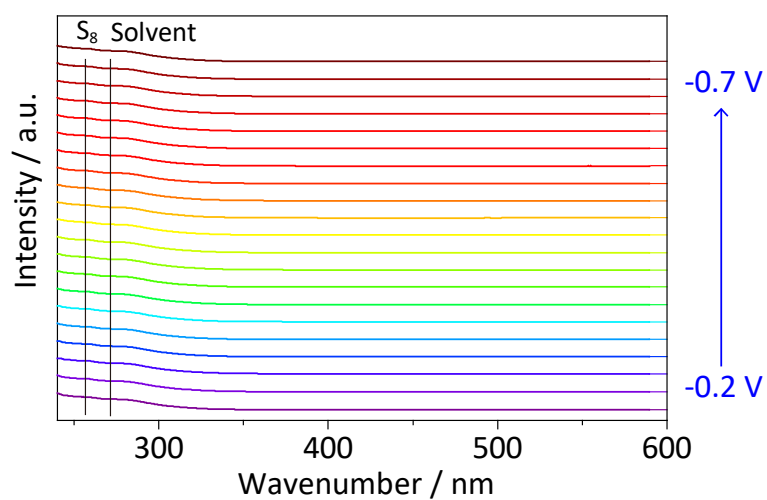
Supplementary Figure 13 UV-vis absorbance plot from -0.2 to -0.7 V at a scan of 0.2 mV s^{-1}. Peaks at ~ 256 and ~ 274 nm are assigned to dissolved S$_8$ and DOL/DME solvent. No polysulfide signals were detected in this voltage region.
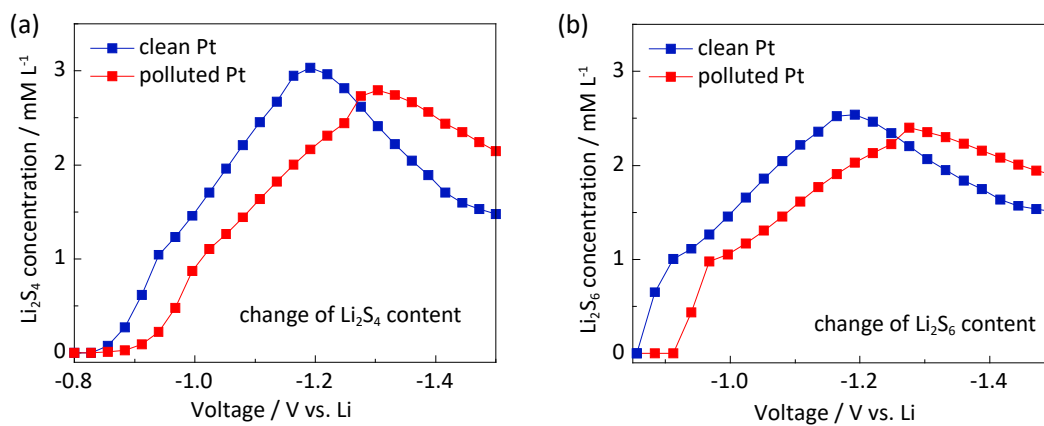
Supplementary Figure 14 Change in (a) Li$_2$S$_4$ and (b) Li$_2$S$_6$ concentration with clean Pt catalyst and polluted Pt catalyst based on UV-vis test. The clean Pt catalyst demonstrates greater activity to catalyze sulfur reduction to polysulfides (voltage > -1.2 V), and from polysulfides to Li$_2$S (voltage < -1.2 V).
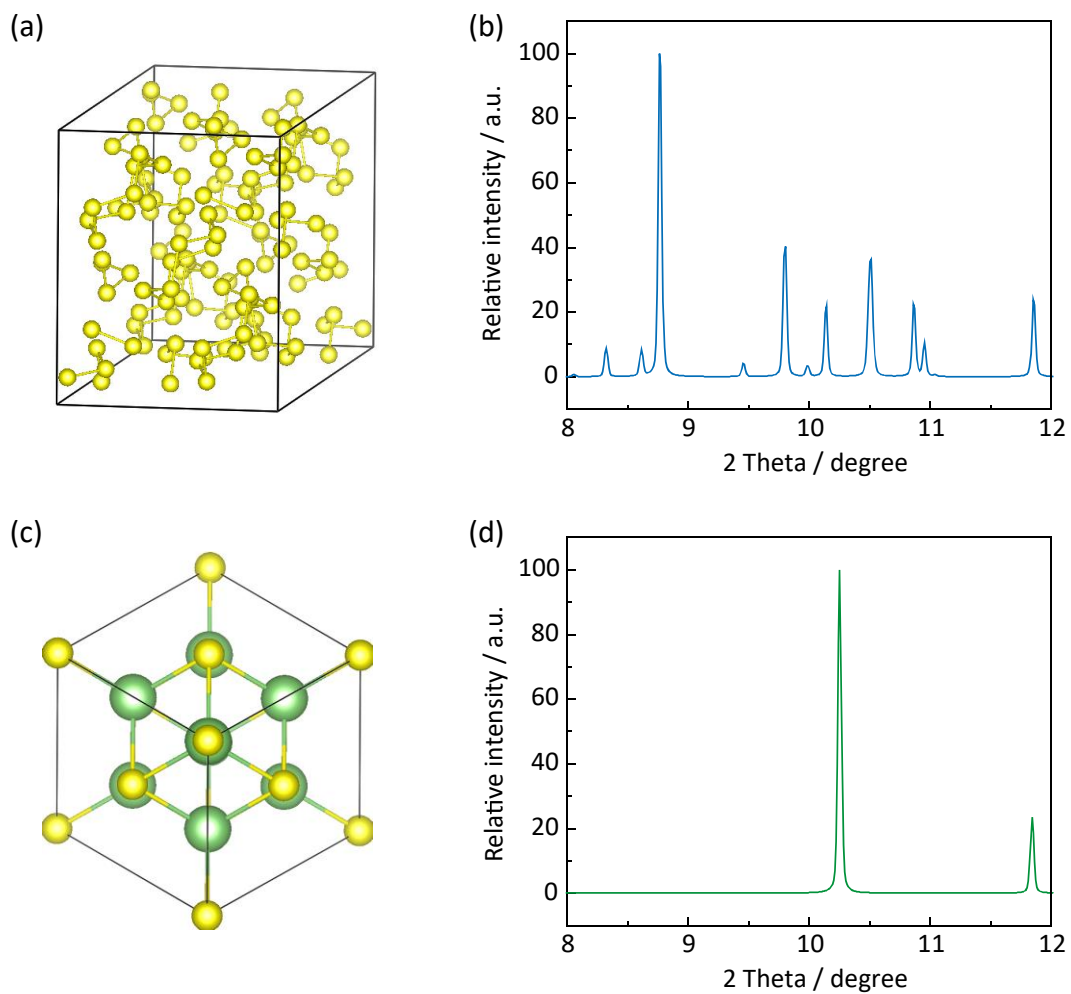
Supplementary Figure 15 Computed model for (a) sulfur and (b) simulated XRD patterns. Model for (c) Li₂S and (d) simulated XRD patterns. Wavelength is 0.5903 nm. The peak positions agree well with *in-situ* synchrotron X-ray diffraction.
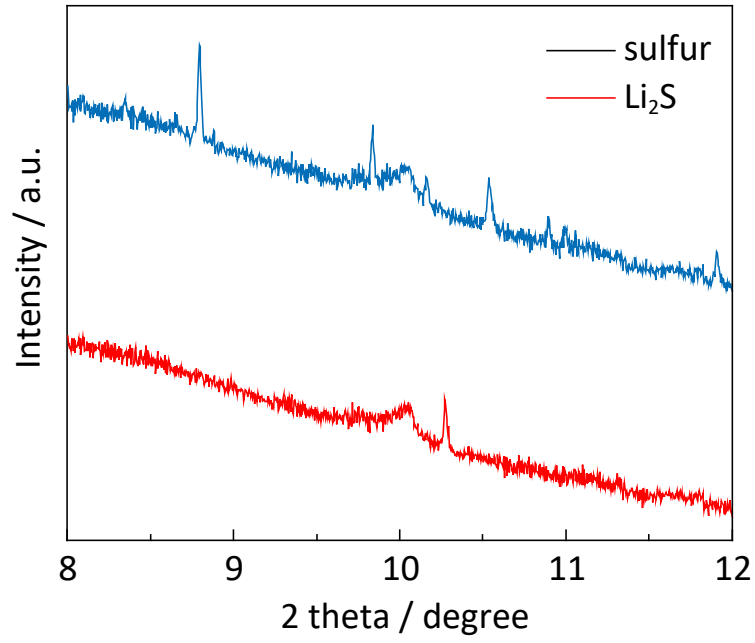
Supplementary Figure 16 Characteristic peaks for sulfur and Li₂S for in-situ synchrotron X-ray diffraction. Wavelength is 0.5903 nm.
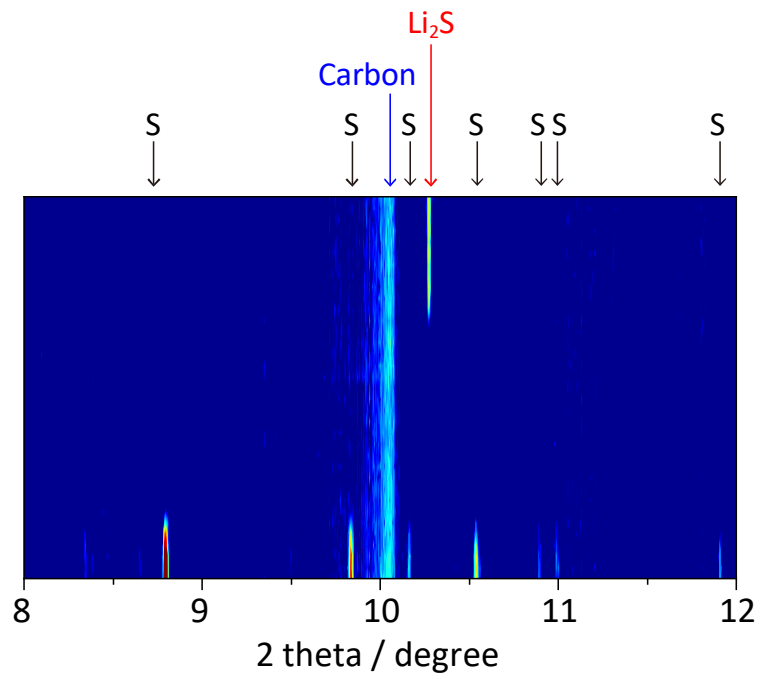
Supplementary Figure 17 *In-situ* synchrotron XRD contour pattern for sulfur cathodes with clean Pt catalyst.
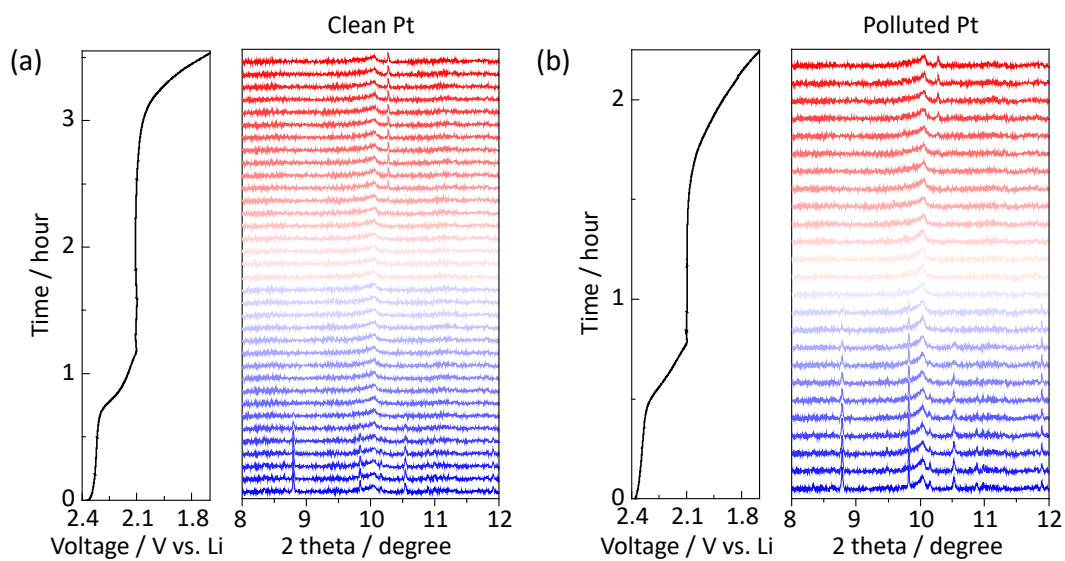
Supplementary Figure 18 *In-situ* synchrotron XRD stacked plots and corresponding discharge curves for sulfur cathodes with (a) clean Pt catalyst and (b) polluted Pt catalyst.
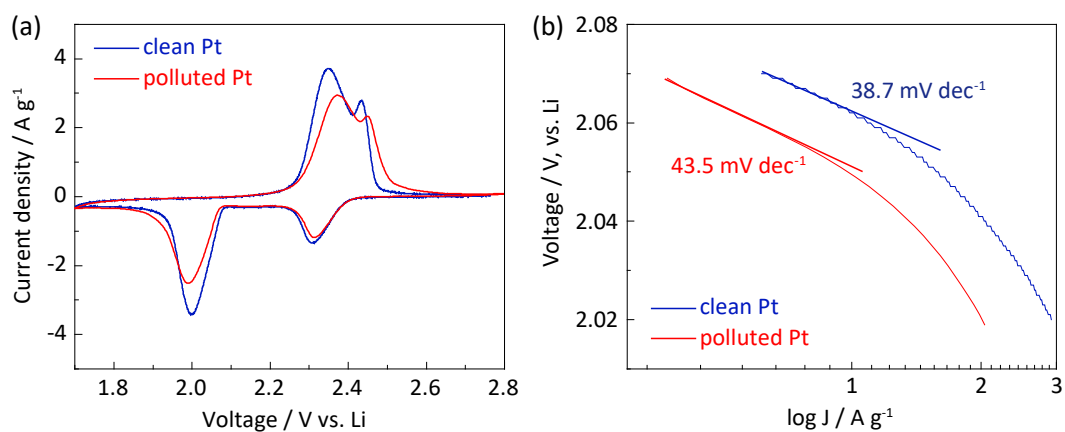
Supplementary Figure 19 (a) Cyclic voltammetry (CV) curves of Li-S batteries with clean Pt and polluted Pt catalysts; (b) Corresponding Tafel plots for the second reduction peak. Clean Pt presents greater activity as evidenced by higher peak current density and lower Tafel slope.
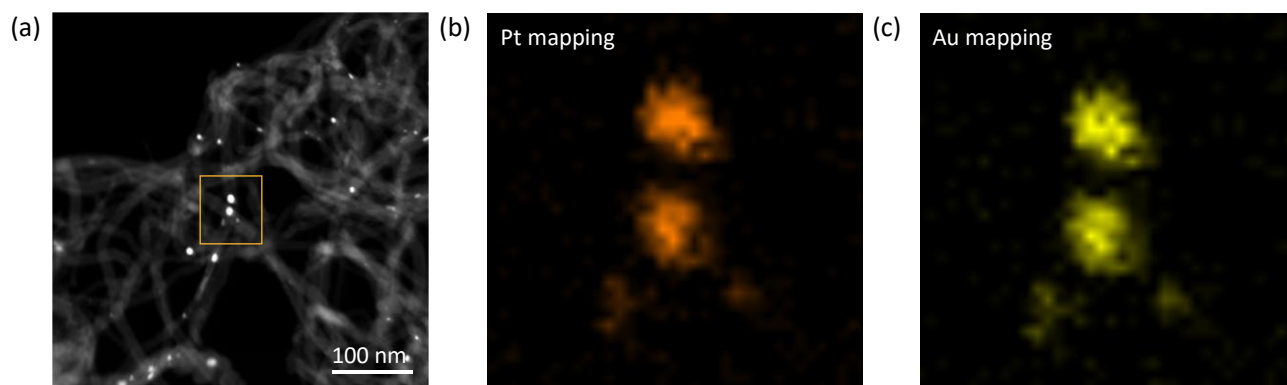
Supplementary Figure 20 (a) Transmission electron microscopy (TEM) image of PtAu nanoparticle on carbon nanotube. The yellow line presents the mapping area; (b) Pt elemental mapping and (c) Au elemental mapping. This suggests the efficient alloying between Pt and Au in PtAu catalyst.
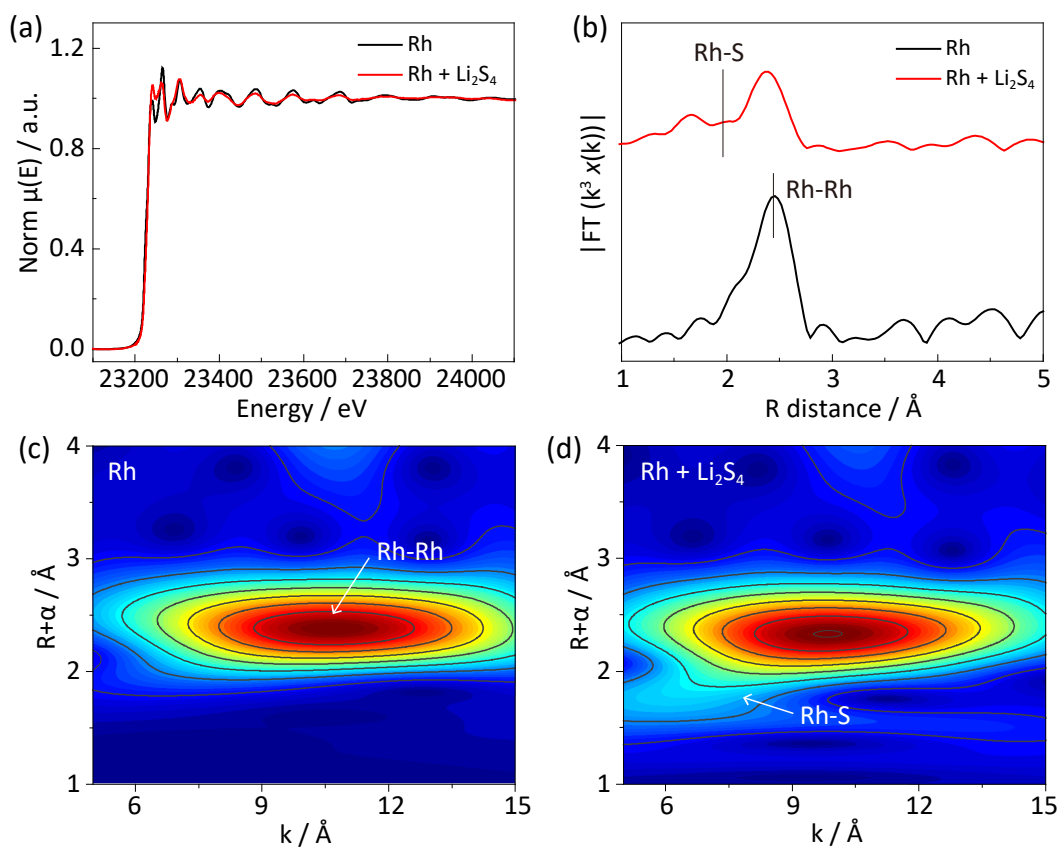
Supplementary Figure 21 (a) Rh K-edge X-ray adsorption curves for Rh and Rh with Li_2S_4 adsorption; (b) R-space transform for Rh and Rh with Li_2S_4 adsorption; Wave-transform for (c) Rh and (d) Rh with Li_2S_4 adsorption.
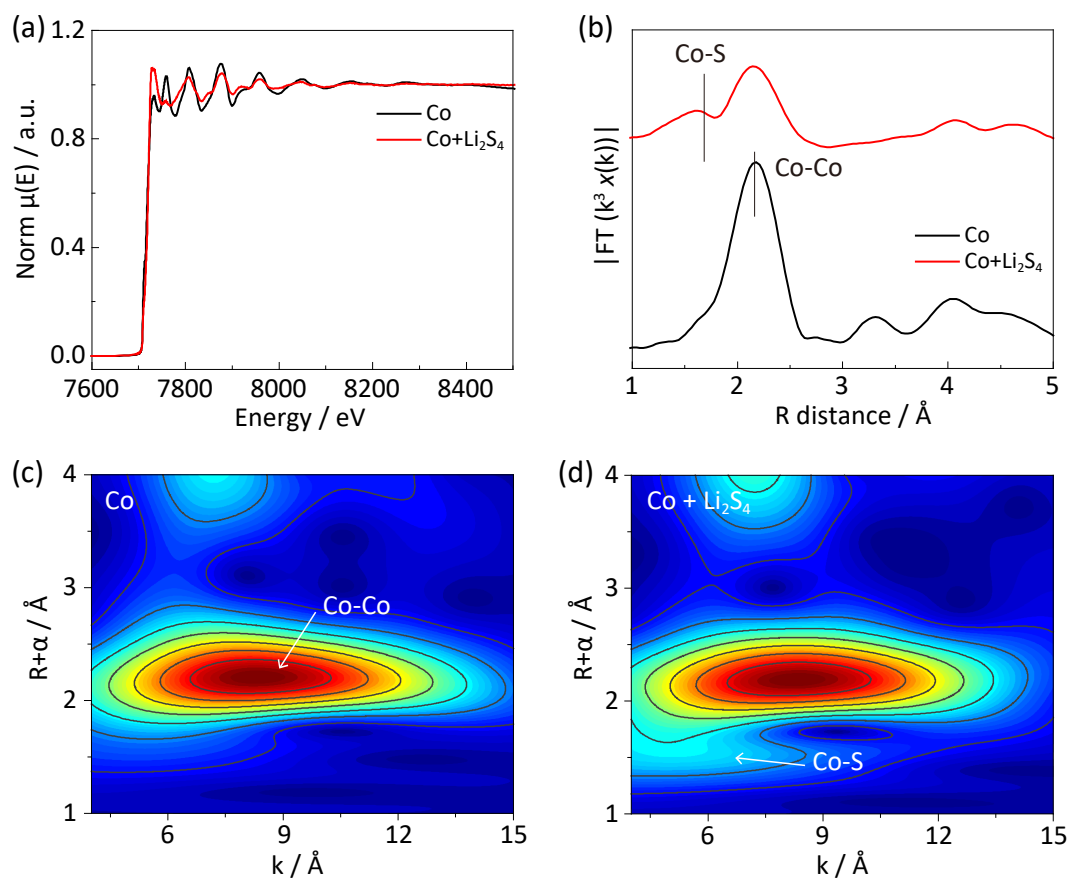
Supplementary Figure 22 (a) Co K-edge X-ray adsorption curves for Co and Co with Li_2S_4 adsorption; (b) R-space transform for Co and Co with Li_2S_4 adsorption; Wave-transform for (c) Co and (d) Co with Li_2S_4 adsorption.

Chapter 8: Conclusions and Perspectives

8.1 Conclusions

This thesis focuses on revealing the conversion mechanisms in metal-sulfur batteries using theoretical computations and in-situ spectroscopy. It includes the designs of both metal anodes and sulfur cathodes. According to the works in this thesis, the following conclusions can be drawn:

1. We have shown a design principle of Li host for lean-electrolyte Li metal anode. To restrain the electrolyte loss, the uneven Li nucleation/deposition and the crack-reformation of high-surface-area derived SEI layer need to be simultaneously controlled. Such a design principle is concluded by studying the Li nucleation and deposition behavior with means of in-situ spectroscopy, including the in-situ synchrotron XRD, in-situ Raman spectra and in-situ EIS spectra. As a proof of concept, we demonstrated a low-surface-area but defective 3D graphene for use as Li anode host. It was found that abundant carbon defects can guide Li nucleation and control the sequential Li growth structure. The low specific surface area contributes to a more homogenous Li/electrolyte interface, which decreases the exposed area of SEI layer into the electrolyte, restraining the crack-reformation of SEI layer and electrolyte consumption. As a result, such a Li host can achieve stable cycles with desirable areal capacities under lean electrolyte conditions.

2. We have demonstrated that sulfur can be electrochemically oxidized in ionic liquid with high reversibility. The reaction pathways, $AlSCl_7$ oxidized products, and SCl_3^+ intermediates are well confirmed by means of *in-situ* synchrotron-based analysis, high-resolution microscopic images, spectroscopic analysis, and theoretical computations. The

electrochemical oxidation from sulfur to AlSCl$_7$ is highly reversible with a stable CE% of ~94%, and the oxidation process is workable within a wide-range of electrochemical potentials. As a result, the Al−S battery based on sulfur oxidation process can run steadily over 200 cycles around ~1.8 V, which is the highest operation voltage for Al−S batteries. It is expected that the sulfur oxidation process can be coupled with other metal anodes for various metal−sulfur batteries, not limited to Al−S batteries.

3. We have for the first time, formulated the design principles to rationally optimize SRR activity via controlling the Gibbs free energy of polysulfide species on the catalysts surface. SRR activity and its origin have been confirmed via series of electrochemical testing, theoretical computations, synchrotron-based analyses and *in-situ* spectroscopy. As a result, SRR reactivity trend is established by quantitatively correlating with *3d*-orbital charges of transition-metal clusters, Gibbs free energies of polysulfides and SRR catalytic activity. Optimized SRR catalyst significantly boosts battery performance, especially at high charge-discharge rate with high areal sulfur loadings. The well-established relationship between apparent SRR activity, reaction thermodynamics and intrinsic electronic structure of materials, will benefit the understanding of SRR mechanism.

4. The presented comparative study of *3d*, *4d*, *5d* metal catalysts demonstrates that the lean-electrolyte sulfur reduction activity can be boosted by controlling the catalyst-solvent interactions. The binding between metal catalysts and solvent molecules have been confirmed via synchrotron-based analysis, *in-situ* spectroscopy and theoretical computations, which showed that the metal-solvent binding strength determines the lean-electrolyte SRR activity, electrolyte consumption and battery stability. Benefitting from the strong binding

between solvent molecules and Co catalyst, the Li−S battery achieves stable cycling with only 0.22% capacity decay per cycle under lean-electrolyte conditions. Compared to the battery with flooded electrolyte, the lean-electrolyte battery with an E/S mass ratio of 4.2 maintains 79% of its capacity. The revealed role of the catalyst-solvent binding should be helpful for the design of electrocatalysts for metal−sulfur batteries under lean-electrolyte conditions.

5. We clarify the failure mechanism of SRR catalysts caused by electrophilic substitution between polysulfides and catalyst. This leads to the surface vulcanization of catalyst and more severely, the concomitant catalyst dissolution into electrolyte. Totally different from other electrocatalytic reactions, the electrophilic substitution between polysulfides and catalyst undergoes a slow chemical process, which does not depend on applied voltage overpotentials. The catalyst failure is confirmed via a series of operando spectroscopic techniques including in-situ synchrotron X-ray diffraction, Infrared and ultraviolet–visible spectra together with theoretical computations. The proposed catalyst failure mechanism appears to be universal that can be extended to a group of 3d, 4d and 5d (e.g. Co, Rh and Pt) metal catalysts.

8.2 Perspectives

Although many progresses have been made in metal-sulfur batteries, additional efforts are still required to unravel the fundamental mechanisms and promote practical battery applications. These include:

1. Theoretical computations under realistic conditions. The current computational simulations are generally based on slab models under 0 K and vacuum conditions. Further

computations need to be investigated by fully considering the real battery conditions, such as local electrolyte environments and applied potentials. This would provide more precise information and practical guidance for metal-sulfur batteries.

2. In-situ spectroscopy with high time resolution and signal sensitivity. Despite the fast-developed in-situ spectroscopic techniques, the time resolution and signal sensitivity still remains unsatisfactory. Further works need to be carried out improve the time resolution and signal sensitivity for in-situ spectroscopy. These improvements require the development of instrumental techniques and more effective design of in-situ cells.

3. Transforming high theoretical energy density into practical uses. Despite the high theoretical energy density of metal-sulfur batteries, the actual energy density at the device level is still not high. Further work needs to be carried out to increase the energy density of metal-sulfur batteries. This requires to improve the utilization of both sulfur cathode and metal anode with high loadings of active materials, and simultaneously to decrease the usage of non-active part, such as separator, current collectors and electrolyte.

4. Lean electrolyte conditions. The operation of metal-sulfur batteries is highly dependent on the dosage of electrolyte. High specific capacity and stable cycling need to be retained under lean electrolyte conditions. This requires the exploration of novel electrolyte or electrolyte additives, as well as the host design for sulfur cathodes and metal anodes.

5. Fast-charge property. The current metal-sulfur batteries generally operate at slow discharge-charge rate due to the conversion-type electrochemical process of both sulfur cathode and metal anodes. The fast-charge property needs host or catalyst design to accelerate the conversion kinetic of sulfur cathode and metal anodes.

6. Cycling stability. Severe polysulfide shuttle effect and dendrite growth restrict the cycling stability of metal-sulfur batteries. These problems need to be further addressed by efficient design of sulfur host and protection of metal anodes.

7. Low cost. Sulfur is a cheap cathode material, however, the excessive dosage of metal anode and electrolyte increase the cost of battery. It is critical to decrease their usage and explore low-cost alternative materials in batteries.

All in all, metal-sulfur batteries represent a significant contribution in both fundamental studies and practical uses in battery applications. The combination of computational methodology and in-situ spectroscopy will elucidate more precise conversion mechanisms in metal-sulfur batteries, which benefits the design of more practical metal-sulfur batteries.

Appendix: Publications during PhD Candidature

[1] <u>Huan Li</u>, Dongliang Chao, Biao Chen, Xiao Chen, Clarence Chuah, Youhong Tang, Yan Jiao, Mietek Jaroniec, and Shi-Zhang Qiao*. Revealing principles for design of lean-electrolyte lithium metal anode via in-situ spectroscopy. *Journal of the American Chemical Society* **2020**, *142* (4), 2012-2022. (**ESI Highly Cited Paper**)

[2] <u>Huan Li</u>, Rongwei Meng, Yong Guo, Biao Chen, Yan Jiao, Chao Ye, Yu Long, Anton Tadich, Quan-Hong Yang, Mietek Jaroniec and Shi-Zhang Qiao*. Reversible electrochemical oxidation of sulfur in ionic liquid for high-voltage Al−S batteries. *Nature Communications* **2021,** *12* (1), 5714.

[3] <u>Huan Li</u>, Rongwei Meng, Anton Tadich, Yan Jiao, Chao Ye, Xiao Chen, Qinfen Gu, Bernt Johannessen, Kenneth Davey and Shi-Zhang Qiao*. Activity origin and design of catalysts for sulfur reduction electrocatalysis*, **To be submitted**.

[4] <u>Huan Li</u>, Rongwei Meng, Yong Guo, Chao Ye, Debin Kong, Bernt Johannessen, Mietek Jaroniec and Shi-Zhang Qiao*. Unraveling the catalyst-solvent interactions in lean-electrolyte sulfur reduction electrocatalysis in Li−S batteries*, *Angew Chemie International Edition*, **In revision**.

[5] <u>Huan Li</u>, Yan Jiao, Jieqiong Shan, Junnan Hao, Chao Ye, Tao Ling, Qinfen Gu, Bernt Johannessen and Shi-Zhang Qiao[*]. Operando unraveling the catalyst failure in sulfur reduction electrocatalysis. **To be submitted**.

[6] Dongliang Chao, Wanhai Zhou, Fangxi Xie, Chao Ye, **<u>Huan Li</u>**, Mietek Jaroniec and Shi-Zhang Qiao*. Roadmap for advanced aqueous batteries: From design of materials to applications. *Science Advances* **2020,** *6* (21), eaba4098. (**ESI Hot Paper**)

[7] Chao Ye, Dongliang Chao, Jieqiong Shan, **<u>Huan Li</u>**, Kenneth Davey and Shi-Zhang Qiao*. Unveiling the advances of 2D materials for Li/Na-S batteries experimentally and theoretically. *Matter* **2020,** *2* (2), 323-344. (**ESI Highly Cited Paper**)

[8] Fangxi Xie, **<u>Huan Li</u>**, Xuesi Wang, Xing Zhi, Dongliang Chao, Kenneth Davey and Shi-Zhang Qiao*. Mechanism for zincophilic sites on zinc-metal anode hosts in aqueous batteries. *Advanced Energy Materials* **2021,** *11* (9), 2003419. (**ESI Hot Paper**)

[9] Chao Ye, Huanyu Jin, Jieqiong Shan, Yan Jiao, **<u>Huan Li</u>**, Qinfen Gu, Kenneth Davey,

Haihui Wang and Shi-Zhang Qiao*. A Mo_5N_6 electrocatalyst for efficient Na_2S electrodeposition in room-temperature sodium-sulfur batteries. *Nature Communications* **2021,** *12* (1), 7195.

[10] Xianlong Zhou, Juncai Dong, Yihan Zhu, Lingmei Liu, Yan Jiao, **Huan Li**, Yu Han, Kenneth Davey, Qiang Xu, Yao Zheng, and Shi-Zhang Qiao*. Molecular scalpel to chemically cleave metal-organic frameworks for induced phase transition. *Journal of the American Chemical Society* **2021,** *143* (17), 6681-6690.

[11] Xin Xu, Dongliang Chao, Biao Chen, Pei Liang, **Huan Li**, Fangxi Xie, Kenneth Davey and Shi-Zhang Qiao*. Revealing the magnesium-storage mechanism in mesoporous bismuth via spectroscopy and Ab-Initio simulations. *Angewandte Chemie International Edition* **2020,** *59* (48), 21728-21735.

[12] Xin Xu, Chao Ye, Dongliang Chao, Biao Chen, **Huan Li**, Cheng Tang, Xiongwei Zhong and Shi-Zhang Qiao*. Synchrotron X-ray spectroscopic investigations of in-situ-formed alloy anodes for magnesium batteries. *Advanced Materials* **2021**, e2108688.

[13] Shao-Jian Zhang, Junnan Hao, **Huan Li**, Peng-Fang Zhang, Zu-Wei Yin, Yu-Yang Li, Bingkai Zhang, Zhan Lin and Shi-Zhang Qiao*. Polyiodide confinement by starch enables shuttle-free Zn-Iodine batteries. *Advanced Materials* **2022,** *34* (23), e2201716.

[14] Biao Chen, **Huan Li**, Huaxiong Liu, Xinqian Wang, Fangxi Xie, Yida Deng, Wenbin Hu, Kenneth Davey, Naiqin Zhao and Shi-Zhang Qiao*. 1T'-ReS_2 confined in 2D-honeycombed carbon nanosheets as new anode materials for high-performance sodium-ion batteries. *Advanced Energy Materials* **2019,** *9* (30), 1901146.